INFORMATION TO USERS

This manuscript has been reproduced from the microfilm master. UMI films the text directly from the original or copy submitted. Thus, some thesis and dissertation copies are in typewriter face, while others may be from any type of computer printer.

The quality of this reproduction is dependent upon the quality of the copy submitted. Broken or indistinct print, colored or poor quality illustrations and photographs, print bleedthrough, substandard margins, and improper alignment can adversely affect reproduction.

In the unlikely event that the author did not send UMI a complete manuscript and there are missing pages, these will be noted. Also, if unauthorized copyright material had to be removed, a note will indicate the deletion.

Oversize materials (e.g., maps, drawings, charts) are reproduced by sectioning the original, beginning at the upper left-hand corner and continuing from left to right in equal sections with small overlaps.

Photographs included in the original manuscript have been reproduced xerographically in this copy. Higher quality 6" x 9" black and white photographic prints are available for any photographs or illustrations appearing in this copy for an additional charge. Contact UMI directly to order.

UMI®

.

ELECTRONIC STRUCTURE INVESTIGATIONS OF MULTIPLE BONDING BETWEEN
ATOMS: FROM METAL-NITROGEN TRIPLE BONDS TO METAL-METAL TRIPLE AND
QUADRUPLE BONDS

by

Jason Blaine English

_____

A Dissertation Submitted to the Faculty of the

DEPARTMENT OF CHEMISTRY

In Partial Fulfillment of the Requirements
For the Degree of

DOCTOR OF PHILOSOPHY

In the Graduate College

THE UNIVERSITY OF ARIZONA

2002

UMI Number: 3053887

UMI®

THE UNIVERSITY OF ARIZONA ®
GRADUATE COLLEGE

As members of the Final Examination Committee, we certify that we have

read the dissertation prepared by __Jason Blaine English__

entitled __ELECTRONIC STRUCTURE INVESTIGATIONS OF MULTIPLE BONDING__

__BETWEEN ATOMS: FROM METAL-NITROGEN TRIPLE BONDS TO__

__METAL-METAL TRIPLE AND QUADRUPLE BONDS__

and recommend that it be accepted as fulfilling the dissertation

requirement for the Degree of __Doctor of Philosophy__

Professor Dennis L. Lichtenberger	6/25/02
	Date
Professor John H. Enemark	6/13/02
	Date
Professor F. Ann Walker	6/13/02
	Date
Professor Steven G. Kukolich	6/13/02
	Date
Professor G. Krishna Vemulapalli	6/13/02
	Date

Final approval and acceptance of this dissertation is contingent upon
the candidate's submission of the final copy of the dissertation to the
Graduate College.

I hereby certify that I have read this dissertation prepared under my
direction and recommend that it be accepted as fulfilling the dissertation
requirement.

Dissertation Director   6/25/02
                                   Date

STATEMENT BY AUTHOR

This dissertation has been submitted in partial fulfillment of requirements for an advanced degree at The University of Arizona and is deposited in the University Library to be available to borrowers under rules of the Library.

Brief quotations from this dissertation are allowable without special permission, provided that accurate acknowledgment of the source is made. Requests for permission for extended quotation from or reproduction of this manuscript in whole or in part may be granted by the head of the major department or the Dean of the Graduate College when in his or her judgment the proposed use of the material is in the interests of scholarship. In all other instances, however, permission must be obtained from the author.

SIGNED: _Jason B. English_

ACKNOWLEDGMENTS

This work would not have been possible without the aid of a number of people. I am indebted to the following persons for their patience, help, and understanding during my graduate work. I had the privilege to work under the direction of Dennis Lichtenberger. The freedom he gave me to pursue my interests was much appreciated.

A number of my fellow graduate students have been instrumental in the completion of this work. These include Dr. John Pollard, Dr. Andrew Uplinger, Dr. Huajun Fan, Dr. Julia Padden Metzker, Kristie Ruddick, and Tonja Bill. I am particularly indebted to Dr. Matthew Lynn, who collected the photoelectron spectra of $M_2(mhp)_4$ (M = Mo, W) and taught me how to use the ADF and Fenske-Hall programs. He also taught me the proper synthetic techniques necessary for the synthesis of air-sensitive compounds.

I had the privilege of working with Aaron Riechers during the completion of this work. His enthusiasm for science always made each day just a little bit better.

I am indebted to Dr. Malcolm Chisholm and his graduate student Andy Kidwell for providing the $(RO)_3M \equiv N$ samples (Chapter 3). In addition, they completed the reactivity studies that are included in this work. I found this project to be both challenging and rewarding.

I thank Dr. Nadine Gruhn for her guidance in all things related to the photoelectron spectroscopy facility. Her patience and guidance while teaching me the art of data collection and instrument troubleshooting were greatly appreciated.

Surviving graduate school would be much more difficult without the love and encouragement from friends and family. I am particularly grateful to my parents and my extended family. Yes, I am finally finished!

I must also thank Dr. Paul Ayers for always reminding me of the importance of theory to the further development of chemistry.

I thank Dona Myers for all her help.

A special thanks goes to Buffy Ann Summers and the Scooby gang for always providing comic relief and giving me a break from work.

I wish to thank my committee members: Dr. John Enemark, Dr. Anne Walker, Dr. Steven Kukolich, and Dr. Krishna Vemulapalli for their assistance during my graduate career.

I thank the National Science Foundation for the support of this work.

To my family

TABLE OF CONTENTS

TABLE OF CONTENTS - *Continued*

TABLE OF CONTENTS - *Continued*

LIST OF TABLES

LIST OF TABLES - *Continued*

LIST OF TABLES - *Continued*

LIST OF ILLUSTRATIONS

LIST OF ILLUSTRATIONS - *Continued*

LIST OF ILLUSTRATIONS - *Continued*

ABSTRACT

The nature of multiple bonding involving transition metal atoms has been explored via photoelectron spectroscopic and computational studies of molecules containing metal-metal quadruple and triple bonds as well as of molecules containing formal metal-nitrogen triple bonds. The principles governing the nature of the multiple bonding in these systems are similar whether the multiple bonding occurs between two transition metals or between a transition metal and a nitrogen atom.

First, the electronic structures of the $R_3M \equiv N$ molecules, where R = ^tBuO (Cr, Mo, W); ^iPrO (Mo); $(CH_3)_2CF_3CO$ (Mo); and Cl (Mo), are examined by photoelectron spectroscopy in conjunction with density functional calculations. To assign the features seen in the photoelectron spectra, close attention is paid to the effects of (1) metal substitution and (2) alkoxide (or Cl) substitution. Examination of the photoelectron spectra of the full series of alkoxide-substituted molecules allows the relative positions of the ionizations from the $M \equiv N$ σ and π orbitals to be identified. Of great importance to the electronic structure of these molecules are the alkoxide orbital combinations that mix strongly with the $M \equiv N$ σ and π orbitals. The importance of the ancillary ligand combinations is clearly demonstrated by the photoelectron spectroscopic and computational studies of $Cl_3Mo \equiv N$. The replacement of the alkoxide ligand with chlorides greatly simplifies the resultant photoelectron spectrum, allowing all of the valence ionizations to be assigned.

Next, the bonding in the $M_2X_4(PMe_3)_4$ molecules, where M = Mo (X = Cl, Br); W (X = Cl); and Re (X = Cl, Br, I), is explored by photoelectron spectroscopic investigations in conjunction with electronic structure calculations. From these investigations, the ionizations from the metal-based orbitals as well as several ligand-based orbitals have been assigned. The

first ionization energies of both the molybdenum (δ) and rhenium (δ^*) molecules decrease as the electronegativity of the halide increases. The origin of this inverse halide effect is explored.

Finally, the nature of the quadruple metal-metal bond in the $M_2(chp)_4$ molecules (M = Cr, Mo, W; chp = 2-chloro-6-oxo-pyridinate) is probed. For all three metal systems, an ionization from the M_2 δ orbital can be seen. This is only the second time a distinct ionization feature has been noted for ionization of the δ orbital from a dichromium molecule. Comparisons with the previously studied $M_2(mhp)_4$ molecules (mhp = 6-methyl-2-oxo-pyridinate) allow for a better understanding of the electronic structure of these molecules.

CHAPTER 1

INTRODUCTION

At the heart of modern chemical investigations is a desire to understand the unique

properties of atoms and molecules. Each molecule has its own set of properties that serve as its

fingerprint, distinguishing it from all other molecules. Whether one is focusing on

electrochemical, spectroscopic, structural, or reactivity studies, etc., the primary goal of chemical

investigations is the determination of some fundamental property or properties of a molecule.

Each spectroscopic technique reveals a part of the overall character of the molecule. In addition,

reactivity studies can reveal clues about molecular properties as diverse as the relative acidity or

basicity of the molecule to the molecular charge distribution within the molecule. When the

information from the investigations is combined, one can obtain a deeper understanding of the

electronic structure and reactivity of the molecule.

Modern chemical research is driven by the desire to understand the reactivity of

molecules from an experimental viewpoint as well as from a theoretical viewpoint. Whether one

is working towards the design of a new anticancer agent or designing a new polymerization

catalyst, one must have a firm knowledge of the molecular and electronic structure of the system

in order to achieve the desired goals. It has long been known that the reactivity of molecules is

dependent on the frontier orbital energies and the charge distribution in molecules.[1,2] Hence, the

first step towards understanding the reactivity in any system is the obtainment of a thorough

knowledge of its electronic structure.

The present study focuses on the electronic structure and reactivity of molecules

containing multiple bonds between atoms. Specifically, this work focuses on the bonding in

systems containing formal metal-nitrogen triple bonds as well as systems containing metal-metal

triple and metal-metal quadruple bonds. While the existence of a quadruple bond is reserved

solely for the description of the bonding between two transition metal atoms, a triple bond can exist between (1) two nonmetal atoms: N_2, (2) a transition metal and a heteroatom: $(^tBuO)_3Mo\equiv N$, or (3) two transition metal atoms: $Mo_2(O^tBu)_6$. It follows that the transition metal-nitrido molecules serve as a bridge between the simple diatomic molecules and the metal-metal multiple bonds. As such, they are of interest to furthering our knowledge of multiple bonding.

Given that the overall goal of this work is to study the multiple bonding that occurs between atoms, a major portion of the work, Chapters 3 and 4, focuses on the bonding in molecules containing triple bonds between a transition metal center and a nitrogen atom. The

1.1
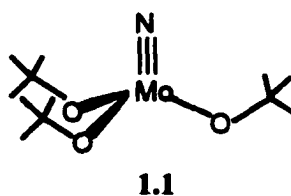
molecular structure of a single $(^tBuO)_3Mo\equiv N$ molecule is presented in **1.1**. Interestingly, the molybdenum and tungsten analogs exist as extended linear polymers in the solid state,[3] but the chromium analog shows no propensity to associate into a polymeric system.[4] The molecular structures of the other alkoxide-substituted species have the same generalized structure. The current interest in molecules containing metal-nitrogen triple bonds originates from the early work of Dehnicke and Strähle who determined that terminal nitrido ligands bond strongly to transition metal atoms.[5] Both molybdenum and tungsten nitrides are known to have significant catalytic properties.[6-10]

Transition metal-nitrogen triple bonds are inorganic functional groups with diverse reactivities, ranging from stabilizing transition metals in high oxidation states to serving as the

center of reactivity in the molecule.[11] Some of the common reactions known to involve the

metal-nitrogen triple bond are nitrogen transfer reactions and metathesis reactions.[12-16]

The second major focus of this work concerns the bonding that occurs between two

transition metal atoms. Because they are unique to the transition metal dimers, quadruple bonds

are of particular interest to chemists. In fact, the very concept of a quadruple bond was

questioned by Linus Pauling.[17] Our current understanding of metal-metal multiple bonding can

be traced to the work of Albert Cotton, who first recognized the existence of a metal-metal

quadruple bond.[18] It is now known that metal-metal bonding is vital to the description of the

electronic structure and reactivity of a wide variety of systems, ranging from molecules to

clusters and materials.[17] Molecules containing metal-metal bonds can also activate small

molecules like H_2,[19] CO,[20] N_2,[15] and CH_3CN.[21,22] In addition, molecules containing metal-metal

bonds can also activate alkenes and alkynes.[17,23-25] The key to understanding the electronic

structure and reactivity of extended systems lies in the accumulated knowledge from studies of

the bonding that occurs between just two transition metal atoms. To this end, Chapter 5 focuses
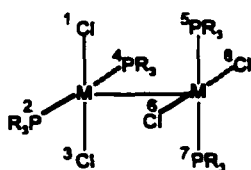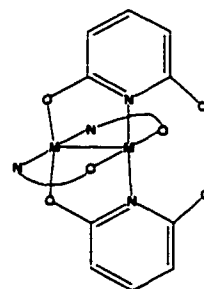
1.2   1.3

on the bonding in the well-known $M_2X_4(PMe_3)_4$ analogs, M = Mo, W, and Re and X = halide,

shown in (1.2). Chapter 6 then explores the quadruple bond that occurs in the $M_2(chp)_4$

molecules (1.3), where M = Cr, Mo, W.

General Bonding Considerations

Before delving into the specific systems studied in this work, it is useful to examine what one can learn about multiple bonding from a consideration of the bonding in a simple diatomic molecule like dinitrogen. Based on the simple Lewis formulation, dinitrogen is best described as :N≡N:. As such, it contains a triple bond and a lone pair of electrons located on both nitrogen atoms. To further explore the bonding interactions present in dinitrogen, the molecular orbital diagram is shown in Figure 1.1. At this level of sophistication, we find that the lone pairs mix extensively with the N-N σ orbital so that one cannot distinguish between the lone pairs and the N_2 σ. Due to mixing between the N(2s) and the $N(p_z)$ orbitals, the orbital combination formed from the N(pz) orbitals is destabilized above the $1\pi_u$ orbital and is best described as a nonbonding orbital.

To gain a more complete picture of the nature of the triple bond, we can look at systems where one of the nitrogen atoms has been replaced by an isoelectronic group such as methylidyne. While this concept will be developed fully in Chapter 3, a brief preview sets the stage for the importance of these bonding considerations. If the description of the triple bond in the organic nitriles correlates to that seen for N_2, then we expect the two highest occupied molecular orbitals to be attributable to the σ and π orbitals. Figure 1.2 contains a correlation diagram of the energies of the σ and π ionizations of :N≡N:, HC≡N:, and $CH_3C≡N$. Unlike N_2, the highest occupied orbital of HC≡N and CH_3C corresponds to the π orbitals, not the σ orbital. This can be attributed to a decrease in s-p mixing for these systems which, in turn, decreases the degree of destabilization of the σ brought about by the s-p mixing. In addition, the π orbital of $CH_3C≡N$ is further destabilized by a filled-filled interaction with the C-H σ orbitals of e symmetry. Interestingly, the nodal character of the orbitals remains faithful to that seen in the σ

and π orbitals of N_2. However, the σ combinations of $HC\equiv N$ and $CH_3C\equiv N$ show a definite polarization towards the nitrogen atom.

Given that the simple orbital model correctly accounts for the triple bond in N_2, HCN, and CH_3CN, it follows that one can expect orbitals of similar nodal character to be responsible for the triple bond that occurs in the $R_3M\equiv N$ molecules where (M = Cr, Mo, W; R = a π donor ligand). To reveal the similarity of the bonding in these species to the previously studied organic nitriles, a qualitative molecular orbital interaction diagram for the simplified system $M\equiv N^{3+}$ is presented in Figure 1.3.

Similarly, the generalized molecular orbital diagram used to describe the orbital interactions present in a metal-metal bond is shown in Figure 1.4. The M-M σ and σ^* orbitals result from the bonding and antibonding combinations of the two d_{z^2} orbitals. Similarly, the π and π^* orbitals are formed by the bonding and antibonding combinations of the d_{xz} and d_{yz} orbitals. The δ and δ^* orbitals are then formed by the combination of the metal ($d_{x^2-y^2}$) orbitals. Focusing on the σ and π orbitals of the metal-metal bond, we see that the nodal properties are similar to those seen for N_2, HCN, CH_3CN, and $Mo\equiv N^{3+}$. Hence, studies of the molybdenum nitrido molecules serve as a bridge between the chemistry of the simple dinitrogen molecule and the more complex molecules containing metal-metal bonds.

Looking at the simple model systems used in Figure 1.3 and Figure 1.4, we see that these idealized systems do not contain ancillary ligands. As such, use of these models to interpret the electronic structure of molecules such as $(^tBuO)_3Mo\equiv N$ or $Mo_2Cl_4(PMe_3)_4$ implies that one does not feel that the ligand orbitals significantly contribute to the the electronic structure of the metal-nitrogen and metal-metal multiple bonds. In reality, both metal-metal and metal-nitrogen multiple bonds could not exist in the absence of ancillary ligands which serve to stabilize these reactive units. Hence, a major focus of this work will be a thorough analysis of the contributions

of the ligands to the overall electronic structure of the molecules. To facilitate this analysis, the ligand orbital contributions will be determined within the constraints of group theory. For the transition metal nitrido complexes the symmetry is best described as C_{3v}, while the $M_2(chp)_4$ and $M_2X_4(PMe_3)_4$ analogs correspond to D_{2d} symmetry. These results will be used as a starting point for revealing the importance of the ancillary ligand sets in determining the overall electronic structure of the molecules studied here.
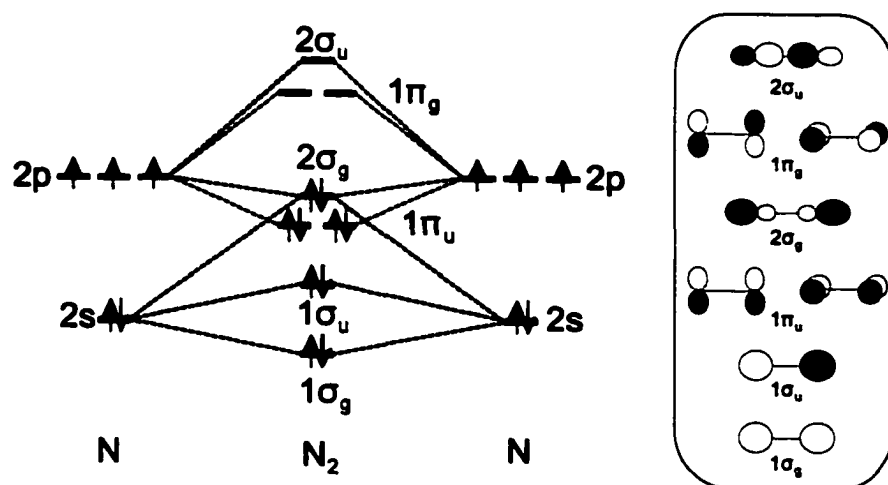
Figure 1.1. Simple Molecular Orbital Diagram for N_2.
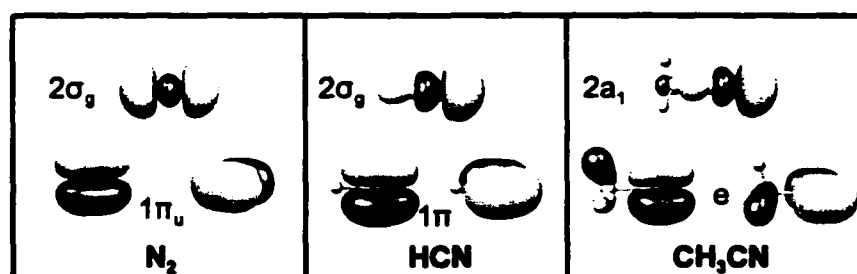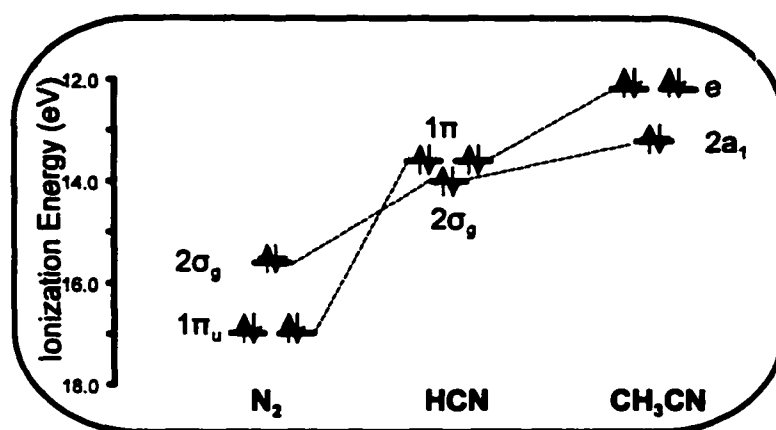
Figure 1.2. Correlation diagram of the σ and π orbitals of N_2, HCN, and CH_3CN. (Contour = 0.04).
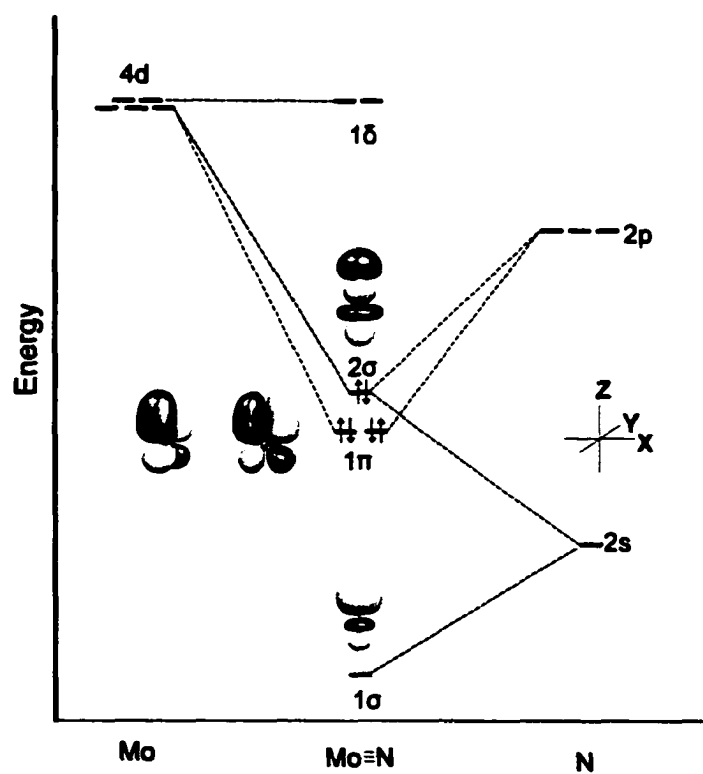
Figure 1.3. Simple molecular orbital diagram for Mo≡N.
(Contour value = 0.04).
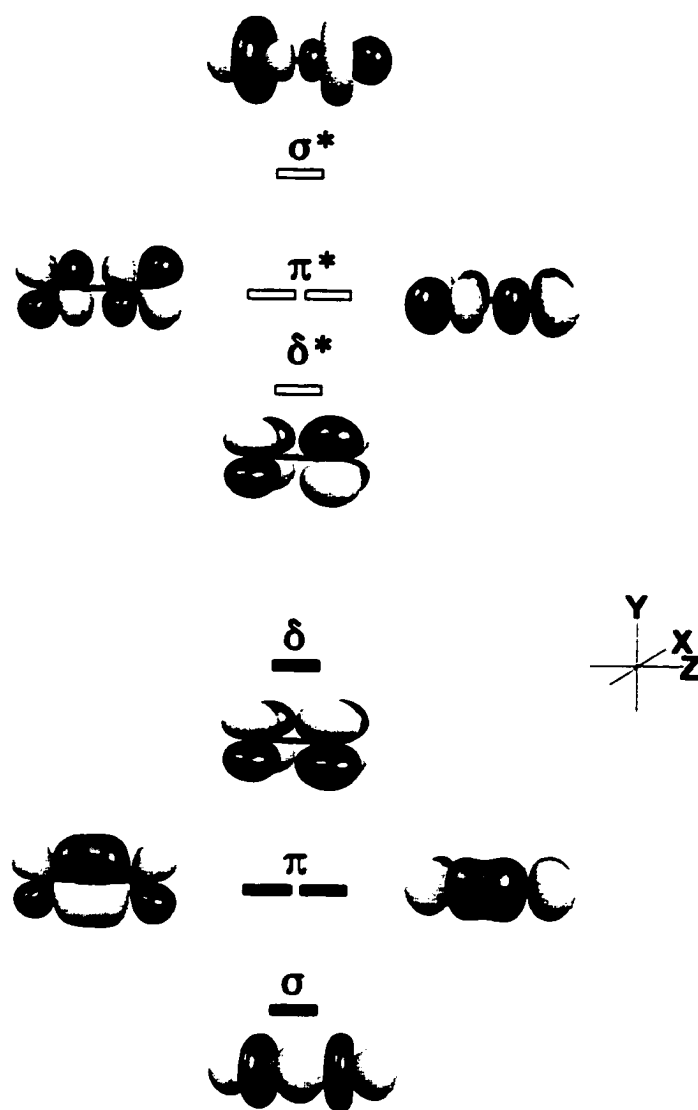
Figure 1.4. Contour plots of the traditional metal-metal bonding orbitals. (Contour = 0.04).

CHAPTER 2

EXPERIMENTAL

The detailed procedures used in this work for the collection of the photoelectron spectra

of inorganic molecules were developed by John Hubbard,[26] Glen Kellogg,[27] Mark Jatcko,[28]

Sharon Renshaw,[29] and Nadine Gruhn.[30] Even so, often these generalized procedures must be

adapted and optimized for the data collection of each molecule. The particular adaptations

required during data collection are presented in the chapters specific to the particular compounds.

This chapter provides a quick reference for the methods used in this work, including generalized

experimental details and generalized computational details.

Preparation of compounds

Due to the air sensitive nature of the compounds used in this study, all manipulations

were carried out using an Argon (Ar) or dinitrogen (N_2) atmosphere and standard air and

moisture sensitive techniques in a Vacuum Atmospheres Glovebox or Schlenk line. Solvents

were distilled from CaH_2 or K/Benzophenone ketyl. Air was removed from all solvents prior to

use in synthetic procedures via freeze-pump-thaw cycles. A list of the compounds studied

(including some not presented in this work) and the photoelectron spectroscopic details are

presented in Table 2.1 along with the name of the file folder in which the raw data can be found.

The sources of the molecules studied in this work are presented in Table 2.2.

Photoelectron spectra

The photoelectron spectra were recorded using an instrument that features a 36 cm

radius, 8 cm gap McPherson hemispherical analyzer with custom-designed sample cells,[28]

detection system, and control electronics.[31] The excitation source was a quartz lamp with the

ability, depending on operating conditions, to produce He Iα (21.218 eV) or He IIα (40.814 eV)

photons.[29] For He I data collection, the ionization energy scale was calibrated by using the $^2E_{1/2}$

ionization of methyl iodide (9.538 eV) and the Ar $^2P_{3/2}$ ionization (15.759 eV). For the He II

data collection, the energy scale was calibrated to the energy separation between the He I Ar

$^2P_{3/2}$(apparent I.E. = 35.36 eV) and the He self ionization (apparent I.E. = 24.587 eV). The argon

$^2P_{3/2}$ ionization was used as an internal calibration lock for the energy scale during He I and He II

data collection runs. For Ne I data collection, the xenon ionization ($^2P_{3/2}$) at 12.130 eV was used

as an internal calibration lock of the energy scale. Resolution (measured as full-width-at-half-

maximum of the argon $^2P_{3/2}$ ionization during He I and He II data collection) was 0.016-0.030 eV

during data collection. The resolution of the Ne I experiments was measured as the full-width-at-

half-maximum of the xenon $^2P_{3/2}$ ionization. Assuming a linear dependence of analyzer intensity

to the kinetic energy of the electrons within the energy range of these experiments, all data were

intensity corrected with the experimentally-determined analyzer sensitivity function.[32]

Because the ionization sources used to collect the photoelectron spectra are not

monochromatic, the spectra must be corrected for ionization features that do not originate from

the desired source line.[33] Specifically, spectra collected with the He Iα (1s^2 $-$ 1s2p; 21.218 eV)

were corrected for ionization features from the He Iβ line (1s^2 $-$ 1s3p; 23.085 eV), which have

3% of the intensity of the ionization features from the He Iα. The spectra collected with the He

IIα line (1s $-$ 2p; 40.814 eV) were corrected for the ionization features from the He IIβ line (1s

$-$ 3p; 48.372 eV), which has 12% of the intensity of the He IIα line. Photoelectron spectra

collected with the Ne Iα line (2s2 $-$ 2s3p; 16.85 eV) were corrected for the spin-orbit splitting of

this line, which produces a line 0.18 eV lower in energy than the main line. Unfortunately, the

intensity of the shadow is found to vary from 12-25% of the intensity of the main line as

measured from the relative intensities of the Xe $^2P_{3/2}$ ionization features produced by the spin-

orbit split ionization source line. The shadow spectrum was found to be dependent on the experimental conditions. Therefore, one must monitor the relative intensities of the Xe $^2P_{3/2}$ throughout the Ne I data collection runs. It must be recognized that these relative intensities will be an inaccurate measure of the intensity of the spin-orbit component of the Ne Iα source if other ionizations occur on top of the Xe $^2P_{3/2}$ ionizations.

Sample Handling. Depending on the nature of the sample, different techniques were used to obtain the gas-phase photoelectron spectra. In every case, the sample cells were thoroughly cleaned to ensure the purity of the spectra. Liquid samples were run from outside the instrument in a Young's tube™ attached to the vapor admission port via Swage-Lock™ fittings. In addition, Teflon ferrules and an ApezionQ® sealing compounds were used to ensure the integrity of the vacuum environment. A variable leak needle valve between the Young's tube and the instrument allowed careful control of the sample pressure present in the spectrometer. In all cases, the sample pressure, as measured by a vacuum ionization gauge, was maintained below 5×10^{-5} Torr. Solid samples were run from inside the instrument in an aluminum or stainless steel sample cell, depending on the conditions necessary for sublimation of the particular sample. The stainless steel and aluminum cells require different cleaning schemes in order to maximize the sensitivity and resolution of the experiment.

Aluminum cell. Prior to each data collection run, the cell was taken apart and cleaned with appropriate solvents (isopropanol, dichloromethane, toluene, etc.) to remove any residue or unused compounds. After the thorough cleaning, the cell was coated with DAG 154® (Acheson) and baked in the instrument to approximately 200°C. In most cases, the cell was maintained at 200°C for at least 4 hours (but usually overnight) to ensure any residual compounds were removed from the cell. All air-sensitive compounds were loaded into the cell in a Vacuum Atmospheres Drybox and placed in a Ziploc® bag for transport of the sample from the box to the

instrument. For samples requiring the cell temperature to be lower than room temperature, the

ionization cell was placed in the freezer inside the box prior to loading the sample. For samples

which were not particularly air sensitive, an alternate technique for cooling the sample involved

placing the loaded cell in a styrofoam cooler filled with dry ice. For samples that required

heating to achieve the sublimation temperature, a resistive Chromalox heating bar was employed.

The temperature was monitored by a K-type thermocouple attached directly to the cell through a

vacuum feedthrough.

In order to determine the working range of the aluminum cell, data collection was

performed using the aluminum sample cell, cleaned and coated with DAG. The temperature was

slowly raised and the spectrum was monitored for signs of decomposition. The background

scattering remains constant until around 228 °C. At this temperature, the DAG begins to

decompose and sublime from the cell surfaces. A photoelectron spectrum collected from 227 to

272 °C is presented in Figure 2.1. To obtain high quality data, the temperature of the aluminum

cell should not be taken above 225 °C to avoid complications from the decomposition of DAG.

Stainless Steel cell. To achieve good sensitivity and resolution with the stainless steel

cell, one must ensure that all surfaces are thoroughly cleaned. In general this requires that the

cell be disassembled and sonicated in dichloromethane. Of course, the choice of solvent is

directly dependent on the compound which one desires to remove from the cell. Following the

thorough cleaning, all surfaces with which photons might come into contact are polished with

emery paper. When reassembling the stainless steel cell, it is important to adjust the height of

the slit so that it matches that of the Cu tube. In addition, the stainless steel cell must be

properly aligned to achieve the maximum sensitivity and resolution.

Data Analysis. In the figures of the photoelectron spectra, the vertical length of each

data mark represents the experimental variance of that point.[34] The ionization bands are

represented analytically with the best fit of asymmetric Gaussian peaks. The number of peaks

used was the minimum necessary to get an analytical representation of the He I spectrum. For

fitting the He II spectra, the peak positions and half-widths were fixed to those of the He I fit.

The same procedure was used to fit the Ne I data.

The confidence limits for the relative integrated peak areas are ±5%. The primary source

of uncertainty is the determination of the baseline. The baseline is caused by electron scattering

and is taken to be linear over the small energy range of these spectra. The fitting procedures

used to fit the spectra have been described in more detail elsewhere.[34] The peak positions are

reproducible to ± 0.01 eV.

Computational methods

Specific details for the computational studies performed in the course of this study can

be found in the individual chapters. Nevertheless, it is useful to provide a brief overview of the

methods used in the studies. All geometries used in the computational studies were taken from

the published crystal structures and optimized to the full symmetry of the particular molecule.

When appropriate geometries were not available, full geometry optimizations were performed.

Computational work was performed using the Gaussian98[35] and ADF[36-38] computational

packages. In addition, Fenske-Hall calculations were performed on the molecules for direct

comparison to the density functional results.[39] All molecular orbital plots were made with the

Molekel® molecular visualization program.

Table 2.1. Experimental details of the photoelectron spectroscopic studies for the molecules studied in this work.

Molecule	Temp (°C)	Photon Source	Resolution	File Names	Energy Region
$Cl_3Mo\equiv N$	83 to 120	He I	18-31	jbe28.c* jbe28.f* jbe28.d*	10.2 - 13.3 8.9 - 15.7 10.6 - 12.5
		He II	13-22	jbe28.z* jbe28.y* jbe28.v* Jbe28.r* jbe28.s* jbe28.t*	10.1 - 20.0 10.2 - 13.3 10.6 - 12.50 9.8 - 25.0 10.2 - 13.3 10.6 - 12.5
		Ne I	16-30	jbe28.n* Jbe28.l* jbe28.o*	10.2 - 13.3 9.4 - 15.0 10.6 - 12.5
$Cl_3CC\equiv N$	N/A	He I	17-27	jbe30.f*	10.3 - 15.0
		He II	N/A	jbe30.z* jbe30.y*	10.5 - 20.0 10.3 - 15.5
		Ne I	16-30	jbe30.n*	10.3 - 15.5
$H_3CC\equiv N$	N/A	He I	15-22	jbe31.c* Jbe31.f*	11.8 - 14.0 11.8 - 15.5
		He II	18-27	jbe31.y* jbe31.z*	11.8 - 14.0 11.8 - 20.0
2-hydroxy-6-methyl pyridine (Hmhp)	71.7 to 90.8	He I	19-22	jbe25.f* jbe26.c*	5.3 - 15.5 7.8 - 11.5
	75.5 to 77.0			jbe25.d* jbe25.g*	7.2 - 11.5 5.49 - 15.7
	136.4 to 150.9			jbe25.i*	5.49 - 15.7
6-chloro-2-pyridinol (Hchp)	21 to 37	He I	21-27	ajr11.f* ajr11.a* ajr11.b*	5.5 - 15.7 8.3 - 12.9 8.3 - 10.2
		He II	N/A	ajr11.y* ajr11.x* ajr11.z*	5.5 - 15.7 8.3 - 12.9 5.5 - 20.0
DAG®	184 to 272	He I	20-23	jbe34.f*	4.8 to 15.0

Table 2.1. - *Continued*

Molecule	Collection Temp (°C)	Photon Source	Resolution	File Names	Energy Region
Cr₂(chp)₄	266 to 341	He I	20-27	jbe38.f* jbe38.c*	5.3 - 15.5 6.4 - 10.5
		He II	28-36	jbe38.y* jbe38.z*	6.4 - 10.5 5.5 - 20.0
Mo₂(chp)₄	196 to 260	He I	28-35	jbe37.f* jbe37.c*	5.5 - 15.7 5.3 - 10.5
		He II	27-37	jbe37.y* jbe37.z*	5.3 - 10.5 5.5 - 20.0
W₂(chp)₄	268 to 353	He I	21-27	jbe36a.f* jbe36a.c*	5.0 - 15.5 4.8 - 10.5
		He II	25-32	jbe36a.y* jbe36a.z*	4.8 - 10.50 4.9 - 20.0
Cr₂(mhp)₄	170 to 208	He I	17-21	jbe21.f* jbe21.c* jbe21.d*	5.3 - 15.5 5.3 - 9.2 6.9 - 9.2
		He II	19-26	jbe21.z* jbe21.y*	5.5 - 20.0 5.3 - 9.2
		Ne I	13-20	jbe21.n* Jbe21.m*	5.1 - 9.2 6.0 - 9.5
Rh₂(mhp)₄	190 to 230	He I	18-26	jbe24.f* jbe24.c*	5.3 - 15.5 6.0 - 9.5
		He II	18-24	jbe24.z* jbe24.y*	5.5 - 20.0 5.8 - 9.5
		Ne I	13-16	jbe24.n*	6.0 - 9.5
Cr₂(map)₄	180 to 222	He I	15-18	jbe26.f* jbe26.c* jbe26.d* jbe26.e*	5.3 - 15.5 6.0 - 9.3 5.4 - 7.5 5.3 - 9.7
2-amino-6-methylpyridine (Hmap)	23 to 24	He I	19-22	jbe27.f* jbe27.c* jbe27.d* jbe27.e*	5.3 - 15.5 6.8 - 12.3 8.4 - 11.5 7.3 - 9.2
		He II	23-27	jbe27.z* jbe27.y*	5.5 - 20.0 6.8 - 12.3

Table 2.1. - *Continued*

Molecule	Collection Temp (°C)	Photon Source	Resolution	File Names	Energy Region
Mo₂Cl₄(PMe₃)₄	133 to 155	He I	15-20	jbe06.f* jbe06.c*	5.4 - 15.5 5.8 - 9.3
		He II	N/A	jbemc.z* jbemc.y*	5.6 - 20.0 5.6 - 9.3
		Ne I	14-23	jbemc.n*	5.6 - 9.3
Mo₂Br₄(PMe₃)₄	130 to 158	He I	18-25	jbeb.hf* jbeb.h*	6.0 - 15.5 5.9 - 10.5
		He II	N/A	jbebmb.z* jbebmb.y*	5.6 - 20.0 5.7 - 10.5
		Ne I	18-25	jbeb.n*	5.9 - 10.5
W₂Cl₄(PMe₃)₄	110 to 144	He I	22-30	jbe02a.c* jbe02a.f*	4.9 - 9.5 4.9 - 15.0
		He II	21-27	jbe02a.y* jbe02a.z*	4.9 - 9.5 4.6 - 20.0
		Ne I	22-27	jbe02a.n* jbe02a.nf*	4.9 - 9.5 4.9 - 11.0
Re₂Cl₄(PMe₃)₄	126 to 165	He I	18-22	jbe04..f* jbe04.c* jbe04.d* jbe04.p*	5.0 - 15.0 5.0 - 9.5 5.0 - 7.1 7.1 - 9.5
		He II	23-28	jberc.z* jberc.y*	5.0 - 20.0 4.9 - 9.5
		Ne I	16-25	jbe.n*	5.0 - 9.5
Re₂Br₄(PMe₃)₄	137 to 186	He I	16-19	jbe03.f* jbe03.c* rhe.c* rhe.d* rhe.f* rhe.j* rhe l* rhe.p*	5.1 - 15.5 4.9 - 9.5 4.9 - 9.3 5.1 - 7.4 5.0 - 15.1 7.1 - 9.6 6.0 - 7.1 5.2 - 6.3
		He II	23-28	jbeb.f* jbeb.c*	20.0 to 4.9 9.5 to 4.9
		Ne I	18-23	jbeb.n*	5.0 - 9.5

Table 2.1. - *Continued*

Molecule	Collection Temp (°C)	Photon Source	Resolution	File Names	Energy Region
$Mo_2(O_2CCH_3)_4$	160 to 173	He I	17-24	ajr01.a* ajr01.b* ajr01.f*	6.3 - 7.5 6.8 - 9.7 6.0 - 15.5
Tri-t-butyl alcohol amine: $N(ROH)_3$	44 to 65	He I	22-27	jbe14.c* jbe14.f*	7.0 - 11.0 6.9 - 15.5
		Ne I		jbe14.n*	6.8 - 11.0
$Mo_2(O_3N)_2$ Bis(tri-t-butylalkoxide amine)dimolybdenum(II)	110 to 140	He I	21-24	jbe15.f* jbe15.c*	5.4 - 15.5 5.3 - 8.2
		Ne I	20-25	jbe15.n*	5.3 - 8.2
$W_2(O_3N)_2$ Bis(tri-t-butylalkoxide amine)ditungsten(II)	102 to 130	He I	15-20	jbe18.f* jbe18.c*	4.5 - 15.5 4.5 - 8.4
		Ne I	17-22	jbe18.n*	4.5 - 8.4
t-butyl alcohol	25 to 27	He I	16-22	jbe40.f* jbe40.d*	9.3 - 15.5 9.8 - 20.0
		He II	N/A	jbe40.y* jbe40.z*	9.3 - 15.5 9.5 - 24.0
Tri(6-fluoro-phenyl)phosphine	50 to 63	He I	19-23	jbe10.f* jbe10.c*	7.2 - 15.5 7.4 - 10.0
Tri(6-chloro-phenyl)phosphine	77 to 106	He I	23-25	jbe11.f* jbe11.c*	6.6 - 15.5 7.2 - 10.0
Tris(6-trifluoromethylphenyl) phosphine	57 to 76	He I	23-27	jbe12.f* jbe12.c* jbe12.d*	6.9 - 15.5 7.3 - 11.0 9.2 - 11.0
Tri(6-methylphenyl) phosphine	101 to 103	He I	19-24	ajr04.f*	5.5 - 15.7

* denotes raw data file name: All files are designated by the names and a number. For example jbe02a.f* applies to jbe02a.f1, jbe02a.f2 ...

Table 2.2. List of compounds studied.

Molecule	Synthetic Origin
$Cl_3Mo\equiv N$	Kristie Winfield
$Cl_3CC\equiv N$	Aldrich
$H_3CC\equiv N$	Aldrich
$('BuO)_3M\equiv N$ (M = Cr, Mo, W)	Andy Kidwell
$('PrO)_3Mo\equiv N$	Andy Kidwell
$(CF_3(CH_3)_2CO)_3Mo\equiv N$	Andy Kidwell
2-hydroxy-6-methyl pyridine (Hmhp)	Aldrich
6-chloro-2-pyridinol (Hchp)	Aldrich
DAG®	Acheson
$M_2(chp)_4$ (M = Cr, Mo, W) (chp = 2-chloro-6-oxopyridinate)	In Lab[231]
$M_2(mhp)_4$ (M = Cr, Mo, W) (mhp = 2-oxo-6-methylpyridnate)	In Lab[230]
$Mo_2Cl_4(PMe_3)_4$ $Mo_2Br_4(PMe_3)_4$	In Lab[144]
$W_2Cl_4(PMe_3)_4$	In Lab[20,149]
$Re_2Cl_4(PMe_3)_4$ $Re_2Br_4(PMe_3)_4$	In Lab[148]
$Re_2I_4(PMe_3)_4$	Garry Hinch
$Mo_2(O_2CCH_3)_4$	In Lab[141]
Tri-t-butyl alcohol amine - $N(ROH)_3$	Dr. Ted Budzichowski
$Mo_2(O_3N)_2$ Bis(tri-t-butylalkoxide amine)dimolybdenum(II)	Dr. Ted Budzichowski
$W_2(O_3N)_2$ Bis(tri-t-butylalkoxide amine)ditungsten(II)	Dr. Ted Budzichowski
t-butyl alcohol	Spectrum
Tri(6-fluoro-phenyl)phosphine	Strem
Tri(6-chloro-phenyl)phosphine	Strem
Tris(6-trifluoromethylphenyl)phosphine	Strem
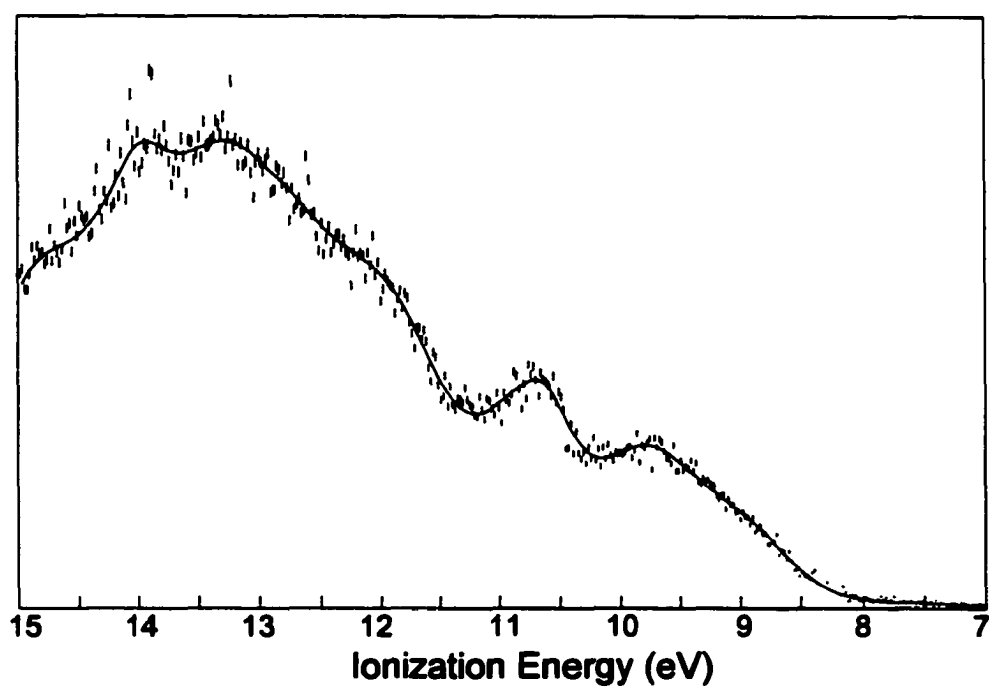
Figure 2.1. He I photoelectron spectrum of DAG collected from the aluminum cell in the temperature range: 227-272 °C.

CHAPTER 3

THEORETICAL AND SPECTROSCOPIC INVESTIGATIONS OF THE BONDING AND
REACTIVITY OF $(^tBuO)_3M \equiv N$ COMPOUNDS, WHERE M = Cr, Mo and W

Introduction

Spurred by the discovery of metal-alkylidyne complexes that are active as catalysts for

alkyne metathesis reactions, the interest in compounds containing metal-heteroatom multiple

bonds has increased rapidly in the last twenty years.[11,40-43] Transition metal-organic and

transition metal-heteroatom triply bonded functional groups have diverse reactivities, ranging

from stabilization of metals in high oxidation states to serving as the center of reactivity in a

molecule.[11] Some common reactions involving the metal-heteroatom bond include atom or group

transfer reactions and metathesis reactions. The reactivity of metal-heteroatom molecules is

greatly influenced by the metal, the electron configuration of the metal, and the particular set of

attendant ligands.

Because the nitrido ligand is one of the strongest π electron donors known,[5] molecules

that contain metal-nitrogen multiple bonds are of particular interest. As pioneered in 1965 by

Dehnicke and Strähle, terminal nitrido ligands form strong bonds to transition metal atoms.[44]

One of the interesting recent advances in the field of metal-heteroatom bonding was the

discovery of metal-nitrido compounds that can serve as catalyst precursors for alkyne metathesis

reactions.[45] Recently, it was recognized that controlled thermolysis of organometallic

molybdenum nitrides could be used as an efficient route to obtaining phase-pure molybdenum

nitrides.[46] Transition metal nitrides, especially molybdenum nitrides, are known to have

significant catalytic properties. Reactions as diverse as NH_3 synthesis,[6] ethane

hydrogenolysis,[7,10] and CO hydrogenation[8] have been shown to be catalyzed by various phase-

pure molybdenum nitrides.

In this work we examine the electronic structure and reactivity of a series of closely related molecules $(RO)_3M\equiv N$, where $M = Cr$, Mo, or W $(R = {}^tBu)$.[3,4,21] To probe the electronic structure of transition metal nitrido complexes, gas-phase UV photoelectron spectroscopic studies have been performed on the molecules, $(RO)_3M\equiv N$ $(M = Cr$, Mo, or W; $R = {}^tBu$, ${}^iPr$, or CF_3Me_2C). Density functional studies provide theoretical support for the experimentally-determined ionization assignments and provide insight into the electronic structure and bonding.

Formally, transition metal nitrides are inorganic analogs of organic nitriles. Organic nitriles are known to undergo metathesis reactions with $W_2(O^tBu)_6$ to produce the transition metal nitrido molecule, $({}^tBuO)_3W\equiv N$, and a transition metal alkylidyne, $({}^tBuO)_3W\equiv CR$.[21] If transition metal nitrides are truly inorganic nitriles one might expect to see similar reactivity between $W_2(O^tBu)_6$ and the transition metal nitrido complexes. To test this hypothesis reactivity studies have been undertaken to explore the reaction between $W_2(O^tBu)_6$ and $({}^tBuO)_3Mo\equiv N$.

Experimental

General Methods. All manipulations were carried out using an Argon (Ar) or dinitrogen (N_2) atmosphere and standard air and moisture sensitive techniques in a Vacuum Atmospheres Glovebox or Schlenk line. Solvents were distilled from CaH_2 or Na/Benzophenone ketyl, purged of oxygen with either Ar or N_2 and stored over 4 Å sieves. All reagents were purchased from Aldrich unless otherwise stated and used without further purification. *tert*-Butanol was vacuum distilled from $CaSO_4$. Fluoroalcohols (Lancaster Synthesis) were distilled under Ar and stored over 4 Å sieves. Molybdenum pentachloride (Strem Chemicals) was used as purchased. Lithium, sodium or potassium alkoxide and fluoroalkoxide salts were prepared using a reported method.[47] Molybdenum tetrachloride-bisacetonitrile $(MoCl_4(CH_3CN)_2)$ was prepared via a reported method.[48,49] Chromium nitrido tris-t-butoxide, tungsten nitrido tris-t-butoxide and $M_2(O^tBu)_6$ (where $M = Mo$ and W) were prepared via reported syntheses.[4,21,50,51] The

molybdenum nitrido alkoxides and fluoroalkoxides were prepared via a modification of a reported synthesis.[3]

Spectroscopic methods. Proton (^{1}H) and fluorine (^{19}F) NMR were carried out on a Varian Gemini 2000 spectrometer operating at a 300 MHz proton and 282 MHz fluorine NMR Larmor frequencies. Infrared (IR) Spectra were taken as KBr pellets on a Nicolet 510P FT-IR spectrophotometer using OMNI E. S. P. software. Mass spectra were taken on a Kratos MS 80 high resolution mass spectrometer using Negative Ion CI with methane (CH_4) as reagent gas. A Kratos MS 25 RFA double focusing magnetic sector mass spectrometer was also used to record the mixed metal spectrum. A positive ion EI source with a trap current of 100 μA at a temp of 225 $^{\circ}$C at 52 eV was used during data collection. A 3 kV analyzer was used with a resolution of 2000 using the 5% peak height definition. The scanning rate was 5 sec/decade with a mass range of 1100 to 275. A third party (MSS) data system was used.

Photoelectron spectra. The photoelectron spectra were recorded using an instrument that features a 36 cm radius, 8 cm gap McPherson hemispherical analyzer with custom-designed sample cells, detection system, and control electronics.[31] The excitation source was a quartz lamp with the ability, depending on operating conditions, to produce He Iα (21.218 eV) or He IIα (40.814 eV) photons. The ionization energy scale was calibrated by using the $^2E_{1/2}$ ionization of methyl iodide (9.538 eV) and the Ar $^2P_{3/2}$ ionization (15.759 eV). The argon $^2P_{3/2}$ ionization was also used as an internal calibration lock for the energy scale during He I and He II data collection runs. Resolution (measured as full-width-at-half-maximum of the argon $^2P_{3/2}$ ionization) was 0.016-0.024 eV during He I data collection. Assuming a linear dependence of analyzer intensity to the kinetic energy of the electrons within the energy range of these

experiments, all data were intensity corrected with the experimentally-determined analyzer

sensitivity function.

Because discharge sources are not monochromatic,[33] each spectrum was corrected for the

presence of ionizations from other source lines. The He I spectra were corrected for ionizations

from the He Iβ line (1.959 eV) higher in energy with 3% of the intensity of ionizations from the

He Iα line. He II spectra were similarly corrected for ionizations from the He IIβ line (7.568 eV

higher in energy and 12% of the intensity of the He IIα line.)

The samples sublimed cleanly with no detectable evidence of decomposition products in

the gas phase or as a solid residue. The sublimation ranges (°C at $\sim 10^{-4}$ Torr) for each molecule

were (^{t}BuO)$_3$Cr$\equiv$N, -4 to 20; (^{t}BuO)$_3$Mo$\equiv$N, 38 to 57; (^{t}BuO)$_3$W$\equiv$N, 58 to 78; (^{i}PrO)$_3$Mo$\equiv$N, 42

to 75; (Me$_2$CF$_3$CO)$_3$Mo$\equiv$N, 28 to 61. The temperatures were measured using a "K" type

thermocouple attached directly to the ionization cell through a vacuum feedthrough.

Data Analysis. In the figures of the photoelectron spectra, the vertical length of each

data mark represents the experimental variance of that point.[34] The ionization bands are

represented analytically with the best fit of asymmetric Gaussian peaks. Due to the extensive

overlap of many ionization features, the individual peaks used to obtain an analytical

representation of a band do not necessarily represent separate ion states. The number of peaks

used was the minimum necessary to get an analytical representation of the He I spectrum. For

fitting the He II spectra, the peak positions and half-widths were fixed to those of the He I fit.

The confidence limits for the relative integrated peak areas are ±5%. The primary source

of uncertainty is the determination of the baseline. The baseline is caused by electron scattering

and is taken to be linear over the small energy range of these spectra. The fitting procedures

used to fit the spectra have been described in more detail elsewhere.[34]

DFT studies. Calculations were performed on the model $(HO)_3M\equiv N$ molecules (where

$M = Cr, Mo, W$) using the Gaussian98[18] suite of programs. The B3LYP method with the CEP-

121G* basis set was used for both the metals and ligands.[35,52,53] The bond lengths and angles

used in the calculations were taken from the crystal structures of $(^tBuO)_3M\equiv N$ $(M = Cr,[4] Mo,[3]$ or

$W[54])$ and idealized to C_{3v} symmetry.

Density functional calculations were performed with the ADF2000.01 program on the

complete molecules including the t-butoxide ligands.[36] The numerical integration procedure was

developed by te Velde and co-workers.[37,38] The PW91 method was used for all calculations.[55]

The atomic orbitals on all centers were described by an uncontracted triple-ζ STO basis set (set

IV) that is readily available with the ADF package. The $1s^2$ configuration on carbon, nitrogen,

oxygen, and fluorine as well as the $1s^22s^22p^6$ configuration for Cr, the $1s^22s^22p^63s^23p^63d^{10}$ for

Mo, and the $1s^22s^22p^63s^23p^63d^{10}4s^24p^64d^{10}$ for W were assigned to the core and treated by the

frozen-core approximation. Relativistic effects were included in all calculations by the scalar

ZORA formalism implemented as a part of the ADF2000 program.[56-60] The molecular structures

of $(^tBuO)_3M\equiv N$ $(M = Cr, Mo,$ or $W)$; $(^iPrO)_3Mo\equiv N$; and $(CF_3(CH_3)_2O)_3Mo\equiv N$ were fully

optimized under C_{3v} symmetry.

Preliminary Considerations

The classic concept of the electronic structure of transition metal nitrido complexes

envisions a triple bond between the metal and the nitrogen atom and a sigma lone pair of

electrons localized on the nitrogen as depicted by the Lewis dot formulation $(M\equiv N:)$. As will

become apparent, this formulation is inadequate for describing the bonding nature of the

molecular orbitals and the associated ionization energies. In order to provide a framework for

discussion of the information provided by the photoelectron spectra, it is necessary to consider a more appropriate description of the symmetry-allowed orbital interactions that combine to define the electronic structure of these molecules. Additionally, it is important to compare and contrast the triple bond between a metal atom and a nitrogen atom with the triple bonds between other atoms and nitrogen atoms. Photoelectron spectroscopy has been a key experimental technique for probing the nature of these bonds.

Dinitrogen. The electronic structure of the most-studied example, N_2, is particularly relevant to the present study. The concept of a triple bond and nitrogen lone pairs in N_2 evolves naturally from the simple Lewis dot formulation ($:N \equiv N:$). In a more complete molecular orbital description of the bonding in N_2, mixing in the σ orbital framework removes the separation of the localized lone pair orbitals from the σ bonding orbitals. Historically, one of the key questions concerning the electronic structure of N_2 was the relative ordering of the σ and π orbitals.[61-64] High level *ab initio* electronic structure calculations yield a ground state valence electronic configuration order of $(1\sigma_g^2)(1\sigma_u^2)(2\sigma_g^2)(1\pi_u^4)$, which agrees with the concept that a σ bond should be stronger than a π bond in the absence of any other considerations. Providing a prime example of the breakdown in Koopmans' approximation,[65] the first ionization of N_2, as measured by photoelectron spectroscopy, is the $^2\Sigma_g^+$ ionization at 15.60 eV followed by the $^2\Pi_u$ ionization then occurs at 16.98 eV.[33,61] The symmetry of the first ion state is confirmed by the emission line spectrum of N_2^+. Interestingly, DFT studies calculate the ground state valence configuration to be $(1\sigma_g^2)(1\sigma_u^2)(1\pi_u^4)(2\sigma_g^2)$ in agreement with the experimentally-determined ordering.[66,67] Information regarding the bonding nature of the orbitals is also important. Ionization from the $2\sigma_g$ orbital results in a short vibrational progression with a frequency of 2100 cm^{-1}, which in comparison to a vibrational frequency of 2330 cm^{-1} for the neutral molecule is consistent with removal of an electron from an orbital that is only weakly bonding. Ionization from the $1\pi_u$

orbital reveals a much longer vibrational progression with a frequency of 1810 cm^{-1}, consistent with ionization of a strongly bonding orbital.[33,61] A challenge for the metal-nitrides is the determination of the relative energy and bonding character of the valence σ and π orbitals that constitute the $M \equiv N$ bond.

Organic Nitriles. Organic nitriles like $HC \equiv N$ or $CH_3C \equiv N$ provide additional insight into triple bonds involving nitrogen atoms. One can consider both $HC \equiv N$ and $CH_3C \equiv N$ as isoelectronic analogs of N_2, the C-N triple bond being formed by the combination of a methylidyne or ethylidyne fragment and a nitrogen atom. From this point of view, the electronic structures of $HC \equiv N$ and $CH_3C \equiv N$ can be easily understood in terms of perturbations of the bonding in N_2. Focusing first on the electronic structure of $HC \equiv N$, both *ab initio* and DFT studies place the C-N 1π as the highest occupied molecular orbital (HOMO) with the 3σ orbital being the second highest occupied molecular orbital (SHOMO).[68,69] These results correlate with the experimentally-determined ionization energies measured by photoelectron spectroscopy,[33,69] where the $^2\Pi$ ion state occurs at 13.60 eV and the $^2\Sigma^+$ state lies at ~ 14.0 eV. The exact position of the $^2\Sigma^+$ ion state cannot be ascertained from the photoelectron spectra because the ionizations overlap extensively, but the relative ordering of the highest occupied σ and π orbitals switches as one goes from N_2 to $HC \equiv N$. In comparison to the corresponding values for N_2, the $^2\Pi_u$ and $^2\Sigma_g^+$ ion states of the $HC \equiv N$ are destabilized by 3.38 eV and 1.60 eV, respectively. The general destabilization follows from the lower electronegativity (and lower orbital stability) of C compared to N, and the smaller shift of the $^2\Sigma_g^+$ ionization in comparison to the $^2\Pi_u$ ionization, which results in the switch in the order of the highest occupied π and σ ionizations, is related to the polarization of the σ orbital toward the N atom.

The photoelectron spectrum of $CH_3C \equiv N$ illustrates the effects of alkyl substitution and reduction in symmetry on the electronic structure of the C-N triple bond. DFT and *ab initio*

computational studies again place the C-N π orbital, formally an e orbital under C_{3v} symmetry, as the HOMO with the highest occupied σ-type orbital of a_1 symmetry as the SHOMO. These results are in agreement with the photoelectron studies of this molecule,[68,70] which place the ^2E ion state (formally analogous to the $^2\Pi$ ion state of HC$\equiv$N) at 12.21 eV and the $^2A_1$ ion state (analogous to the $^2\Sigma^+$ state of HC$\equiv$N) at 13.14 eV. Substitution of CH_3 for H destabilizes the highest occupied σ and π orbitals by 0.86 eV and 1.39 eV, respectively. The extra destabilization of the highest π-type ionization (from the 2e orbital) is attributed to the filled-filled interaction of the e symmetry combinations of the CH_3 fragment (formed from the appropriate combinations of the C-H σ bonds) with the C-N π bonds.[33] This filled-filled interaction is illustrated in the
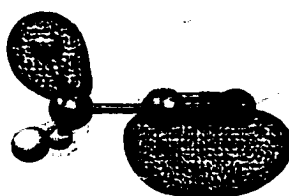
3.1

orbital plot shown in **3.1**.[71] This mixing is relevant to later discussion, where the mixing of the oxygen lone pairs with the M$\equiv$N valence orbitals in $(RO)_3M\equiv N$ is expected to be even greater than the mixing of the C-H bonds with the C$\equiv$N valence orbitals shown above because the oxygen lone pairs are both closer in distance and more similar in energy to the M$\equiv$N valence orbitals than are the C-H orbitals of $CH_3C\equiv N$ to the C$\equiv$N valence orbitals. As expected for ionization of an electron from a strongly bonding orbital, the ^2E (π-type) ionization displays significant vibrational fine structure while the $^2A_1$ (σ-type) ionization is sharp and shows little vibrational structure, as expected for ionization of an electron from a nonbonding or weakly bonding orbital. Ionization of the electrons from the C-N π orbital excites multiple vibrational

modes including the $C \equiv N$ stretching mode and the CH_3 symmetric deformation mode. Both the ^2E and $^2A_1$ ionizations occur at lower ionization energy than the corresponding ionizations of N_2, consistent with the view that acetonitrile is more basic than N_2.

Transition metal nitriles. In the simple valence-bond picture the M-N σ bond is formed by the interaction of the $M(d_{z^2})$ with the N(sp hybrid); the M-N π is formed by the interaction of the $M(d_{xz}, d_{yz})$ and the N(px,py). Although this simple picture does account for the M-N triple bond, it does not acknowledge the influence of the axial ligands (R) on the electronic structure. To further the understanding of the electronic structure of simple transition metal nitrides, Roald Hoffmann and coworkers performed an extended Hückel computational study on $(HO)_3W \equiv N.^{72}$ To facilitate the analysis of the bonding in $(HO)_3W \equiv N$, the molecule was treated as two separate fragments, $(HO)_3W^{3+}$ and N^{3-}. Figure 3.1 contains an interaction diagram for these fragments excluding the charges on the fragments. This diagram provides a good starting point for describing the electronic structure of the $(RO)_3M \equiv N$ systems. The oxygen donors of the $(HO)_3W^{3+}$ fragment simply serve to determine the relative ordering of the d orbitals: $(d_{z^2} < d_{xz}=d_{yz} << d_{x^2-y^2}=d_{xy})$ based on the ligand field environment. The HOMO, the most destabilized bonding component of the M-N σ framework, is designated with the label 2σ, while the M-N π bond is labeled 1π. These orbitals are directly analogous to the $2\sigma_g$ and $1\pi_u$ orbitals of N_2, the 3σ and 1π orbitals of HCN, and the $4a_1$ and $2e$ orbitals of $CH_3C \equiv N$. The degree of polarization of the 2σ orbital will depend on the amount of mixing that occurs between the $N2p_z$ and the $N2s$ orbitals. Unlike $HC \equiv N$ and $CH_3C \equiv N$ where the the LUMO is a C-N π^* orbital, the LUMO of $(RO)_3M \equiv N$ is the metal $d_{x^2-y^2}$ and d_{xy} orbitals labeled 1δ.

Although Hoffmann's treatment is quite useful for describing the $M \equiv N$ interaction, it obscures the importance of the alkoxide ligands on the electronic structure. An alternative approach is to view the system in terms of $M \equiv N^{3+}$ and $(RO)_3^{3-}$ fragments. For $(^tBuO)_3M \equiv N$ (M

= Cr, Mo, W), this approach effectively separates the alkoxide ligand framework (the constant in the system) from the variable $M \equiv N$ framework. Hence, it allows ready analysis of the effects of M substitution on the electronic structure of the system. Conversely, for the $(RO)_3Mo \equiv N$ molecules, the constant, the MoN^{3+} framework is separated from the alkoxide framework so that the effects of alkoxide substitution on the electronic structure can be effectively probed.

Symmetry considerations. To begin the analysis, it is useful to consider the symmetry-allowed interactions. The metal s, p_z, and d_{z^2} atomic orbitals are all of a_1 symmetry so the M-N σ are combinations of $N(2s)$, $N(2p_z)$, $M(nd_{z^2})$, $M(n+1)s$, and $M(n+1)p_z$. From Hoffmann's studies, it is known that the highest occupied MN σ-type orbital is the 2σ composed primarily of the $M(d_{z^2})$ and $N(2p_z + 2s)$ orbitals. The M-N π bonds are formed by the combination of the $N(p_x,p_y)$ and the $M(d_{xz},d_{yz})$ atomic orbitals. Although the $M(p_x,p_y)$ orbitals are also of e symmetry, they are a poor energy match with the $N(p_x,p_y)$ orbitals and will not mix strongly with them. The metal $d_{x^2-y^2},d_{xy}$ orbitals also are of e symmetry, but do not have direct overlap with the $N(p_x,p_y)$ orbitals.

The oxygen lone pairs of the alkoxide ligands are expected to have a good energy match with the metal d orbitals and therefore significant interaction with the $M \equiv N$ valence orbitals. The symmetry combinations of the oxygen p orbitals directed at the metal are shown in **3.2**. The

3.2
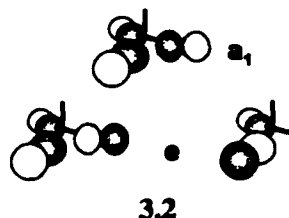
a_1 and e combinations are primarily used to form the M-R σ bonds and probably will not interact with the M-N σ and π orbitals to a great extent.

For simplicity, the oxygen p orbitals that are π with respect to the metal are separated

into two groups: those perpendicular to the M-N framework, and those parallel to the M-N

framework. The parallel combinations (a_1 and e(‖) shown in 3.3) can interact directly with the

e(‖)

a_1

3.3

e($\perp$)

a_2

3.4
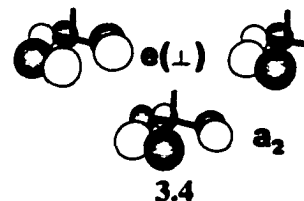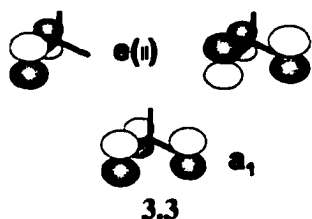
M-N σ and π orbitals. The a_1 combination has reasonable overlap with the M-N σ orbital, and

the e, combination has reasonable overlap with the M-N π orbitals. The perpendicular ligand

combinations (a_2 and e($\perp$) shown in **3.4**) will interact much less significantly with the M-N

orbitals. In fact, by symmetry the a_2 combination does not interact with the M-N orbitals at all.

The e($\perp$) combination does not have the correct nodal properties to have good overlap with the

M-N π orbital. The relative ordering of the six oxygen pπ combinations ($a_1 <$ e($\perp$) $<$ e(‖) $< a_2$)

follows from the nodal and overlap properties of the orbitals. The a_1 is the most stable

combination because it is a completely bonding orbital with zero nodes, and the a_2, a completely

antibonding orbital, is obviously the most destabilized of the combinations. Since both sets of e

orbitals are one node systems, one must consider the overlap effects to obtain the relative

orderings. The e(‖) is a net antibonding orbital, while the e($\perp$) is a net bonding orbital.

Therefore, the e($\perp$) will be stabilized relative to e(‖).

A simple molecular orbital diagram illustrating the interactions of the $(RO)_3^{3-}$ π-type

combinations with the NM^{3+} orbitals is presented in Figure 3.2. The diagram represents two

possibilities with regards to the M-N fragment energies relative to the ligand orbitals: the M-N σ

and π orbitals are lower in energy than the alkoxide orbitals (left) or the M-N σ and π orbitals

are slightly higher than the energies of the alkoxide orbitals (right). Depending on the particular transition metal, the actual electronic structure of the $(RO)_3M \equiv N$ molecules probably lies somewhere between these two extremes. Regardless, the ligand a_1 and $e(\Pi)$ orbitals form bonding and antibonding combinations with the M-N σ and π orbitals, respectively. Hence, the simple definitions of localized M-N σ and π orbitals are no longer valid because of significant orbital mixing with the strong π donor ligand orbitals.

The relative ordering and distribution of the orbitals is partly related to electronegativity. The electronegativities of the transition metals decrease as a group is descended: Cr(VI) = 3.37, Mo(VI) = 2.20, and W(VI) = 1.67.[73] Therefore, the description of the Cr molecule would be expected to lie to the left of the descriptions of the Mo and W molecules in the interactions depicted in Figure 3.2. For comparison, the electronegativities of N and O are 3.19 and 3.65, respectively. Based on these considerations, the M-N σ and π orbital energies should increase as M = Cr < Mo < W, and the relative amount of mixing between the ligand orbitals and the MN^{3+} orbitals should be greatest for Cr. The M-N polarity as well as the N atom basicity should increase as the group is descended (M = Cr < Mo < W).

This simple molecular orbital diagram assumes that the relative energies of the ligand symmetry combinations remain constant as the metal is changed. This is definitely not true. As the M-O distances decrease (M = W > Mo > Cr), the distances between the oxygens also decrease and the intramolecular interactions between the oxygen atoms increase. The spread of the ligand SALCS will be greatest for $(RO)_3Cr \equiv N$ molecule because the bonding or antibonding nature of each particular SALC becomes much more important as the overlap between the oxygen p orbitals increases. With this in mind, it is quite likely that the HOMO of the Cr analog will not be the Cr-N σ or π orbitals but the ligand a_2 combination.

The model system also neglects the effects of mixing the alkyl σ framework of the

alkoxides with the oxygen p orbitals. That is, the alkoxide ligands were simplified to the

cylindrical π donor, O^{2-}. In reality, the O-R σ orbital combinations will mix with the oxygen

lone pairs to form new linear combinations with different orbital energies. All of these

interactions influence the relative energies, bonding, and polarity of the orbitals that make up the

metal-nitride triple bond in these tris-alkoxide complexes. Just as in the studies of triple bonds to

nitrogen in simpler molecules, photoelectron spectroscopy helps to quantify the nature of these

interactions.

Results and Discussion

He I Photoelectron Spectra. The He I photoelectron spectra of the $(^tBuO)_3M\equiv N$ (M =

Cr, Mo, or W) in the 8.5 to 15.0 eV ionization energy range are presented in Figure 3.3. For

comparison the spectrum of ^tBuOH is included. The ^tBuOH spectrum provides a benchmark for

elucdiating the contribution of the alkoxide ligands to the $(^tBuO)_3M\equiv N$ spectra. The alcohol

spectrum consists of three distinct regions in the 10 to 15 eV region. Band A at 10.22 eV

derives from the oxygen p orbital (lone pair) that is perpendicular to the C-O-H plane, and band

B derives from the oxygen p orbital (lone pair) that is in the C-O-H plane, bisecting the C-O-H

angle. Both are strongly mixed with the C-C and C-H σ bonds of the t-butyl group, and the in-

plane orbital is additionally mixed with the O-H σ bond. The different mixings, particularly with

the O-H bond, account for the different energies of the ionizations. The mixing in band B is

more bonding in nature than the mixing in band A, as evidenced by the width of the ionization

band. Band C can be assigned to the O-C(σ), C-C(σ), as well as the C-H(σ) ionizations. All

ionizations due to the alkoxide ligands have counterparts in the alcohol spectrum, but the

ionizations of the alkoxide are first destabilized relative the corresponding ionizations in the

alcohol by the formal negative charge on the alkoxides and second are mixed with the appropriate orbitals of the $M \equiv N$ framework.

One of the most helpful means of assigning ionizations is to look at a series of molecules with the same ligand set but different transition metals, because ionizations from metal-based orbitals will shift as the metal is changed. Looking at the spectra of the transition metal nitrides, the spectra can once again be separated into three separate regions: A + A* (8.5-10.5 eV), B (10.5 to 11.5 eV), and C (11.5 to 15.0 eV). Region C is essentially the same as M is changed, implying the region is dominated by ionizations from ligand-based orbitals. The region contains the C-C(σ), C-H(σ), as well as the C-O(σ) ionizations. Not surprisingly, this region closely matches the corresponding region of 'BuOH. Band B is fairly consistent as M is changed, once again implying dominant ligand character. However, subtle changes are apparent in the spectra that signal the presence of ionizations from orbitals containing some metal character. Not surprisingly, the leading bands (A + A*) of the spectra show the largest changes. This implies that this region contains the ionizations from the orbitals that contain the most metal character.

It is useful to compare the relative areas of the ionization bands of the Cr, Mo, and W analogs, shown in Table 3.1. This is particularly relevant to determining whether the ionization feature labeled A* in ('BuO)$_3$Cr$\equiv$N spectrum shifts into band A in the spectra of the Mo and W compounds. The ionization feature A* must become part of band A in the Mo and W analogs because the relative area of A* + A agrees well with the relative areas of band A for ('BuO)$_3$M$\equiv$N (M = Mo or W). Interestingly, the relative areas of the He I spectra of the ('BuO)$_3$M$\equiv$N molecules imply that combined region (B + C) contains approximately four times as many ionizations as band A. In terms of the simple molecular orbital model shown in Figure 3.3, band A contains the ionizations from the first cluster of molecular orbitals (a$_2$, e($\perp$), and the 3antibonding combinations of M-N σ and π with the ligand a$_1$ and e($\parallel$), respectively, while band

B contains the bonding combinations of the M-N σ and π with the ligand a_1 and $e(\text{II})$, respectively.

Focusing on the region containing the M-N ionizations, photoelectron spectra were recollected in the 8.5 to 10.5 eV region, Figure 3.4, so that a more detailed analysis of the ionization features could be obtained. The ionization energies of the prominent features of the $(^tBuO)_3M\equiv N$ spectra are given in Table 3.2. The experimental trend for the onset of ionization[74] is Mo > Cr > W. For ionizations from orbitals containing metal character, the expected trend of ionization energy based solely on electronegativity is Cr > Mo > W. An additional unexpected trend is obtained from the positions of the first band of each molecule, where the experimental trend in ionization energies follows as Cr < W < Mo. The observation that the Cr analog does not fall in line with the Mo and W systems leads to the proposition that the first spectral feature of the Cr molecule is not due to ionization of the Cr-N σ and/or π orbitals. From the molecular orbital considerations outlined above, the first ionization of $(^tBuO)_3Cr\equiv N$ more than likely corresponds to ionization of the a_2 ligand combination. This orbital is completely antibonding between the oxygens and nonbonding with the metal. The antibonding character is strongest in the chromium molecule because of the shorter interatomic distances. On the other hand, the first spectral features of the Mo and W analogs do follow the expected trend for metal-based ionizations so it is likely that the first ionization feature of the these molecules is due to ionization of the M-N σ and/or π orbitals. Using the same rationale, one can tentatively assign the second band of $(^tBuO)_3Cr\equiv N$ to the Cr-N σ and/or π ionizations. The ligand a_2 ionization, being completely non-bonding with respect to the metal, should be stabilized as one moves from Cr to Mo to W. Therefore, the ionization from the a_2 orbital more than likely occurs under b for the Mo analog and under b or c in the spectrum of $(^tBuO)_3W\equiv N$. This then leaves band c to be tentatively assigned to the ionization of the other ligand e combination.

Alkoxide Substitution Effects. Another useful technique for assigning ionizations in

photoelectron spectroscopy is to study a series of molecules with varying ancillary ligands

attached to the same transition metal center. In this particular instance, we have studied the

$(RO)_3Mo{\equiv}N$ molecules where $R = C(CH_3)_3$, $CH(CH_3)_2$, or $CCF_3(CH_3)_2$. This allows one to study

the effects of alkoxide substitution on the electronic structure of the transition metal nitrides.

Looking at the spectra in Figure 3.5, it is observed that the general layout of the spectra is

unaffected by alkoxide substitution; the spectra still consist of three distinct regions: A, B, and

C. The spectral features all shift in accordance with the expected donor capacity of the alkoxide

ligand: $^-OC(CH_3)_3 > ^-OCH(CH_3)_2 > ^-OCCF_3(CH_3)_2$. In general, the shifts correlate well with the

shift of the lone pair ionizations of the free alcohols, where $(CH_3)_3COH = 10.22$ eV,

$(CH_3)_2HCOH = 10.36$ eV, and $(CH_3)_2CF_3COH = 11.11$ eV.) Although the overall layout of the

spectra does not change as the alkoxide donor identity is changed, subtle changes are present in

ionization band A, where the ionizations from the highest occupied N-M σ and π combinations

along with some alkoxide π-type orbitals are expected to occur. As shown in Figure 3.6, the

prominent ionization features in band A are labeled a, b, and c, and, as seen in Table 3.2, these

features shift in accordance with the overall donor ability of the alkoxide ligand.

He II photoelectron studies. To provide experimental proof of the position of the N-M

σ and π ionizations, the photoelectron spectra were recollected using a He II photon source.

Experimental cross-sections for ionizations from molecules roughly follow the trends predicted

by the Gelius model, where molecular cross sections are treated as the sum of the atomic cross

sections of the atoms that contribute to the molecular orbital character.[75,76] Yeh and Landau

have performed calculations to predict the cross-sectional behavior of the atomic elements.[77] The

calculated valence atomic He II/He I ionization cross-sections for the atoms in these molecules

are H (0.153); C2p (0.306); N2p (0.4); O2p (0.639); F2p (0.905); Cr3d (0.925); Mo4d (0.323);

and W5d (0.322). Although ionizations from Mo and W-based orbitals are predicted to drop in intensity when He II is used as the photon source, experimentally they are known to grow under He II radiation.[78] The calculated cross-sections do not account for the Super-Koster Kronig transitions that occur for second and third row transition metals; these processes increase the intensity of ionizations from orbitals containing metal character.[78] Thus in comparing He II spectra with He I spectra, ionizations with metal character are expected to grow with respect to those with oxygen character, which are in turn expected to grow with respect to those with carbon and hydrogen character.

The He II spectra of the $(RO)_3M \equiv N$ analogs in the 8.0 to 15.0 eV region are presented in Figure 3.7. The top three spectra correspond to the $(^tBuO)_3M \equiv N$ molecules, where M = Cr, Mo, and W, respectively. In the spectra, the raw data points correspond to the He II spectra while the solid lines correspond to the He I spectra. Significant relative cross-section changes occur where the intensity of the He II data deviates from the He I spectrum, i.e. where the He II data lies above the He I spectrum, the relative ionization cross-sections have increased in He II and vice-versa. The ionizations in the 8.5 to 11.5 eV region (bands A, A* and B) grow in relative intensity under He II radiation, consistent with substantial oxygen and metal character, and band B is at least partially due to ionization of the totally bonding combinations of the N-M σ and π orbitals with the ligand a_1 and e(II) ionizations, respectively. Not surprisingly, the ionizations between 8.0 and 10.5 eV region (bands A and A*) show the most growth in intensity when He II is used as the photon source. This is in agreement with the information obtained by looking at the shifts in the He I data upon changing the metal; region A + A* contains the ionizations assigned to the M-N σ and π ionizations along with some oxygen-based ionizations. In all cases, region C shrinks dramatically in relative intensity under He II radiation. This is consistent with

the assignment that region C is associated with the C-C σ and C-H σ ionizations of the alkoxide framework and contains no ionizations from metal-containing orbitals.

Looking at the $(^tBuO)_3Cr\equiv N$ spectra, the most growth under He II radiation occurs around 9.5 eV (the high end of band A designated by (*); therefore, the Cr-N σ and π ionizations must occur in this region of the spectrum. Interestingly, this does not correspond to the first ionization feature of the Cr spectra, and is further proof that the first ionization does not correspond to ionization of a Cr-containing orbital. This is not surprising considering the information garnered earlier from the He I data along with the simple molecular analysis. The first ionization of the Cr compound is assigned to the a_2 ligand combination. Band A* behaves in a similar manner to the first shoulder of band A (ligand a_2 ionization) so it is quite likely that this feature is due to ionization of a ligand-based orbital. Looking at the 11.5 to 8.5 eV region of the Mo and W analogs, it is clear that the most growth occurs in the beginning of band A under He II radiation. Thus, the tentative assignment of the M-N σ and π to the first ionization feature of the spectra based on the shifts seen in the He I spectra is confirmed by the He II data analysis. Although the positions of the ionizations containing the most metal character are easily identified in the He II spectral analysis, the overall growth in the region points toward extensive mixing between the M-N orbitals and the alkoxide framework.

A similar analysis of the He II spectra of $(RO)_3Mo\equiv N$, where $R = (CH_3)_2HC$ or $(CH_3)_2CF_3C$, provides experimental evidence for the position of the M-N σ and π ionizations. Looking at Figure 3.7 again, the cross-sectional changes seen in the $(^tBuO)_3Mo\equiv N$ He II spectrum are also seen in the He II spectra of the substituted alkoxide systems. That is, region C shrinks under He II radiation while regions A and B grow under He II radiation. Close inspection of the spectral features reveals that the leading edge of band A once again grows substantially with respect to the rest of the spectrum for all of the substituted molybdenum

nitrides. Hence, the Mo-N σ and π ionizations occur in the leading portion of band A for each of the $(RO)_3Mo \equiv N$ molecules studied. Changing the alkoxide donor group serves only to shift the overall ionization positions in the spectra with the ionizations from the M-N σ and π remaining as the first ionizations in the photoelectron spectra.

Density Functional Studies. As a starting point for the computational studies of the $(RO)_3M \equiv N$ molecules, density functional calculations were performed on molecules in which the alkoxide ligands were modeled with hydroxides. The calculated orbital eigenvalues for the first six molecular orbitals are presented in Table 3.3. To aid the interpretation of the trends seen in the eigenvalues as the metal is changed from Cr to Mo and finally to W, a correlation diagram of the first five eigenvalues is presented in Figure 3.8. The model calculations give results that are similar to those obtained by simple molecular orbital theory presented earlier. That is, there is a group of four ionizations for each molecule that is well-separated from the other ionizations. In terms of the photoelectron spectra, these four ionizations are observed as the ionization bands A and A*. Focusing on the chromium system, the HOMO is the ligand-based a_2 combination of the oxygen lone pairs. The next two highest occupied molecular orbitals correspond to the Cr-N σ and π orbitals, respectively. For the Mo and W analogs, the HOMO corresponds to the M-N σ orbital, and the SHOMO corresponds to the M-N π orbital. The a_2 oxygen lone pair combination becomes the third highest occupied orbital for the Mo and W systems. Focusing on the trends, the ionizations corresponding to the M-N σ and π orbitals are destabilized as the metal is changed from Cr to Mo to W as expected by electronegativity ,while the ligand a_2 orbital displays the exact opposite trend as expected from the interatomic distances between the oxygen atoms. For clarity, it is important to emphasize the highest occupied M-N σ ionization, $2a_1$, contains oxygen character; in fact, the orbital is more appropriately labeled, M-N σ - OH(a_1), to emphasize the orbital mixing that occurs in these molecules. Similarly, the M-N π orbital also

contains a substantial amount of oxygen character. So, the oxygen lone pair combinations discussed earlier do indeed mix with the M-N σ and π orbitals and the importance of this mixing cannot be ignored.

Although DFT calculations on the $(HO)_3M \equiv N$ molecules adequately reproduce the experimental orbital orderings, some questions remain unanswered from these studies. In particular, one must wonder how appropriate it is to model the $(^tBuO)_3M \equiv N$ systems with $(HO)_3M \equiv N$. The amount of mixing among the ligand orbitals will be much greater for the alkoxide molecules relative to the hydroxide models. Based on the photoelectron spectra of ^tBuOH and water, the oxygen-based ionizations of the alkoxides are expected to be destabilized on the order of 2 eV compared to those of hydroxide. Since the degree of mixing is inherently dependent upon the relative energy of the OR_3^{3-} and M-N^{3+} fragments, one might infer that the degree of mixing in the $(HO)_3M \equiv N$ might not accurately represent that in the full molecules. The model calculations do not give any insight into the effects of alkoxide substitution on the electronic structure of the transition metal nitrides. Given the fact that the Mo and W analogs crystallize as linear polymers, it is questionable to use the bond distances and angles from these crystal structure determinations to model the molecules in the gas-phase, where there are no intermolecular interactions. Since these molecules are formally d^0 systems, another important unanswered question concerns determining the relative amounts of metal and ligand character in the M-N σ and π orbitals. Although the overall molecular orbital orderings from the model calculations agree well with those obtained from the photoelectron spectroscopic studies, the calculations do not reproduce the unusual first ionization energy trends seen in the photoelectron spectra. That is, the calculations on the model hydroxides do not predict that the chromium molecule is the most easily ionized molecule among the series.

In order to address the applicability of using OH as a model for OR, we have completed

a computational study employing density functional theory as implemented in the ADF2000

package. Specifically, geometry optimizations were performed on the alkoxide systems in order

to model the molecules in the gas phase, where intermolecular interactions are minimized.

Because $(^tBuO)_3Cr\equiv N$ does not crystallize as a linear polymer but as a single molecule in the

solid phase, the experimental geometry of this system can be used a test of the ability of the ADF

package to reproduce the experimental geometries. The calculated geometrical parameters are

presented in Table 3.4. For comparison, the computational as well as the experimental values are

given. Focusing on the results for the chromium molecule, the experimental distances are all

reproduced to within 0.03 Å, while the experimental bond angles are all reproduced to within 5°.

Most significantly, the calculated value for the $Cr\equiv N$ distance, 1.550 Å, agrees well with the

experimental value of 1.538 Å. Also, the calculated value for the N-Cr-O angle, 107.60°, closely

matches the experimental value of 108.16°. Looking at the results for the molybdenum and

tungsten analogs, the calculated bond distances of the $(^tBuO)_3M\equiv N$ systems also closely

correspond to the experimental values. Focusing on the $M\equiv N$ distances, the calculated $Mo\equiv N$

bond length, 1.679 Å, is only slightly longer than the crystal structure distance, 1.661 Å; while

the calculated $W\equiv N$ bond distance, 1.696 Å, is significantly shorter than the experimental value

of 1.740 Å. Considering the tungsten molecule displays the strongest intermolecular

interactions in the solid phase, it is logical that the calculated $W\equiv N$ distance, in the absence of

intermolecular interactions, is shorter than the experimental distances. Interestingly, all of the

other calculated distances for the Mo and W molecules are within 0.03 Å of the experimental

values. All of the calculated bond angles, excluding the N-M-O angles, are slightly shorter than

the crystal structure values for the Mo and W analogs. In the absence of intermolecular

interactions, the N–M–O angles expand slightly (3-5°).

Although the simple treatment of the alkoxide ligands as cylindrical π-donors in the preliminary discussion or as hydroxides in the model calculations is a starting point for understanding the interactions between the M-N framework and the alkoxide framework, the description developed using these approximations neglects the effects of the alkyl framework on the alkoxide orbitals. Figure 3.9 shows the orbital plots of the six highest occupied orbitals (a_2, e, e, and a_1) of the ligand fragment $(^tBuO)_3^{3-}$. These orbitals are similar to those presented in the preliminary discussion section. However, the $(^tBuO)_3^{3-}$ orbitals are noticeably tilted from the planar orientation used in the development of the model system. A second major difference between the model orbitals and the $(^tBuO)_3^{3-}$ orbitals is that the $e(\|)$ and $e(\perp)$ labels are no longer applicable because the two sets of e orbitals mix together.

Figure 3.10 contains the orbital plots for the two a_1 orbitals along with the a_2 orbital of $(^tBuO)_3Cr\equiv N$; orbital plots for the molybdenum and tungsten analogs are essentially the same and will not be included. Focusing on the two a_1 orbitals, it is evident that the highest occupied M-N σ combination is split by interaction with an alkoxide-based a_1 orbital to form a bonding interaction, $1a_1$, and the corresponding antibonding interaction, $2a_1$. The bonding combination also contains some C-C σ interactions that mix into the orbital in an antibonding fashion with respect to the oxygen orbitals. Unlike the $(^tBuO)_3^{3-}$ fragment orbital of a_2 symmetry (Figure 3.9), the corresponding orbital of $(^tBuO)_3Cr\equiv N$ undergoes a further destabilization due to mixing in of C-C σ character into the orbital in an antibonding fashion with respect to the oxygens. The high concentration of negative charge on the oxygens in the $(^tBuO)_3^{3-}$ fragment calculation destabilizes the oxygen combinations from the alkyl σ orbitals and hinders mixing of the alkyl framework with the oxygen atoms. The negative charge on the oxygens, in $(^tBuO)_3Cr\equiv N$, is significantly less than -3 so the orbital energies of the oxygen combinations are much closer in energy to the alkyl energies and mixing becomes possible. In particular, it must be noted that the C-C and C-H

σ orbitals can form symmetry combinations and mix with the oxygen lone pairs to form bonding and antibonding combinations between the alkyl orbitals and the appropriate oxygen symmetry combination.

Figure 3.11 contains the orbital plots of the first three orbitals of e symmetry. For simplicity the orbitals are labeled 3e, 2e, and 1e. One of the most important features of the e orbitals is the extensive mixing that is readily evident in the orbital plots. Clearly, the M-N π orbital is being spread through the three orbitals by extensive mixing with the oxygen framework. The amount of mixing, along with the specific oxygen orbitals that mix with the M-N π orbitals depend on the particular metal. The most stable of the three e orbitals is the one that contains $M(d_{x^2-y^2}$ or $d_{xy})$ character.

To illustrate the trends seen in the Kohn-Sham orbital energies as the metal is changed, the orbital eigenvalues are presented in the form of a correlation diagram in Figure 3.12. The top four ionizations ($2a_1$, a_2, 3e, and 2e) are well-separated from the rest of the ionizations. This is similar to the pattern seen for the $(HO)_3M\equiv N$ model calculations and as expected from the molecular orbital diagram developed from symmetry considerations and basic chemical principles. The Kohn-Sham orbital energies of the first seven orbitals are presented in Table 3.5. The HOMO of $(^tBuO)_3Cr\equiv N$ is the ligand a_2 combination. This orbital is well-separated from the next two orbitals: 3e and $2a_1$. In turn, these two orbitals are then well-separated from the last of the group of four orbitals designated as 2e. These separations are similar to those seen in the photoelectron spectra. For the molybdenum and tungsten analogs, the separation in the top four ionization is less than in the chromium molecule. The ligand a_2 ionization, in particular, is stabilized as the group is descended. This is the expected trend given the fact that the distance between the oxygen is shortest in the case of the chromium nitride molecule (2.92 Å) in comparison to the corresponding distances in the Mo and W analogs, 3.17 Å and 3.15 Å,

respectively. Since this orbital is completely antibonding, the shorter the distance between the

oxygen atoms, the more the orbital is destabilized. The M-N σ and π orbital combinations

follow the expected trend: metal-containing orbitals are destabilized as the group is descended

from chromium to tungsten. In fact the $2a_1$ orbital, M-N σ - $OR(a_1)$, is the HOMO of the

molybdenum and tungsten analogs; this is the same ordering that the $(HO)_3M \equiv N$ calculations

gave. Well-separated from the top four orbitals, the next two orbitals, of a_1 and e symmetry

correspond directly to band feature B in the photoelectron spectra. The splitting patterns of the

Kohn-Sham orbitals agree with the photoelectron spectra. Although the absolute energies are too

low by about two eV, the relative energies match well with the experimental data. Comparing

the energies of the HOMOs for the Cr (-6.19 eV), Mo (-6.33 eV), and W (-6.24) analogs, the

calculations reproduce the unusual trend seen in the energies of the first ionization band feature

in the photoelectron spectra: Cr < W < Mo.) Given that the previous calculations on the

$(HO)_3M \equiv N$ molecules (M = Cr, Mo, W) did not produce the correct ionization trend for the

highest occupied molecular orbital, it can be inferred that inclusion of the alkyl substituent

groups is vital to producing an accurate picture of the bonding in these systems. In reality this is

not a surprising result because, as was mentioned previously, the C-C σ bonds form symmetry

combinations that interact strongly in an antibonding fashion with the oxygen lone pair

combinations. This antibonding interaction serves to destabilize the ligand combination orbitals

in comparison to those of the model hydroxide calculations, and, as a direct result of the

destabilization of the oxygen lone pair combinations, the chromium analog becomes the most

easily ionized of the $NM(O^tBu)_3$ molecules.

The % atomic characters of the molecular orbitals are presented in Table 3.6. It is seen

that the M-N σ and π orbitals undergo extensive mixing with the alkoxide orbitals. Although

this is already known from the orbital plots, these values give numerical data to support the

pictorial representations. The two orbitals of a_1 symmetry are actually two of a three orbital set. The three orbitals are the N(2p), the metal (d_{z^2}), and the R-O (a_1) combination that is in close proximity. From the three combinations, one gets a totally bonding orbital, a non-bonding orbital with a node through the central atom, and an antibonding orbital. The unfilled antibonding combination is further perturbed by the mixing in of M(pz) to polarize the orbital towards the metal. The highest occupied orbital of a_1 symmetry is the non-bonding orbital, which has a node through the metal atom and hence very little Cr d_{z^2} character. Looking at the values for the highest occupied orbital of a_1 symmetry ($2a_1$), it is interesting to note that both the M(d_{z^2}) and N(2p) characters in this orbital increases as the metal is changed from Cr to W. Interestingly, the N(2s) atomic character also increases as the group is descended, but, in all cases, the amount of N(2s) character in the orbitals remains below 7% of the total orbital makeup. This mixing results in the slight polarization of the orbital toward N. The opposite trend in orbital characters is seen for the completely bonding combination of $M \equiv N$ σ with the alkoxide a_1 combination, $1a_1$. That is, the amounts of N(2p) and M(d_{z^2}) character decrease as the metal is changed from Cr to Mo to W. Similar trends are seen for the M-N π combinations so these will not be discussed in detail. The key concept is mixing of the alkoxide orbitals with M-N orbitals causes the traditional M-N σ and π orbitals to be spread among the valence orbitals of the appropriate symmetry.

The reactivity and behavior of molecules is directly dependent on the frontier orbitals and the charge distribution in the molecules. For comparison, Mulliken charge analyses were performed using the Gaussian98 and ADF2000 programs. The G98 results are from the calculations on the model compounds, $(HO)_3M \equiv N$, while the ADF2000 results are from the calculations on ($^tBuO)_3M \equiv N$ The results are presented in Table 3.7. Both the model calculations as well as the calculations on the full molecules show that the M-N charge distribution is polarized: $M^{\delta+}$ and $N^{\delta-}$, and the polarity of the M-N bond increases as one descends

the group. That is, the N-atom basicity increases as the group is descended. The M-O bonds are polarized in a similar manner. For comparison the Mulliken charges for $CH_3C \equiv N$ are also included in Table 3.7. The charge polarization within the multiple bond is much more important for the inorganic nitriles than the organic nitriles as would be expected due to the relative energy of M and C.

To directly probe the effects of alkoxide substitution, calculations also were performed on $(RO)_3Mo \equiv N$, where R = $(CH_3)_2HC$ or $(CH_3)_2CF_3C$. The geometries were optimized under idealized C_{3v} symmetry. Interestingly, the geometry at the metal center, including the $Mo \equiv N$ and Mo-O distances and the M-Mo-O angle, is not sensitive to the alkoxide donor as shown in Table 3.8. Given this, it seems logical that, excluding the obvious charge effects, the electronic structure will probably not be perturbed to any great extent by alkoxide substitution. The correlation diagram involving the Kohn-Sham orbital energies (Figure 3.13) shows that changing the alkoxide donor does not change the orbital ordering. To allow for a better interpretation of the effects of alkoxide substitution, the orbital eigenvalues of the six highest occupied molecular orbitals are presented in Table 3.9. The orbitals simply shift in accordance with the overall donor ability of the alkoxides: $C(CH_3)_3 > CH(CH_3)_2 > CCF_3(CH_3)_2$. The highest occupied orbital of a_1 symmetry, $2a_1$, remains the HOMO of the $(RO)_3Mo \equiv N$ systems even though the R group changes. The calculations do not predict a strong influence of the alkoxide on the orbital character of the valence orbitals. The makeup of the valence molecular orbitals shows very little change as the alkoxide donor is changed. That is not to say that the alkoxides are not important to the electronic structure of the $(RO)_3Mo \equiv N$ systems. As shown in Table 3.10, all of the valence orbitals contain significant amounts of alkoxide character. Taking a quick look at the Mulliken charges presented in Table 3.11, the charges on N, M, and O are not sensitive to the identity of the alkoxide.

Reactivity of $(RO)_3M \equiv N$. From the theoretical analysis of the bonding described

earlier, these compounds can be viewed as inorganic nitriles. The tendency for these compounds

to associate forming extended chains in the solid-state by way of $(M \equiv N \rightarrow M \equiv N \rightarrow)_\infty$ bears

testimony to the nucleophilic nature of the nitrogen and the electrophilicity of the metal

center.[3,54] From the experimental and computational studies presented here, it is shown that the

basicity of the nitrogen atom increases as M is changed from chromium to molybdenum to

tungsten. Given the known reactivity of organic nitriles towards $W_2(O^tBu)_6$ shown in Reaction

3.1, the reactivity of $(^tBuO)_3Mo \equiv N$ towards $W_2(O^tBu)_6$ was explored. If the transition metal

nitrides truly are inorganic nitriles, then it follows that they should undergo the same reactivity as

$RC \equiv N$, where R = alkyl or aryl.

$$(3.1) \quad W_2(O^tBu)_6 + H_3CC \equiv N \longrightarrow (^tBuO)_3W \equiv N + (^tBuO)_3W \equiv CCH_3$$
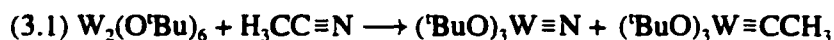
The reaction between $(^tBuO)_3Mo \equiv N$ and $W_2(O^tBu)_6$ was monitored in toluene-d^8 by ^1H

NMR spectroscopy and also carried out on the benchtop in hexanes. At room temperature a

reaction occurs leading to the formation of $(^tBuO)_3W \equiv N$, $Mo_2(O^tBu)_6$, and a third product taken

to be the mixed metal compound, $MoW(O^tBu)_6$. Evidence for the formation of the mixed metal

compound comes from both ^1H NMR and mass spectroscopy. In the ^1H NMR spectra, the

$MoW(O^tBu)_6$ molecule appears as two singlets of equal intensity due to the three ^tBuO ligands

attached to each metal. By mass spectroscopy, we can reliably identify the $MoW(O^tBu)_6^+$ ion

from its characteristic isotopic distribution pattern. From these studies, we conclude that a

metathesis reaction has occurred, Reaction 3.2. The first metathesis reaction can then be

followed by another metathesis reaction (3.3) which together yield all three products detected.

$$(3.2) \quad W_2(O^tBu)_6 + (RO)_3Mo \equiv N \longrightarrow (^tBuO)_3W \equiv N + MoW(O^tBu)_6$$

$$(3.3) \ MoW(O^tBu)_6 + (RO)_3Mo \equiv N \longrightarrow (^tBuO)_3W \equiv N + Mo_2(O^tBu)_6$$
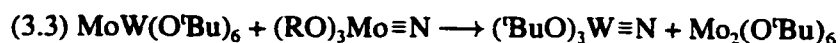
To further probe the reactivity of the transition metal nitrides, $(^tBuO)_3Cr \equiv N$ and

$W_2(O^tBu)_6$ were mixed together in the same manner as the molybdenum nitride and $W_2(O^tBu)_6$.

From this reaction mixture, the formation of $(^tBuO)_3W \equiv N$ was again observed. The chromium-

containing products, on the other hand, were not as straightforward as the molybdenum-

containing products for the corresponding reaction with the molybdenum analog. The only

chromium-containing compound that has been isolated from this reaction is $Cr(O^tBu)_4$.[79]

Obviously, the reaction pathway followed by the chromium molecule is not quite the same as that

followed by $(^tBuO)_3Mo \equiv N$; however, this is not unexpected because the formation of a $Cr \equiv W$ or

$Cr \equiv Mo$ bond in the course of these reactions would be a novel discovery. To date, no triply-

bonded dimers involving chromium in the +3 oxidation state have been obtained.[17] The

formation of $Cr(O^tBu)_4$ implies other redox reactions as well as ^tBuO group transfer reactions

have occurred.

Although the reactivities of the chromium and molybdenum compounds do not follow

the same pathway, the N atom transfer reaction does occur in both cases. This implies that

formation of $(^tBuO)_3W \equiv N$ must be the thermodynamic driving force for this reaction. It is highly

unlikely that formation of $MoW(O^tBu)_6$ will be more thermodynamically favored than formation

of $W_2(O^tBu)_6$. In order to calculate the bond dissociation energies, the $(^tBuO)_3M$ fragment was

optimized using the ADF2000 program. For $(^tBuO)_3M$, where M = Cr, Mo, or W, the quartet

ground state was observed. Values of 127, 163, and 186 kcal/mol for M = Cr, Mo, and W,

respectively, were found for the $D(M \equiv N)$.[80] These values are reasonably close to the

experimentally determined values in related systems.[16,81] Unfortunately, experimental bond

dissociation energies for these particular systems have not been determined, and the bond

dissociation energies of M-M multiple bonds are also not known with reliable accuracy. In any case, the calculated bond dissociation energies do show the tungsten nitride molecule to be thermodynamically favored in relation to the molybdenum and chromium analogs.

Conclusions.

From the experimental and computational studies reported herein, the molecules $(RO)_3M \equiv N$ behave as inorganic nitriles. The electronic structure of these systems can be understood in terms of a simple perturbation of the multiple bonding in $N \equiv N$ and $CH_3C \equiv N$.

Unlike previous studies of transition metal nitrido complexes, the studies of $(RO)_3M \equiv N$ reported herein probe the importance of the alkoxide donors to the electronic structure of the molecules. Because of extensive mixing with the oxygen orbitals, the HOMO of the tungsten and molybdenum analogs is largely non-bonding. Therefore, it donates electrons with little cost to the stability of the molecule. This explains the small structural changes that occur in the molecule upon formation of linear chains in the solid state. The HOMO of the chromium molecule is the highest-occupied OR (a_2) orbital because of the strong antibonding character between the oxygen atoms and the smaller metal atom that serves to provide short Cr-O and O-O distances. Therefore, the chromium molecule is easier to oxidize than would be anticipated in comparison to the molybdenum and tungsten molecules.

Both the charge distribution of the molecules and the N-atom basicity are directly dependent on the identity of M. The polarization of the M-N bond increases as M = Cr < Mo < W. Hence, the basicity of the N-atom also increases in the same order. It is clear from the reactivity studies as well as consideration of bond dissociation energies that the $M \equiv N$ bond strength increases as the metal is changed from Cr to Mo to W.

Substitutions on the alkoxide donor ligands also affect the electronic structure of the $(RO)_3Mo \equiv N$ molecules. The orbital energies of the $(RO)_3Mo \equiv N$ molecules are all shifted in accordance with the overall donor ability of the alkoxide ligand set. The orbital compositions and relative orbital positions, on the other hand, are not substantially changed upon substitution at the alkoxide donor ligand because all of the orbitals are shifted in a similar manner.

The reactivity of the transition metal nitrides, analogous to that of the organic nitriles, is not particularly surprising in light of this understanding of the electronic structure and bonding. The $W \equiv N$ molecule not only has the greatest charge dipole $(M^{\delta+}- N^{\delta-})$ but also the greatest N-atom basicity. In addition, the $M \equiv N$ bond strength increases as $M = Cr < Mo < W$. Therefore, it is logical that the molybenum and chromium molecules react with $W_2(O^tBu)_6$ to produce the thermodynamically favorable nitrido-containing species, $(O^tBu)_3W \equiv N$. In more precise terms, the alkoxides play an important role in destabilizing the occupied frontier orbitals and diminishing the amount of bonding character in these orbitals, thereby facilitating reaction pathways.

Table 3.1. Relative areas of the He I spectral regions (A, A*, B+C) of 'BuOH and ('BuO)₃M≡N relative to the total area (A + A* + B + C).

	ROH	(RO)₃M≡N		
		Cr	Mo	W
8.5 - 10.0 eV (A)	0.09	0.13	0.21	0.18
10.0 - 10.5 eV (A*)		0.065		
10.5 - 14.5 eV (B +C)	0.91	0.80	0.77	0.82

Table 3.2. Prominent features in the He I photoelectron spectra. See Figure 3.4 for definitions.

(RO)$_3$M≡N		Ionization Energy (eV)			
M	R	(*)[29]	a	b	c
Cr	(CH$_3$)$_3$C	8.77	9.03	9.43 9.57	10.20
Mo	(CH$_3$)$_3$C	8.89	9.27	9.58	9.96
W	(CH$_3$)$_3$C	8.75	9.21	9.39 9.71	10.03 10.16
Mo	(CH$_3$)$_2$HC	9.10	9.48	9.85	10.26
Mo	CF$_3$(CH$_3$)$_2$C	9.73	10.36	10.36	10.91

Table 3.3. Kohn-Sham orbital energies (eV) calculated by the G98 program for $(HO)_3M\equiv N$.

Label	Orbital Description	Cr	Mo	W
		Kohn-Sham Energy (eV)		
$2a_1$	$M\equiv N\ \sigma - OH\ (a_1)$	9.20	8.57	8.39
$3e$	$M\equiv N\ \pi$ and OH (e)	9.29	8.96	8.51
a_2	OH (a_2)	8.83	9.05	9.30
$2e$	OH (e) and $Md(\pi)-Op(\pi)$	9.79	9.50	9.74
$1a_1$	$M\equiv N\ \sigma + OH\ (a_1)$	11.14	10.97	11.11

Table 3.4. Comparison of the ADF2000 optimized geometrical parameters with the crystal structure parameters for (^{t}BuO)$_3$M≡N.

(^{t}BuO)$_3$M≡N	Cr		Mo		W	
	Exp.	Calc.	Exp.	Calc.	Exp.	Calc.
M-N (Å)	1.538	1.550	1.661	1.679	1.740	1.696
M-O (Å)	1.739	1.766	1.882	1.907	1.872	1.896
O-C (Å)	1.442	1.461	1.452	1.469	1.475	1.463
C-C (Å) (avg.)	1.499	1.521	1.522	1.533	1.526	1.534
N-M-O (°)	108.2	107.6	103.3	106.5	101.6	106.8
M-O-C (°)	137.4	132.3	135.1	134.3	136.6	134.4
O-C-C (°) (avg.)	106.9	107.8	108.1	107.4	108.6	107.6
O⋯O (Å)	2.86	2.92	3.17	3.17	3.18	3.15

Table 3.5. Ionization energies estimated by Kohn-Sham orbital energies (eV) for (^{t}BuO)$_3$M≡N (M = Cr, Mo, W). The highest occupied orbitals are underlined.

Label	Orbital Makeup	Cr	Mo	W
a$_2$	OR (a$_2$)	6.19	6.39	6.51
2a$_1$	M≡N σ - OR (a$_1$)	6.63	6.33	6.24
3e	OR (e) and M≡N π	6.53	6.56	6.41
2e	M≡N π and OR (e)	7.05	6.87	6.81
1e	M≡N π and OR (e) and M(dxy, dx^2-y^2)	7.80	7.86	7.81
1a$_1$	M≡N σ + OR (a$_1$)	8.04	7.95	7.82

Table 3.6. Primary orbital characters for $(^tBuO)_3M\equiv N$ calculated with ADF2000 program.

	Cr	Mo	W
a₂	75% O p 18% C p	74% O p 18% C p	71% O p 21% C p
2a₁	2% N s 37% N p 4% Cr dz² 34% O p 15% C p	3% N s 42% N p 6% Mo dz² 33% O p 8% C p	6% N s 52% N p 10% W dz² 19% O p 5% C p
3e	7% N p 7% Cr dxz,dyz 57% O(p) 17% C(p)	8% N p 5% Mo dxz,dyz 58% O p 17% C p	10% N p 3% W dxz,dyz 55% O p 15% C p
2e	30% N p 11% Cr dxz,dyz 4% dxy,dx²-y² 25% O p 15% C p	35% N p 12% Mo dxz,dyz 1% dxy,dx²-y² 27% O p 7% C p	41% N p 18% W dxz,dyz 21% O p 7% C p
1e	13% N p 12% Cr dxz,dyz 11% dxy,dx²-y² 9% O p 36% C p 11% H	10% N p 10% Mo dxz,dyz 9% dxy,dx²-y² 10% O p 41% C p 14% H	5% N p 7% W dxz,dyz 8% W dxy,dx²-y² 13% O p 45% C p 15% H
1a₁	3% N s 25% N p 27% Cr dz² 7% O p 24% C p 6% H	3% N s 18% N p 20% Mo dz² 11% O p 29% C p 10% H	2% N s 10% N p 15% W dz² 17% O p 35% C p 12% H

Table 3.7. Mulliken charges for the $(RO)_3M \equiv N$ molecules, where M = Cr, Mo, or W; R = H or 'Bu and $CH_3C \equiv N$.

| | $(RO)_3M \equiv N$ | | | | | | $H_3C\text{-}C \equiv N$ | | |
| | Cr | | Mo | | W | | | | |
	ADF	G98	ADF	G98	ADF	G98		ADF	G98
M	+1.49	+0.66	+1.96	+1.2	+2.04	+1.4	C	+0.11	+0.02
N	-0.53	+0.02	-0.63	-0.27	-0.67	-0.34	N	-0.28	-0.13
O	-0.67	-0.68	-0.75	-0.77	-0.77	-0.81	CH_3	+0.18	+0.11
Δ (M-N)	2.02	0.64	2.58	1.47	2.71	1.74	Δ (C-N)	0.39	0.15
Δ (M-O)	2.16	1.34	2.70	1.97	2.80	2.21	Δ (C-CH_3)	0.07	0.09

Table 3.8. ADF2000 optimized geometry parameters for $(RO)_3Mo \equiv N$.

	(RO)₃Mo≡N		
	$(CH_3)_2HC$	$(CH_3)_3C$	$(CH_3)_2CF_3C$
Mo-N (Å)	1.678	1.679	1.675
Mo-O (Å)	1.908	1.907	1.906
O-C (Å)	1.448	1.468	1.438
N-Mo-O (°)	107.18	106.51	106.05
Mo-O-C (°)	131.76	134.26	135.41

Table 3.9. ADF2000 Kohn-Sham orbital energies (eV) for $(RO)_3Mo \equiv N$.

		Bu^t	Pr^i	$(CH_3)_2CF_3C$
2a$_1$	Mo$\equiv$N σ - RO (a$_1$)	6.33	6.36	7.40
a$_2$	RO (a$_2$)	6.39	6.52	7.44
4e	Mo$\equiv$N π and RO (e)	6.56	6.65	7.62
3e	Mo$\equiv$N π and RO (e)	6.87	6.96	7.97
2e	Mo$\equiv$N π; RO (e); and M(dx^2-y^2,dxy)	7.86	7.98	8.95
1a$_1$	Mo$\equiv$N σ + RO (a$_1$)	7.95	7.99	8.94

Table 3.10. Orbital character analysis for $(RO)_3Mo \equiv N$ from ADF2000.01.

	% character		
	$(CH_3)_2HC$	$(CH_3)_3C$	$(CH_3)_2CF_3C$
$2a_1$	41% N(p)	42% N(p)	42% N(p)
	31% O(p)	33% O(p)	31% O(p)
	6% Mo(z^2)	8% C(p)	7% Mo(z^2)
	6% C(p)	6% Mo(z^2)	4% C(p)
a_2	75% O(p)	74% O(p)	73% O(p)
	18% C(p)	18% C(p)	18% C(p)
3e	56% O(p)	58% O(p)	56 % O(p)
	14% C(p)	17% C(p)	12% N(p)
	7% N(p)	8% N(p)	13 % C(p)
	5% Mo(xz,yz)	5% Mo(xz,yz)	6% Mo(xz,yz)
2e	38% N(p)	35% N(p)	31% N(p)
	26% O(p)	27% O(p)	30% O(p)
	13% Mo(xz,yz)	12% Mo(xz,yz)	10% Mo(xz,yz)
	8% C(p)	7% C(p)	11% C(p)
	1% Mo(x^2-y^2,xy)	1% Mo(x^2-y^2,xy)	2% Mo(x^2-y^2,xy)

Table 3.11. Mulliken charges calculated by ADF2000 for the $(RO)_3Mo\equiv N$ systems.

	(RO)₃Mo≡N		
	$(CH_3)_2HC$	$(CH_3)_3C$	$(CH_3)_2CF_3C$
Mo	+1.95	+1.96	+1.99
N	-0.62	-0.63	-0.61
O	-0.74	-0.75	-0.73
Δ (Mo-N)	2.574	2.58	2.60
Δ (Mo-O)	2.694	2.70	2.72
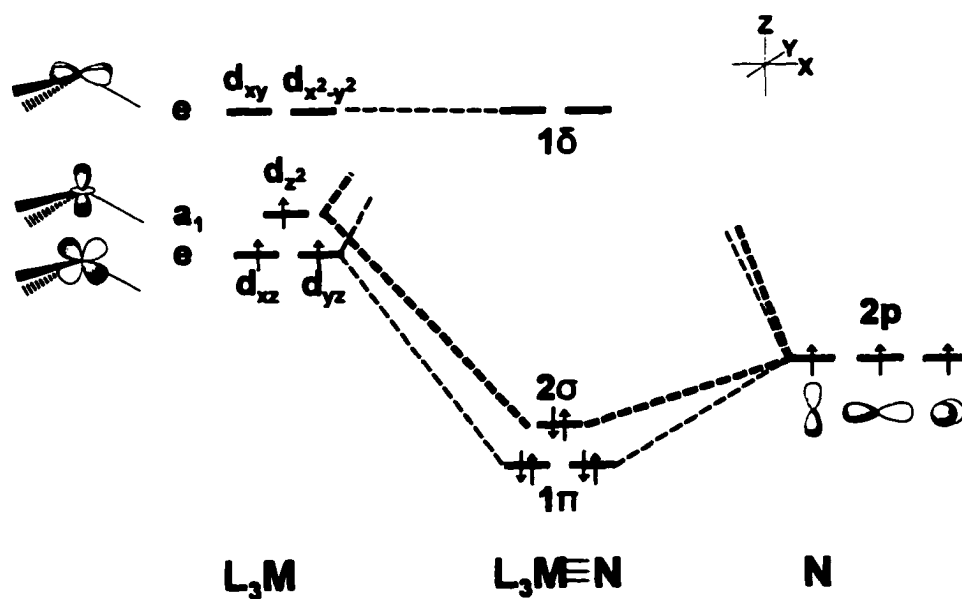
Figure 3.1. Molecular orbital diagram for the formation of the M≡N bond from the interaction of the L_3M and N(p) fragments. The splitting of the $2a_1$ and 1π orbitals is small and depends on the identity of the ancillary ligands.
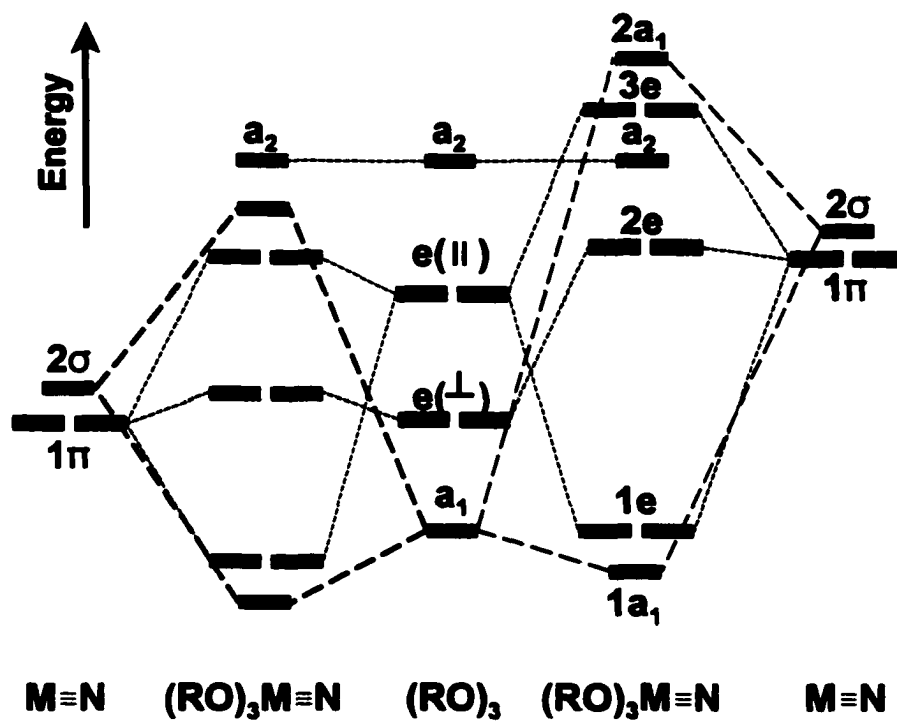
Figure 3.2. Molecular interaction diagram showing the possible interactions between the six highest occupied π-type combinations of the $(RO)_3^{3-}$ fragment (middle) and the $M\equiv N$ σ and π orbitals when the $M\equiv N$ orbitals are lower in energy than the ligand orbitals (left) or higher in energy than the ligand orbitals (right).
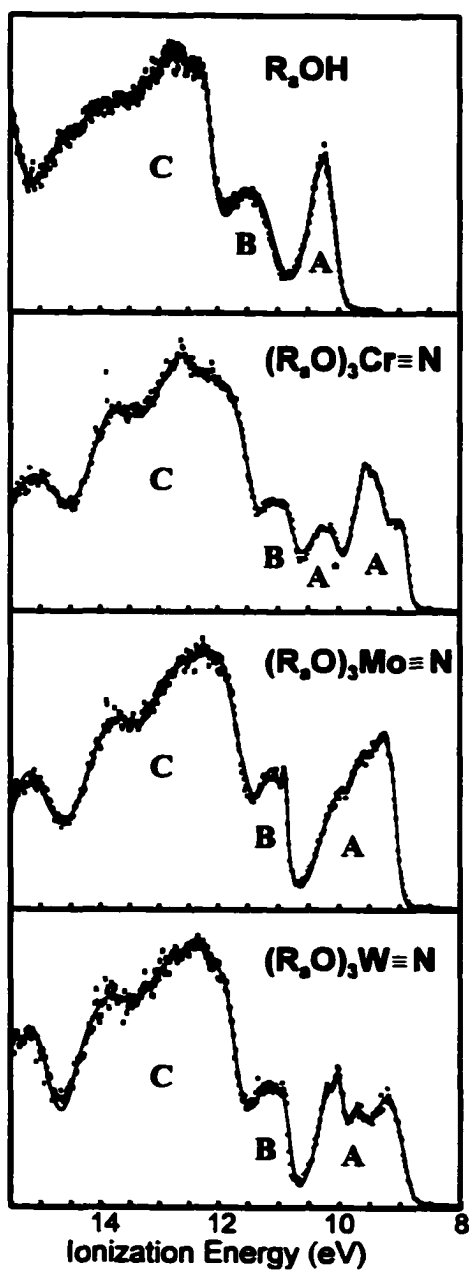
Figure 3.3. He I photoelectron spectra of 'BuOH and ('BuO)₃M≡N (M = Cr, Mo, or W).
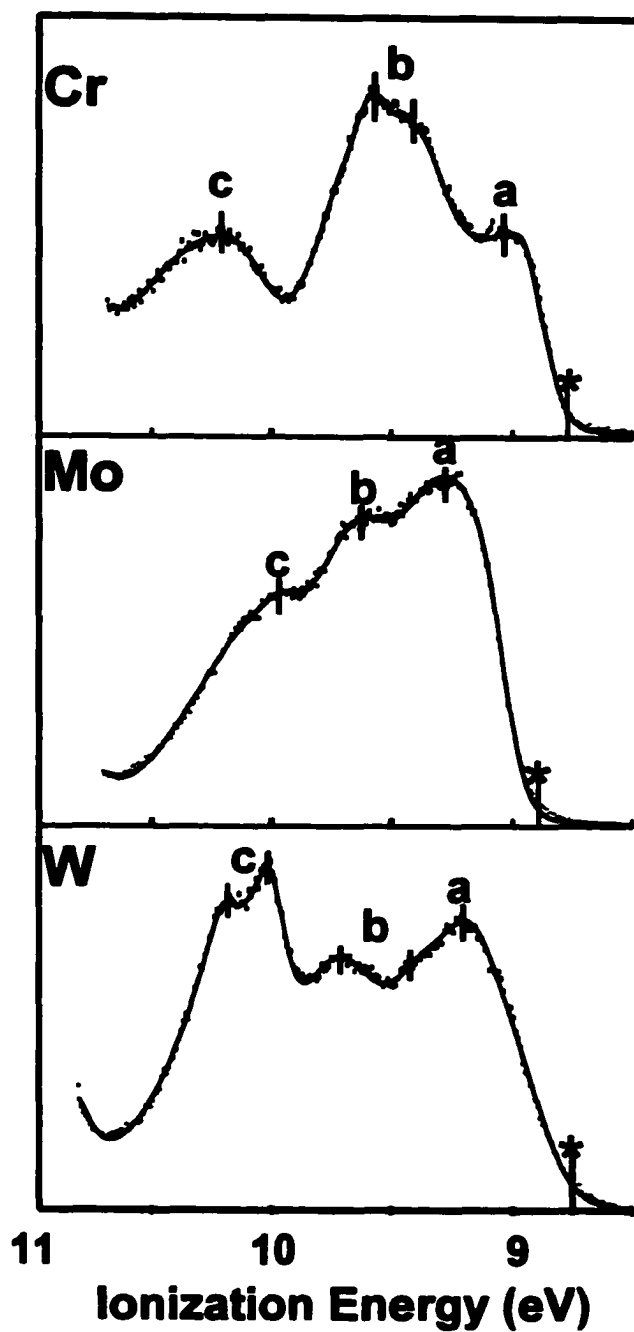
Figure 3.4. He I photoelectron spectra of
(^{t}BuO)$_3$M≡N (M = Cr, Mo, and W) in the 8 to 11 eV
range. The major features in the spectra are labeled
a, b, and c. The onset of ionization is designated by
a (*).
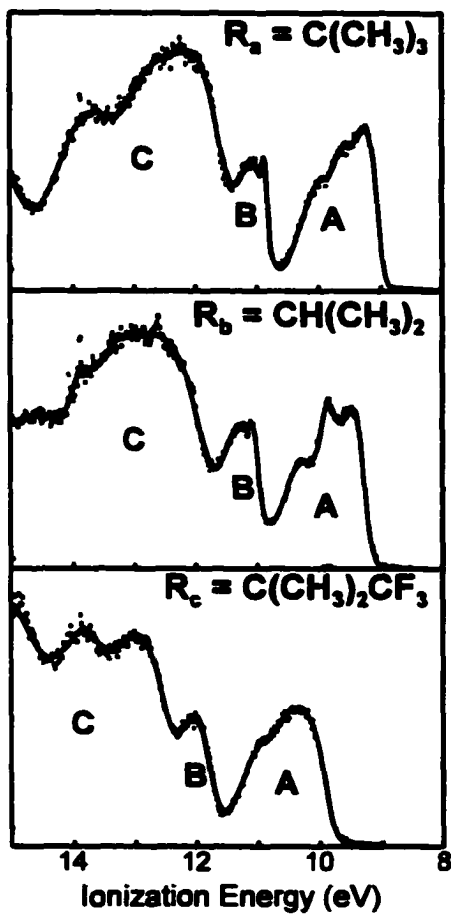
Figure 3.5. He I photoelectron spectra of $(RO)_3Mo\equiv N$ (R_a = ^tBu, R_b = ^iPr, and R_c = $(CH_3)_2CF_3C$.
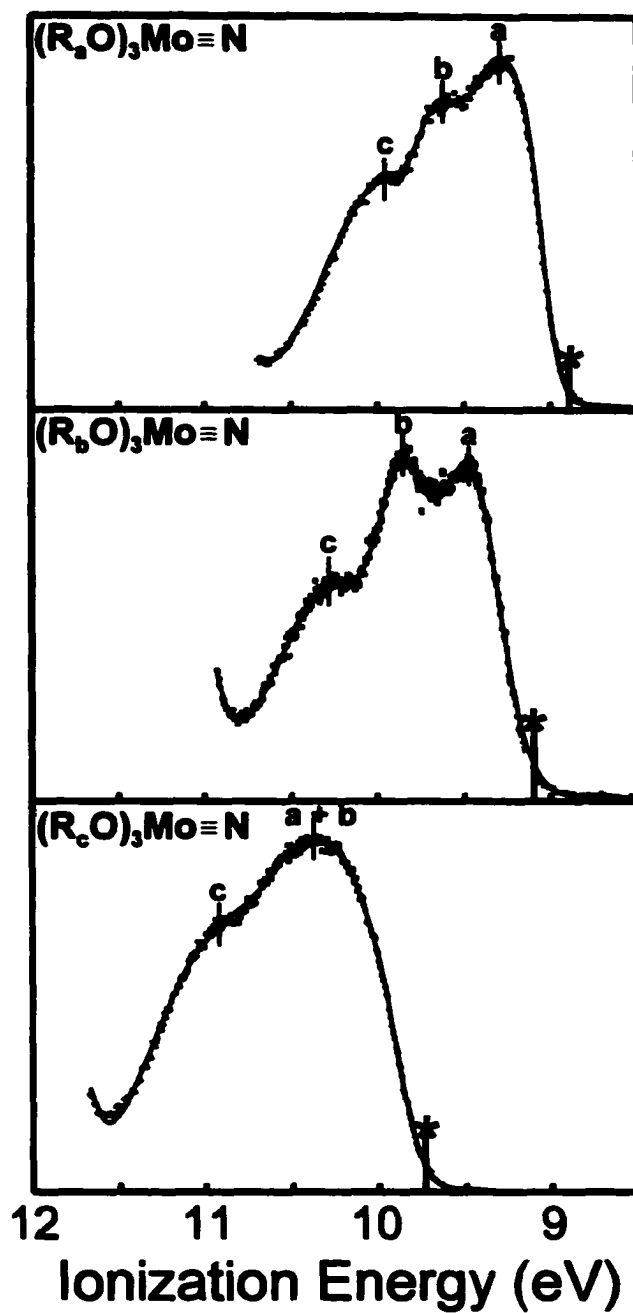
Figure 3.6. He I photoelectron spectra of
$(RO)_3Mo \equiv N$ (R_a = ^tBu, R_b = ^iPr, R_c = $(CH_3)_2CF_3C$)
from 3.5 to 12 eV. The major features in the spectra
are labeled a, b, and c. The onset of ionization is
designated by a (*).
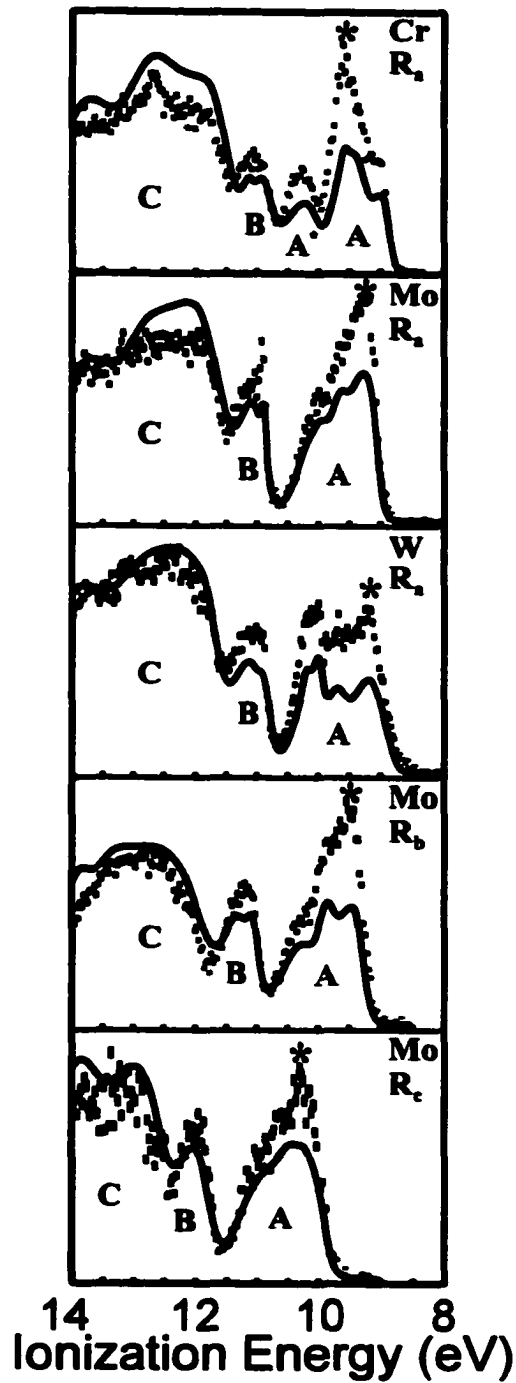
Figure 3.7. He II photoelectron spectra of
(R$_a$OM≡N (M = Cr, Mo, and W; R$_a$ = ^{t}Bu), and
(RO)$_3$Mo≡N (R$_b$ = ^{i}Pr, and R$_c$ = (CH$_3$)$_2$CF$_3$C)). The
data points represent the He II data while the solid
lines are the respective He I fits. The positions of
the M≡N σ and π ionizations are designated by a
(*).
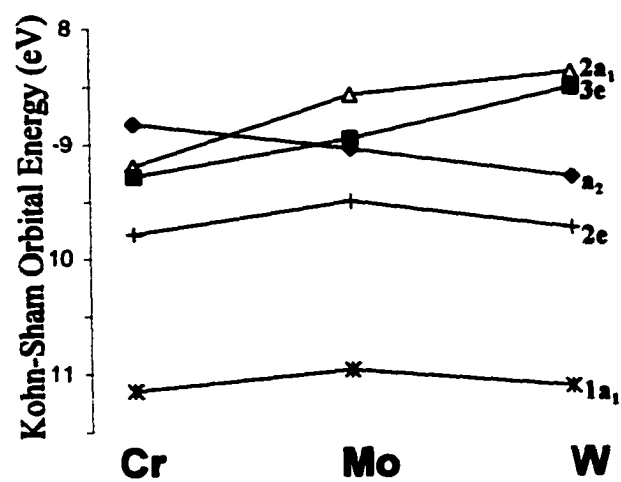
Figure 3.8. Correlation diagram of the Kohn-Sham orbital energies of $(HO)_3M \equiv N$ (M = Cr, Mo, W).
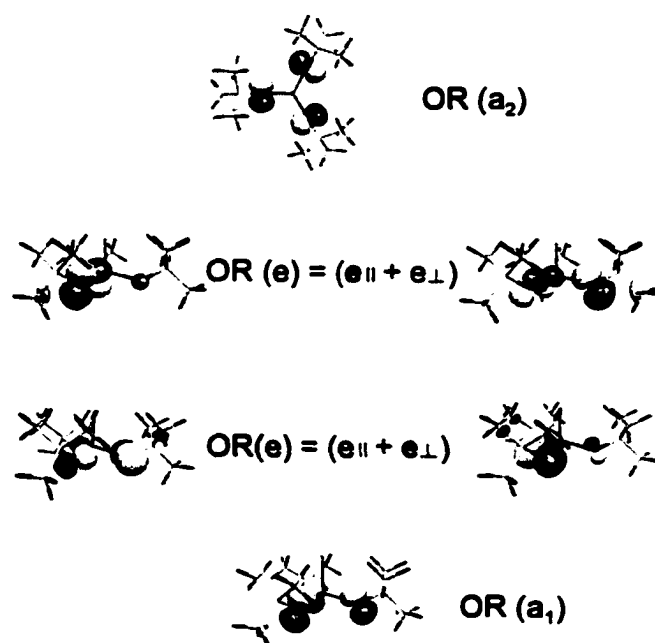
Figure 3.9. The six highest occupied orbitals of
(^{t}BuO)$_3^{3-}$ fragment calculated by the ADF2000
program (Contour = 0.05).

$$2a_1 = MN\ \sigma - OR(a_1)$$

$$1a_1 = MN\ \sigma + OR(a_1)$$

$$a_2 = OR(a_2)$$
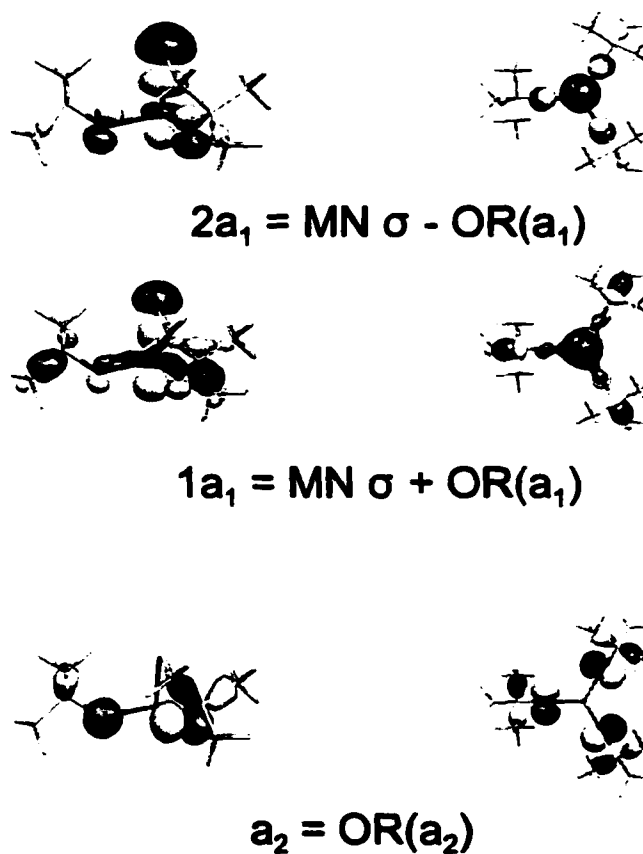
Figure 3.10. Molecular orbital plots of the $2a_1$, $1a_1$, and a_2 valence orbitals (Contour = 0.05) of ($^tBuO)_3Mo \equiv N$. For each orbital, a side view (left) and a top view (right) are presented.

3e = M≡N π and OR (e)

2e = M≡N π and OR (e)

1e = M≡N π and OR (e) and
M(dx²-y²,dxy)
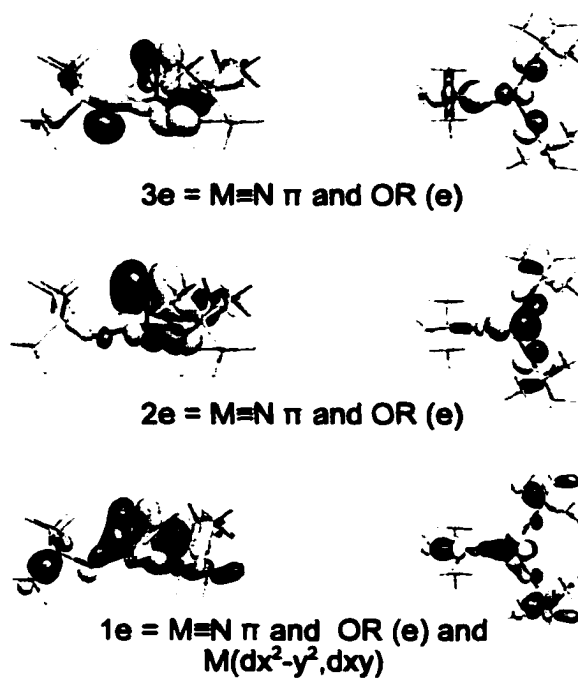
Figure 3.11. Molecular orbital plots of the 3e, 2e, and 1e orbitals (Contour = 0.05) of ('BuO)₃Mo≡N. For each of the molecular orbitals a side view (left) and a top view (right) are presented.
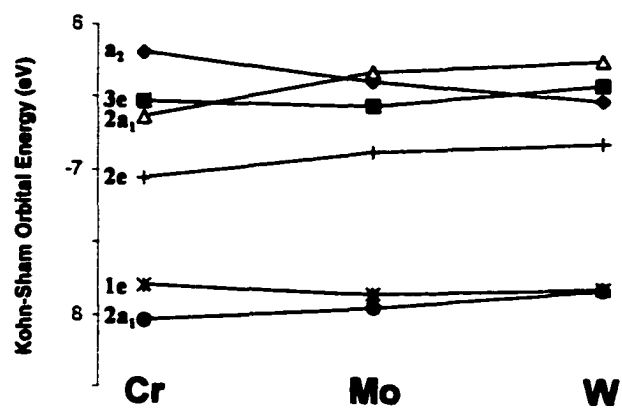
Figure 3.12. Correlation diagram of the Kohn-Sham orbital energies of ($BuO)_3M \equiv N$ (M = Cr, Mo, W).
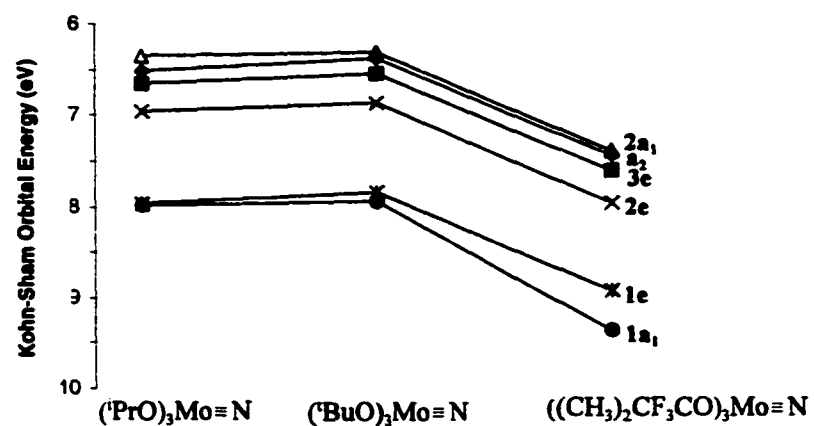
Figure 3.13. Correlation diagram of the Kohn-Sham orbital energies of $(RO)_3Mo \equiv N$, $R = {}^iPr$, ${}^tBu$, and $(CH_3)_2CF_3C$.

CHAPTER 4

THEORETICAL AND SPECTROSCOPIC INVESTIGATIONS OF THE BONDING OF $Cl_3Mo{\equiv}N$: AN INVESTIGATION INTO THE TRIPLE BOND BETWEEN MOLYBDENUM AND NITROGEN.

Introduction

Because molecules containing multiple metal-nitrogen bonds display a wide variety of reactivities and structural motifs, interest in these molecules has grown in the last twenty years.[5,11,45] Recognized as one of the strongest π-donor ligands in existence, nitrido ligands form strong bonds to transition metals in high oxidation states.[5,44] Much of the interest in molecules containing transition-metal nitrido bonds results from the known ability of phase-pure transition metal nitrides to catalyze the activation of small molecules like N_2 and CO.[6,8] In addition, transition metal nitrides, especially molybdenum and tungsten nitrides, are active catalysts for the hydrodenitrogenation and hydrodesulfurization reactions that are the lifeblood of the oil and gas industry.[10] In general, the reactivity of a molecule is dependent on the frontier orbital energies and the charge distribution within the molecule. Hence, to understand the reactivity of transition metal nitrido molecules, one must first understand their electronic structures.

Investigations into the electronic structure of the $('BuO)_3M{\equiv}N$ analogs (M = Cr, Mo, W) have revealed the importance of the ancillary ligands in determining the electronic structure of the transition metal nitrido molecules. Due to extensive overlap of ionization bands in the photoelectron spectra of these molecules, a detailed analysis of the photoelectron spectra, including peak positions, relative areas, etc., proved to be unobtainable. Unfortunately, changing the nature of the alkoxide donor was not a significant enough perturbation to spread the ionizations apart and allow a more rigorous study of the photoelectron spectra. In order to obtain a more quantitative analysis of the nature of the triple bond between the molybdenum and

nitrogen, a completely different ancillary ligand set was chosen. One of the simplest π-donor

ligands that can be used in place of an alkoxide is a halide. Interestingly, it has been stated that

the $Cl_3M \equiv N$ analogs are among the most important starting materials for the synthesis of

transition metal-nitrido compounds.[44,45] Given that $Cl_3Mo \equiv N$ is the starting material for making

the previously-studied $(RO)_3Mo \equiv N$ molecules,[54] $Cl_3Mo \equiv N$ is the logical choice for studies

aimed at further probing the bonding in these systems.

From formal oxidation state considerations, the molybdenum exists as Mo(VI). That is,

there are formally no metal-based ionizations in the photoelectron spectrum of $Cl_3Mo \equiv N$. A

major question that arises from consideration of the bonding in these systems is the applicability

of the formal oxidation state method to assigning oxidation states in these systems. If these

systems are more covalent in nature, then the formal oxidation state method will overestimate the

ionicity of the bonding. Photoelectron spectroscopy along with density functional studies

provide a route for probing the electronic structure of $Cl_3Mo \equiv N$.

Experimental

General Methods. All manipulations were carried out using an Argon (Ar) or

dinitrogen (N_2) atmosphere and standard air and moisture sensitive techniques in a Vacuum

Atmospheres Glovebox or Schlenk line. Solvents were distilled from CaH_2 or Na/Benzophenone

ketyl. Air was removed via freeze-pump-thaw cycles. All reagents were purchased from

Aldrich unless otherwise stated and used without further purification. Molybdenum

pentachloride (Strem Chemicals) was used as purchased. $Cl_3Mo \equiv N$ was prepared via a reported

method.[48,49]

Spectroscopic methods. Infrared (IR) Spectra were taken as KBr pellets on a Nicolet

510P FT-IR spectrophotometer using OMNI E. S. P. software. Mass spectra were taken on a

Kratos MS 80 high resolution mass spectrometer using Negative Ion CI with methane (CH_4) as reagent gas. A positive ion EI source with a trap current of 100 μA at a temp of 225 °C at 52 eV was used. A 3 kV analyzer was used with a resolution of 2000 using the 5% peak height definition. The scanning rate was 5 sec/decade with a mass range of 1100 to 275.

Photoelectron spectra. The photoelectron spectra were recorded using an instrument that features a 36 cm radius, 8 cm gap McPherson hemispherical analyzer with custom-designed sample cells, detection system, and control electronics.[31] The excitation source was a quartz lamp with the ability, depending on operating conditions, to produce He Iα (21.218 eV) or He IIα (40.814 eV) photons. The ionization energy scale was calibrated by using the $^2E_{1/2}$ ionization of methyl iodide (9.538 eV) and the Ar $^2P_{3/2}$ ionization (15.759 eV). The argon $^2P_{3/2}$ ionization was also used as an internal calibration lock for the energy scale during He II data collection runs. Resolution (measured as full-width-at-half-maximum of the argon $^2P_{3/2}$ ionization) was 0.016-0.024 eV during He I data collection. Assuming a linear dependence of analyzer intensity to the kinetic energy of the electrons within the energy range of these experiments, all data were intensity corrected with the experimentally-determined analyzer sensitivity function.

Because discharge sources are not monochromatic,[33] each spectrum was corrected for the presence of ionizations from other source lines. The He I spectra were corrected for ionizations from the He Iβ line that lie 1.959 eV higher in energy with 3% of the intensity of ionizations from the He Iα line. He II spectra were similarly corrected for ionizations from the He IIβ line (7.568 eV higher in energy and 12% of the intensity of the He IIα line.)

The sample sublimed cleanly with no detectable evidence of decomposition products in the gas phase or as a solid residue. To test the reproducibility of the spectrum, spectra were collected on different days. No changes were detected in the spectrum. The sublimation range

(°C at ~ 10^{-4} Torr) was 90 to 120. The temperatures were measured using a "K" type

thermocouple attached directly to the ionization cell through a vacuum feedthrough.

Data Analysis. In the figures of the photoelectron spectra, the vertical length of each

data mark represents the experimental variance of that point.[34] The ionization bands are

represented analytically with the best fit of asymmetric Gaussian peaks. The number of peaks

used was the minimum necessary to get an analytical representation of the He I spectrum. For

fitting the He II spectra, the peak positions and half-widths were fixed to those of the He I fit.

The confidence limits for the relative integrated peak areas are $\pm 5\%$. The primary source

of uncertainty is the determination of the baseline. The baseline is caused by electron scattering

and is taken to be linear over the small energy range of these spectra. The fitting procedures

used to fit the spectra have been described in more detail elsewhere.[34]

DFT studies.

Gaussian98.[35] Density functional calculations were performed using the Gaussian98

package. A full geometry optimization employing the default convergence criterion was

performed on $Cl_3Mo \equiv N$ using the Gaussian98 suite of programs. The B3LYP method with the

CEP-121G* basis set was used for both the metals and ligands.[35,52,53,82]

ADF2000.01 program.[36] The numerical integration procedure was developed by te

Velde and co-workers.[37,38] The PW91 method was used for all calculations.[55] The atomic

orbitals on all centers were described by an uncontracted triple-ζ STO basis set (set IV) that is

readily available with the ADF package. The $1s^2$ configuration on nitrogen, $1s^2s^2 2p^6$

configuration on Cl as well as the $1s^2 2s^2 2p^6 3s^2 3p^6 3d^{10}$ for Mo were assigned to the core and

treated by the frozen-core approximation. Relativistic effects were included in all calculations

by the scalar ZORA formalism implemented as a part of the ADF2000 program.[56-60] The

molecular structure of $Cl_3Mo{\equiv}N$ was fully optimized under C_{3v} symmetry using the default convergence criterion.[36]

Calculated Ionization Energies. Values for ionization energies can be determined by two different computational procedures. As a first approximation, the Kohn-Sham orbital energies from the ground state calculations of the "neutral" molecule are directly analogous to the experimental ionization energies ($\epsilon_i \approx$ -I. E.).[66,67] In order to obtain a more direct comparison of the relative Kohn-Sham energies, the calculated orbital energies are shifted according to equation (4.1), where Δ_i = 3.48 eV. It is important to note that this scaling equation is only

$$\varepsilon_{shifted} = |\varepsilon_i| + \Delta_i$$
$$\Delta_i = I.E.(MN\,\pi) - |\varepsilon(MN\,\pi)| \quad (4.1)$$

applicable for orbitals with negative eigenvalues. More rigorous calculated ionization energies can be determined by comparing the total energy of the neutral molecule to the total energies of the successive ionic states, where one electron has been removed from the orbital of interest. Ionization energies obtained in this manner are vertical ionization energies (the geometry is assumed to be constant in the neutral and the cation states). These ΔE_{SCF} energies more correctly represent the ionization process because they account for the electron relaxation that occurs in the molecule when an electron is removed.

For comparison, Fenske-Hall molecular orbital calculations have also been performed.[39] The ADF-optimized coordinates were used as the input coordinates for the Fenske-Hall calculations. Contracted double-zeta basis functions were used for the Mo valence d atomic orbitals, the valence 2p atomic orbitals of N, and the 3p atomic orbitals of Cl.[39,83-85] Basis functions for the metal atoms were obtained for the 1+ oxidation state. Ground state atomic

configurations were used for the basis functions of all other atoms. The Fenske-Hall method

overestimates the spread of orbital energies in molecules. To account for this, the energy scale

of the Fenske-Hall method is scaled to match the experimental energy scale. For this case, the

experimental energy difference between the 4e and the $4a_1$ ionizations was used to calibrate the

energy scale of the Fenske-Hall calculation. In order to facilitate a direct comparison between

the density functional results and the Fenske-Hall results, the orbital energies from the Fenske-

Hall calculation were scaled according to equation (4.2).

$$
\begin{aligned}
\varepsilon_{scaled} &= 0.62 \times |\varepsilon_i| + \Delta_1 \\
\Delta_1 &= I.E.(MN\,\pi) - |\varepsilon(MN\,\pi)|
\end{aligned}
\quad (4.2)
$$

Preliminary Considerations

In the simple valence-bond picture the transition metal-nitrogen triple bond of $R_3M \equiv N$:

is composed of the M-N σ bond, formed by the interaction of the $M(d_{z^2})$ with the N(sp hybrid),

and the M-N π, formed by the interaction of the M(xz,yz) and the N(x,y). Placement of a lone

pair of electrons on the nitrogen atom serves to satisfy the octet of the nitrogen atom. Although

this simple picture qualitatively accounts for the M-N triple bond, it does not acknowledge the

influence of the axial ligands (R) on the electronic structure and overestimates the contribution of

the N(2s) to the M-N σ orbital. Figure 4.1 shows a simple orbital interaction diagram in terms

of d^3-Cl_3M and N fragments. As a first approximation, the chlorine atoms of the Cl_3M fragment

are used only to determine the splitting of the d-orbitals: $(d_{z^2} \le d_{xz}=d_{yz} < d_{x^2-y^2}=d_{xy})$ in the ligand

field environment. The actual splitting of the $M(d_{z^2})$ and $M(d_{xz},d_{yz})$ orbitals of the Cl_3M

fragment will be small and depend on the N-M-Cl bond angle. As a starting point, only the

interactions between the N(p) orbitals and the Cl_3M fragment orbitals are included in the figure.

Using this simple interaction diagram, the HOMO of the $Cl_3M \equiv N$ molecule is the $M \equiv N$ π, and

the SHOMO corresponds to the $M \equiv N$ σ orbital. For simplicity, the $M \equiv N$ π is labeled 1π with

the $M \equiv N$ σ, designated as 2σ. It is important to emphasize the 2σ and 1π orbitals will be close

in energy. If the N(2s) is allowed to mix with the $M \equiv N$ σ, the net effect is the destabilization of

the 2σ.[72] Nevertheless, it remains unclear whether the interaction of the N(2s) is significant

enough to destabilize the 2σ above the 1π. In addition, mixing N(2s) character into the $M \equiv N$ σ

orbital polarizes the orbital towards the nitrogen atom so that the orbital looks more like a N lone

pair orbital.[72,86] According to this simple model, the degree of polarization of the 2σ depends on

the amount of N(2s) character that mixes into the orbital. By comparison, the highest occupied

orbitals of $Cl_3Mo \equiv N$ are directly analogous to the $2\sigma_g$ and $1\pi_u$ orbitals of N_2. In the case of N_2,

the mixing of N(2s) into the $2\sigma_g$ orbital (35 % N2s)[87] is substantial and results is a destabilization

of the $2\sigma_g$ orbital above the $1\pi_u$ orbital; an interesting question which must be addressed is the

relative importance of the N(2s) in determining the position of the $M \equiv N$ σ orbital.

Although the simple treatment developed above is useful for describing the $M \equiv N$

interaction, it obscures the importance of the chlorides in determining the electronic structure of

$Cl_3Mo \equiv N$. Clearly, to get an accurate portrait of the bonding, it is important to look at the

influences of the chlorine atoms on the electronic structure. To this end, an alternative approach

for probing the electronic structure of $Cl_3Mo \equiv N$ involves viewing the system in terms of $M \equiv N^{3+}$

and Cl_3^{3-} fragments. This approach effectively separates the chloride ligand framework from the

$M \equiv N$ framework, allowing a detailed analysis of the interactions between the two fragments.

$Mo \equiv N$. Although the electronic structure of $Mo \equiv N$ has been the subject of many

previous studies, the focus of these studies was strictly aimed at determining the electronic states

of the molecule as probed by Stark spectroscopy.[81,88,89] Hence, little work had been done to

explore the orbital ordering of the $Mo \equiv N$ molecule. Before addressing the electronic structure

of the full molecule, $Cl_3Mo \equiv N$, it is useful to consider the symmetry-allowed interactions

between the metal and the nitrogen in the $Mo \equiv N$ fragment. Under C_{3v} symmetry, the metal s, p_z,

and d_{z^2} atomic orbitals are all of a_1 symmetry so the M-N σ is composed of some combination of

N(2s), N($2p_z$), Mo($4d_{z^2}$), Mo 5s, and Mo($5p_z$). Similarly, the N(p_x,p_y), Mo(p_x,p_y), Mo(d_{xz},d_{yz}), and

Mo($d_{x^2-y^2},d_{xy}$) are all of e symmetry. It follows that the M≡N π orbitals are of e symmetry and

are formed by the combination of the M(d_{xz},d_{yz}) and N(p_x,p_y). Although the M(p_x,p_y) and M($d_{x^2-y^2},d_{xy}$) orbitals are also of e symmetry, the former are a poor energy match with the N(p_x,p_y)

orbitals and the latter do not have direct overlap with the N(p_x,p_y) orbitals. Previous theoretical

studies of the L_3M≡N molecules predicted a substantial contribution of the N(2s) to the M-N σ

which served to destabilize the M≡N σ above the M≡N π in an analogous manner to the

destabilization of the dinitrogen σ above the π.[72,86] Considering the substantial energy difference

between the Mo($4d_{z^2}$) and the N(2s), 15.62 eV as calculated by the Fenske-Hall method, mixing

between these two orbitals is not expected to be extensive. Nevertheless, any interaction

between the N(2s) and the Mo($4d_{z^2}$), no matter how small, will serve to destabilize the Mo≡N σ.

To study the importance of the N(2s) in determining the position of the M≡N σ in

relation to the M≡N π, the electronic structure of the Mo≡N fragment was probed via

computational studies. These calculations allow ready analysis of the orbital energies and orbital

makeups of the Mo≡N σ and π orbitals. According to ADF density functional calculations, the

splitting between the Mo≡N σ and π orbitals is quite small, 0.155 eV, so that the orbitals are

almost degenerate with the Mo≡N σ being less stable than the Mo≡N π. The orbital energies

and makeups of the Mo≡N fragment are given in Table 4.1. The bonding is much more simple

for the Mo≡N π than the corresponding Mo≡N σ because it is composed of only the Mo(d_{xz},d_{yz})

and the N(p_x,p_y). Interestingly, while the majority of the Mo≡N σ character originates from the

Mo($4d_{z^2}$) and the N(p_z), accounting for 82 % of the total molecular orbital character, one can not

dismiss the small percentages of N(s) and Mo($5d_{z^2}$) character that contribute to the orbital

makeup of the molecular orbital. Plots of the atomic orbitals used to compose the Mo≡N 2σ are

shown in Figure 4.2. Clearly, both the N(2s) and Mo($5d_{z^2}$) orbitals can contribute to the polarization of the orbital toward N. For comparison, the corresponding orbital energies and makeups from the Fenske-Hall calculations are given in Table 4.2. The Fenske-Hall Mo$\equiv$N σ and π orbitals are calculated to be split by 0.65 eV. Both computational methods predict only a 7-8 % contribution from the N(2s) to the highest occupied Mo$\equiv$N σ. What is not clear from either calculation is the relative importance of the N(2s) in determining the position of this Mo$\equiv$N σ. Simple overlap considerations from the Fenske-Hall program lead one to believe that the M-N π ionization should be more stable than the M-N σ ionization because the overlap between the Mo($4d_{z^2}$) and the N(p_z), 0.132, is half the overlap of the M($4d_{xz},d_{yz}$) with the N(p_x,p_y), 0.264. In order to obtain a direct analysis of the importance of the N(2s) in destabilizing the Mo$\equiv$N σ above the Mo$\equiv$N π, the N(2s) orbital was removed from the valence orbital set of the N atom and treated as a core orbital. The orbital energies and makeups can then be directly compared to those from the calculation where the N(2s) was included as part of the valence set (Table 4.2). As expected, the removal of the N(2s) from the valence set has very little effect on the 1δ orbital energy. On the other hand, the 2σ orbital undergoes a significant stabilization, 3.01 eV, upon removal of the N(2s) from the valence. In comparison, the 1π under the same conditions is only stabilized by 0.42 eV. That is, the M$\equiv$N σ is stabilized below the M$\equiv$N π when the N(2s) is treated as a core orbital.

Energy Decomposition Analysis.[90] To probe the origin of this significant energy shift, the energies of the 2σ and 1π were subjected to an energy decomposition analysis. The orbital energies from the Fenske-Hall calculations are calculated according to equation (4.3),

$$\varepsilon_i = \sum_i c_i^2 F_{ii} + 2\sum_{i>j} c_i c_j F_{ij} \quad (4.3)$$

where c_i and c_j are the coefficients (eigenvector values) of the fragment orbitals in the molecular

orbital of interest and F_{ij} is the Fock matrix element describing the interaction of the two

fragment orbitals.[39,91] The first term in equation (4.3) describes the diagonal contributions to the

molecular orbital energy, while the second term provides the off-diagonal contributions to the

orbital energy. The energy contributions from the overlap of the transition metal d orbitals with

the nitrogen atomic orbitals are by definition described by the off-diagonal terms.

For the Mo≡N molecule, the fragments are the Mo and N valence atomic orbitals. The

results from this analysis for the 2σ and 1π orbitals of the Mo≡N molecule are given in Table

4.3. Looking at the contributions from the diagonal elements, 88% of the energy of the 2σ

molecular orbital is from the diagonal contributions. In fact, the two major contributors to the

diagonal energy of this orbital are the N(2s) and N(pz), indicating that the N(2s) is indeed an

important stabilizing factor in the orbital energy of the 2σ. Only 50% of the energy of the 1π

orbital can be traced to the diagonal terms, and 64% of the 1σ lies in the diagonal energy

contributions. Interestingly, the diagonal energy of the 1σ derives almost completely from the

N(2s) contribution.

The off-diagonal elements contribute heavily to the orbital energies and must be

considered in any full analysis of the orbital energy. Looking at the off-diagonal contributions

for the 2σ orbital, the stabilization provided by the bonding overlap between the nitrogen p_z

orbital and the metal d_{z^2}, -4.923 eV, is largely countered by the destabilization due to the

antibonding interactions between the N(2s) and the metal orbitals, +3.732 eV. The overall result

is that the off-diagonal contributions result in a stabilization of only -1.191 eV, and this orbital is

largely nonbonding between the Mo and N. By comparison, the stabilization that occurs due to

the favorable overlap between the $M(d_{xz}, d_{yz})$ and the $N(p_x, p_y)$ in the 1π orbital is -5.264 eV, and

there are no other interactions to counteract this stabilization, attesting to the strong bonding

interaction between the Mo and N in the orbital. Analysis of the off-diagonal energy contributions to the 1σ orbital yields evidence for a strong bonding interaction between the N(2s) and the Mo orbitals, providing a -7.913 eV stabilization of the orbital energy. Clearly, the N(2s) is not an inert pair in this molecule. In essence, while the 1π and 1σ are strongly bonding between the Mo and N, the 2σ is largely nonbonding between the Mo and N due to the strong influence of the N(2s) on the orbital energy.

To further establish the importance of the N(2s) in determining the relative positions of the 2σ and 1π orbitals, the same energy decomposition analysis was performed on the Fenske-Hall calculation where the N(2s) was removed from the valence set and treated as a core orbital (Table 4.4). The diagonal contributions to the 2σ and 1π orbitals are -5.466 eV and -5.723 eV, respectively. In comparison to the previous results, the diagonal energy contribution for the 2σ orbital has dropped by 3.303 eV, indicating that the N(2s) is an important stabilizing component of the Mo$\equiv$N 2σ orbital energy. In addition, the diagonal energy contribution of the 1π orbital increases by 0.378 eV when the N(2s) is treated as a core orbital.

The off-diagonal terms are also sensitive to the presence of the N(2s). For the 2σ orbital, the off-diagonal contributions increase dramatically from -1.191 eV when N(2s) is included in the valence to -7.510 eV when the N(2s) is treated as a core orbital. The increase in the off-diagonal contributions to the 1π are must less dramatic, increasing by just 0.416 eV when the N(2s) is treated as a core orbital. The major differences in the energy contributions when the N(2s) is treated as a core orbital can be attributed to the importance of the N(2s) in determining the overall electronic structure of these systems. When the N(2s) is treated as a core orbital, the 2σ becomes strongly bonding between the Mo and N. Just because the N(2s) contribution to the orbital makeup is small (7%), does not mean it does not significantly affect the electronic structure of the molecule. An orbital interaction diagram depicting the important interactions

between the valence atomic orbitals of Mo and N is presented in Figure 4.3. For direct comparison of the scenarios when the N(2s) is treated as a valence and alternately as a core orbital, both scenarios are shown in Figure 3. The left side of the diagram shows the case when the N(2s) is included in the valence, and the right side of the diagram represents the bonding in the $Mo \equiv N$ when N(2s) is treated as a core orbital. The orbital interaction diagrams, calculated by the Fenske-Hall method, again demonstrate the importance of the N(2s) in determining the overall order of the $Mo \equiv N$ σ and π orbitals. The stabilization of the N(2s) orbital upon formation of the $Mo \equiv N$ bond, as shown on the left side of Figure 4.3, testifies to the fact that the N(2s) is involved in a bonding interaction with the $Mo(d_z2)$; this interaction is clearly seen in the orbital plot of the $Mo \equiv N$ 1σ. It is clear that the N(2s) is responsible for the order of the 2σ and 1π orbitals in $Mo \equiv N$. In the absence of interaction between the N(2s) and the $Mo(d_z2)$, the 2σ is strongly bonding between the Mo and N. Allowing the N(2s) to interact with the metal serves to make the 2σ a nonbonding orbital.

Ancillary ligand effects. Now that the bonding of the $Mo \equiv N$ fragment has been explored, we can shift our focus to the interaction of the ancillary ligands (Cl_3) with the $Mo \equiv N$ subunit. The degree of interaction between the $Mo \equiv N$ orbitals and the Cl_3 orbitals will directly depend on the relative energy matching (including charge effects) and the overlap between the orbitals of the two fragments. One of the simple means of analyzing charge effects is to consider the relative electronegativities of the interacting fragments. Since we know that the $(RO)_3$ combination orbitals mix extensively with the $Mo \equiv N$ orbitals in the $(RO)_3Mo \equiv N$ molecules, it can be assumed that the same type of interactions will occur in $Cl_3Mo \equiv N$. To gauge the extent of interaction that is expected to occur between the $Mo \equiv N$ and Cl_3 fragments, it is useful to compare the relative electronegativities of the Cl_3 and $(RO)_3$ fragments. The differences between the two systems can be modeled from the differences in the electronegativities of chloride and t-

butoxide. In order to make this comparison, group electronegativities must be used to determine

the electronegativity of t-butoxide. Unfortunately, the group electronegativity of the t-butoxy

group is not well-established by the Pauling method. As a good approximation, one can use a

methoxide group as a model for the t-butoxide. Replacement of the hydrogen atoms in the

methoxide group by methyl groups should reduce the electronegativity of the group because the

methyls are better donors than hydrogen atoms. This is clearly illustrated in the group

electronegativities of OH (χ_P = 2.82 eV) vs. OCH_3 (χ_P = 2.52 eV). Hence, the electronegativity

of the $OC(CH_3)_3$ should be less than 2.52 eV. The net result is that the electronegativity of Cl

(χ_P = 3.16 eV) is greater than the electronegativity of the alkoxide ligand. In comparison to the

oxygen p orbitals in the alkoxides, the corresponding orbitals of the chlorine atoms are expected

to have a slightly worse energy match with the metal d orbitals. Nevertheless, the chlorine lone

pairs should still interact significantly with the M≡N valence orbitals.

In order to address the possible interactions of the chlorine orbitals with the M≡N

valence orbitals, it is useful to determine the symmetry-allowed combinations of the Cl p

orbitals. For simplicity, the chlorine p orbitals directed towards the metal center will be treated

separately. The symmetry-allowed combinations of the three chlorine orbitals that are pointed

4.1
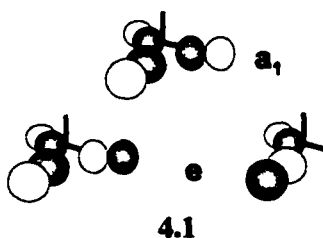
directly at the metal center are shown in **4.1**. These a_1 and e combinations are primarily used to

form the M-Cl σ bonds and probably will not interact with the M-N σ and π orbitals to any

great extent. In essence, the $a_1(\sigma)$ combination has the appropriate symmetry and nodal

properties to interact with the metal (s) orbital, but it also has the appropriate nodal character to interact with the torus of the Mo d_z2 orbital. The $e(\sigma)$ combination orbitals interact strongly with the $Mo(p_x, p_y)$ orbitals, but they will also have some interaction with the $Mo(d_{xz}$ and d_{yz} orbitals).

For simplicity, the chlorine p combinations that are π with respect to the metal are separated into two groups: those perpendicular to the M-N framework, and those parallel to the M-N framework. The parallel combinations, a_1 and $e(\shortparallel)$, shown in **4.2**, can interact directly with the M-N σ and π orbitals. The a_1 combination has reasonable overlap with the M-N σ orbital.

e(‖) a₁

4.2

e(⊥) a₂

4.3
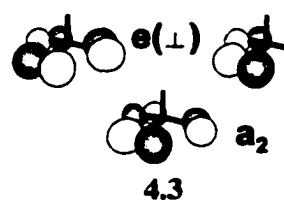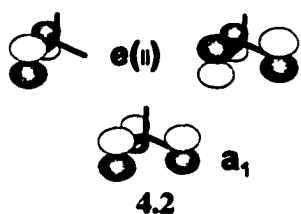
Similarly, the $e(\shortparallel)$ combination has reasonable overlap with the M-N π orbitals. The perpendicular ligand combinations a_2 and $e(\perp)$ shown in **4.3** will interact much less significantly with the M-N orbitals. In fact, by symmetry the a_2 combination does not interact with the M-N orbitals at all. The $e(\perp)$ combination lacks the correct nodal properties to have good overlap with the M-N π orbital. The relative ordering of the six chlorine $p\pi$ combinations ($a_1 < e(\perp) < e(\shortparallel) < a_2$) follows from the nodal and overlap properties of the orbitals. The a_1 is the most stable combination because it is a completely bonding orbital with zero nodes, and the a_2, a completely antibonding orbital, is obviously the most destabilized of the combinations. Since both sets of e orbitals are one node systems, one must consider the overlap effects to obtain the relative orderings. The $e(\shortparallel)$ is a net antibonding orbital, while the $e(\perp)$ is a net bonding orbital. Therefore, the $e(\perp)$ will be stabilized relative to $e(\shortparallel)$. In all likelihood, the $e(\perp)$ orbital set should

be energetically close to the $a_1(II)$ because the overlap of the Cl p-orbitals in the $e(\perp)$ orbitals is greater than the overlap of the p orbitals that make up the $a_1(II)$ orbital.

$Cl_3Mo\equiv N$. A simple molecular orbital diagram illustrating the interactions of the Cl_3^{3-} combinations with the NM^{3+} orbitals is presented in Figure 4.4. This analysis proves quite useful in quantifying the interactions that occur between the $M\equiv N^{3+}$ fragment orbitals and the Cl_3^{3-} orbital combinations. Not surprisingly, the ligand-based orbitals of the appropriate symmetry form bonding and antibonding combinations with the M-N σ and π orbitals. In addition, Figure 4.4 defines the orbital labels that will be used throughout the rest of the discussion. Since there are numerous filled orbitals of e and a_1 symmetry, the orbitals cannot be differentiated by their symmetry alone. To distinguish between the orbitals of the same symmetry, they will be designated by a number in conjunction with the symmetry label. That is, the four filled orbitals of e symmetry are designated 1e, 2e, 3e, 4e. The 1e orbital corresponds to the σ-bonding combination of the $e(\sigma)$ with the 1δ. 2e corresponds to the bonding combination of the 1π with the Cl_3 $e(II)$ orbital. 3e designates the $e(\perp)$ ligand combination, and 4e corresponds to the antibonding combination of the 1π with the Cl_3 $e(II)$. The lowest unoccupied orbital of e symmetry is 5e, and it corresponds to the unfilled metal-based 1δ orbital set. Similarly, the four filled orbitals of a_1 symmetry are designated: $1a_1$, $2a_1$, $3a_1$, and $4a_1$. The $1a_1$ orbital corresponds to the 1σ orbital of $Mo\equiv N$ (the N2s orbital). The $2a_1$ is the bonding combination of the Cl_3 $a_1(\sigma)$ with the $Mo\equiv N$ 2σ. The $3a_1$ is the bonding combination of the $Mo\equiv N$ 2σ and the Cl_3 $a_1(II)$. Finally, the $4a_1$ represents the antibonding combination of the $Mo\equiv N$ 2σ with the Cl_3 $a_1(II)$. Hence, the simple definitions of localized M-N σ and π orbitals are no longer valid because of significant orbital mixing with the π donor ligand orbitals. The mixing that occurs in this system will depend on the degree of overlap that exists between the orbitals of the $M\equiv N$ framework and

the Cl_3 orbitals of appropriate symmetry. Therefore, the orbital interactions depicted in Figure 4.4 are only qualitative and must be confirmed experimentally.

Results

He I Photoelectron Spectroscopic Studies. Just as in the studies of triple bonds to nitrogen in organic nitriles, photoelectron spectroscopy helps to quantify the nature of the interactions between the metal and the ligands because it directly probes the orbital energy levels. Previous photoelectron studies of $(^tBuO)_3Mo\equiv N$ proved to be quite challenging to interpret due to extensive overlap of ionization bands.[92] In order to obtain a more quantitative measure of the bonding in the transition metal nitrido molecules, the alkoxide ligands were replaced with chlorides. Based on the information gleaned from the studies of the alkoxide analogs, one would expect the ionizations from the orbitals containing the most $M\equiv N$ σ and π character to occur as the first ionizations of the molecule. In addition, since the simple orbital model developed in the previous section worked well for understanding the electronic structure of the $(RO)_3M\equiv N$ molecules, it seems clear that the model will be a good starting point for probing the electronic structure of the $Cl_3Mo\equiv N$. In fact, since this system is much more simple in terms of the molecular interactions, it could be argued that this system should serve as a model for understanding the relative positions of the $Mo\equiv N$ σ and π ionizations and the dependence of their order on the π donor ability of the ligand set.

The He I spectrum of $Cl_3Mo\equiv N$, collected in the 11.0 to 15.0 eV energy region, is shown in Figure 4.5 as a stack plot of the He I and He II spectra. Due to the simplified nature of the system, the spectrum can be interpreted in terms of the best fit of asymmetric ionization bands. The fit details are presented in Table 4.5. The minimum number of peaks necessary to fit the spectrum is eight. Incidently, the number of ionizations present in the valence region of this

system as set forth previously is eight. Therefore, each peak of Figure 4.5 represents a separate

ionization event. Based on the simple molecular orbital model developed earlier, the third

ionization band should correspond to ionization of the a_2 combination of in-plane chlorine lone

pairs. Again, this particular orbital is completely non-bonding with respect to the $M \equiv N$

fragment. Hence, the ionization band should be fairly symmetric. Looking at the fit parameters

in Table 4.5, the asymmetric Gaussian used to fit this peak is indeed fairly symmetric with the

high binding energy half-width being only 0.02 eV larger than the low binding half-width. Using

this ionization as the standard to which the other ionization peaks are compared, the He I relative

areas are presented in Table 4.5.

Experimental cross-sections for ionizations from molecules roughly follow the trends

predicted by the Gelius model, where molecular cross sections are treated as the sum of the

atomic cross sections of the atoms that contribute to the molecular orbital character.[77] As a

crude approximation, the relative areas of the ionization bands are proportional to the degeneracy

of the orbital from which the electron is ionized. That is, ionizations from orbitals of e symmetry

should be twice as intense as those from orbitals of a_1 or a_2 symmetry. This leads to the

assignment of the first ionization band as being due to ionization of the $M \equiv N$ π (4e) with the

second ionization originating from the $M \equiv N$ σ ($4a_1$). The fourth ionization would then

correspond to the ionization of the 3e orbital (schematically identified as the e($\perp$) orbital set).

The fifth ionization corresponds to the ionization of the $3a_1$ orbital.

The use of the relative areas is a crude method of assigning ionization bands because the

relative area model only holds true for ionizations from orbitals containing the same orbital

makeups. The crude nature of the model becomes most noticeable in the analysis of the last

three ionizations. Looking at the relative areas, one of the ionizations has half the intensity of the

other two even though the relative areas with respect to the a_2 ionization, 1.28:0.60:1.33 for

ionization of the 2e, $1a_1$, and 1e orbitals, respectively, are all much less than the expected ratios

of 2:1:2. Again, this is simply due to the fact that molecular cross-sections depend on the atomic

orbital characters that make up the orbital and will not correlate directly with the degeneracy of

the orbitals.

He II photoelectron spectra. To confirm the qualitative assignments based on the

simple orbital model, the spectra were recollected using a He II source. As previously stated, the

Gelius model of the photoionization process predicts that molecular cross sections are the sum of

the atomic cross-sections. Yeh and Landau have performed calculations to predict the cross-

sectional behavior of the atomic elements.[77] The calculated valence atomic He II/He I ionization

cross-section ratios for the atoms in these molecules are N2p (0.4); Mo4d (0.323); and Cl3p

(0.047).[77] Although ionizations from Mo-based orbitals are predicted to drop in intensity when

He II is used as the photon source, experimentally they are known to grow under He II

radiation.[78,93-96] The calculated cross-sections do not account for the Super-Koster Kronig

transitions that occur in second and third row transition metals; these processes increase the

intensity of ionizations from orbitals containing metal character.[78] Thus in comparing He II

spectra with He I spectra, ionizations from chlorine-based orbitals should shrink in comparison to

those from the M-N σ and π combinations. Looking again at Figure 4.5, a comparison of the

spectral intensities obtained with He I and He II photon sources reveals a substantial dependence

of the ionization intensities on the photon source. To confirm the spectral changes seen in the

11.0 to 15.0 eV range, the He II spectra were also collected in the 11.0 to 14.0 eV energy range

(Figure 4.6) as well as the 11.0 to 12.5 eV energy range (Figure 4.7). Because the a_2 ionization is

a chlorine-based orbital with no symmetry-allowed interaction with the metal-based orbitals, this

orbital is well-suited to serve as the reference by which the change in cross-section as the photon

source is changed from He I to He II is measured. The relative cross-section changes seen in the

spectra are tabulated in Table 4.5. Any growth in the relative areas with respect to the a_2 ionization implies that the orbital contains metal and nitrogen atomic character. Given that the cross section for this ionization band drops dramatically when the photon source is changed from He I to He II, it is no surprise that the relative growths in the ionization bands are substantial. Although the ionization from the 3e orbital shrinks drastically under He II radiation as expected for an ionization from a chlorine-based orbital,[97,98] the intensity drop is not as dramatic as that seen for ionization of the a_2 orbital because the 3e orbital is not a pure Cl-based orbital. The first ionization band feature contains substantial metal character as expected for ionization from the $M \equiv N$ π and σ orbitals, respectively. Based on the ionization band profile, the $M \equiv N$ π is the highest occupied molecular orbital of $Cl_3Mo \equiv N$. Although the $Mo \equiv N$ σ ionization occurs under the same ionization band, it clearly appears as a shoulder on the high binding energy side of the peak. In the He II spectrum, the $4a_1$ ionization grows substantially with respect to the 4e ionization. Hence, the $4a_1$ orbital must contain more metal and nitrogen character than the 4e orbital. In any case, both of the orbitals contain substantially more metal character than either the a_2 or 3e, which are essentially chlorine-based ionizations. The next ionization, $3a_1$, contains substantial metal and nitrogen character, because it does not shrink substantially upon changing the photon source from He I to He II. This ionization band is then followed closely by a complicated band containing three different ionizations, the first of which corresponds to the ionization of the 2e orbital. Again, in comparison to the a_2 ionization, this ionization feature grows substantially under He II radiation. The 2e ionization is then followed by ionization of the $2a_1$ and 1e combinations of the Mo-Cl σ bonds. Interestingly, the last three ionizations grow almost as much as the ionizations from the highest occupied combinations of the $Mo \equiv N$ σ $(4a_1)$ and π (4e), indicating these orbitals contain substantial amounts of metal character. In any case,

the simple molecular orbital model successfully accounts for the spectral features seen in the

photoelectron spectrum of $Cl_3Mo\equiv N$.

Computational Studies of $Cl_3Mo\equiv N$. Although the molecular orbital model provides a

nice starting point for understanding the electronic structure of $Cl_3Mo\equiv N$, the simple model must

be supported by more sophisticated computational studies. In the solid state, $Cl_3Mo\equiv N$ exists as

a tetramer, $[Cl_3Mo\equiv N]_4$ as shown in **(4.4)**. The four nitrogen atoms and the four molybdenum

4.4
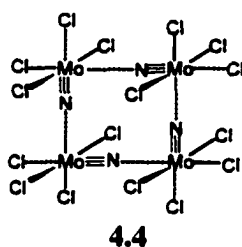
atoms define a planar ring. Two distinct Mo-N distances exist in the solid state: 1.64 Å and 2.14

Å, resulting from the alternating multiple and single bonds in the ring system.[99] Each

molybdenum center in the discrete tetramer is coordinated by five atoms, producing a distorted

square pyramidal geometry. The apex of the distorted square pyramid is formed by the multiply

bonded nitrogen atom with three chlorides and a nitrogen in the basal plane. An additional

chlorine atom from an adjacent tetramer is weakly bonded (Mo-Cl = 2.937 Å) in the open

coordination site that is trans to the Mo-N multiple bond.

However, in the gas phase the molecules sublime as single molecules (as determined by

mass spectrometry). Hence, the bond distances and angles obtained in the solid state will not

necessarily be an accurate model of the distances and angles of the molecule as it exists in the

gas phase. From the previous studies on the $(^tBuO)_3M\equiv N$ analogs, it was established that the

ADF2000.01 program is an effective tool for probing both molecular and electronic structures of

molecules containing formal triple bonds between a transition metal atom and a nitrogen atom.

In order to test the ability of density functional theory to describe the bonding in the $Cl_3Mo \equiv N$

systems, the ADF2000.01 package was used to perform geometry optimizations on $Cl_3Mo \equiv N$.[60]

The optimized parameters under C_{3v} symmetry are given in Table 4.6. For comparison,

the values calculated by both ADF2000 as well as the Gaussian98 programs are included. By all

accounts, the calculated structures agree well with the bond distances from the crystal structure

determination. In the crystal structure two distinct values have been obtained for the $Mo \equiv N$

distance, 1.64 Å and 1.67 Å, and the calculated $Mo \equiv N$ distances all lie within this range.[5,44,45]

Focusing on the Mo-Cl distances, the calculated distances lie within ±0.02 Å of the experimental

distance, well within the acceptable limits for computational modeling.

Once the intricacies of the molecular structure have been highlighted, one can proceed to

analyzing the ability of density functional theory to model the electronic structure of $Cl_3Mo \equiv N$.

The calculated ionization energies are presented in Table 4.7. Both the shifted Kohn-Sham

orbital energies and the ΔE_{SCF} energies correlate well with the experimental ionization energies.

In order to obtain a better understanding of the mixing that occurs in the molecular orbitals of the

$Cl_3Mo \equiv N$, plots of the valence orbitals are presented in Figures 4.8 and 4.9. The orbital plots

show significant mixing between the Cl_3 combination orbitals of the appropriate symmetry and

the orbitals of the $Mo \equiv N$ fragment (2σ and 1π). The mixing that is seen in the orbital plots is

the same as that predicted from considerations of the symmetry and nodal properties of the

orbitals. Hence, the orbital plots validate the bonding model developed in the preliminary

discussion section.

To provide further evidence of the delocalized bonding in these systems, Fenske-Hall

calculations were run using the optimized geometries from the ADF calculations. The results are

presented in Table 4.8. Direct comparisons between the density functional calculations and the

Fenske-Hall calculations will be given later, but both computational methods predict the highest

occupied $M \equiv N$ π orbital as the highest occupied orbital with the $M \equiv N$ σ being the second

highest occupied molecular orbital.

Discussion and Analysis

Although earlier computational studies on the molecule $Cl_3Mo \equiv N$ did not address the

importance of the Cl_3 orbital combinations in determining the relative ordering of the σ and π

orbitals,[72,86,100] the computational results here reveal a strong influence of the Cl_3 orbital

combinations on the $Mo \equiv N$ σ and π orbitals of $Cl_3Mo \equiv N$. This mixing is not unexpected

considering the simple symmetry analysis points to the possibility of extensive mixing between

the classic $Mo \equiv N$ σ and π orbitals and the Cl_3 symmetry combinations. Previous studies of the

electronic structure of $R_3M \equiv N$ analogs, produced the $Mo \equiv N$ 2σ as the HOMO of the molecule

with the $Mo \equiv N$ 1π being the SHOMO. Hoffmann and coworkers attributed the destabilization

of the 2σ above the 1π to the mixing in of $N(2s)$ character into the 2σ.[72] This argument is valid

for the isolated $Mo \equiv N$ molecule, but it does not hold true for the full molecule, $Cl_3Mo \equiv N$.

Interestingly, Schoeller and coworkers also published a paper reporting the same molecular

orbital ordering as Hoffmann in a broader study looking at the formation of ring structures from

multiple $Cl_3Mo \equiv N$ molecules.[86] There is no doubt that the $N(2s)$ contribution to the σ

framework is indeed an important consideration, but it is certainly not the only consideration

because the highest occupied orbital of this molecule, as determined by photoelectron

spectroscopy as well as our computational studies, is the highest occupied $Mo \equiv N$ π combination

$(4e)$, not the $Mo \equiv N$ σ $(4a_1)$.

Computational Studies. Taking a closer look at the results from the computational

studies allows one to determine which orbital interactions are important in determining the

overall electronic structure of the molecule. The basis for understanding the electronic structure of this molecule was developed from simple symmetry and overlap considerations. Clearly, it is necessary to validate the approach by analyzing the results from high level density functional and *ab initio* calculations. To this end, the results from the computational studies are presented so as to allow the most direct comparison between the simple model and the advanced computational studies.

One issue concerning the Cl_3 symmetry combinations revolves around the amount of mixing that occurs between the combinations that are of the same symmetry. Logically, orbitals that are of the same symmetry will mix if the energy matching is favorable. To address this issue, the computational studies were performed in terms of a Cl_3 fragment interacting with the $Mo \equiv N$ fragment. In particular, the Fenske-Hall method is useful for creating a molecular orbital diagram to emphasize the energy matching as well as the orbital interactions that are important in the bonding of $Cl_3Mo \equiv N$. Figure 4.10 contains the orbital interaction diagram obtained from the Fenske-Hall method. The calculated molecular orbital diagram is remarkably similar to the diagram developed using only simple overlap and symmetry considerations and validates the method used to understand the bonding in $Cl_3Mo \equiv N$. In addition, the calculated molecular orbital diagram obtained by the Fenske-Hall method qualitatively agrees with the experimental results.

Both computational methods (Fenske-Hall and DFT) predict extensive mixing between the Cl_3 combinations and the $M \equiv N$ orbitals. The $M \equiv N$ σ and π orbitals are split by interactions with the Cl_3 $a_1(\textsf{n})$ and Cl_3 $e(\textsf{n})$ combination, respectively. That is, each of the $M \equiv N$ orbitals forms a bonding and antibonding combination with the Cl_3 combination of the appropriate symmetry. The splitting between the bonding and antibonding combinations of the aforementioned orbital combinations provides a measure of the strength of the interactions between the $Mo \equiv N$ and

$(RO)_3$ fragment orbitals. Table 4.9 contains the splitting values obtained experimentally and via computational modeling. In all cases, the splitting of the $Mo \equiv N$ π by the Cl_3 $e(\shortparallel)$ is almost twice the analogous splitting of the $Mo \equiv N$ σ. The implication is that the interaction between the $Mo \equiv N$ π and the Cl_3 $e(\shortparallel)$ is stronger than the interaction between the $Mo \equiv N$ σ and the Cl_3 $a_1(\shortparallel)$.

The orbitals from the computational runs show extensive mixing of the classical $Mo \equiv N$ σ and π with the Cl_3 $a_1(\shortparallel)$ and $e(\shortparallel)$ orbitals, respectively, in accordance with the expectations from the simple molecular orbital model. This mixing is readily evident in the orbital characters obtained from both the ADF and Fenske-Hall calculations listed in Tables 4.7 and 4.8, respectively. Interestingly, both computational procedures reveal similar mixing, further validating the simple model used to understand the bonding in this molecule. As expected, the a_2 orbital is completely nonbonding with respect to the metal and nitrogen. The $e(\perp)$ combination is also chlorine-based, but it is not completely nonbonding because some $e(\shortparallel)$ and $e(\sigma)$ character mix into the orbital. Although this orbital is still identifiable as $e(\perp)$, the $e(\shortparallel)$ and $e(\sigma)$ contributions allow the $Mo \equiv N$ 1π to mix into this orbital. Both the ΔE_{SCF} energies and the shifted Kohn-Sham orbital energies agree well with the experimental assignments. For both the Fenske-Hall and DFT studies, the HOMO of the molecule is the highest occupied combination of $Mo \equiv N$ π with the SHOMO being attributable to the highest occupied combination of $Mo \equiv N$ σ. In addition, these two orbitals are calculated to be close in energy, in agreement with the photoelectron spectroscopic studies. Clearly, both ADF and Fenske-Hall are effective tools for studying the molecular and electronic structures of $Cl_3Mo \equiv N$.

In the most simple terms, the degree of splitting between bonding and antibonding orbital combinations depends on two factors, the energy matching and the overlap between the two orbital combinations. Of course, the picture becomes cloudier when there are more than two fragment orbitals contributing to the overall character of the molecular orbital. Fenske-Hall

calculations on $Cl_3Mo\equiv N$ are amenable to the thorough energy decomposition analysis used previously to analyze the bonding in $Mo\equiv N$. The energy decomposition analysis of $Cl_3Mo\equiv N$ allows a direct probe of the source of the destabilization of the 4e orbital above the $4a_1$ orbital. The results of the energy decomposition analysis for the $4a_1$ and 4e orbitals, the highest occupied combinations of the $Mo\equiv N$ σ and π, respectively, are presented in Table 4.10.

Looking at the 4e orbital, the diagonal energy contributions sum to -15.80 eV. By comparison, the total energy of this orbital is only -12.70 eV. The off-diagonal energy terms must contribute significantly to the orbital energy in a destabilizing fashion. Looking at the off-diagonal energy terms, there is a +4.12 eV destabilizing contribution originating from to the strong antibonding interaction between the Cl_3 e(ɪɪ) and the $M\equiv N$ 1π. This destabilization is only partially offset by the bonding interaction between the Cl_3 e(ɪɪ) and the $M\equiv N$ π^*, which contributes -0.89 eV to the overall orbital energy. The net destabilization is still quite large, +3.23 eV. There is also a contribution from the Cl_3 e(σ) interaction with the $M\equiv N$ π orbitals, but this is only a minor contributor to the overall energy.

For the $4a_1$ orbital, the diagonal energy contribution, -13.10 eV, is similar to the total energy of the orbital, -12.89 eV. Again, the major off-diagonal contribution is a destabilization due to the antibonding interaction between the Cl_3 a_1(ɪɪ) and the $M\equiv N$ 2σ, contributing +0.44 eV to the overall orbital energy. This destabilization is partially offset by the bonding interaction between the Cl_3 a_1(ɪɪ) and the unfilled $M\equiv N$ 3σ which results in a stabilization of -0.23 eV so that the net destabilization is only +0.21 eV. The overall effect is that the $4a_1$ orbital is largely a nonbonding orbital. It is the strong antibonding interaction between the $M\equiv N$ π and Cl_3 e(ɪɪ) that serves to destabilize the 4e orbital above the $4a_1$ orbital.

N(2s) Contribution to $Cl_3Mo\equiv N$. One of the remaining questions pertaining to the electronic structure of this molecule involves the relative importance of the N(2s) in determining

the energy of the $4a_1$ orbital. From the energy decomposition analysis on the $Mo \equiv N$ fragment presented earlier, the N(2s) is known to be an important destabilizing factor in the $Mo \equiv N$ fragment. Given that the Fenske-Hall calculations were performed in terms of the $Mo \equiv N$ fragment interacting with a Cl_3 fragment, one can infer that the N(2s) is also an important factor in determining the position of the $4a_1$ orbital. However, the importance of the N(2s) in determining the total energy of the $4a_1$ orbital was not directly probed in the two fragment analysis scheme.

To explore the contribution of the N(2s) to the overall orbital energy of the $4a_1$ orbital, the energy decomposition analysis was performed once again on $Cl_3Mo \equiv N$ in terms of the Cl_3 fragment interacting with Mo and N atomic fragments. Tables 4.11 and 4.12 contain the results of the analysis for the 4e and $4a_1$ orbitals, respectively. Focusing first on the $4a_1$ orbital, the N(2s) contributes about 25% of the total diagonal energy. The dominant contributor to the diagonal energy term is the N(z) which provides -7.23 eV of the total -12.06 eV. Incidently, the Cl_3 a_1(II) diagonal energy contribution is really quite minor, -0.83 eV, in comparison to the contributions from the N(2s) and N(pz).

The 4e orbital, on the other hand, possesses a much more substantial diagonal energy contribution from the Cl_3 fragment than does the $4a_1$ orbital. In fact, over 50% of the total diagonal energy contribution comes from the Cl_3 e(II). In comparison, the Mo(xz,yz) and N(x,y) together account for only 41% of the total diagonal contribution to the orbital energy.

As stated previously, all overlap effects are by definition off-diagonal effects in Hartree-Fock theory. Hence, one cannot get an accurate view of the importance of the bonding and/or antibonding interactions in determining the total orbital energy without analyzing the off-diagonal energy contributions. Since the question of interest revolves around determining the importance of the N(2s) in determining the overall orbital energy of the $Mo \equiv N$ σ, the off-

diagonal contributions to this orbital will be addressed first. At first glance, one might guess that the off-diagonal energies are only a minor contributor to the total orbital energy because the diagonal energy contribution, -12.06 eV, accounts for the vast majority of the total orbital energy, -12.89 eV. However, this is quite misleading because it simply treats the net effect of all the off-diagonal energy contributions. Looking at the breakdown of the off-diagonal energy contributions, the bonding interaction between the N(z) and Mo($_z$2) provides a strong stabilizing contribution of -3.28 eV to the total orbital energy. In addition the bonding interactions between the N(z) and the Mo(s) as well as the Mo(z) provide a further stabilization of -1.63 eV. The combined stabilization energy provided by the interaction of the Mo atom with the N atom is -4.91 eV; clearly, much larger than the net off-diagonal energy contribution, -0.83 eV, to the 4a$_1$ orbital. This is an indication that there are strongly destabilizing off-diagonal contributions that serve to counteract the majority of the stabilization provided by the bonding interactions between the nitrogen p and the molybdenum atoms. The source of this destabilization lies in both the N(2s) contributions to the orbital as well as the Cl$_3$ a$_1$(ii) contributions to the orbital. The strong antibonding interactions between the N(2s) and the Mo atom provides a destabilization energy of +3.93 eV. In addition, the Cl$_3$ a$_1$(ii) contribution to the off-diagonal energy is +0.21 eV. The overall effect is that most of the stabilization provided by the bonding interactions between the nitrogen and the molybdenum is countered by the destabilizing influences of the N(2s) and Cl$_3$ a$_1$(ii) orbitals.

The off-diagonal contributions to the 4e orbital are much less complicated than the corresponding contributions in the 4a$_1$ orbital. The diagonal energy contributions account for -12.25 eV of the total bond energy, -12.70 eV. However, as was the case for the 4a$_1$, it is necessary to look at the individual contributions to the off-diagonal energy of the 4e to get an accurate picture of the orbital energy. Again, the off-diagonal contributions can be divided into

two categories: those that destabilize the orbital and those that stabilize the orbital. The major

off-diagonal stabilizing contribution comes from the bonding interaction between the N(x,y) and

Mo(xz,yz), -3.28 eV. An additional -0.35 eV of stabilization is provided by the bonding

interaction of the N(x,y) with the Mo(x,y). Overall, the stabilization provided by the interaction

of the N(x,y) with the Mo orbitals is -3.63 eV, significantly less than the corresponding

stabilization provided by the interaction of the N and Mo atoms in the $4a_1$ orbital, -4.91 eV.

Unlike the 4a1 orbital, the destabilization contribution to the 4e orbital originates solely in the

strong antibonding interaction of the Cl_3 e(ιι) with the Mo(xz,yz) and N(x,y), providing +3.23 eV

to effectively counteract the majority of the off-diagonal stabilization provided by the bonding

interaction between the Mo and N. In any case, one cannot overemphasize the importance of the

Cl_3 orbital combinations in determining the energies of the molecular orbitals.

Comparisons to (^{t}BuO)$_3$Mo≡N. Of particular interest is the comparison of the

electronic structure of the Cl_3Mo≡N to that of the previously studied (^{t}BuO)$_3$Mo≡N. Due to the

complex nature of the mixing of the alkoxide framework with the orbitals from the formal metal

nitrogen triple bond, exact positions of the Mo≡N σ and π ionization could not be determined.

It is interesting to reevaluate the spectrum of (^{t}BuO)$_3$Mo≡N in terms of the information obtained

from the detailed analysis of the Cl_3Mo≡N spectra. Comparing the spectra in Figure 4.11, it is

clear that much more information can be gleaned from the analysis of the Cl_3Mo≡N. This is not

an unexpected result because a halogen donor atom is clearly much more simple than an alkoxide

donor. In many ways, the photoelectron studies of Cl_3Mo≡N provide further support for the

spectral assignments made for the (^{t}BuO)$_3$Mo≡N analogs. The photoelectron spectrum of

Cl_3Mo≡N serves as an example of another system, besides (^{t}BuO)$_3$Mo≡N, where the highest

occupied combinations of σ and π are the highest occupied orbitals and occur under the same

ionization band. In addition, the Cl_3Mo≡N spectra provide clear evidence for the importance of

the mixing between the orbitals constituting the triple bond between the molybdenum and nitrogen atoms and the π-donor combinations of the ancillary ligands. As expected from the higher electronegativity of the chlorine atoms in comparison to the oxygens of the alkoxide ligands, all of the ionizations of the $Cl_3Mo\equiv N$ are significantly stabilized (~ 2.0 eV) relative to the ionization positions in the $(RO)_3Mo\equiv N$ analogs. For the $(^tBuO)_3Mo\equiv N$ spectrum, the first ionization band was determined to contain ionizations from four different orbitals (two e orbitals, one a_2 orbital and one a_1 orbital). The width of this first band was approximately 1.5 eV. The first ionizations of the $Cl_3Mo\equiv N$ are also of e, a_1, and a_2 symmetry, and the ionizations occur within an energy range of approximately 1.75 eV. The degree of splitting amongst the orbitals will be dependent on the relative donor ability of the ancillary ligands as well as the relative energies. For the $Cl_3Mo\equiv N$ molecule, the relative energies and the overlap between the orbitals of the $M\equiv N$ and Cl_3 fragments are such that the orbitals occur as separate ionization bands in the photoelectron spectrum. Even so, the energy range is still quite similar to the corresponding range in the $(^tBuO)_3Mo\equiv N$, only increasing by approximately 0.25 eV for the $Cl_3Mo\equiv N$ molecule. The $(^tBuO)_3Mo\equiv N$ spectra are complicated by vibrational structure that originates from the ancillary alkoxide ligands, indicating extensive mixing between the alkoxide orbitals and the $M\equiv N$ orbitals. In any case, the $Cl_3Mo\equiv N$ studies validate the method used to elucidate the electronic structure of the $(^tBuO)_3M\equiv N$ analogs.

Another interesting comparison to make is the atomic charges in $Cl_3Mo\equiv N$ versus those in $(^tBuO)_3Mo\equiv N$. Although Mulliken atomic charges are ill-defined, trends in atomic charges can still be used to rationalize the behavior of molecules. In previous studies of the $(RO)_3Mo\equiv N$ analogs, the Mulliken charges were found not to be dependent on the identity of the particular R group. Table 4.13 contains the calculated Mulliken atomic charges for the $Cl_3Mo\equiv N$ in comparison to those for the previously reported $(^tBuO)_3Mo\equiv N$. The polarity of the $Mo\equiv N$ is

significantly less for $Cl_3Mo\equiv N$. Looking at the calculated charge from the density functional

calculations, it is clear that the Mo atom of $Cl_3Mo\equiv N$ is much less positively charged than the

Mo atom in $(^tBuO)_3Mo\equiv N$. Similarly, the atomic charge of the N atom in $Cl_3Mo\equiv N$ is less

negative than the corresponding charge for $(^tBuO)_3Mo\equiv N$. Even more interesting is the negative

charge placed on the Cl atoms versus the O atoms since the calculated atomic charge on the Cl

atoms is calculated to be much less than the charge on the O atoms of the alkoxide ligands.

Clearly, the calculated atomic charge on the Mo center does not come close to approaching the

+6 formal charge, and the charge on the nitrogen atom (-0.41) does not approach the formal

charge of -3. These charge distributions agree well with other studies of these compounds using

Bader's "atoms in Molecules" model as well as the Natural Bond Orbital analysis model.[86] In all

cases the atomic charges are much less than the formal charges. Nevertheless, it is clear that the

molybdenum has donated electron density to the nitrogen and the chlorine. Of course, it must be

recognized that although the Cl atom is quite electronegative it is still a strong π donor. The key

point from the charge analysis is that the Mo is electrophilic and the N is nucleophilic. Hence, it

is certainly no surprise that the molecule does not exist as a single molecule in the solid state. In

fact, as shown by Hoffmann and coworkers, the LUMO of the molecule is the unfilled

$Mo(d_{x2-y2},d_{xy})$ set. One can envisage the $4a_1$ orbital of one $Cl_3Mo\equiv N$ donating electron density to

the LUMO of another molecule. Even though the $4a_1$ is not the HOMO of the molecule, it is still

available as a donor orbital. In addition, the 4e orbital of one molecule could also donate

electrons to the LUMO.

Conclusions

Replacement of the alkoxide donors of $(RO)_3Mo\equiv N$ with chlorides has provided a more

complete picture of the bonding in transition metal nitrido molecules. In fact, the photoelectron

spectrum is simplified to the extent that all of the valence ionizations are readily assigned. The $Cl_3Mo\equiv N$ photoelectron and computational studies provide direct evidence of the importance of the ancillary donor combinations in understanding the electronic structure of the transition metal nitrido complexes containing π-donor ligands. In essence, the traditional $Mo\equiv N$ σ and π orbitals are no longer applicable because each is split by interaction with the Cl_3 $a_1(\text{ii})$ and $e(\text{ii})$ orbitals, respectively, to form bonding and antibonding combinations. The highest occupied orbitals then correspond to these antibonding combinations of the $M\equiv N$ σ and π orbitals.

The photoelectron spectra of $Cl_3Mo\equiv N$ can be readily interpreted in terms of the interaction of the Cl_3 π-donor combinations with the traditional $Mo\equiv N$ σ and π. From the He II/ He I comparison, it is quite simple to determine the origin of the ionization features. Since the photoelectron spectrum can be assigned using basic principles, this molecule is an excellent test of the ability of density functional theory as well as Fenske-Hall calculations to model the bonding in molecules containing triple bonds between a transition metal and a nitrogen atom. Both of the computational methods give results that correlate well with the results obtained experimentally. Photoelectron spectroscopic studies of $Cl_3Mo\equiv N$ clearly show the 4e orbital as the highest occupied molecular orbital with the $4a_1$ orbital appearing as a shoulder on the high binding energy end. Interestingly, this is in direct contrast to earlier computational studies that placed the $Mo\equiv N$ σ as the highest occupied molecular orbital of the molecule. These studies all de-emphasized the relative importance of the Cl_3 combination orbitals in determining the electronic structure of $Cl_3Mo\equiv N$. Our studies indicate that understanding the contributions from the Cl_3 combination orbitals is vital to understanding the orbital splittings that are seen in the photoelectron spectra of $Cl_3Mo\equiv N$.

Table 4.1. ADF2000 Orbital Energies and Compositions of Mo≡N.

Orbital	Energy (eV)	Orbital Makeup	S_{MN}
1δ	-6.21	100% Mo(xy, x^2-y^2)	NA
2σ	-8.60	50% N($2p_z$) 8% N(2s) 32% Mo($4z^2$) 4% Mo($5z^2$)	0.116[a] 0.328[b]
1π	-8.89	53% N($2p_{x,y}$) 46% Mo(4xz,yz)	0.284
1σ	-18.39	86% N(2s) 11% Mo($4z^2$) 1% Mo(5s) 2% Mo($5p_z$)	0.328[b] 0.363 0.171

[a]Overlap of N($2p_z$) with the Mo($4d_{z^2}$)
[b]Overlap of N(2s) with the Mo($4d_{z^2}$)

Table 4.2. Fenske-Hall Orbital Energies and Compositions of Mo≡N with and without including N(2s) in the valence.

| Orbital | Energy eV | | Orbital Makeup | |
	N2s (valence)	N2s (core)	N2s (valence)	N2s (core)
1δ	-5.52	-5.50	100% Mo(xy,x^2-y^2)	100% Mo(xy, x^2-y^2)
2σ	-9.96	-12.97	82 % N(2pz) 10 % Mo(4_z2) 7 % N(2s)	61% N(z) 30 % Mo($_z2$) 5 % Mo(s) 4 % Mo(z)
1π	-10.61	-11.03	59 % N($p_{x,y}$) 41 % Mo(4xz,yz)	62 % N(x,y) 38 % Mo(xz,yz)
1σ	-23.24	-20.85	79 % N(2s) 15 % Mo($4z^2$) 2 % Mo(5s) 2 % Mo($5p_z$)	100 % N(2s)

Table 4.3. Fenske-Hall Orbital Energy Decomposition Analysis of Mo≡N.

Orbital	Diagonal Energy Contributions (eV)		Off-diagonal Energy Contributions (eV)		Orbital Energy (eV)
	Components	Sum	Components	Sum	
2σ	N(2s) -2.567		N(2s); Mo(d_{z^2}) 2.908		
	N(pz) -5.662		N(2s); Mo(5s) 0.272	3.732	
	Mo(d_{z^2}) -0.560	-8.769	N(2s); Mo($5p_z$) 0.552		-9.96
	Mo(5s) -0.002		N(p_z); Mo(d_{z^2}) -3.826		
			N(p_z); Mo(5s) -0.391	-4.923	
	Mo($5p_z$) $+0.022$		N(p_z); Mo($5p_z$) -0.706		
1π	N(p_x,p_y) -3.671	-5.345	N(p_x,p_y); Mo(d_{xz}) -5.246	-5.264	-10.61
	Mo(d_{xz},d_{yz}) -1.674		N(p_x,p_y); Mo(p_x,p_y) -0.018		
1σ	N(2s) -14.516		N(2s); Mo(d_{z^2}) -6.055		
	N(pz) -0.035		N(2s); Mo(5s) -1.048	-7.913	
	Mo(d_{z^2}) -0.430	-14.979	N(2s); Mo($5p_z$) -0.810		-23.24
	Mo(5s) -0.006		N(p_z); Mo(d_{z^2}) -0.265		
			N(p_z); Mo(5s) -0.050	-0.349	
	Mo($5p_z$) $+0.008$		N(p_z); Mo($5p_z$) -0.034		

Table 4.4. Fenske-Hall Orbital Energy Decomposition Analysis of Mo≡N with the N(2s) treated as a core orbital.

Orbital	Diagonal Energy Terms (eV)		Off-diagonal Energy Contributions (eV)		Orbital Energy (eV)
	Components	Sum	Components	Sum	
2σ	N(p$_z$) -4.145		N(p$_z$) + Mo(d$_z$2) -5.045		
	Mo(d$_z$2) -1.401		N(p$_z$) + Mo(5s) -1.150		
	Mo(5s) -0.027	-5.466	N(p$_z$) + Mo(5p$_z$)	-7.510	-12.98
	Mo(5p$_z$) 0.108			-1.315	
1π	N(px,py) -4.199	-5.723	N(p$_x$,p$_y$) + Mo(d$_{xz}$) -5.276	-5.307	-11.03
	Mo(d$_{xz}$,d$_{yz}$) -1.524		N(p$_x$,p$_y$) + Mo(p$_x$,p$_y$) -0.031		

Table 4.5. Peak positions, parameters, and relative areas (Peak X/Peak a_2) of $Cl_3Mo \equiv N$.

Orbital		Position	Width (eV)		He I Relative Area	He II Relative Area	He II/He I
Label	Makeup		High	Low	Peak X/Peak a_2		
4e	$Mo \equiv N\ \pi - Cl_3\ e(\text{ii})$	11.40	0.36	0.29	1.70	8.59	5.05
$4a_1$	$Mo \equiv N\ \sigma - Cl_3\ a_1(\text{ii})$	11.57	0.28	0.21	0.84	6.22	7.40
a_2	$Cl_3\ a_2(\perp)$	11.95	0.17	0.15	1.00	1.00	1.00
3e	$Cl_3\ e(\perp);\ Cl_3\ e(\text{ii})$	12.66	0.23	0.23	2.38	3.38	1.42
$3a_1$	$Mo \equiv N\ \sigma + Cl_3\ a_1(\text{ii} + \sigma)$	12.99	0.28	0.16	0.83	2.64	3.18
2e	$Mo \equiv N\ \pi + Cl_3\ e(\text{ii} + \sigma)$	13.68	0.37	0.29	1.28	7.66	5.95
$2a_1$	$Cl_3\ a_1(\sigma);\ Cl_3\ a_1(\text{ii});\ Mo \equiv N\ \sigma$	14.04	0.34	0.33	0.60	4.09	6.82
1e	$Cl_3\ e(\sigma);\ Mo \equiv N\ \delta;\ Mo \equiv N\ \pi$	14.25	0.40	0.40	1.33	6.07	4.56

Table 4.6. Optimized Geometrical Parameters of $Cl_3Mo \equiv N$.

	Experimental		ADF2000 PW91 ZORA (IV)	G98 B3LYP CEP-121G
Mo≡N (Å)	1.64	1.67	1.66	1.67
Mo-Cl (Å)	2.29		2.27	2.31
∠ N-Mo-Cl	N/A[a]		105.74	105.27

[a] $Cl_3Mo \equiv N$ exists as a tetramer in the solid state. Therefore, experimental values are not available for the ∠ N-Mo-Cl

Table 4.7. ADF ΔE_{SCF} Energies, K-S Orbital Energies, and Orbital Compositions for the valence orbitals of $Cl_3Mo \equiv N$.

Orbital	Ionization Energy (eV)	ΔE_{SCF} (ev)	Kohn-Sham Energies (eV)[a]	Orbital Makeup	
				Cl_3 + Mo + N	Cl_3 + Mo≡N
4e	11.40	11.22	11.40	30 % N(x,y) 47% Cl_3 e(ıı) 11 % Cl_3 e(σ) 9% Mo(xz,yz)	34% Mo≡N π 47% Cl_3 e(ıı) 11 % Cl_3 e(σ) 6% Mo≡N π*
$4a_1$	11.57	11.56	11.65	41% N(z) 40 % Cl_3 a_1(ıı) 5% N(s) 12% Mo($_z$2)	53% Mo≡N 2σ 40 % Cl_3 a_1(ıı) 5 % Mo≡N 3σ
a_2	11.95	11.93	12.12	100% Cl_3 a_2(⊥)	100% Cl_3 a_2(⊥)
3e	12.66	12.36	12.67	64% Cl_3 e(⊥) 19% Cl_3 e(ıı) 8% N(x,y) 5% Mo(x,y)	64% Cl_3 e(⊥) 19% Cl_3 e(ıı) 8% Mo≡N π 4% Mo≡N π*
$3a_1$	12.99	12.69	12.92	38% Cl_3 a_1(ıı) 25% Cl_3 a_1(σ) 14% N(z) 7% Mo($_z$2) 3 % N(s)	38% Cl_3 a_1(ıı) 25 % Cl_3 a_1(σ) 30% Mo≡N 2σ
2e	13.68	13.45	13.58	29% Mo(xz,yz) 25% Cl_3 e(ıı) 20% Cl_3 e(⊥) 15% N(x,y) 11% Mo($_{x^2-y^2,xy}$)	40% Mo≡N π 25% Cl_3 e(ıı) 20% Cl_3 e(⊥) 10% Mo≡N δ
$2a_1$	14.04	13.91	14.24	59% Cl_3 a_1(σ) 13% Cl_3 a_1(ıı) 6% Mo(s) 14% Mo(z2)	59% Cl_3 a_1(σ) 13% Cl_3 a_1(ıı) 13% Mo≡N 2σ 9% Mo≡N 3σ
1e	14.25	13.93	14.17	57% Cl_3 e(σ) 20 % Mo($_{x^2-y^2,xy}$) 11 % Mo(xz,yz) 3 % N(x,y)	57% Cl_3 e(σ) 20% Mo≡N δ 13 % Mo≡N π

[a]Kohn-Sham orbital energies are shifted according to equation (4.1).

Table 4.8. Fenske-Hall Orbital Energies and Orbital compositions of the valence orbitals of $Cl_3Mo\equiv N$.

Orbital	- Orbital Energy (eV)	Orbital Makeup	
		Cl_3 + Mo + N	Cl_3 + Mo$\equiv$N
4e	11.40	41% N(x,y) 42% Cl_3 e(ıı) 11% Mo(xz,yz)	48% Mo$\equiv$N π 42% Cl_3 e(ıı) 8 % Mo$\equiv$N π*
4a$_1$	11.52	79% N(z) 7% N(s) 5% Mo($_{z^2}$) 6 % Cl_3 a$_1$(ıı)	91 % Mo$\equiv$N 2σ 6 % Cl_3 a$_1$(ıı)
a$_2$	12.36	100% Cl_3 a$_2$($\perp$)	100% Cl_3 a$_2$($\perp$)
3e	12.80	54% Cl_3 e($\perp$) 17% Cl_3 e(σ) 20% Cl_3 e(ıı) 4% N(y) 4% Mo(y)	54% Cl_3 e($\perp$) 17% Cl_3 e(σ) 20% Cl_3 e(ıı) 4% Mo$\equiv$N π
3a$_1$	12.94	85% Cl_3 a$_1$(ıı) 5 % Cl_3 a$_1$(σ) 3% Mo($_{z^2}$) 2% N(z)	85% Cl_3 a$_1$(ıı) 5 % Cl_3 a$_1$(σ) 5% Mo$\equiv$N 2σ
2e	14.09	32% e(ıı) 27% Mo(xz,yz) 21% e($\perp$) 11% N(x,y) 7 %Mo($_{x^2-y^2,xy}$)	32% e(ıı) 38% Mo$\equiv$N π 21% e($\perp$) 7 % Mo($_{x^2-y^2,xy}$)
2a$_1$	14.03	76% a$_1$(σ) 10% Mo(s) 7% Mo($_{z^2}$) 3% a$_1$(ıı)	76% a$_1$(σ) 13% Mo$\equiv$N 3σ 3% Mo$\equiv$N 2σ 3% a$_1$(ıı)
1e	14.25	59% e(σ) 9% e($\perp$) 19% Mo($_{x^2-y^2,xy}$) 7% Mo(xz,yz)	59% e(σ) 9% e($\perp$) 7% Mo$\equiv$N π 19% Mo(xz,yz)

Table 4.9. Splitting of the $M \equiv N$ σ and π orbitals by the Cl_3 symmetry combinations.

	Experimental (eV)	ADF2000		Fenske-Hall Koopmans
		ΔE_{SCF} (eV)	K-S Orbital Energy (eV)	
Δ (4a$_1$ - 3a$_1$)	1.42	1.13	1.27	1.42
Δ (4e - 2e)	2.27	2.23	2.18	2.68

Table 4.10. Fenske-Hall Orbital Energy Decomposition Analysis of $Cl_3Mo \equiv N$.

Orbital	Diagonal Energy Contributions (eV)		Off-diagonal Energy Contributions (eV)		Orbital Energy (eV)
	Major Components	Sum	Major Components	Sum	
4e	Cl_3 e(ıı) -6.91		Cl_3 e(ıı); $M \equiv N$ 1π +4.12		-12.70
	$M \equiv N$ 1π -8.32		Cl_3 e(ıı); $M \equiv N$ π^* -0.89	+3.23	
	$M \equiv N$ π^* -0.23				
		-15.80	Cl_3 e(σ); $M \equiv N$ 1π +0.42		
	Cl_3 e(σ) -0.29			-0.05	
			Cl_3 e(σ); $M \equiv N$ π^* -0.49		
			Cl_3 e(σ); other +0.02		
			Other contributions -0.08	-0.08	
4a₁	$M \equiv N$ 2σ -12.06		Cl_3 a₁(ıı); $M \equiv N$ 2σ +0.44	+0.21	-12.89
	Cl_3 a₁(ıı) -0.83	-13.10	Cl_3 a₁(ıı); $M \equiv N$ 3σ -0.23		
	$M \equiv N$ 3σ -0.11		Cl_3 a₁(σ); $M \equiv N$ 2σ +0.04		
			Cl_3 a₁(σ); $M \equiv N$ 3σ -0.12	-0.07	
	$M \equiv N$ 1σ -0.05		Cl_3 a₁(σ); other +0.01		
			Other contributions +0.07	+0.07	

Table 4.11. Fenske-Hall Orbital Energy Decomposition Analysis of the 4e orbital of $Cl_3Mo{\equiv}N$.

Orbital	Diagonal Energy Contributions (eV)		Off-diagonal Energy Contributions (eV)			Orbital Energy (eV)
	Major Components	Sum	Major Components		Sum	
4e	Cl_3 e(ıı) -6.91		Cl_3 e(ıı); Mo(xz,yz)	+2.20		
	N(px,py) -3.93		Cl_3 e(ıı); N(x,y)	+0.92	+3.23	
	Mo(xz,yz) -1.08		Cl_3 e(ıı); Mo(x,y)	+0.08		
			Cl_3 e(ıı); Mo($_x2-_y2$,xy)	+0.03		
	Cl_3 e(σ) -0.29	-12.25	N(x,y); Mo(xz,yz)	-3.28	-3.63	-12.70
			N(x,y); Mo(x,y)	-0.35		
	Cl_3 e(⊥) -0.04		Cl_3 e(σ); Mo(xz,yz)	+0.36		
			Cl_3 e(σ); N(x,y)	-0.21	-0.05	
			Cl_3 e(σ); Mo(x,y)	-0.20		

Table 4.12. Fenske-Hall Orbital Energy Decomposition Analysis of the $4a_1$ orbital of $Cl_3Mo \equiv N$.

Orbital	Diagonal Energy Contributions (eV)		Off-diagonal Energy Contributions (eV)			Orbital Energy (eV)
	Major Components	Sum	Major Components		Sum	
4a₁	N(z)	-7.43	$Cl_3 a_1(\text{ii})$; N(2s)	+0.18		-12.89
	N(2s)	-3.04	$Cl_3 a_1(\text{ii})$; N(z)	-0.31		
			$Cl_3 a_1(\text{ii})$; Mo($_z$2)	+0.44	+0.21	
	$Cl_3 a_1(\text{ii})$	-0.83				
			$Cl_3 a_1(\text{ii})$; Mo(z)	-0.11		
	Mo($_z$2)	-0.69	N(2s); Mo($_z$2)	+2.69		
			N(2s); Mo(s)	+0.63	+3.93	
	Mo(s)	-0.03				
		-12.06	N(2s); Mo(z)	+0.61		
			N(z); Mo($_z$2)	-3.28		
	Mo(z)	+0.01	N(z); Mo(s)	-0.89	-4.91	
			N(z); Mo(z)	-0.73		
			$Cl_3 a_1(\sigma)$; N(2s)	+0.07		
			$Cl_3 a_1(\sigma)$; N(z)	-0.19		
	$Cl_3 a_1(\sigma)$	-0.04	$Cl_3 a_1(\sigma)$; Mo($_z$2)	+0.12	-0.07	
			$Cl_3 a_1(\sigma)$; Mo(s)	-0.10		
			$Cl_3 a_1(\sigma)$; Mo(z)	+0.03		

Mo(s) = Mo(5s)

Table 4.13. Mulliken charges for the
$(R)_3Mo \equiv N$ molecules, where R = Cl or ^tBuO.

	$R_3Mo \equiv N$	
	Cl	O^{t}Bu
M	+1.18	+1.96
N	-0.41	-0.63
R	-0.26	-0.75
Δ (M-N)	1.59	2.58
Δ (M-R)	1.44	2.70
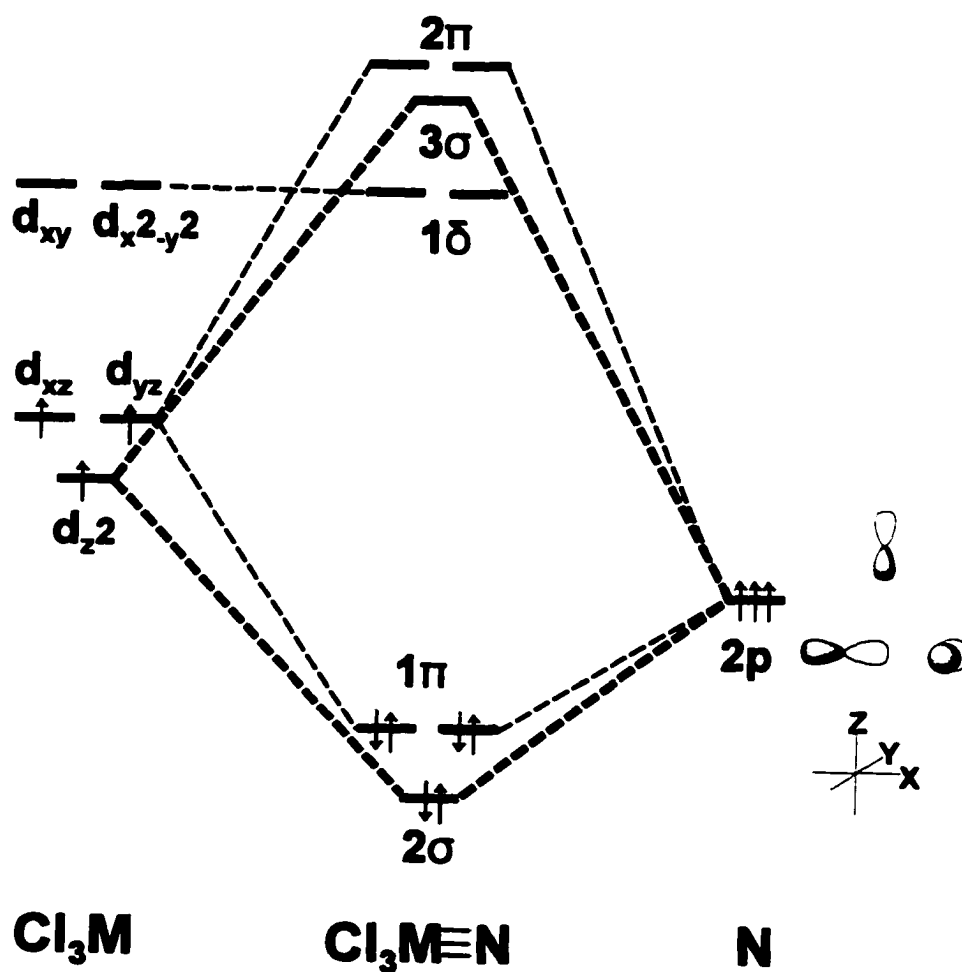
Figure 4.1. Orbital interaction diagram of a d^3-L^3M fragment, where L is a simple σ donor ligand (left), with the N(p) orbitals (right).

32%
Mo(4d$_{z^2}$)

4%
Mo(5d$_{z^2}$)

50%
N(2p$_z$)

8%
N(2s)
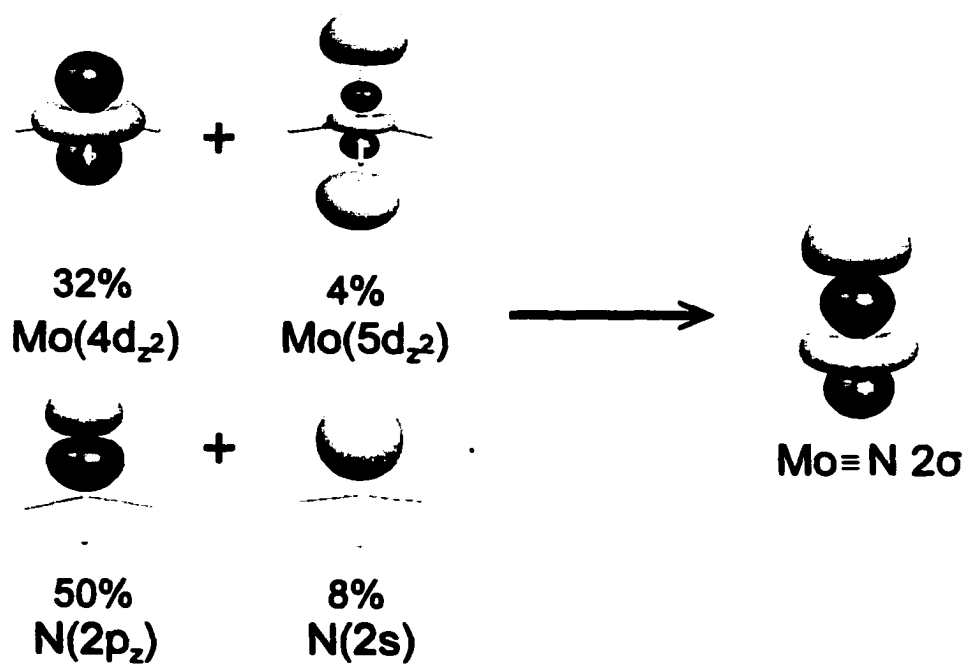
Mo≡N 2σ

Figure 4.2. Contour plots (Contour value = 0.05) of the atomic orbitals and their relative contribution to the Mo≡N 2σ.
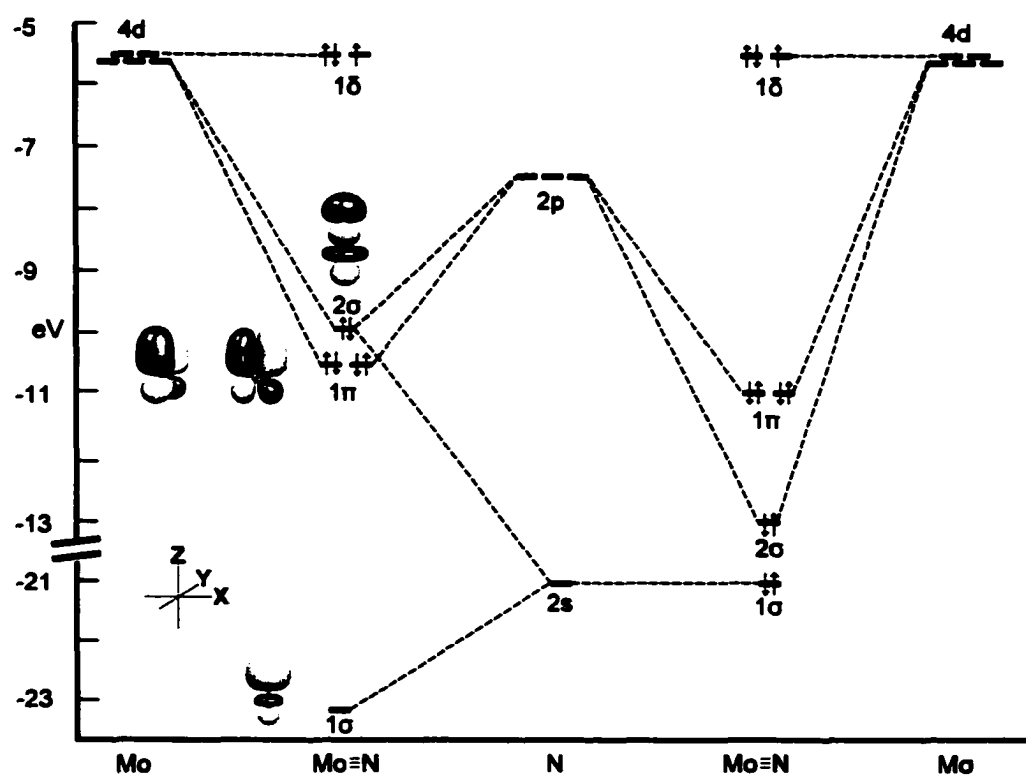
Figure 4.3. Correlation diagram for Mo≡N calculated by the Fenske-Hall method with the N(2s) included in the valence set (left) and with the N(2s) treated as a core orbital (right).
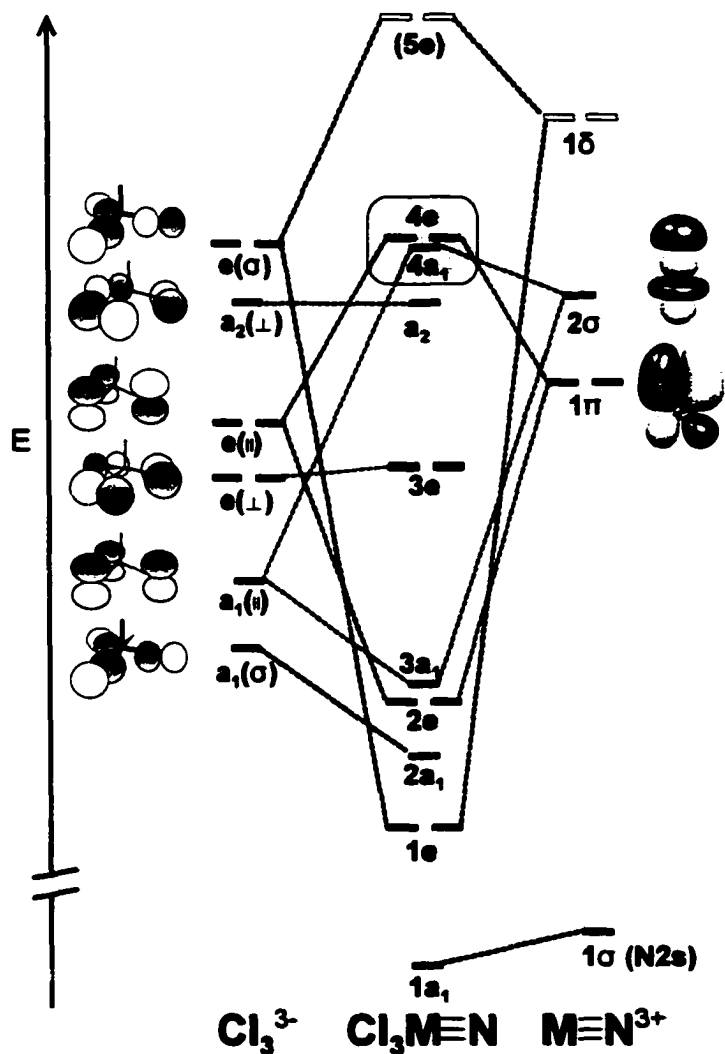
Figure 4.4. Simple correlation diagram for $Cl_3Mo \equiv N$ showing the possible interactions between the orbital of the Cl_3^{3-} and $Mo \equiv N^{3+}$ fragments. Unfilled orbitals are represented by hollow rectangles.
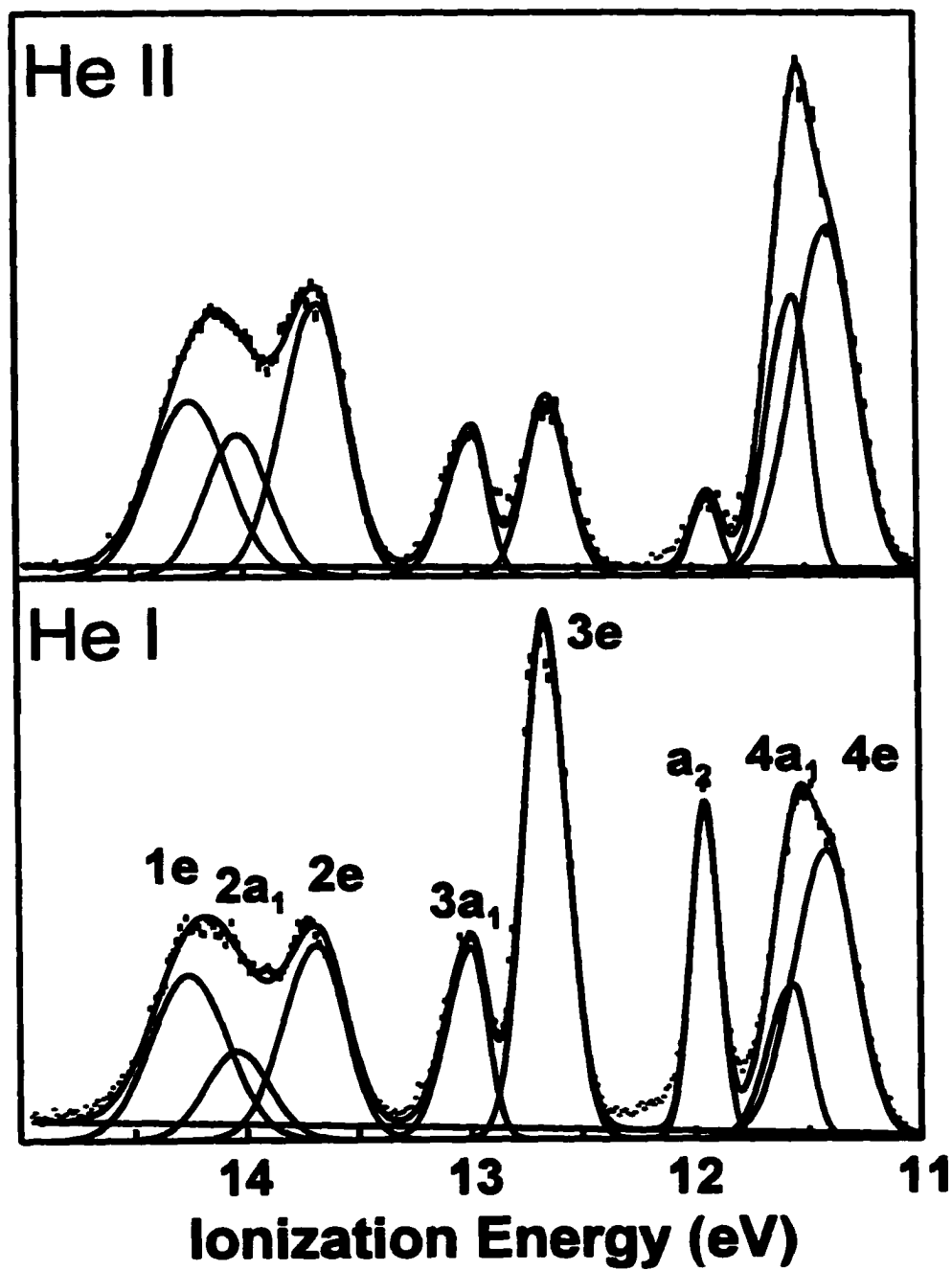
Figure 4.5. He II and He I photoelectron spectra of $Cl_3Mo \equiv N$.
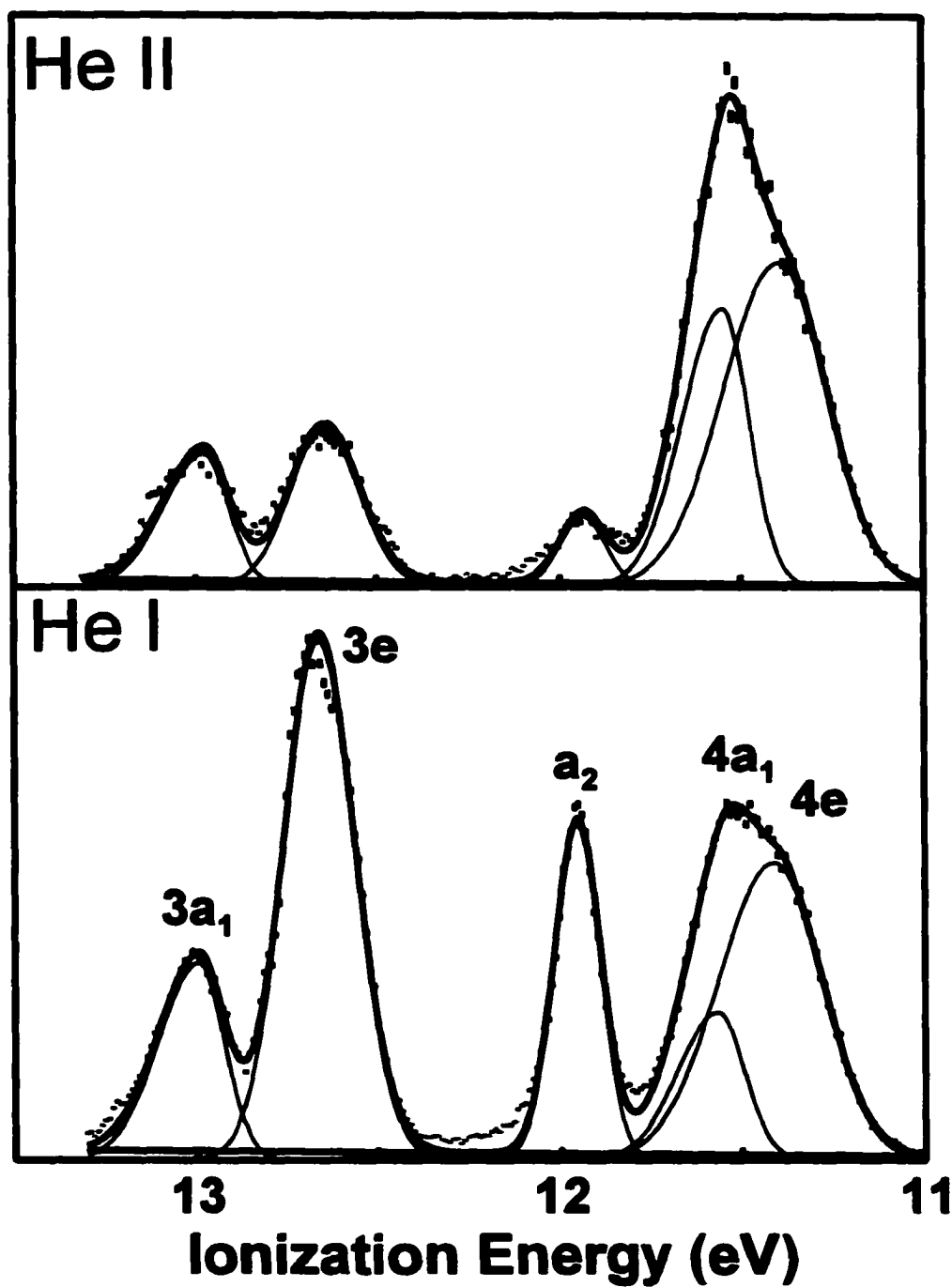
Figure 4.6. He I and He II photoelectron spectra of $Cl_3Mo\equiv N$ collected in the 11 to 13.5 eV energy range.
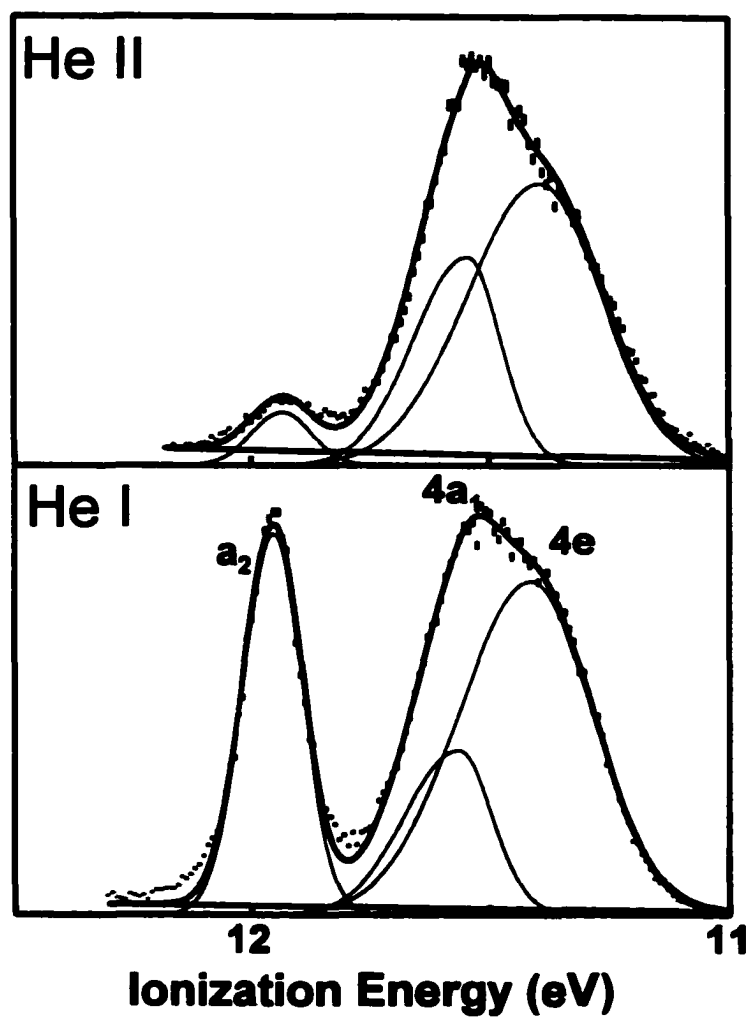
Figure 4.7. He I and He II photoelectron spectra of $Cl_3Mo \equiv N$ collected in the 11 to 12.5 eV energy range.
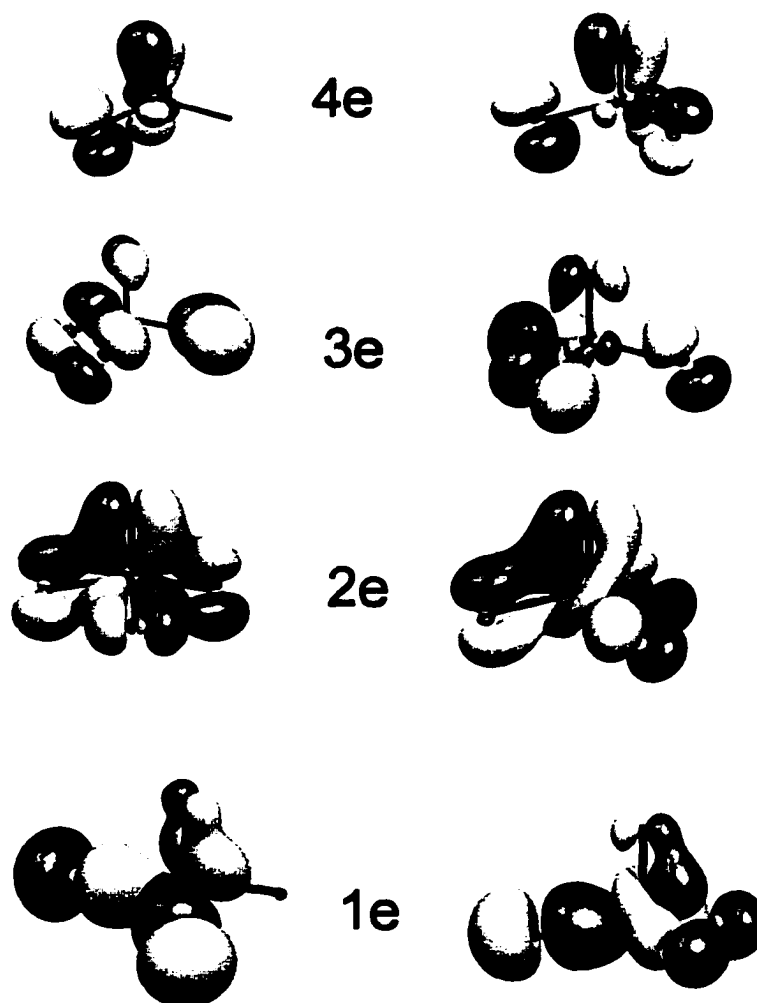
Figure 4.8. Contour plots of the four "e-symmetry" combination orbitals from an ADF calculation on $Cl_3Mo\equiv N$ (Contour = 0.04).
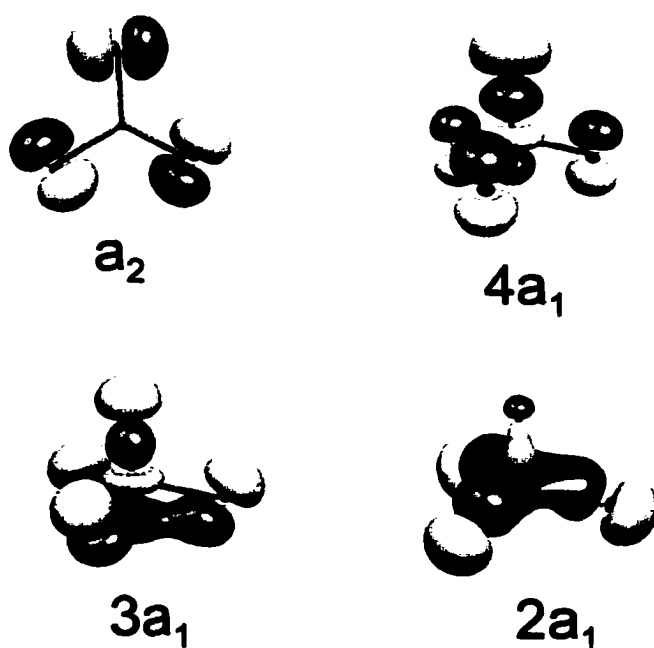
Figure 4.9. Contour plots of the three a_1 symmetry orbitals and the a_2 orbital from an ADF calculation on $Cl_3Mo \equiv N$ (Contour = 0.04).
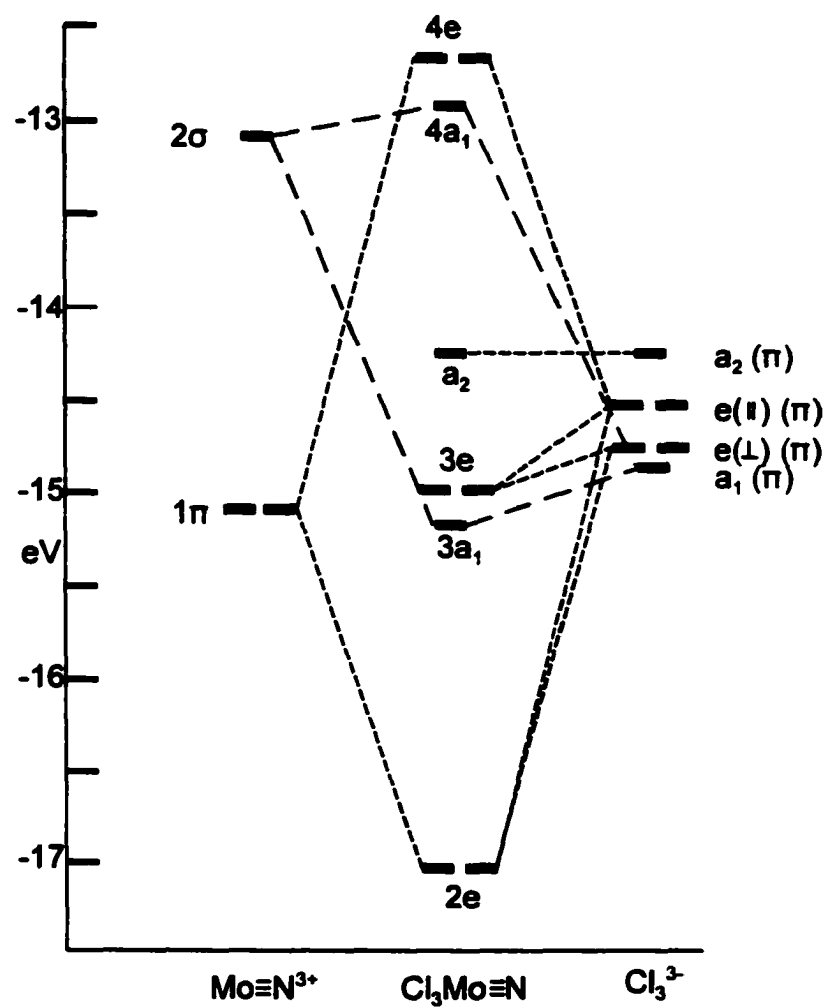
Figure 4.10. Correlation diagram for $Cl_3Mo\equiv N$ calculated by the Fenske-Hall method for the interaction of the orbitals of the $Mo\equiv N$ fragment with the Cl_3^{3-} fragment orbitals.
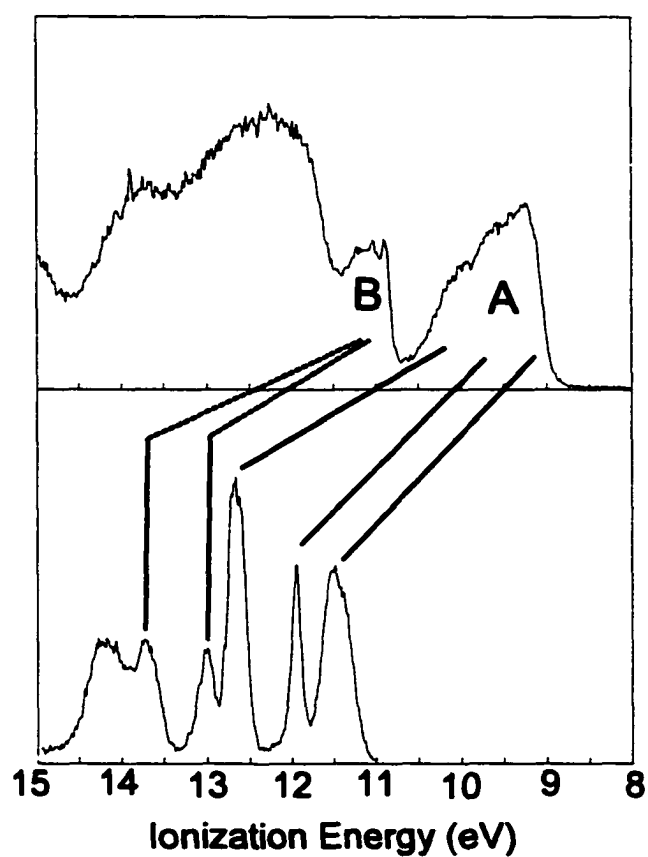
Figure 4.11. He I photoelectron spectra of
$R_3Mo \equiv N$, where $R = {}^tBuO$ (top) and Cl (bottom).

CHAPTER 5

THE INVERSE HALOGEN EFFECT: A PHOTOELECTRON SPECTROSCOPIC AND COMPUTATIONAL STUDY OF THE BONDING IN $Mo_2X_4(PMe_3)_4$ (X = Cl, Br), $W_2Cl_4(PMe_3)_4$, AND $Re_2X_4(PMe_3)_4$ (X = Cl, Br, I)

Introduction

Compounds containing close metal-metal interactions provide unique opportunities to explore the factors that influence the electronic structure and chemical reactivity of these compounds. Metal-metal interactions are essential to the accurate description of the electronic structure and reactivity of a variety of systems, ranging from molecules to clusters and materials.[101-113] The heart of understanding the reactivity of more complex systems containing close metal-metal interactions lies in a thorough comprehension of the bonding that can occur between just two transition metal atoms. As put forth by Cotton, the electrons of the dimetal system can be allotted to molecular orbitals of σ, π, δ, δ^*, π^*, and σ^* symmetries.[18] For a particular dimetal system, the metal-metal and metal-ligand bond distances, electronic transitions, redox activity, and ionization energies can all be understood within the constructs of the molecular orbital model.[17] Of utmost concern to the chemist is the study of the dependence of the electronic structure of a molecule containing a metal-metal multiple bond on the choice of metal and the choice of ligands.

A large portion of the molecules known to contain a multiple metal-metal bond are formed from multidentate ligands that bridge the two metal centers, thereby facilitating close contact between the two metal centers. In many cases, the bridging ligands are considered vital to stabilizing the highly reactive multiple metal-metal bonds.[17,114] This class of molecules is typified by the $M_2(O_2CCH_3)_4$ molecules where M = Cr, Mo, or W. In simple terms both metal centers are in the formal oxidation state II, leading to two d^4 metal centers. Rather than exist as

two separate metal centers with approximate C_{4v} symmetry, the metal-based electrons are used to form a quadruple bond between the two metals ($\sigma^2\pi^4\delta^2$).

In the absence of bridging ligand systems, the M-M bond distances are known to be much longer than seen in the bridged systems. Indeed, the number of transition metals that are known to form unsupported multiple metal bonds is quite limited.[17] The vast majority of the known species are formed by the second and third row group 6 and 7 transition metals. To date, no molecules containing unsupported multiple metal-metal bonds have been found for the first row transition metals. Molecules containing unsupported metal-metal bonds are of interest for elucidating the importance of the ligand system in determining the electronic structure of the metal-metal bond.

Detailed features of the bonding manifold have been widely studied for molecules of the general formula $M_2X_4L_4$ (M = Mo, W, Tc, or Re, X = F, Cl, Br, I, OR, or R, and L = a neutral donor ligand (PR$_3$ or NR$_3$).[17,115-118] In terms of the traditional metal-metal bonding scheme, the group 6 analogs involve bond formation between two d^4 metal centers, giving a $\sigma^2\pi^4\delta^2$ electron configuration. It follows that the Group VII analogs correspond to bond formation between two d^5 metal centers, providing two additional electrons that occupy the M-M δ^* orbital. Among this diverse group of compounds only three isomers have been found in the solid state when L = PR$_3$. To distinguish the isomers, Cotton and coworkers developed a numerical scheme to distinguish the isomers from one another. The three known isomers (along with the numbering scheme) are shown below in 5.1. Of these three isomers, the D_{2d} isomer is by far the most prevalent, owing to the minimization of steric interactions between the phosphines.[119] Even so, the existence of the

1,3,5,8 (D_{2d}) 1,2,7,8 (C_{2h}) 1,3,5,7 (D_{2h})
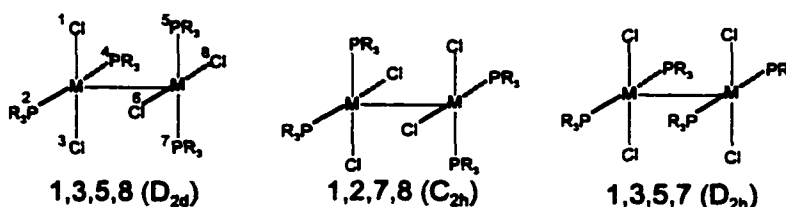
5.1

other isomers has spurred much interest in the bonding and reactivity of these systems.[120-128]

[114,129-135] In particular, much work has been done to explore the possibility of using other neutral ligand donors, particularly nitrogen donors like NR_3 and pyridines, where R = alkyl.[119,136-141]

To understand the reactivity and spectroscopic properties of molecules containing metal-metal multiple bonds, one must have knowledge of the electronic structures of these molecules. For the $M_2X_4(PR_3)_4$ analogs, much information concerning the electronic structure of the M-M quadruple bond has been gleaned from electronic spectroscopy (particularly the measurement of the δ-δ^* transition of the group 6 analogs) as well as electrochemistry. Unfortunately, these methods provide only limited information concerning the highest occupied molecular orbital (HOMO) and the lowest unoccupied molecular orbital (LUMO). To understand the electronic structure of these molecules, one needs to obtain information about all the valence interactions of the metal-metal bonded unit. To this end, photoelectron spectroscopy has proven to be an invaluable tool for probing the intricacies of the bonding in molecules that contain quadruple,[94,96,142,143] electron-poor triple,[144-147] and electron-rich triple metal-metal bonds.[148]

The present study involves a systematic examination of the effects of the halide donors on the electronic structure of the $M_2X_4(PMe_3)_4$ analogs. Although the He I photoelectron spectra of the $M_2Cl_4(PMe_3)_4$ (M = Mo,[149-151] W,[149] or Re[148,150]) analogs have been reported previously, numerous questions concerning the assignment of the photoelectron bands of these systems have arisen. Both the position of the M-M σ ionization as well as the importance of spin-orbit

coupling in describing the electronic structure of these systems have been the source of much

debate. In fact, the original assignments of the the Mo and W analogs were in error due to a

misunderstanding of the strength of the M-M σ bond.

The origin of our interest in the electronic structure of the $Mo_2X_4(PMe_3)_4$ molecules can

be traced to the early electrochemical studies of these molecules reported by Gray and

Hopkins.[152-155] Specifically, Gray and Hopkins noted that these molecules are more easily

oxidized as the electronegativity of the halogen atom increases.[152] Interestingly, the unexpected

trends also extend to the reduction chemistry of these molecules where the reduction potentials

shift in opposition to the electronegativity of the attached halogen atom. Subsequent

electrochemical studies of the $Re_2X_4(PMe_3)_4$ analogs (X = Cl, Br, I) revealed a similar trend in

the oxidation potentials. Studies of other phosphine analogs, $Mo_2Cl_4(PR_3)_4$, (R = Et, ^nPr, ^nBu,

PH_2Ph, PMe_2Ph, PEt_2Ph, $PHPh_2$, $PMePh_2$, and $PEtPH_2$) have shown the oxidation potential to be

highly dependent upon the relative σ-donor and π-acceptance abilities of the phosphine ligands,

with the most easily ionized molecules being those containing bulky alkyl phosphine donors.[156]

Based on these electrochemical studies, Gray and coworkers erroneously attributed the inverse

halide order to M(d)-halide(d) back-bonding.[152] One must question the logic of invoking π-

acceptance by the halide atoms to explain any trend in the oxidation potentials because the

halogen atoms are known to be π-donor ligands, not π-acceptor ligands. It seems clear that other

avenues for explaining the inverse halide order should be explored. In addition, electrochemical

studies are complicated by the solvent dependence of the oxidation and reduction potentials.

Hence, one must be careful when looking at trends from electrochemical studies. To address the

solvent dependence of the oxidation potentials, Gray and coworkers completed their

electrochemical studies in two different solvent: THF and CH_2Cl_2. The measured potentials in

both solvents revealed the same inverse halide order so they concluded that the trend could not

be attributed to a solvent effect. Nevertheless, an intriguing question is whether the inverse halide order would remain in the absence of any solvent.

In hopes of observing the inverse halide effect in the gas-phase phase photoelectron spectra, we have obtained the photoelectron spectra of a series of molecules: $Mo_2X_4(PMe_3)_4$ (X = Cl, Br), $W_2Cl_4(PMe_3)_4$; and $Re_2X_4(PMe_3)_4$ (X = Cl, Br, I). Through the use of different photon sources (Ne I, He I, and He II), we have been able to ascertain both the positions of the ionizations from the metal-metal orbitals as well as information about the relative atomic character of these molecular orbitals. Density functional calculations as well as Fenske-Hall calculations provide support for the experimentally-determined assignments of the ionization bands and allow a ready analysis of the orbital makeups and electron distributions within the molecules. Through computational studies, the origin of the inverse halide order will be readdressed.

Experimental

General Methods. All manipulations were carried out using an Argon (Ar) or dinitrogen (N_2) atmosphere and standard air and moisture sensitive techniques in a Vacuum Atmospheres Glovebox or Schlenk line. Solvents were freshly distilled from CaH_2 or K/Benzophenone ketyl. Air was removed via freeze-pump-thaw cycles. All reagents were purchased from Aldrich unless otherwise stated and used without further purification. Tungsten tetrachloride (Strem Chemicals) and Trimethylphosphine (Strem Chemicals) were used as purchased. Molybdenum acetate was synthesized and purified via literature procedures.[150] The $Re_2X_4(PMe_3)_4$ (X = Cl, Br, I) molecules were prepared and purified according to the method developed by Walton.[157] $Mo_2X_4(PMe_3)_4$ (X = Cl, Br, and I)[153] and $W_2Cl_4(PMe_3)_4$ [22,158] were prepared by standard procedures. All products were characterized with mass spectrometry and ^1H

NMR to check for the purity of the samples. The $Re_2I_4(PMe_3)_4$ sample was prepared by Dr. Gary Hinch.[150]

Spectroscopic methods. Mass spectra were taken on a Kratos MS 80 high resolution mass spectrometer using Negative Ion CI with methane (CH_4) as reagent gas. A positive ion EI source with a trap current of 100 μA at a temp of 225 $^\circ$C at 52 eV and a 3 kV analyzer with a resolution of 2000 using the 5% peak height definition were used to obtain the mass spectra. The scanning rate was 5 sec/decade with a mass range of 1100 to 275.

Photoelectron spectra. The photoelectron spectra were recorded using an instrument that features a 36 cm radius, 8 cm gap McPherson hemispherical analyzer with custom-designed sample cells, detection system, and control electronics.[31] The excitation source was a quartz lamp with the ability, depending on operating conditions, to produce He Iα (21.218 eV), He IIα (40.814 eV), or NeIα (16.6709, 16.8482 eV) photons. The He I ionization energy scale was calibrated to the energy separation between the $^2E_{1/2}$ ionization of methyl iodide (9.538 eV) and the Ar $^2P_{3/2}$ ionization (15.759 eV). For the He II data collection, the energy scale was calibrated to the energy separation between the He I Ar $^2P_{3/2}$(Apparent I.E. = 35.36 eV) and the He self ionization (Apparent I.E. = 24.587 eV). During individual data collection scans, the argon $^2P_{3/2}$ ionization was used as an internal calibration lock for the energy scale during He I and He II data collection runs. To test the calibration of the He II energy scale, data collection runs were repeated using the He self ionization (24.587 eV) as the internal calibration lock for the energy scale. During Ne I data collection the Xe $^2P_{3/2}$ (12.130 eV) was used as the internal lock for the energy scale. Resolution (measured as full-width-at-half-maximum of the argon $^2P_{3/2}$ ionization) was 0.016-0.024 eV during He I data collection. The drift in the ionization scale was always less than $\pm$0.003 eV. Assuming a linear dependence of analyzer intensity to the kinetic energy of the

electrons within the energy range of these experiments, all data were intensity corrected with the experimentally-determined analyzer sensitivity function.

Because discharge sources are not monochromatic,[33] each spectrum was corrected for the presence of ionizations from other source lines. The He I spectra were corrected for ionizations from the He Iβ line at (1.959 eV) higher in energy with 3% of the intensity of ionizations from the He Iα line. He II spectra were similarly corrected for ionizations from the He IIβ line (7.568 eV higher in energy and 12% of the intensity of the He IIα line.) The NeI source, a doublet due to strong spin-orbit coupling, yields a spin-orbit coupled shadow spectrum at 0.18 eV higher binding energy. This shadow spectrum has an intensity that is 15-20% the intensity of the primary Ne I spectrum, depending on the experimental conditions. The intensity of the shadow spectrum was monitored by recording the relative intensities of the Xe $^2P_{3/2}$ ionization and its spin-orbit shadow.

The sublimation temperatures during data collection (°C at $\approx 10^{-4}$ Torr), measured using a "K" type thermocouple attached directly to the ionization cell through a vacuum feedthrough, were $Mo_2Cl_4(PMe_3)_4$ (132-155); $Mo_2Br_4(PMe_3)_4$ (126-155); $W_2Cl_4(PMe_3)_4$ (110-153); $Re_2Cl_4(PMe_3)_4$ (138-150); $Re_2Br_4(PMe_3)_4$ (136-165); $Re_2I_4(PMe_3)_4$ (136)[150]. The $Re_2X_4(PMe_3)_4$ analogs sublimed cleanly with no detectable evidence of decomposition products in the gas phase or as a solid residue. $W_2Cl_4(PMe_3)_4$ and the $Mo_2X_4(PMe_3)_4$ analogs, on the other hand, sublime with some decomposition depending on the rate of heating. A CHROMALOX USA® resistive heating bar (175 watt and 120V) was used to heat the cell via applied voltage. Primary evidence for decomposition of the samples during data collection is the appearance of spectral features attributable to the ionization of free PMe_3. In addition, a green-yellow residue is left in the sample cell after data collection is completed. This tendency toward decomposition has been noted previously[150] and can be minimized (if not totally avoided) by careful temperature control.

In addition, it was found that freshly-made samples were necessary in order to obtain the photoelectron spectrum of $Mo_2Br_4(PMe_3)_4$. To test the reproducibility of the spectrum and check for decomposition, spectra were collected on different days. No significant changes were detected in the spectra. Attempts to obtain the spectra of $Mo_2I_4(PMe_3)_4$ proved unfruitful, yielding only ionizations from the decomposition product, PMe_3.

Data Analysis. In the figures of the photoelectron spectra, the vertical length of each data mark represents the experimental variance of that point.[34] The ionization bands are represented analytically with the best fit of asymmetric Gaussian peaks. The number of peaks used was the minimum necessary to get an analytical representation of the He I spectrum. For fitting the He II and Ne I spectra, the peak positions and half-widths were fixed to those of the He I fit.

The confidence limits for the relative integrated peak areas are $\pm 5\%$. The primary source of uncertainty is the determination of the baseline. The baseline is caused by electron scattering and is taken to be linear over the small energy range of these spectra. The procedures used to fit the spectra have been described in more detail elsewhere.[34]

Computational studies. All computational studies were performed using the model compound $M_2Cl_4(PH_3)_4$. All bond distances and angles were obtained from the crystal structures of the $M_2X_4(PMe_3)_4$ molecules and optimized to the full symmetry of the molecule (D_{2d}).[117,153,159] The values used in the computational studies are presented in Table 5.1. For the systems with no known crystal structures, the bond distances and angles were extrapolated from the analogous $M_2X_4(PEt_3)_4$ molecules.

Density functional studies were performed with the Amsterdam Density Functional package (versions ADF 2.3.0 and 2000.01).[36] The numerical integration procedure was developed by te Velde and co-workers.[37,38] The BLYP method was used for all calculations.

Calculations using PW91 and X(α) closely match the BLYP results.[160] The atomic orbitals on all

centers were described by an uncontracted triple-ς STO basis set (set IV) that is available with

the ADF package. Calculations employing other basis sets were also performed, and the relative

orbital energies were not found to be basis set dependent.[160] The $1s^2s^22p^6$ configurations of Cl

and P, the $1s^22s^22p^63s^23p^63d^{10}$ for Mo, and the $1s^22s^22p^63s^23p^63d^{10}4s^24p^64d^{10}$ were assigned to

the core and treated by the frozen-core approximation. In a similar manner, the relativistic

effects were incorporated into the computational studies of $Re_2X_4(PH_3)_4$ (X = Cl, Br, I) and

$W_2Cl_4(PH3)4$ by the scalar Pauli formalism.[161-164] As a check of these calculations, calculations

were also run employing the ZORA scalar formalism as implemented in the ADF2000.01

package.[56-60] However, these results are not included because they did not differ significantly

from the results obtained from the Pauli formalism.

Values for ionization energies can be determined by two different computational

procedures. As a first approximation, the Kohn-Sham orbital energies from the ground state

calculations of the "neutral" molecule are directly analogous to the experimental ionization

energies ($-\epsilon_i \approx$ I. E.).[66,67] For a more direct comparison of the relative Kohn-Sham energies, the

calculated orbital energies are adjusted so that the highest occupied MO energy matches the

experimental vertical ionization energy. For the $Re_2X_4(PH_3)_4$ analogs, the scaled Kohn-Sham

orbital energies are described by equation (5.1),

$$\varepsilon_{scaled} = |\varepsilon_i| + \Delta_i$$
$$\Delta_i = I.E.(\delta) - |\varepsilon_i(\delta)| \quad (5.1)$$

where Δ_i = 2.38, 2.35, and 2.07 eV for X = Cl, Br, and I, respectively. Analogously, the scaled

Kohn-Sham orbital energies of the $M_2X_4(PH_3)_4$ molecules where M = Mo or W are also

described by (5.1) with the exception that the Δ_i pertains to orbital and ionization energies of δ,

not δ^*. The relevant values of Δ_i for the $Mo_2X_4(PH_3)_4$ analogs are 2.25 eV and 2.20 eV when X

= Cl and Br, respectively. For $W_2Cl_4(PH_3)_4$, Δ_i = 2.26 eV.

Calculated ionization energies can also be determined by comparing the total energy of

the neutral molecule to the total energies of the successive ionic states, where one electron has

been removed from the orbital of interest. Ionization energies obtained in this manner are

vertical ionization energies (the geometry is assumed to be constant in the neutral and the cation

states). These ΔE_{SCF} energies more correctly represent the ionization process because they

account for the electron relaxation that occurs in the molecule when an electron is removed. The

ΔE_{SCF} energies of the $Re_2X_4(PH_3)_4$ molecules are scaled according to equation (5.2),

$$\Delta E_{SCF(scaled)} = 1.075 \times (\Delta E_{SCF}) + \Delta_i \quad (5.2)$$
$$\Delta_i = I.E.(\delta^*) - \Delta E_{SCF}(\delta^*)$$

where Δ_i = -0.36, -0.31 and -0.30 eV for the Cl, Br, and I analogs, respectively. The scaling

equation serves to make the calculated separations between the δ^* and δ ionizations match the

experimental-determined separation of the two ionizations. For the $Mo_2X_4(PH_3)_4$ (X = Cl, Br)

and $W_2Cl_4(PH_3)_4$ molecules, the ΔE_{SCF} energies were scaled according to equation (5.3),

$$\Delta E_{SCF(scaled)} = 1.00 \times (\Delta E_{SCF}) + \Delta_i \quad (5.3)$$
$$\Delta_i = I.E.(\delta) - \Delta E_{SCF}(\delta)$$

where Δ_i = -0.03 eV (Mo;Cl), +0.05 eV(Mo,Br), and -0.03 eV (W,Cl).

For comparison with the density functional studies presented here, Fenske-Hall

molecular orbital calculations have been performed.[39] The ADF-optimized coordinates were

used as the input coordinates for the Fenske-Hall calculations. Contracted double-zeta basis

functions were used for the Mo, W, and Re valence d atomic orbitals, and the 3p atomic orbitals

of Cl and P.[39,83-85] Basis functions for the metal atoms were obtained for the 1+ oxidation state.

Ground state atomic configurations were used for the basis functions of all other atoms. To

facilitate comparison between the results from the Fenske-Hall calculations and the density

functional, studies, the Koopmans' energies were adjusted so that the experimental energy

difference between the δ^* and δ ionizations of the $Re_2X_4(PH_3)_4$ was obtained in the

computational studies. The shifted eigenvalues were obtained according to equation (5.4),

$$\varepsilon_{scaled} = 0.57 \times |\varepsilon_i| + \Delta_i$$
$$\Delta_i = I.E.(\delta^*) - |\varepsilon(\delta^*)| \quad (5.4)$$

where Δ_i = 2.85 eV(Cl), 2.89 eV(Br), and 2.78 eV(I). For the $Mo_2X_4(PH_3)_4$ analogs (X = Cl, Br)

and $W_2Cl_4(PH_3)_4$, the orbital eigenvalues were scaled according to equation 5.4 with the

exception that the Δ_i contains the values for δ instead of δ^*. For the $Mo_2X_4(PH_3)_4$ analogs, Δ_i =

2.46 eV(Cl) and 2.70(Br); the corresponding value of Δ_i for $W_2Cl_4(PH_3)_4$ is 2.75 eV.

Preliminary considerations

In order to gain an appreciation for the significance of the present work, one must first

obtain a firm grasp of the information gleaned from previous photoelectron studies of molecules

containing metal-metal bonds. These works provide the groundwork for understanding the

photoelectron spectra of the $M_2X_4(PMe_3)_4$ series. Of particular interest are the previous

photoelectron spectroscopic studies of molecules containing multiple metal bonds between Mo,

W, and Re.

$Re_2Cl_8^{2-}$. As the first species in which the quadruple bond was postulated to exist, the

bonding in $Re_2Cl_8^{2-}$ is of primary interest to the field of metal-metal bonding.[17] Due to the highly

charged nature of this species, traditional photoelectron spectroscopic studies were precluded.

Recently, Wang and coworkers have reported the negative anion photodetachment spectrum of

this species and interpreted it in terms of the traditional metal-metal bonding orbital scheme.[165]

In the spectrum, three separate ionization features were assigned to the removal of an electron

from the δ, π, and σ orbitals, respectively. Although this assignment correlates with the

generalized metal-metal bonding scheme, the only experimental justification for the assignment

comes from comparisons to photoelectron studies of neutral species. Much more work needs to

be done in order to prove that the experimental assignments are correct.

$M_2(O_2CCH_3)_4$. The vast majority of the systems studied via photoelectron spectroscopy

to date are of the classic paddlewheel type typified by the $M_2(O_2CCCH_3)_4$ molecules shown in

5.2. Although the photoelectron spectra of these systems have been around for quite some time,

5.2
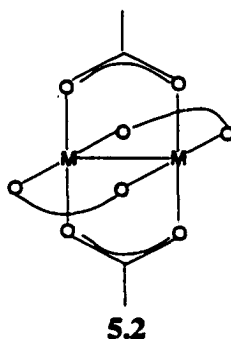
a definitive assignment of the ionization manifold proved elusive until recently. Of primary

concern for these systems was the relative strength of the M-M σ bond. Without a proper

understanding of the strength of the M-M σ bond, the assignment of the ionization feature due to

this orbital is not possible. For many years, the M-M σ bond was thought to be the strongest of

the metal-metal bonds due to the direct overlap of the valence Md_z^2 orbitals on the two metal

centers. The misconception concerning the strength of the M-M σ bond was fueled by scattered

wave $X\alpha$ computational studies that predicted the M-M σ ionization to lie several eV higher in

binding energy than the M-M π.[149] To add to the confusion, *ab initio* calculations on similar

systems predicted the M-M σ orbital to be nearly degenerate with the M-M π orbital.[166-168] On

first glance, it seems quite logical that the M-M σ should indeed be the most stable orbital

combination of the M-M bonding manifold based on the direct overlap of the two dz^2 orbitals.

However, this is a flawed conclusion because it neglects the unfavorable overlap of the ndz^2 on

one metal center with the np_z on the other metal center, which will serve to counteract the

stabilization provided by the favorable overlap of the two dz^2 orbitals. This is essentially the

same phenomenon seen for N_2 where the N-N σ is destabilized above the π due to significant

overlap of the pz on one N atomic center with the 2s of the other atom.[33,61]

With the conflicting computational results, the only chance of resolution of the

controversy surrounding the assignment of the M-M σ ionization was to obtain direct

experimental evidence of its position. The much-desired experimental evidence came in the

form of a combined gas-phase and thin-film study of the $M_2(O_2CCH_3)_4$ series where M = Cr, Mo,

W.[169] From this study, it was determined that the M-M σ was indeed much less stable than

expected with the vast majority of the M-M bond strength originating not from the σ interaction

but from the π interaction.[170,171] As our test case for molecules containing quadruple bonds

between two metal centers, the photoelectron spectrum of $Mo_2(O_2CCH_3)_4$ contains a wealth of

information concerning the nature of the M-M bond. In the photoelectron spectrum of this

molecule, the M-M σ and π are found to be degenerate in the gas phase with an energy 1.70 eV

higher than the Mo-Mo δ.[169,172] This assignment was possible due to a strong filled-filled

interactions between an oxygen lone pair on one dimetal molecule with the filled M-M σ on the

neighboring molecule, resulting in a destabilization of the M-M σ ionization in the thin-film

spectrum as evidenced by the appearance of a shoulder on the low ionization energy side of the

Mo-Mo π ionization in the thin-film spectrum. By a similar argument, the W-W σ ionization

was found to occur as a sharp ionization on the high energy side of the W-W π ionization in the

gas phase. While the gas-phase spectrum contains three distinct ionization bands below 11 eV,

the thin-film spectrum contains just two ionization features. In the thin-film spectrum, the W-W

σ ionization is destabilized and occurs under the same ionization band as the W-W π. The

experimental evidence for this assignment comes from an examination of the relative intensities

of the W-W π and δ bands. For the thin-film spectra, the relative intensity of the W-W $\sigma+\pi$

band increases with respect to the δ band, providing clear evidence for the assignment of the σ

ionization.

Other evidence for the M-M σ ionization. Further support for the assignments of the

Mo-Mo and W-W σ ionizations is found in the photoelectron spectra of $M_2(np)_2(O_2CCH_3)_4$

where M = Mo, W and np = neopentyl. These systems are directly related to the aforementioned

$M_2(O_2CCH_3)_4$ molecules by the oxidative addition of the two neopentyl groups, yielding two

5.3
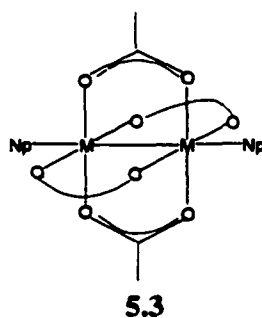
Mo(III) centers as shown in **5.3**. From comparisons of the photoelectron spectra of these systems

with those of $M_2(O_2CCH_3)_4$, it was found that the oxidative addition involves the electrons from

the M-M σ ionization because the sharp ionization feature attributed to the W-W σ ionization

disappears in the spectrum of the $W_2(np)_2(O_2CCH_3)_4$. In the spectrum of the Mo analog, a new

ionization feature appears in between the Mo-Mo δ and the Mo-Mo π which is attributable to the

Mo-C(σ) ionizations. Clearly, these spectroscopic results provide strong support for the position

of the M-M σ ionzation.

More evidence for the position of the M-M σ ionization can be found in the

photoelectron spectra of the $M_2(OCMe_3)_6$ analogs (M = Mo, W).[146,147,173] The generalized

5.4
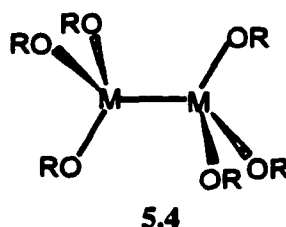
molecular structure of these molecules is shown in **5.4**. These systems can be described as being

formed by two metal atoms with a formal oxidation state III, thereby facilitating a $\sigma^2\pi^4$

occupation of the M-M bonding orbitals. For these systems, the M-M σ and π ionizations are not

degenerate so a definite position can be attributed to these ionizations for both the Mo and W

analogs. Interestingly, the $W_2(OCMe_3)_6$ spectrum contains a sharp ionization analogous to that

seen in the $W_2(O_2CH_3)_4$ spectrum. Like the W-W σ ionization of the $W_2(O_2CCH_3)_4$ molecule, the

W-W σ ionization lies 1.52 eV higher in ionization energy than the W-W π. By comparison, the

splitting of the Mo-Mo σ and π ionizations is only 1.01 eV. The key interest in this result lies in

the large splitting of the two bands in the tungsten analog because it clearly eliminates the

possibility of assigning the two ionization features to the spin-orbit split W-W π because the

spin-orbit coupling constant ($\lambda_W = 0.19$ eV[174]) is much too small to account for the large splitting

seen in the spectrum.[149] Regardless of the particular compound, the M-M σ and π are found to

be close in energy and the effects of spin-orbit coupling are not distinguishable at the resolution

of this experiment.

General bonding considerations

Charge and Overlap effects. When considering the bonding in any molecule, two major effects must be considered: the charge effect and the overlap effect. The charge effect relates directly to the electronegativities of the constituent atoms. To get a true measure of the charge effect, the orbital of interest must be a nonbonding orbital, where contributions from the overlap effect are not present. A classic illustration of the charge effect can be found in the energies of the highest occupied lone pair ionizations of the HX analogs (X = F, Cl, Br, I) as shown in Table 5.2. The reported ionization energies vary linearly with the electronegativity of the halogen atom ($R^2 = 0.9977$).

A comparison of the highest occupied molecular orbitals of benzene and chlorobenzene provides a good example of the overlap effect. The first ionization energy of chlorobenzene is actually 0.15 eV lower than the first ionization energy of benzene. Clearly, this is not the expected result based on the charge effect alone. The answer to this unexpected ionization energy trend lies in the overlap effect. The highest occupied molecular orbital of benzene is the e_{1g} set. As shown in Figure 5.1, substitution of chlorine splits this (one-node) degenerate set of orbitals due to the strong interaction of one of the set with the Cl p_z orbital. Although the other e_{1g}-based orbital is nonbonding with respect to the chlorine p_z orbital and therefore contains no halogen character, it is still stabilized due to the charge effect. It then follows that the highest occupied orbital of the substituted benzene corresponds to the antibonding combination of the e_{1g}-based orbital with the Cl p_z orbital. Clearly, one cannot ignore either effect if a complete understanding of the bonding in a molecule is desired. In order to have significant mixing between two fragment orbitals, two criterion must be met: (1) the energies of the two fragment orbitals must be closely matched and (2) the two fragment orbitals must overlap significantly.

Symmetry considerations. Before addressing the electronic structure of the

$M_2X_4(PMe_3)_4$ molecules in detail, it is useful to focus first on the symmetry of the molecule and

the information one can gain from a simple symmetry analysis of the bonding. According to

basic principles, in order for orbitals to mix in the absence of spin-orbit coupling they must be of

the same symmetry. Hence, a symmetry analysis will give the symmetry labels associated with

the molecular orbitals and reveal the possible ligand combination orbitals that can mix with the

orbitals of the M-M subunit. However, to obtain a true picture of the possible bonding that can

occur between the ligand and the dimetal unit, one must consider the nodal properties of each

ligand combination orbital.

M-M orbitals. Under D_{2d} symmetry, the metal-metal bonding orbitals of the M_2^{++} unit

have the symmetry labels: $\sigma(a_1)$, $\pi(e)$, $\delta(b_1)$, $\delta^*(a_2)$, $\pi^*(e)$, and $\sigma^*(b_2)$. In reality, there is

another set of δ orbitals that are used to form the M-L and M-X σ bonds that can be labeled as

$\delta_{M-L}(b_2)$ and $\delta^*_{M-L}(a_1)$. Excluding those orbitals involved in M-L and M-X σ bonding, all of the

molecular orbitals of the M-M bond have different symmetries and should give rise to separate

ionization features in the photoelectron spectrum.

Metal-Ligand σ bonding combinations. By a similar analysis, one can derive the

Cl e(σ)

Cl b$_2$ (σ)

Cl a$_1$(σ)

5.5

P e(σ)

P b$_2$ (σ)

P a$_1$(σ)

5.6
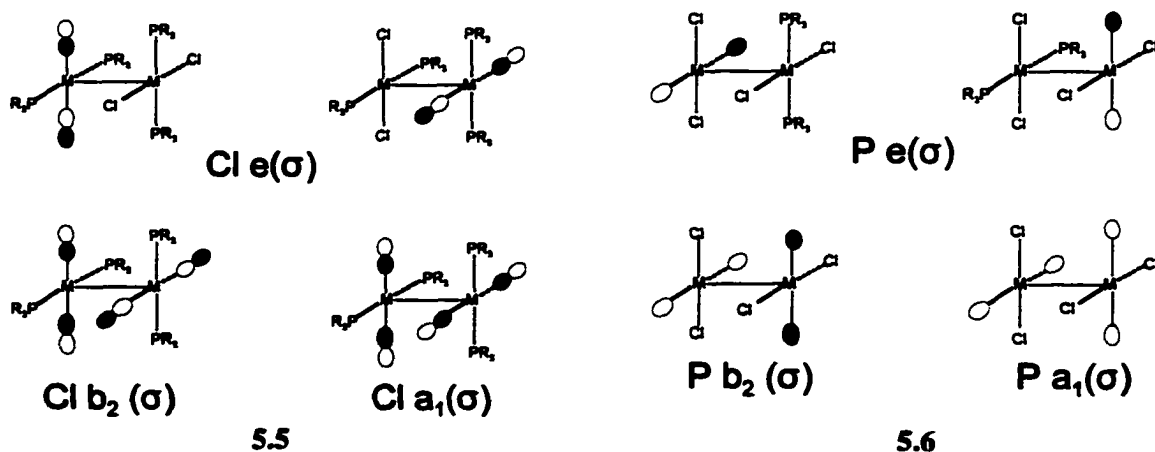
ligand orbital combinations that are involved in forming σ-type bonds with the metal centers. As

required by symmetry considerations, the Cl_4^+ combinations are treated separated from the

$(PMe_3)_4$ combinations. Even so, the symmetry types will be the same regardless of the ligand

identity. From this analysis one gets combinations of a_1, b_2, and e symmetry for both the Cl_4^+

and $(PMe_3)_4$ fragments. The nodal properties of these combinations are demonstrated in 5.5 and

5.6 for the Cl_4^+ and $(PMe_3)_4$ fragments, respectively. From the nodal properties of these orbitals

it is clear that the b_2 and a_1 combinations have the appropriate symmetry for the expected σ

interaction with the M_2 δ(b_2) and δ*(a_1). The e symmetry combinations, on the other hand, do

not have the correct nodal properties to interact with any of the metal d orbital combinations and

will be nonbonding with respect to the M-M framework. These e combinations do, on the other

hand, have the appropriate symmetry to interact with the $M(p_x,p_y)$ orbitals.

   $Cl_4(PMe_3)_4^+$ σ-type combinations. The $Cl_4(PMe_3)_4^+$ σ-type combinations can be derived

as combinations of the separate Cl_4^+ and $(PMe_3)_4$ σ combinations. In this manner, we can build

up the bonding from the simple atomic units to the more complex molecular fragments.

Although these two sets of combination orbitals have no impetus for mixing on their own, they

can mix together through the orbitals of the M-M unit. Since the Cl_4^+ and $(PMe_3)_4$ e(σ)

combinations do not have the appropriate symmetry to interact with the M_2 π or π* orbitals (the

only e symmetry orbitals of the M_2 unit), it is expected that they will not mix significantly with

Cl_4P_4 a_1 (σ) Cl_4P_4 b_2 (σ)

5.7
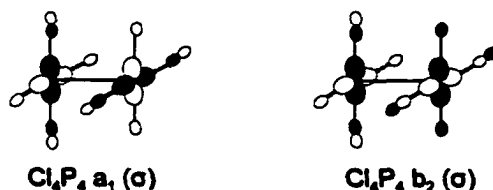
one another and can be treated as separate orbitals sets. On the other hand, the Cl_4^+ and $(PMe_3)_4$

combinations of the appropriate symmetry (b_2 and a_1) will mix through the M-M $\delta(b_2)$ and $\delta^*(a_1)$

orbitals, respectively as shown in 5.7. That necessarily means that there is another set of Cl_4P_4

orbitals that are net nonbonding with respect to the d-based orbitals of the dimetal unit but

completely bonding with respect to one other (all phases on each metal center being the same).

As shown below in 5.8, these combinations can interact with the bonding and antibonding

Cl$_4$P$_4$ a$_1$ (σ)   Cl$_4$P$_4$ b$_2$ (σ)

5.8
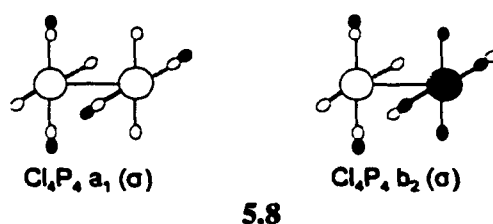
combinations of the metal (n+1) s orbitals. It must be acknowledged that the Cl_4P_4 $a_1(\sigma)$ orbital

can also interact weakly with the torus of the d_{z^2} on each metal center; this means that this

combination can interact to some extent with the metal-metal σ orbital. Of course, expansion of

the M-M-L and M-M-P angles from 90° will decrease this interaction to the extent that it can be

ignored. Through the use of simple principles one can achieve a thorough picture of the σ-type

orbital interactions.

π-type combinations of [(PMe$_3$)$_4$Cl$_4$]$^{4+}$. Although understanding the makeup of the

orbitals involved in σ bonding between the metal and the ligands is important to the overall

description of the electronic structure, it does not reveal any information about the interactions

between the ligands and the orbitals of the M-M unit. Although it is possible the PMe$_3$ units can

interact with the M-M unit through the P-C σ and σ^* combinations, these combinations should

not interact strongly with the orbitals of the M_2 unit and will not be considered here. The π-type

combinations of the chlorides, on the other hand, cannot be ignored because they will overlap

significantly with the M-M orbitals. From the symmetry analysis, the symmetry of the π-type

combinations are a_1, a_2, e, e, b_1, and b_2. Again, these labels only reveal the overall symmetry of

the combination and reveal nothing about the nodal symmetry of the combinations. For

simplicity, the π-type combinations of the idealized geometry where all angles are 90° will be

presented. To simplify the problem even further, the π-type combinations will be treated as two

separate classes: those parallel to the M-M axis and those perpendicular to it. The perpendicular

and parallel combinations are presented in **5.9** and **5.10**, respectively. The orbitals combinations

Cl$_4^+$ b$_1$ ($\pi_\perp$)   Cl$_4^+$ a$_2$ ($\pi_\perp$)   Cl$_4^+$ a$_1$ ($\pi_\parallel$)   Cl$_4^+$ b$_2$ ($\pi_\parallel$)

Cl$_4^+$ e ($\pi_\perp$)   Cl$_4^+$ e ($\pi_\perp$)   Cl$_4^+$ e ($\pi_\parallel$)   Cl$_4^+$ e ($\pi_\parallel$)

5.9   **5.10**
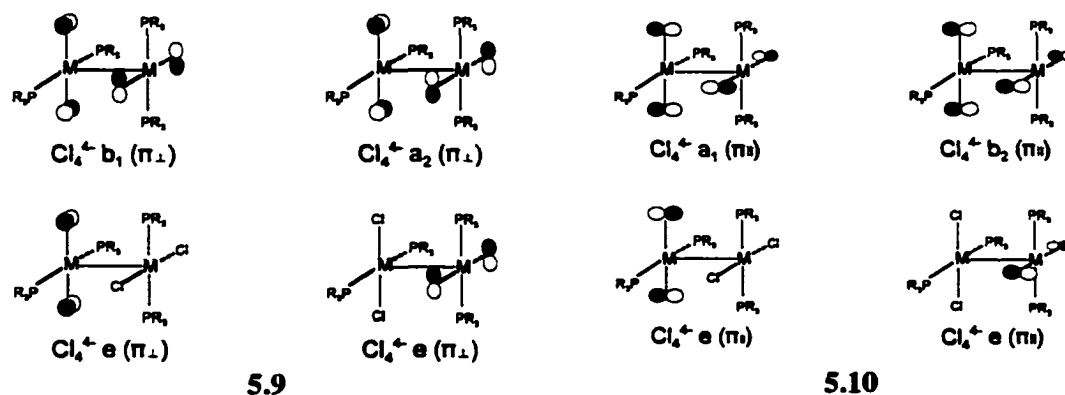
of b_1 and a_2 symmetry have the correct nodal symmetry to interact strongly with the M_2 δ and δ^*

orbitals, respectively as shown in **5.11**. The M_2 δ and δ^* interact with p orbitals from each of

$M_2(\delta)$ and Cl$_4$(b$_1$) $M_2(\delta^*)$ and Cl$_4$(a$_2$)

5.11
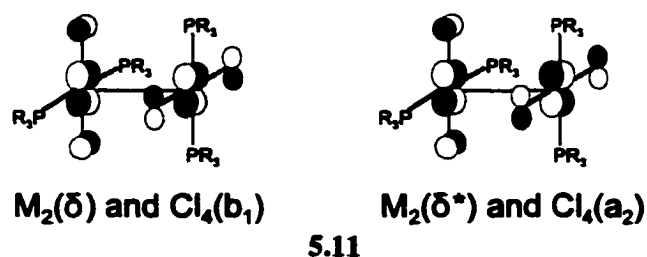
the four chlorine atoms. Similarly, the a_1 and b_2 combinations have the correct nodal symmetry

to interact with the M_2 σ and σ^* orbitals, respectively. By the same reasoning, the e(π) orbitals

also have the appropriate symmetry to interact with M-M π and π^* orbitals. The interaction

between the e(ıı) orbital set and the M_2 π orbitals are shown in **5.12**.

$$M_2(\pi_{yz}) \text{ and } Cl_4(e) \qquad M_2(\pi_{xz}) \text{ and } Cl_4(e)$$

5.12
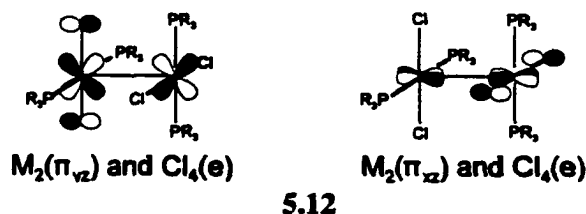
It is important to note that each M_2 π orbital can interact with the orbitals of only two chlorine

atoms. Therefore, the effects of the chlorine π combinations on the orbital character and

energies should be less for the M_2 π orbitals than for the δ and δ^* orbitals.

Although the two e-symmetry Cl_4P_4 π combination orbitals have the appropriate nodal

properties to mix together (**5.9** and **5.10**), the orbital overlap will not be extensive so the mixing

is expected to be minimal in the idealized geometry. From the standpoint of forming the best

interactions between the metal-metal π and the ligand, mixing of the e($\perp$) with the e(ıı) does

nothing to improve the interaction between the π and the ligand because the e($\perp$) is nonbonding

with respect to the π orbitals. It should also be noted that the e($\perp$) set has the correct nodal

properties to mix with the $(PMe_3)_4$ e(σ) orbitals as shown in **5.13**. In fact, given that these

$$Cl_4^{4+} \text{ e } (\pi_\perp) + (PMe_3)_4 \text{ e}(\sigma)$$

5.13
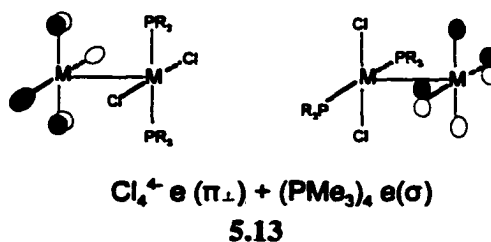
orbitals should have significant overlap with one another, it is quite likely that these orbital sets

mix together to form bonding and antibonding combinations. The bonding combination should

be a stable ligand-based orbital. The corresponding antibonding combination should be a fairly high energy combination since it is both a filled antibonding combination and non-bonding with respect to the M-M bonding orbitals.

At this point, it is important to reevaluate the applicability of the idealized geometry to describe the π-type interactions between the orbitals of the M_2 unit and the ligand set. In reality, the $\angle$M-M-L and $\angle$M-M-X are all at least ten degrees larger than the 90° angles used in the discussion above. For the most part, the overlaps do not change significantly. As it turns out, the expanded angles allow for significant mixing between the ligand combination orbitals of e symmetry because it removes the nonbonding nature of the Cl_4^+ e($\perp$) with the M_2 π as shown in

$M_2(\pi_{yz})$ and $Cl_4(e)$ $M_2(\pi_{xz})$ and $Cl_4(e)$

5.14
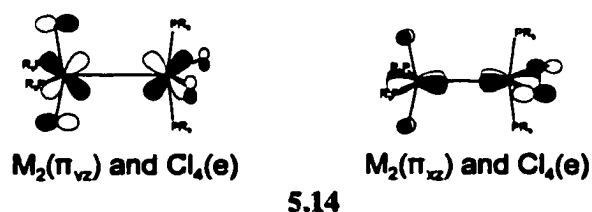
5.14. Favorable interactions with the M_2 π orbitals allow mixing of the two sets of e orbitals to some extent.

A simplified molecular orbital diagram depicting the interactions of M_2 σ, π, and δ orbitals with the ligand π combination orbitals of the appropriate symmetry is shown in Figure 5.2. The energies of the $X_4(PMe_3)_4^+$ orbitals will vary directly with the electronegativity of the halogens. The molecular orbital energies of the $M_2X_4(PMe_3)_4$ will then depend on the energy matching as well as the overlap between the orbitals of the M_2^{++} fragment and the $[(PMe_3)_4X_4]^+$ combination orbitals. In any case, the ligand combinations will definitely exert an influence on the energies and orbital makeups of the traditional metal-metal bonding orbitals.

Electronegativity considerations. Based on simple atomic electronegativities, one can make predictions concerning the relative energies of the metal-based ionizations of the $M_2Cl_4(PMe_3)_4$ series (M = Mo, W, Re). Because electronegativity decreases as one descends a group of the periodic table, the Mo-based orbitals should be more stable than the W-based orbitals. Therefore, the metal-based orbitals of $W_2Cl_4(PMe_3)_4$ should be more easily ionized than those of the molybdenum analog. For the $Re_2X_4(PMe_3)_4$ species, the metal-based orbitals are stabilized relative to the positions of the orbitals in the tungsten analog due to the increased effective nuclear charge of the Re atoms in comparison to the W atoms (the poor shielding ability of the d electrons.)[62]

Based on charge effects alone, one would expect the ionization features to be stabilized as the electronegativity of the halide atom is increased. However, the overlap effect will cause a generalized destabilization of the predominantly metal-based orbitals and, therefore, at least partially counteract the stabilization from the charge effect. Each of the molecules contains four halide atoms so one can expect both the charge and overlap effects to be fairly strong in these systems. Prior to collecting the photoelectron spectra, it is a tough call to predict which effect will be the dominant effect for these molecules in the gas phase.

Results and Discussion

He I Photoelectron spectra. The He I photoelectron spectra of $M_2Cl_4(PMe_3)_4$ (M = Mo, W, Re), collected in the 5 to 15 eV energy range, are presented in Figure 5.3. All of the spectra contain very similar ionization features in the 9 to 15 energy range, as expected for ionizations from predominantly ligand-based orbitals. The M-P σ, M-Cl σ, the Cl lone pair combinations, as well as the P-C σ and C-C σ ionizations are all expected to occur in this region of the spectrum. Each of the spectra contains a sharp ionization feature around 10 eV. From previous

photoelectron studies of chlorine-containing species, this ionization feature is tentatively

assigned to the ionization of chlorine-based orbital combinations. Previous studies of the Mo

and W analogs mistakenly assigned the M-M σ ionization to an ionization feature at

approximately 11.0 eV. Although this region of the spectrum does change upon metal

substitution, the hallmark for the ionization of metal-containing orbitals, it must be recognized

that this portion of the photoelectron spectra is expected to contain the ionizations from M-Cl σ

and M-P σ orbitals which will also shift as M is varied. For comparison, this ionization feature

is designated by a (*) in the photoelectron spectra. A major argument against this assignment is

the anomalous shift in the ionization energy of this feature from M = Mo to W. As stated

previously, the ionizations from the metal-based orbitals should be destabilized as the metal is

changed from Mo to W; the ionization feature originally assigned to the M-M σ ionization shifts

in the opposite trend, providing strong evidence that this ionization feature is not due to the

M-M σ.

He I photoelectron spectra of the halide-substituted spectra of Mo (X = Cl, Br) and Re

(Cl, Br, I) are presented in Figures 5.4 and 5.5, respectively. To allow a full comparison of the

ionization features, the photoelectron spectra are shown in the 5 to 15 eV energy range. The

substitution of the halide atoms allows a definitive assignment of the ionizations from the halide

lone pair combinations. As expected, the lone pair combinations are destabilized according to

the overall electronegativity of the halide donor (X = Cl > Br > I). Clearly, the spectral features

become more complicated as the halogen is changed from Cl to I. Given that the spin-orbit

coupling of the halogens increases as X = Cl < Br < I, it seems clear that spin-orbit splitting of

the e-type halogen-based orbitals will increase as X = Cl < Br < I. The presence of spin-orbit

splitting would account for the increased complexity of the halogen-based ionizations for X = Br

and I. The tentative assignment of the sharp ionization feature at 10 eV in the $M_2Cl_4(PMe_3)_4$ to

ionization of Cl lone pair ionizations is confirmed by the disappearance of this feature in the Br

and I substituted spectra. When X = I, the lone pair combinations are destabilized into the

region where the M_2-based ionizations occur.

To obtain more information about the ionization characteristics of the spectra in the

region containing the ionizations from the metal-based orbitals, the He I photoelectron spectra

were recollected in the 5 to 9 energy region. As a preliminary method for assigning the

ionization features, the $M_2X_4(PMe_3)_4$ spectra are presented in a stack plot with the $M_2(O_2CCH_3)_4$

spectra (M = Mo and W), Figure 5.6. Since the assignments of the $M_2(O_2CCH_3)_4$ are well-

established, preliminary assignments for the $M_2Cl_4(PMe_3)_4$ spectra can be extrapolated from

these acetate assignments. One obvious difference between the acetate analogs and the

$M_2Cl_4(PMe_3)_4$ molecules is that the metal-metal bonds between the acetates are shorter than those

between the molecules of the present study: $Mo_2Cl_4(PMe_3)_4$ (2.130 Å) and $Mo_2(O_2CCH_3)_4$ (2.093

Å). As a simple model, a shorter metal-metal distance implies greater overlap of the metal

orbitals and hence a stronger bond between the two metal atoms. The stronger the interactions

between the metal, the greater the spread between the orbitals of the traditional metal-metal

bonding scheme. The reality is much more complicated than this model, but it suffices for

providing a preliminary assignment of the ionization features in the spectra of the present

systems. Another important difference between the two molecular systems lies in the inherent

symmetries of the molecules: $M_2Cl_4(PMe_3)_4$ (D_{2d}) and $Mo_2(O_2CCH_3)_4$ (D_{4h}). Lowering the

symmetry from D_{4h} to D_{2d} allows increased mixing between the ligand and metal orbitals. The

symmetry of the molecule controls the interactions between the ligand and the orbitals of the

dimetal unit.

An initial comparison of the spectra reveals that the $M_2Cl_4(PMe_3)_4$ spectra contain an

extra ionization in comparison to the $M_2(O_2CCH_3)_4$ spectra. Given that the position of this

"extra" ionization does not change significantly when the metal is changed, this feature must be a ligand-based ionization feature. Once this feature is eliminated as a possible ionization feature of the M-M bonding orbitals, the correlation of the two systems is 1:1, providing a simple assignment of the ionization features of the present systems of study. It is certainly no surprise that the spectral shifts for the different M-M ionizations are not constant because, as developed in the preliminary discussion, each component of the M-M bond will interact with a different ligand combination and will contain varying amounts of ligand character. The metal-metal bonding orbitals of the $M_2Cl_4(PMe_3)_4$ molecules are all destabilized relative to the metal-metal bonding orbitals of the $M_2(O_2CCH_3)_4$ molecules. This is indicative of stronger interactions between the ligand orbital combinations and the metal-metal bonding orbitals in the $M_2Cl_4(PMe_3)_4$ series.

At the same time, the spread of the ionizations from the metal-metal bond decreases for the $M_2Cl_4(PMe_3)_4$ (M = Mo, W) molecules in comparison to the $M_2(O_2CCH_3)_4$ analogs, as expected for the weaker metal-metal bonds of the $M_2Cl_4(PMe_3)_4$ series. In fact, the energy difference between the δ and the $\sigma+\pi$ ionization of the molybdenum analogs is 1.29 for $Mo_2Cl_4(PMe_3)_4$ and 1.80 eV for $Mo_2(O_2CCH_3)_4$. The corresponding spread between the δ and σ ionizations for the tungsten analogs is 1.67 eV for $W_2Cl_4(PMe_3)_4$ and 2.48 eV for $W_2(O_2CCH_3)_4$. In terms of percentages, the $M_2Cl_4(PMe_3)_4$ ionization energy spreads are 72% (Mo) and 67% (W) of the spread seen for the $M_2(O_2CCH_3)_4$ analogs.

Interestingly, the $M_2Cl_4(PMe_3)_4$ series where M = Mo, W, and Re provides a self-consistent system for assigning the ionization features of the metal-metal bond. That is, the preliminary assignments achieved by direct comparison of the Mo and W analogs to the well-known acetates can be checked by analysis of the ionization features of the Mo, W, and Re analogs. The spectra of these analogs are presented in Figure 5.7. The ionization energies and

fit parameters are presented in Table 5.3. As mentioned previously, inspection of the spectra

reveals an ionization feature at ~ 8.5 eV that remains fairly constant upon changing the metal

center. Considering all of the other ionization features shift significantly upon changing the

metal, this particular ionization feature must correspond to a predominantly ligand-based

ionization. Clearly, the first ionization of the Mo and W analogs corresponds to the ionization of

the M_2 δ. The assignment of the ionization features in the framework of the traditional M-M

orbitals is further substantiated by the appearance of an extra ionization feature in the spectrum

of the rhenium analog, as expected from the population of the δ^* orbital in the $Re_2Cl_4(PMe_3)_4$

spectrum. Hence, the second ionization feature of the rhenium analog corresponds to ionization

of the δ orbital. Assignment of the M_2 σ and π ionizations follows directly from an analysis of

the shifts seen in the ionization features that have yet to be assigned. The molybdenum spectrum

contains only one peak which has not been assigned to an ionization event. The tungsten and

rhenium analogs, on the other hand, contain two ionization features that have yet to be assigned.

By a process of elimination, the σ and π ionizations of $Mo_2Cl_4(PMe_3)_4$ are assigned as being

coincident and occurring under the band at 7.68 eV. As the metal center is changed from Mo to

W to Re, the splitting between the two remaining ionization features increases from 0 eV (Mo) to

0.44 eV (W) and finally to ~0.88 eV (Re). As the metal is changed from Mo to W to Re, the two

ionizations are seen to move further apart and appear as distinct ionization features. This trend is

consistent with the assignment of the W_2 π ionization at 7.00 eV with the σ ionization following

at 7.44 eV. As expected, the σ ionization has a much more narrow bandwidth profile than the π

ionization. Then, for the rhenium spectrum, the Re_2 π ionization occurs at ~ 7.94 eV with the σ

ionzation occurring at 8.82 eV. The assignment of the the tunsten molecule presented here is

significantly different from that in the literature where the ionizations assigned to the W_2 π and

σ were originally assigned to the spin-orbit split components of the W_2 π. What was never clear

for this assignment was the origin of the extreme differences in the ionization profiles for the two spin-orbit components of the π ionization.[149] Further studies of the acetates as well as other metal-metal bonded molecules have failed to produce strong evidence for extensive spin-orbit coupling effects due to the transition metal centers. Studies of the mixed metal dimer $MoWCl_4(PMe_3)_4$ further support the assignments presented here with the splitting between the σ and π ionizations being 0.32 eV.[175] The rest of the spectrum looked identical to the spectra of the homologous analogs (Mo_2 and W_2). These spectra provide strong evidence for the M_2 σ ionization being in the same region of the spectrum as the δ and π ionizations.

In order to further analyze the effects of halogen substitution on the electronic structure of the $M_2X_4(PMe_3)_4$ series, the spectra from 9.0 to 5.0 eV are presented in Figure 5.8. For direct comparison, all of the spectra collected (with the expection of $Re_2I_4(PMe_3)_4$) are presented as a stack plot. Although the spectra become more complicated as the halogen orbitals are destabilized into the region of the spectrum containing the ionizations from the metal-metal bonding orbitals, the assignments derived for the $M_2Cl_4(PMe_3)_4$ are clearly applicable to the bromine-substituted analogs.

Although evidence of spin-orbit coupling was not found in the photoelectron spectrum of $W_2Cl_4(PMe_3)_4$, the larger spin-orbit coupling constant of atomic rhenium provides allows for the resolution of the spin-orbit split components of the π ionization. For comparison, reported estimates of the spin-orbit coupling constants of Mo, W and Re are 0.08 eV, 0.19 eV, and 0.26 eV, respectively.[176] Although these values are crude, they do reveal the expected trend: $\lambda_{Mo} <$ $\lambda_W < \lambda_{Re}$. Under the effects of spin-orbit coupling, the symmetry is reduced from D_{2d} symmetry so that all ionizations can be described by one of two symmetry types: $E_{1/2}$ and $E_{3/2}$. Under the influences of spin-orbit coupling, extensive orbital mixing is likely. Since the photoelectron spectra reproduce the expected electronic structure of the metal-metal bonding orbitals, any

influences of spin-orbit coupling must be subtle. Spin-orbit effects, if an important

consideration, should split the degenerate π orbital into two components: $\pi_{3/2}$ and $\pi_{1/2}$. In order

to probe subtle effects in the band profile, photoelectron spectra must be collected in the energy

window containing just band profile known to contain the ionization from the π orbital. The

photoelectron spectra, focusing solely on the region containing the π ionization, is presented in

Figure 5.9. A closeup spectrum of the π-ionization region of the $Re_2Cl_4(PMe_3)_4$ provides direct

evidence of the importance of spin-orbit coupling, where the π ionization is split into the $e_{3/2}$ and

$e_{1/2}$ components which are separated by 0.30 eV. Unfortunately, the corresponding region of

$Re_2Br_4(PMe_3)_4$ does not show similar evidence of spin-orbit splitting of the π orbitals. Hence,

we cannot make any arguments based on the spin-orbit splitting of the π orbitals as the halogen

is changed from X = Cl to Br. However, not seeing the spin-orbit splitting of the Re_2 π

ionization does imply that the amount of metal character present in the π ionization decreases as

X = Cl > Br. Due to the complexity of the $Re_2I_4(PMe_3)_4$ spectrum, complete assignment of the

ionization features is not possible at this time. The iodine lone pair combinations are all

occurring on top of the ionizations from the π, and σ orbitals. In addition the spin-orbit splitting

of iodine itself results in extensive splitting of each iodine lone pair combination. The net effect

is the spectrum in this region contains overlapping ionizations from numerous orbitals. Looking

back at the spectrum of the $W_2Cl_4(PMe_3)_4$ molecule, we find no evidence for this same type of

splitting so we conclude that the effects of spin-orbit coupling on the W-W π ionization must be

a small effect that cannot be seen at the resolution of this experiment. It is important to note the

the spectra contain direct evidence that the effects of spin-orbit coupling due to the halogen alone

become an important consideration when the halogen is changed from chloride to bromide or

iodide. In fact, the spin-orbit coupling seen in the ionizations due to the iodide lone pair

combinations becomes a dominant feature of the spectra. Naturally, spin-orbit coupling only

splits ionizations from orbitals that are degenerate in the absence of spin-orbit coupling.

Although the Re-Re σ and π ionizations of the $Re_2I_4(PMe_3)_4$ are not readily assignable,

the positions of the δ and δ^* ionizations, the two low-lying ionizations, occur as well-separated

ionizations. In order to obtain the exact positions and study the band-widths of these ionizations,

photoelectron spectra were recollected in the energy region containing the δ and δ^* ionizations

(5 to 7 eV). These spectra are presented in Figure 5.10. The positions and bandwidths for the

$Re_2X_4(PMe_3)_4$ analogs are reported in Table 5.3. For each molecule studied, the band profile for

the δ^* ionization is more slightly more narrow than the corresponding δ ionization. In the

simple molecular orbital model, ionization of the δ orbital results in a metal-metal order of 2.5,

while ionization of the δ^* orbital results in a metal-metal bond order of 3.5. The different band

profiles seen for these ionization features point to the band intensity being influenced by factors

more complicated than the simple bond order of the metal-metal bond. The more narrow band

widths of the δ^* ionization bands in comparison to the δ bands indicates that the equilibrium

bond distance changes that occur upon ionization of the δ^* orbitals are slightly less than those

that occur upon removal of an electron from the δ orbital. As established previously, the change

in formal oxidation state that accompanies the ionization of an orbital is an important factor in

determining the amount of interaction that occurs between the orbitals of two metal atoms. As

the formal oxidation state of the metal atom increases, the orbitals of the metal undergo a

contraction and are less available for bond formation, etc. Previous studies have established that

the effects of formal oxidation state change will be similar for the ionization of both the δ and δ^*

orbitals.[177-180] Upon ionization of the δ and δ^* orbitals, numerous molecular vibrations

(predominantly ligand-based) will be activated, and these vibrational modes will also lead to

ionzation band broadening.[153,154,177,181] Attempts to obtain vibrational fine structure in the δ and

δ* were not successful, implying that the vibrational fine structure is unresolved at the resolution of the experiment (18 meV). Interestingly, the slightly narrower ionization band seen for the δ* in comparison the δ is consistent with removing an electron from an antibonding orbital as opposed to a bonding orbital.

A quick perusal of the ionization energies of the δ* and δ for the $Re_2X_4(PMe_3)_4$ series is that the orbitals become more difficult to ionize as the electronegativity of the halide atom decreases. This same trend is seen in the energies of the δ orbital for $Mo_2X_4(PMe_3)_4$ (X = Cl and Br). The origins of this unusual trend will be discussed in detail later.

Studies with He II and Ne I photon sources. In order to confirm the assignments of the ionization bands, photoelectron spectra were recollected using Ne I and He II photon sources. According to the Gelius model of photoionization cross-sections, the intensity of an ionization band is directly dependent upon the photon energy as well as the atomic character of the particular molecular orbital. Although molecular cross-sections are more complicated than this model predicts, the Gelius model can still be used to identify the predominant atomic character of the molecular orbital from which the electron was ionized. Yeh and Landau have compiled an extensive list of calculated atomic ionization cross-section values.[77] The values pertinent to this study are presented in Table 5.4. One notable error in the calculated cross-sections is the neglect of the Super-Koster-Kronig transitions that are known to occur for second and third row transition metal atoms.[182] These absorption processes feed intensity to ionizations from molecular orbitals containing metal nd character, thus providing a resonant enhancement of the observed intensity. By the same token, ionizations from halogen-based orbitals are predicted to grow in intensity when the photon source is changed from He I to Ne I and drop dramatically in intensity when He II is used as the photon source. Different photon sources, particularly the He II photon source, should be of great use in validating the experimental assignments of the

ionization bands. Although the Ne I photoelectron spectroscopic experiment is much less time-consuming than the He II experiment, the relative intensities obtained from the Ne I experiment are not well-understood at this time.[32] Nevertheless, the experiment does in fact allow one to determine the positions of the ionizations from ligand-based orbitals. Therefore, the Ne I and He II photoelectron spectra were collected in the 5 to 9.5 eV energy range. In addition, the He II photoelectron spectra were also collected from 5 to 15 eV range in order to include the ionization feature assigned to the Cl lone pair combinations. The band areas obtained for the Ne I, He I and He II spectra are presented in Table 5.2.

$Mo_2Cl_4(PMe_3)_4$. In order to demonstrate how changing the photon source can help confirm the experimental assignment of photoionization bands, the He I and He II spectra collected in the 5 to 15 eV energy range are presented in Figure 5.11. The changes in the spectral intensities are dramatic with the metal-based ionizations growing significantly with respect to the ligand-based ionizations. From these spectral changes, the spectral assignment of the Mo-Mo δ, π, and σ ionizations is confirmed. In addition, the position of the chlorine lone pair combinations is also confirmed from the He II studies. Interestingly, the ionization originally assigned to the Mo-P (σ) ionization drops dramatically in intensity, indicative of significant halogen character in this molecular orbital.

In order to obtain a quantitative evaluation of the intensity changes that occur in the photoelectron spectrum of $Mo_2Cl_4(PMe_3)_4$ as the photon source is changed, the spectra obtained in the 9.5 to 6.0 eV range are presented in Figure 5.12. It is clear that the ionization originally assigned as the Mo-P σ at 8.39 eV combination must contain substantial amounts of halogen character. In fact, the cross-section changes suggest this ionization originates from an orbital that is predominantly halogen in character, Table 5.2. This is not a surprise considering the P(σ) e orbitals were shown by a symmetry analysis, see 5.13, to have the appropriate nodal properties to

interact strongly with the e($\perp$) combination. Additionally, the σ and π orbitals must contain less

metal character than the δ orbitals because the He II band intensity of the ($\sigma+\pi$) ionization band

drops by 39 % relative to the band intensity of the δ ionization. Interestingly, the relative

intensities obtained in this study do not quantitatively agree with those of the previously

published spectra. Although the discrepancy does not change the assignment of the ionizations

bands, it is, nevertheless, a concern. The major difference between the previous He II

spectroscopic study and the present one is that the e(P,Cl) ionization does not drop as

significantly under He II radiation in the literature study (-60%) as it does in the present study

(-84%). Since these compounds are known to lose PMe_3 when the heated for extended periods of

time, one explanation for the different relative intensities in the two studies is that the literature

spectrum is contaminated by the presence of free phosphine. Given that the phosphorous lone

pair ionization of PMe_3 lies at 8.69 eV, this explanation becomes even more plausible. Further

casting doubt on the accuracy of the previous photoelectron studies, the relative intensities of the

ionization features in the He I spectra were not self-consistent for spectra collected in different

energy regions. The relative intensities of the ionization features should not depend on the

energy region in which the spectrum is collected. If the He I relative areas are questionable, one

must necessarily question the band intensities from the He II studies and the subsequent intensity

changes that occur in the spectra collected with the different photon sources. In order to

establish the reproducibility of the present studies, the photoelectron spectra were collected on

multiple days.

$\underline{Mo_2Br_4(PMe_3)_4}$. As seen in Figure 5.13, the He II and Ne I photoelectron studies of the

$Mo_2Br_4(PMe_3)_4$ molecule also support the experimental ionization band assignments obtained

from comparing the spectra of the Mo, W, and Re analogs. Of particular interest is the similarity

seen in the band intensity changes that occur between He II and He I for the chloride and

bromide analogs. Specifically, the relative band intensities of the δ band and the (σ+π) band are identical to within 2 % (Table 5.2). The amount of metal character in the ionizations does not change markedly with the change in halide. Interestingly, the ligand orbital designated as e(P σ; Br π⊥) does not shrink as much as the corresponding ionization of the chlorine-substituted analog when a He II photon source is used. Analogously, this band does not grow as strongly when a Ne I photon source is used. The atomic cross-section must not drop as significantly as the calculated value might suggest because the intensity changes seen in the spectra are less than those seen for the chloride analog. The variable photon studies do support the assumption that the e(P σ; Br π⊥) ionization contains a substantial amount of halogen character because the relative intensity changes seen in the spectra for this ionization closely match the changes seen for the spectral features attributable to the ionizations from the Br lone pair combinations that occur from 9 to 11 eV.

W₂Cl₄(PMe₃)₄. The Ne I, He I, and He II spectra of $W_2Cl_4(PMe_3)_4$ are shown in Figure 5.14. Once again, the metal-based orbitals grow under He II irradiation in comparison to the ligand-based ionization band. The intensity of the ionization from the δ orbital grows by 24% and 30% in comparison to the intensities of the ionizations from the π and σ orbitals, respectively, when a He II photon source is used in place of the He I source (Table 5.2). This is clearly indicative of more halogen character mixing into the π and σ orbitals in comparison to the δ orbital. The cross-section changes imply that the σ orbital of $W_2Cl_4(PMe_3)_4$ contains more ligand character than the π orbital, but the overlapping nature of these ionization features does not allow any definitive measure of the cross-section changes. As expected, the ionizations from the π and σ orbitals grow slightly (around 10%) relative to the δ when the photon source is Ne I instead of He I. The intensity of the ionization erroneously assigned to the W-P σ ionization in the original work shrinks substantially when the photon source is changed from He I to He II,

indicating ionization from a molecular orbital with significant chlorine character. As expected for the ionization of an orbital that contains a substantial amount of chlorine character, this ionization feature grows under the influence of a Ne I photon source. Although the present He II spectra agree qualitatively with those collected previously, the relative areas do differ by as much as 16% in comparison to the present studies.[149] The most disturbing aspect of the previously published spectra is the fact that the relative intensities of the bands collected in different energy regions are in no way self-consistent as was seen for the previous studies of $Mo_2Cl_4(PMe_3)_4$. The previously published spectra must be viewed with extreme caution especially for interpreting changes in the relative intensities of bands when photon energy is changed. The photoelectron spectra for $W_2Cl_4(PMe_3)_4$ reported here are both self-consistent and reproducible, although the sample does tend to decompose under the conditions of the He II experiment.

$Re_2X_4(PMe_3)_4$ (X = Cl, Br). The Ne I, He I, and He II spectra of the $Re_2X_4(PMe_3)_4$ spectra (X = Cl, Br) are shown in Figure 5.15 and Figure 5.16, respectively. Although the He I photoelectron spectrum of $Re_2Cl_4(PMe_3)_4$ was reported previously, the spectra were assigned strictly based on comparisons to the Mo and W analogs. The most direct method for determining the position of the σ ionization lies in comparing the photoelectron spectra of the molecule obtained using different photon sources, particularly the He II source. Hence, the present studies are essential to validating the ionization band assignments. For both the Cl and Br derivatives, the relative areas are referenced to the δ^* area. As expected, ionizations from orbitals predominantly metal in character grow in intensity under the influence of He II radiation. The growth of the high energy shoulders at 8.86 eV and 8.70 eV respectively, for the Cl and Br analogs in the He II spectra supports the assignment of this ionization feature to the Re-Re σ. A more detailed analysis of the He I and He II spectra demonstrates that the δ orbital of both analogs grows in comparison to the δ^* orbitals, indicating that the δ orbitals contains more metal

character than the δ* orbitals. Interestingly, the ligand-based ionizations located at 8.46 eV and 8.36 eV, respectively, in the photoelectron spectra of the Cl and Br analogs do not undergo the same drastic changes seen in the spectra of the molybdenum and tungsten analogs. This is not surprising because the ionizations overlap extensively in this region. If this ionization band overlaps extensively with metal-based ionizations, it will not decrease in intensity nearly as much as an isolated ligand-based band under the influence of a He II photon source. Nevertheless, the trend is quite clear that the e(X, P) ligand-based ionizations decrease significantly, Br (-30%) and Cl (-23%) when the photon source is changed from He I to He II.

Computational studies. In order to further probe the electronic structures of the $M_2X_4(PMe_3)_4$ analogs, density functional studies were initiated. Since all of the components of the M-M bonding framework have now been experimentally identified, computational studies provide a unique opportunity to test the ability of density functional calculations and Fenske-Hall calculations to reproduce the experimentally-determined electronic structures. In order to optimize the efficiency of the computational studies the PMe_3 ligands were modeled with PH_3 ligands. Although the electronic structures of the two ligands are not equivalent, the PH_3 certainly models the strong donor ability of the PMe_3 molecule. To establish that the $M_2X_4(PH_3)_4$ analogs are acceptable models of the electronic structure of the $M_2X_4(PMe_3)_4$ molecules, density functional calculations were first run on the full molecule, $Mo_2X_4(PMe_3)_4$, where X = Cl and Br. Table 5.5 contains the calculated orbital energies and orbital makeups of the δ, π, and σ orbitals the $Mo_2X_4(PMe_3)_4$ molecules. From these calculations it is apparent that the density functional calculations model the electronic structure of these molecules quite well. Significantly, the σ and π orbitals are calculated to be separated by only 0.03-0.07 eV in agreement with the assignment of the ionizations from these two orbitals as occurring under the same band in the photoelectron spectra of the molecules. Although the Fenske-Hall energies of the δ orbitals of

the chloride and bromide analogs are good in comparison to the experimental values, the Fenske-Hall calculations do not model the electronic structure of the molecules as well as the density functional calculations. Unfortunately, the Fenske-Hall method places too much halide character in the M-M σ and places a ligand-based orbital in between the σ and π. Nevertheless, the Fenske-Hall calculations clearly reveal the same orbital interactions that are seen in the ADF calculations.

For comparison, the calculated orbital energies and orbital compositions of the model complexes $Mo_2X_4(PH_3)_4$ are presented in Table 5.6. The calculated electronic structures of the $M_2X_4(PMe_3)_4$ and $M_2X_4(PH_3)_4$ are extremely similar. Orbitals plots of the filled components of the M-M bond of the $Mo_2Cl_4(PMe_3)_4$ and $Mo_2Cl_4(PH_3)_4$ are presented in Figures 5.17 and 5.18, respectively. These orbital plots reveal extensive interactions between the Cl p orbitals and the components of the M-M bond. Not surprisingly, the interactions shown are those predicted from the simple symmetry analysis, and they are not significantly changed when the methyl groups of PMe_3 are modeled as hydrogens. As expected from the symmetry analysis, the e($P\sigma$) orbital combination does mix strongly with the Cl_4 ($\pi\perp$) as shown in Figure 5.18. Interestingly, the calculated orbitals energies of the $Mo_2X_4(PH_3)_4$ model the experimental electronic structure as well or better than those from the $Mo_2X_4(PMe_3)_4$ calculations. Hence, calculations for the tungsten and rhenium analogs were run as $M_2X_4(PH_3)_4$ models. The present results compare favorably with previous calculations on the $M_2X_4(PH_3)_4$ molecules.[183-187] It is important to note that the previous calculations on the $Re_2Cl_4(PH_3)_4$ were completed before the crystal structure of $Re_2Cl_4(PMe_3)_4$ was obtained so the bond distances and angles used in the calculation are incorrect.[178] The calculated energies and orbital compositions of the $W_2Cl_4(PH_3)_4$ are presented in Table 5.6, and the calculated energies of $Re_2X_4(PH_3)_4$ (X = Cl, Br, and I) are presented in Table 5.7. As was the case for the molybdenum analogs, the Kohn-Sham orbital energies of

$W_2Cl_4(PH_3)_4$ and the $Re_2X_4(PH_3)_4$ ($X = Cl$, Br, I) closely match the relative spacing seen in the

experimental ionization energies. The ΔE_{SCF} values for the $M_2X_4(PH_3)_4$ series accurately

reproduce the experimental ionization energies. Of particular interest are the calculated

ionization energies of the metal-metal σ and π for the $Mo_2X_4(PH_3)_4$ series because the

ionizations from these orbitals are computed to be nearly degenerate as seen in the photoelectron

spectra of these molecules. The calculated values for the σ and π ionizations of $M_2Cl_4(PH_3)_4$

separate as the metal is changed from Mo (0.02 eV) to W (0.50 eV) to Re (0.66 eV). The actual

separation of the σ and π ionizations, as determined by photoelectron spectroscopy, are 0.44 eV

and 0.90 eV for $M = W$ and Re, respectively. The density functional computational results

support the experimentally-determined assignments. For direct comparison to the density

functional calculations, results from Fenske-Hall molecular orbital calculations are also

presented. The calculated orbital makeups are consistent between the two computational

methods and predict significant contributions from the halide p orbitals to the traditional metal-

metal bonding orbitals. The Fenske-Hall method overestimates the separation of the molecular

components of the metal-metal bond. In order to facilitate the comparison of the Fenske-Hall

energies with the density functional energies and the experimental ionization energies, the orbital

energies are scaled. The scaling procedures are described in detail in the experimental section.

From the results of these calculations, the Fenske-Hall method effectively models the electronic

structure of the $M_2X_4(PMe_3)_4$ molecules. Unfortunately, the position of the e[$X(\perp)$ - P(σ)]

symmetry combination is calculated to be less stable than is seen experimentally for the

molecules. This is particularly problematic for the $Mo_2X_4(PH_3)_4$ molecules, where the Mo-Mo σ

ionization is calculated to lie below the highest occupied ligand combination. Nevertheless, the

Fenske-Hall calculations still effectively model the components of the metal-metal bond. All of

the computational studies support the experimentally-determined assignments of the ionization

bands in the photoelectron spectra.

The Inverse Halogen Effect. Now that the spectral features corresponding to the

ionization of the filled orbitals of the M-M bond framework have been identified, we can take a

closer look at the changes that occur in the photoelectron spectra as the halide donor is changed.

While electronegativity considerations would lead one to predict that the ionization energies

should be stabilized as the electronegativity of the constituent atoms increases, the observed

ionization energies of the δ orbital of the $Mo_2X_4(PMe_3)_4$ series display the opposite trend: Cl

(6.39 eV) < Br (6.50 eV). In addition, the energy of the $(\sigma+\pi)$ band also shifts in opposition to

the electronegativity trend: Cl (7.71 eV) < Br (7.68 eV). However, considering the uncertainty

of the ionization band positions is ±0.02 eV, the reported ionization energies of the $(\sigma+\pi)$ bands

are essentially degenerate in the spectra of the bromide and chloride analogs. Nevertheless, the

trend seen in the ionization energies of these bands do not correlate with the simple charge effect.

Unfortunately, attempts to obtain the photoelectron spectrum of $Mo_2I_4(PMe_3)_4$ proved

unsuccessful so the trend can not be extended to the iodide analog. In order to confirm that this

trend is not an anomaly, we need to find another similar system in which the halides can be

substituted. The ideal case would be to have a system where at least three different halide

analogs can be studied.

The $Re_2X_4(PMe_3)_4$ series (X = Cl, Br, I) fits the desired criterion for further exploration

of the effects of halide substitution on the ionization energies of the M-M bonding (and

antibonding) orbitals. In addition to providing information on the halide dependence of the σ, π,

and δ components of the metal-metal bond, the study of the rhenium analogs provides

information regarding the halide dependence of the δ^* orbital energy. The photoelectron spectra

collected in the region of the δ and δ^*ionizations clearly show that the δ and δ^* ionizations shift

in opposition to the electronegativity trend. As was the case for the $Mo_2X_4(PMe_3)_4$ series, the

energy of the highest occupied orbital shows the greatest sensitivity to the nature of the halide

donor. As the halide donor is changed from Cl to Br to I, the δ^* ionization shifts from 5.65 eV

to 5.71 eV to 5.80 eV, clearly indicating that the charge effect is not responsible for the energy

trend. The corresponding trend in the position of the δ ionization for the $Re_2X_4(PMe_3)_4$ series is

X = Cl (6.49 eV) < Br(6.53 eV) < I(6.56 eV). Interestingly, the π and σ ionizations shift in

accordance with the expected trends based on electronegativity. (Unfortunately, the energies of

these ionizations are not available from the $Re_2I_4(PMe_3)_4$ spectrum due to the complexity of the

region in which these ionizations are expected to occur.) To illustrate the inverse halogen effect,

the δ^* and δ ionization energies for the $Re_2X_4(PMe_3)_4$ series are plotted versus the Pauling

electronegativities of the halogen atoms in Figure 5.20. For the ionization of the δ^* and δ

orbitals, the inverse relation between ionization energy and electronegativity of the halogen atom

is displayed. In fact, the relationship between the δ^* ionization energy and the electronegativity

of the halogen atom is perfectly linear ($R^2 = 1$), and the relationship between the δ ionization

energy and the halogen is also quite linear ($R^2 = 0.96$). These linear relationships allow an

estimate of the ionization energies of the δ^* and δ energies of the hypothetical molecule

$Re_2F_4(PMe_3)_4$. The linear regression analysis yields values of 5.40 eV and 6.38 ±0.01 eV for the

energies of the δ^* and δ ionizations, respectively.

As mentioned previously, the inverse halogen effects seen in the ionization energies of

the δ^* orbitals of the $Re_2X_4(PMe_3)_4$ molecules and the δ orbitals of the $Mo_2X_4(PMe_3)_4$ correlate

with the inverse halide orders obtained for the oxidation potentials of these molecules measured

in CH_2Cl_2. The measured oxidation potentials for the $Mo_2X_4(PMe_3)_4$ series are 0.47 V and 0.59

V for X = Cl and Br, respectively. Analogously, the oxidation potentials of the $Re_2X_4(PMe_3)_4$

analogs, referenced to Ag/AgCl in CH_2Cl_2, show the inverse halogen order with the measured

oxidation potentials being -0.23 V and -0.11 V for the oxidation of the Cl and Br analogs, respectively. Significantly, these trends also exist for the oxidation potentials measured in THF, indicating the observed trend is most likely not due to solvent effects. Interestingly, electrochemical studies have shown the inverse halide order remains present when the phosphine ligand is changed.[152]

Evidence of the inverse halide order is also seen in other spectroscopic studies of the $M_2X_4(PMe_3)_4$ analogs. In particular the δ-δ* transition energies of the $Mo_2X_4(PMe_3)_4$ series (X = F, Cl, Br, I) as well as the $[Re_2X_4(PMe_3)_4]^+$ (X = Cl, Br) series show a distinct dependence on the nature of the halide donor. For the $Mo_2X_4(PMe_3)_4$ series, the δ-δ* transition shifts as X = F > Cl > Br > I.[188] The δ-δ* transition energies of the $[Re_2X_4(PMe_3)_4]^+$ series correspond to 0.90 eV and 0.87 eV for X = Cl and Br, respectively.[148] In the photoelectron spectrum, the energy difference between the δ and δ* orbitals is 0.84 eV and 0.82 eV for X = Cl and Br, respectively.

One must have a thorough knowledge of the charge and overlap effects if one is to understand the bonding between two orbitals. In essence, the degree to which two orbitals (atomic or otherwise) will interact depends on the energy matching of the two orbitals and the overlap between the two orbitals. For the bonding in the $M_2X_4(PMe_3)_4$ series, consideration of the relative importance of the charge and overlap effects provides strong evidence against the metal-(d)-to-halide(d) backbonding explanation of the inverse halide order. As a consequence of this filled-filled interaction, the metal-based orbitals are π-antibonding with respect to the ligand. This antibonding interaction serves to destabilize the orbitals of the metal-metal bond with the degree of destabilization being directly dependent on both the overlap and the energy matching. In essence the inverse halogen effect is simply a consequence of the known π-donor abilities of the halogens which increases as X = I < Br < Cl < F.[189-191]

Other studies of transition metal systems containing halide ligands have also produced

evidence for the inverse halide order. Of particular relevance to the present study, Hascall and

coworkers recently found that the ease of oxidative addition of $M(PMe_3)_4X_2$ (M = Mo, W; X = F,

Cl, Br, I) to $M(PMe_3)_4H_2X_2$ increases as X = I < Br < Cl < F.[192] In the course of the studies on

these molecules, computational studies attributed the inverse halide order to the greater π-donor

abilities of the lighter halogens. Electrochemical studies of the Cp*Fe(dppe)X (X = F, Cl, Br, I)

series also follow the inverse halide order.[193,194] Other systems that have produced an inverse

halide order in the electrochemical oxidation and reduction potentials include: $Cr(CO)_5X^-$,[195]

$CpMo(NO)X_2$,[196] $Cp*Mo(NO)X_2$,[196] mer-$Mn(CO)_3(L-L)X$,[197] $Mn(PhNC)_5X$,[198] $CpFe(CO)_2X$,[199,200]

$Rh(CO)(PPh_3)_2X$,[201] $WX(CO)MeC\equiv CMe)Tp'$,[202] and $CpMo(CO)_{3-n}(PR_3)_nX$.[203,204] Much

confusion has existed concerning whether the inverse halide order is due to halogen π-

acceptance by the unfilled d orbitals of the halogen[204] or the more straightforward filled-filled

interaction between the filled metal orbitals and the filled halogen p orbitals.[192] Unfortunately,

none of these studies were performed in the gas-phase so solvent effects cannot be ruled out as a

contributing factor to the inverse halide order. One thing that all of these systems have in

common is that the HOMO of the molecule corresponds to a filled metal orbital that is

antibonding with respect to the halogen (a filled-filled interaction). Interestingly, the inverse

halide order has not been seen in the photoelectron spectroscopic studies of $Mn(CO)_5X$ (X = Cl,

Br, I),[205] $Re(CO)_5X$ (X = Cl, Br, I),[206] $CpRe(NO)(CO)X$ (X = Cl, Br, I),[207] $Cp*Re(NO)(CO)X$ (X

= Cl, Br, I),[207] or $Cp*Re(NO)(PPh_3)X$ (X = Cl, Br, I).[207] Of course, all of the above systems

contain strong π-accepting ligands that serve to remove electron density from the metal center.

This, in turn, reduces the filled-filled interaction between the filled metal orbitals and the filled

halogen orbitals because the lowered electron density at the metal center results in poorer overlap

between the metal and halide orbitals.

Further insight into the origin of the inverse halogen effect can be found in the computational studies of the $M_2X_4(PH_3)_4$ molecules. Although the computational studies have been discussed in terms of their support of the assignments of the photoelectron spectra, no discussion has been made concerning the dependence of the calculated orbital energies on the nature of the halogen. In fact, the Kohn-Sham orbital energies do indeed show an inverse halide order. The energy of the δ orbital of $Mo_2X_4(PH_3)_4$ shifts from -4.14 eV to -4.30 eV when Cl is replaced by Br. Similarly, the same trend is reflected in the calculated energy of the δ^* orbital of $Re_2X_4(PH_3)_4$, where the orbital energies are: -3.27 eV (Cl), -3.36 eV (Br), and -3.73 eV (I). Although the basis sets used in the density functional computational studies included the unfilled valence orbitals on the halogen atoms, they were not found to contribute significantly to the molecular orbital makeups.[208] The inverse halide order is also reproduced in the δ^* orbital energies of the $Re_2X_4(PH_3)_4$ series calculated with by the Fenske-Hall method, where the orbital energies are 4.92 eV, 4.94 eV, and 5.29 eV for X = Cl, Br, and I, respectively. The Fenske-Hall calculations are of particular significance because the calculations were run with basis sets that did not include unfilled d orbitals on the halogen ligands. The source of the inverse halide order displayed in the Fenske-Hall calculations cannot be attributed to M(d)-to-X(d) backbonding. Additional calculations using basis sets containing d orbitals on the halogen atoms did not change the trend seen in the orbital energies and the atomic makeups also remained constant.[209]

To facilitate a more complete understanding of the inverse halide order, further computational studies were performed in terms of the molecular fragments: M_2^{4+} and $X_4(PH_3)_4^{4-}$. Instead of thinking about the overlap of the atomic orbitals, the focus must now be placed on the overlap of the molecular fragment orbitals. In addition, to expand the range of molecules studied, the $Mo_2F_4(PH_3)_4$ was included in the computational studies. The $Mo_2F_4(PH_3)_4$ molecule is of interest because the fluorine atoms do not have unfilled d orbitals available for interaction

with the metal. The computational results related to the filled components of the metal-metal

bond for these molecules are presented in Table 5.8. For the $Mo_2X_4(PH_3)_4$ series, the energy of

the δ orbital increases as X = F < Cl < Br, indicative of the inverse halide effect. In addition, the

orbital compositions, in terms of the M_2^{++} fragment orbitals interacting with the $X_4(PH_3)_4^+$

orbitals, are those expected from simple symmetry considerations, clearly validating the model

developed using simple group theory. For the δ orbital of the $Mo_2X_4(PH_3)_4$ molecules, the

overlap of the ligand b_1 fragment with the M_2 δ increases as X = F (0.143) > Cl (0.127) > Br

(0.113). Similarly, for the δ^* orbital of the $ReX_4(PH_3)_4$ series, the overlap of the ligand a_2

combination with the Re-Re δ^* increases as X = Cl (0.189) > Br (0.117) > I (0.0981). For

comparison, the results from transform Fenske-Hall calculations based on the M_2^{++} and

$X_4(PH_3)_4^+$ fragments are presented in Table 5.9. The results are in agreement with those from

the density functional studies. Given that the δ^*, δ, π, and σ orbitals of the $M_2X_4(PH_3)_4$

molecules all contain significant halogen character mixed in an antibonding fashion with the

metal orbitals, it follows that there are also a set of orbitals that have halogen character mixed in

a bonding fashion with the metal orbitals. The bonding combinations will be predominantly

ligand-based orbitals. The splitting between the bonding and antibonding combinations is

dependent on the overlap of the ligand orbital combination with the M_2 orbital combination of

the appropriate symmetry. Hence, as illustrated in Table 5.10 for the δ^* and δ orbitals, the

splitting of the ligand- and metal-based δ^* and δ orbitals increases as F > Cl > Br > I. The

bonding in these systems can be understood in terms of the basic charge and overlap effects

without resorting to the invocation of π-acceptance by the halogen atoms.

Energy Decomposition Analysis. The bonding in Fenske-Hall calculations can be

readily analyzed to determine the energetic contributions that determine the overall molecular

orbital energy. The Fenske-Hall molecular orbital energies are calculated according to equation

(5.5), were c_i and c_j are the coefficients of the fragment orbitals in the molecular orbital of

$$\varepsilon_i = \sum_i c_i^2 F_{ii} + 2 \sum_{i>j} c_i c_j F_{ij} \quad (5.5)$$

interest and F_{ij} is the Fock matrix element describing the interaction of the two fragment orbitals. The first term in equation (5.5) describes the diagonal contributions to the molecular orbital energy, while the second term accounts for the off-diagonal contributions to molecular orbital energy. The diagonal energy term reflects the one-center contributions of the orbital character, while the off-diagonal terms reflect the overlap effects.

In order to obtain a firm understanding of the contributions to the δ^* energy, an energy decomposition analysis of the bonding in $Re_2X_4(PH_3)_4$ was initiated in terms of interacting Re_2^{4+} and $X_4(PH_3)_4^{4-}$ fragments. Since all overlap effects are by definition off-diagonal effects in Hartree-Fock theory, one cannot ascertain the importance of the bonding (and antibonding) interactions between the ligands and the dimetal unit in determining the absolute energy of the molecular orbital without analyzing the off-diagonal contributions to the orbital energy. From the energy decomposition analysis, the relative contributions of the charge and overlap effects to the overall molecular orbital energy will be clearly defined.

Focusing first on the $Re_2Cl_4(PH_3)_4$ δ^* energy (Table 5.11), the diagonal contribution to the total energy is -8.02 eV. The vast majority of this energy results from the Re_2 δ^* contribution (-5.71 eV) and the a_2 $\pi(\perp)$ combination of Cl lone pairs (-2.19 eV). Nevertheless, two other ligand orbital combinations contribute significantly to the diagonal energy. Both of these orbitals are a_2 combinations of P-H σ bonds: one is the filled bonding combination and the other is the unfilled antibonding combination. The a_2 bonding combination of P-H σ orbitals contributes -0.31 eV to the total diagonal energy while the P-H σ^* contributes +0.22 eV to the diagonal energy.

Considering the fact that the total orbital energy is only -4.91 eV, it is clear that the off-diagonal interactions must play a pivotal role in determining the overall orbital energy. Not surprisingly, the majority of the off-diagonal energy comes from the antibonding (filled-filled) interaction between the Re-Re δ^* orbital and the a_2 $\pi(\perp)$ combination, resulting in a net destabilization of +3.09 eV. The contribution from the antibonding interaction between the Re-Re δ^* and the bonding combination of P-H σ orbitals, +0.65 eV, is completely cancelled by the energy contribution from the bonding interaction between the P-H σ^* combination and the Re-Re δ^*.

For the $Re_2X_4(PH_3)_4$ analogs, the total diagonal energy contributions are only -7.75 eV and -7.52 eV, respectively, for the bromide and iodide analogs. The major contributions to the diagonal energies of the $Re_2X_4(PH_3)_4$ analogs (X = Br and I) come from the Re_2 δ^* and the a_2 $\pi(\perp)$ combinations of halogen p orbitals. The P-H σ combinations are minor contributors to the overall diagonal energies. It is clear that the off-diagonal energy contributions are significant factors in determining the total orbital energies because the total orbital energies are only -4.94 eV and -5.29 eV, respectively, for the bromide and iodide analogs. The off-diagonal contributions can be traced to the antibonding interaction between the Re_2 δ^* and the a_2 $\pi(\perp)$ combination of halogen p orbitals. This antibonding interaction contributes +2.78 eV and +2.18 eV to the total orbital energies of the bromide and iodide analogs, respectively. Again, both the bonding and antibonding P-H σ combinations interact with the Re_2 δ^*, but the interactions effectively cancel one another.

Comparing the results for the $Re_2X_4(PH_3)_4$ analogs, the charge and overlap contributions are clear. As expected from the electronegativities of the halogen atoms, the diagonal energy contributions increase as X = I < Br < Cl. However, the destabilization provided by the antibonding interaction between the a_2 $\pi(\perp)$ combination and the Re_2 δ^* orbital increases in the

opposite direction: X = Cl > Br > I. For the δ^* orbital, the off-diagonal contributions whelm the diagonal contributions with the net result being the δ^* orbital energies shift in opposition to the electronegativity trend. In reality, the energy contributions from the charge effects (diagonal contributions) are of the same magnitude as the overlap effects (off-diagonal contributions) for these systems so they essentially cancel one another. This is the reason the shifts in the energy of the δ^* orbital as the halide donor is changed are not more dramatic. To see an inverse halide effect, the overlap of the halogen p orbitals must be large enough to counter the charge effects.

A similar energy decomposition analysis of the δ bond in $Re_2X_4(PH_3)_4$ (X = Cl, Br, I) is presented in Table 5.12. The results are directly analogous to those obtained for the δ^* orbital energies. The major contributors to the overall orbital energy are the Re_2 δ and the b_1 $\pi(\perp)$ combination of halogen p orbitals. Other minor contributors to the orbital energy include the b_1 combination of P-H σ orbitals as well as the b_1 combination of P-H σ^* orbitals. As expected, the diagonal energy contributions increase as X = I (-9.33 eV) < Br (-9.62 eV) < Cl (-9.95 eV). To counteract this trend, the off-diagonal contributions follow as X = I (+2.65 eV) < Br (+3.23 eV) < Cl (+3.51 eV). As was seen previously for the δ^* orbital energies, the charge effects (diagonal energies) and the overlap effects (off-diagonal energies) work against one another to yield the final orbital energy. For the most part, the two trends contribute almost equally to the overall orbital energy so even small differences become important to determining the overall orbital energy. The calculated trend for the δ orbital is I (-6.66 eV) > Cl (-6.44 eV) > Br (-6.39 eV). Although the calculated orbital energy trend does not match with the experimental trend, the results still support the argument that the inverse halide order is a direct consequence of a filled-filled interaction between the M_2 δ orbital and the filled b_1 $Cl_4(\perp)$ combination.

Conclusions

From the photoelectron spectroscopic studies presented here, all of the ionizations from the components of the metal-metal bond have been identified for the molecules: $Re_2X_4(PMe_3)_4$ (X = Cl, Br), $Mo_2X_4(PMe_3)_4$ (X = Cl, Br), and $W_2Cl_4(PMe_3)_4$. In opposition to previous studies of these systems, no evidence was found for the W_2 π ionization being split into its spin-orbit components. On the other hand, strong evidence was found in support of the Re_2 π ionization being split into the two components of $e_{1/2}$ and $e_{3/2}$ symmetry. Unlike the previous studies of the molybdenum and tungsten analogs, the ionization from the metal-metal σ orbital was found to occur in the same region of the spectrum as the ionizations from the metal-metal δ and π. In addition, the ionization feature originally assigned to the M-P (σ) ionization of e symmetry is in reality better an antibonding combination of P(σ) and $X_4(\pi_\perp)$ and contains very little metal character. Because it is an antibonding ligand combination, the ionization energy of this ionization does **not** provide a good measure of the charge effect as was initially proposed.

Of particular interest in these spectra is the inverse halide order seen in the position of the δ ionization of $Mo_2X_4(PH_3)_4$ (X = Cl, Br) and the position of the δ^* orbital of the $Re_2X_4(PH_3)_4$ series (X = Cl, Br, I). The $M_2X_4(PMe_3)_4$ analogs are unique molecules in that they have four halide atoms attached directly to the metal pair in a manner that allows direct overlap with the filled metal-metal orbitals. For the filled orbitals of the metal-metal bond, the interaction with the filled halogen combinations results in a filled-filled interaction so that the highest occupied combinations are antibonding between the metal-metal orbitals and the halogen donor orbitals. This antibonding interaction lies at the source of the inverse halide order seen in these systems. The amount of destabilization provided by the antibonding interaction will depend on the degree of overlap between the orbitals of the metal-metal bond and the halogen donor combinations. As expected, the π-donor ability of the halogens, as seen in the

computational studies presented here, increases as X = I < Br < Cl < F. Hence, the inverse

halide order results from the greater donor ability of the lighter halogens (filled-filled interaction)

whelming the inherent charge effects of the halogen.

Essentially, these molecules are designed for seeing an inverse halide order because they

each contain an electron-rich metal-metal bond interacting with four electron-rich halogen atoms.

The metal-metal bonds are made even more electron rich by strong σ-donation from the

trimethylphosphine ligands. Given that the trimethylphosphine ligands are not good π-acceptors,

the metal centers in these molecules are electron-rich, and, as a result, the metal orbitals are

diffuse in nature, favoring overlap with the halide orbitals. In any case, these molecules meet the

basic requirement for seeing the inverse halogen order: an electron-rich metal center interacting

with strong π-donor ligands. However, even though these molecules have four halogen atoms

attached to the dimetal center, a strong inverse halide order in the experimentally-determined

ionization energies is seen only for the δ^* and δ orbitals. The inverse halide order is much less

prominent, although still present, for the energy of the $\sigma+\pi$ band in the photoelectron spectra of

the $Mo_2X_4(PMe_3)_4$. Interestingly, the inverse halide order does not hold for the π and σ

ionizations of the $Re_2X_4(PMe_3)_4$ analogs. Considering the δ^* and δ orbitals have the ability to

strongly interact with all four of the halogen atoms, it is not surprising that the effect is seen most

strongly for the ionization of these orbitals. In comparison, each π orbital interacts strongly with

only two of the halogen atoms while the interaction with the other two halide atoms is much less

significant and highly dependent on the M-M-L angle as shown in the preliminary

considerations. Even though the σ orbital can interact with all four halogen atoms, the overlaps

are simply not sufficient, at least for the $Re_2X_4(PH_3)_4$ analogs, to overcome the charge effects.

Table 5.1. Optimized crystal structure
parameters used for computational work.

$Mo_2X_4(PMe_3)_4$			
	F	Cl	Br
Mo-Mo (Å)	2.110	2.130	2.125
Mo-P (Å)	2.444	2.545	2.547
Mo-X (Å)	2.105	2.414	2.549
∠Mo-Mo-X (°)	101.1	112.23	113.50
∠Mo-Mo-P (°)	104.63	102.32	103.50

$Re_2X_4(PMe_3)_4$			
	Cl	Br	I
Re-Re (Å)	2.247	2.248	2.247
Re-P (Å)	2.417	2.429	2.437
Re-X (Å)	2.380	2.509	2.717
∠Re-Re-X (°)	113.05	113.98	115.95
∠Re-Re-P (°)	101.18	101.56	102.38

$W_2Cl_4(PMe_3)_4$	
W-W (Å)	2.262
W-P (Å)	2.507
W-Cl (Å)	2.393
∠W-W-Cl (°)	111.73
∠W-W-P (°)	101.12

Table 5.2. Spin-orbit split $^2\pi_u$ lone pair
ionizations of HX (X = F, Cl, Br, I)
follow electronegativity trend.

	$^2\Pi_u$ energy (eV)	λ_X (eV)	$\chi_P(X)$
HF	16.05	0.0	3.98
HCl	12.77 12.85	0.08	3.16
HBr	11.71 12.03	0.32	2.96
HI	10.38 11.05	0.67	2.66

$^a\chi_P$ = Pauling Electronegativity

Table 5.3. Ionization peak fit parameters and relative areas for the Ne I, He I, and He II spectra of the $M_2X_4(PMe_3)_4$ series.

	Position (eV)	High width	Low Width	He I area	Ne I area	He II area	$\frac{Ne\ I}{He\ I}$	$\frac{He\ II}{He\ I}$
$Mo_2Cl_4(PMe_3)_4$								
δ	6.39	0.36	0.32	1.00	1.00	1.00	1.00	1.00
π + σ	7.68	0.49	0.45	4.31	4.27	2.63	0.99	0.61
P(e); Cl(e)	8.31	0.50	0.37	8.71	13.44	1.37	1.54	0.16
	8.46	0.87	0.41					
$Mo_2Br_4(PMe_3)_4$								
δ	6.50	0.34	0.32	1.00	1.00	1.00	1.00	1.00
π + σ	7.71	0.41	0.40	4.00	3.87	2.36	0.97	0.59
P(e); Cl(e)	8.33	0.44	0.40	12.71	16.71	3.14	1.31	0.25
	8.69	0.53	0.43					
$Re_2Cl_4(PMe_3)_4$								
δ*	5.65	0.38	0.29	1.00	1.00	1.00	1.00	1.00
δ	6.49	0.43	0.28	0.90	0.78	0.99	0.87	1.10
π	7.79	0.48	0.38	2.44	2.60	2.65	1.07	1.09
	8.09	0.48	0.37					
P(e); Cl(e)	8.47	0.36	0.30	2.19	2.80	1.65	1.28	0.59
σ	8.84	0.45	0.44	1.92	2.34	2.28	1.22	0.97
$Re_2Br_4(PMe_3)_4$								
δ*	5.71	0.36	0.29	1.00	1.00	1.00	1.00	1.00
δ	6.53	0.37	0.29	0.79	0.71	0.91	0.90	1.15
π	7.77	0.34	0.34	2.23	2.74	2.12	1.23	0.95
	8.02	0.34	0.29					
P(e); Cl(e)	8.39	0.47	0.30	3.67	4.89	2.67	1.33	0.73
σ	8.74	0.61	0.23	0.81	1.22	0.83	1.51	1.02
$Re_2I_4(PMe_3)_4$								
δ*	5.80	0.32	0.23	1.00	N/A			
δ	6.56	0.37	0.26	0.96	N/A			
$W_2Cl_4(PMe_3)_4$								
δ	5.77	0.39	0.31	1.00	1.00	1.00	1.00	1.00
π	7.00	0.87	0.55	2.84	3.10	2.16	1.09	0.76
σ	7.44	0.33	0.23	0.70	0.77	0.49	1.10	0.70
P(e); Cl(e)	8.34	0.43	0.31	3.33	5.00	1.20	1.50	0.36

Table 5.4. Theoretical atomic photoionization cross sections (MB) for Ne I, He I, and He II.

	Ne I	He I	He II	$\dfrac{\text{Ne I}}{\text{He I}}$	$\dfrac{\text{He II}}{\text{He I}}$
Mo 4d	23.49	26.27	8.49	0.89	0.32
W 5d	21.01	24.83	7.99	0.84	0.32
Re 5d	19.63	28.08	12.10	0.70	0.43
Br 4p	38.63	15.57	0.96	2.48	0.06
Cl 3p	47.39	13.84	0.65	3.42	0.05
P 3p	5.22	1.23	0.51	4.23	0.41
C 2p	8.32	6.13	1.87	1.36	0.31
H	3.63	1.89	0.29	1.92	0.15

Table 5.5. Computational results for $Mo_2X_4(PMe_3)_4$ (X = Cl, Br) from density functional and Fenske-Hall calculations.

Orbital Description	Experimental I.E. (eV)	Energies (eV)				Orbital Compositions	
		ADF		Fenske-Hall			
		K-S		Koopmans'		ADF	Fenske-Hall
		Raw	Scaled[a]	Raw	Scaled[b]		
			$Mo_2Cl_4(PMe_3)_4$				
Mo-Mo δ (b₁)	6.39	3.74	6.39	6.64	6.39	75% Mo(d) 22% Cl(p)	80% Mo(d) 20% Cl(p)
Mo-Mo σ (a₁)	7.68	4.87	7.52	9.82	8.21	71% Mo(d) 19% Cl(p)	32% Mo(d) 52% Cl(p)
Mo-Mo π (e)		4.94	7.59	8.65	7.54	63% Mo(d) 27% Cl(p)	64% Mo(d) 24% Cl(p)
e(Cl and P)	8.39	5.45	8.14	9.76	8.17	34% Cl(p) 34% P(p) 9% C(p)	66% Cl(p) 18% P(p)
			$Mo_2Br_4(PMe_3)_4$				
Mo-Mo δ (b₁)	6.50	3.95	6.50	6.87	6.50	73% Mo(d) 23% Br(p)	77% Mo(d) 23 % Br(p)
Mo-Mo σ (a₁)	7.71	5.04	7.59	9.39	7.45	63% Mo(d) 28% Br(p)	12% Mo(d) 78% Br(p)
Mo-Mo π (e)		5.07	7.62	8.55	7.93	46% Mo(d) 37% Br(p)	47% Mo(d) 38 % Br(p)
e(Br and P)	8.51	5.44	7.99	9.20	7.82	58% Br(p) 18% P(p)	83% Br(p) 8% P(p)

[a] ε = εᵢ + Δ [Δ = 2.65(Mo;Cl); 2.55(Mo;Br)]
[b] ε = 0.57εᵢ + Δ [Δ = 2.46(Mo;Cl); 2.70(Mo;Br)]

Table 5.6. Computational results for $Mo_2X_4(PH_3)_4$ (X = Cl, Br) and $W_2Cl_4(PH_3)_4$ from density functional and Fenske-Hall calculations.

Orbital Description	Experimental I.E. (eV)	Energies (eV)						Orbital Compositions	
		ADF				Fenske-Hall			
		K-S		ΔE_{SCF}		Koopmans'		ADF	Fenske-Hall
		Raw	Scaled[a]	Raw	Scaled[b]	Raw	Scaled[c]		
Mo₂Cl₄(PH₃)₄									
Mo-Mo δ (b₁)	6.39	4.14	6.39	6.42	6.39	6.69	6.39	71% Mo(d) 25% Cl(p)	78% Mo(d) 22% Cl(p)
Mo-Mo σ (a₁)	7.68	5.30	7.55	7.72	7.69	9.17	7.69	68% Mo(d) 23% Cl(p)	31% Mo(d) 57% Cl(p)
Mo-Mo π (e)		5.49	7.74	7.70	7.67	10.17	8.26	55% Mo(d) 33% Cl(p)	60% Mo(d) 28% Cl(p)
e(Cl and P)	8.39	6.03	8.28	8.05	8.02	10.22	8.29	65% Cl(p) 29% P(p)	78% Cl(p) 14% P(p)
Mo₂Br₄(PH₃)₄									
Mo-Mo δ (b₁)	6.50	4.30	6.50	6.45	6.50	6.66	6.50	68% Mo(d) 28% Br(p)	74% Mo(d) 25% Br(p)
Mo-Mo σ (a₁)	7.71	5.33	7.53	7.55	7.60	8.82	7.72	60% Mo(d) 32% Br(p)	17% Mo(d) 74% Br(p)
Mo-Mo π (e)		5.52	7.72	7.56	7.61	9.57	8.15	42% Mo(d) 43% Br(p)	51% Mo(d) 37% Br(p)
e(Br and P)	8.51	5.90	8.10	7.83	7.88	9.44	8.08	69% Br(p) 25% P(p)	84% Br(p) 9% P(p)
W₂Cl₄(PH₃)₄									
W-W δ (b₁)	5.77	3.51	5.77	5.74	5.77	5.30	5.77	71% W(d) 21% Cl(p)	83% W(d) 16% Cl(p)
W-W π (e)	7.00	4.87	7.13	7.15	7.12	8.06	8.06	63% W(d) 18% Cl(p)	73% W(d) 17% Cl(p)
W-W σ (a₁)	7.44	5.13	7.39	7.65	7.62	9.57	9.57	65% W(d) 14% Cl(p) 21% W(s)	48% W(d) 31% Cl(p) 13% W(s)
e(Cl and P)	8.35	6.02	8.28	8.09	8.06	10.27	10.27	38% Cl(p) 55% P(p)	79% Cl(p) 12% P(p)

[a] $\epsilon = \epsilon_i + \Delta$ [Δ = 2.65(Mo;Cl); 2.55(Mo;Br); 2.26(W;Cl)]
[b] $\epsilon = \epsilon_i + \Delta$ [Δ = -0.03(Mo;Cl); +0.05(Mo;Br); -0.03(W;Cl)]
[c] $\epsilon = 0.57\epsilon_i + \Delta$ [Δ = 2.46(Mo;Cl); 2.70(Mo;Br); 2.75(W;Cl)]

Table 5.7. Computational results for Re$_2$X$_4$(PH$_3$)$_4$ (X = Cl, Br, I) from density functional and Fenske-Hall calculations.

Orbital Description	Experimental I.E. (eV)	Energies (eV)						Orbital Compositions	
		ADF				Fenske-Hall			
		Kohn-Sham		ΔE_{SCF}		Koopmans'		ADF	Fenske-Hall
		Raw	Scaled[a]	Raw	Scaled[b]	Raw	Scaled[c]		
Re$_2$Cl$_4$(PH$_3$)$_4$									
Re-Re δ* (a$_2$)	5.65	3.27	5.65	5.59	5.65	4.91	5.65	72% Re(d) 18% Cl(p)	85%Re(d) 14% Cl(p)
Re-Re δ (b$_1$)	6.49	4.10	6.48	6.37	6.49	6.44	6.52	67% Re(d) 27% Cl(p)	79% Re(d) 20% Cl(p)
Re-Re π (e)	7.79; 8.09	5.66	8.04	7.90	8.13	8.92	7.93	52% Re(d) 34% Cl(p)	65% Re(d) 24% Cl(p)
e(Cl and P)	8.47	5.98	8.36	8.09	8.34	10.23	8.68	60% Cl(p) 32 % P(p)	83% Cl(p) 9 % P(p)
Re-Re σ (a$_1$)	8.84	6.27	8.65	8.56	8.84	10.22	8.68	34% Re(d) 54% Cl(p)	24% Re(d) 62% Cl(p)
Re$_2$Br$_4$(PH$_3$)$_4$									
Re-Re δ* (a$_2$)	5.71	3.36	5.71	5.60	5.71	4.94	5.71	72% Re(d) 20% Br(p)	84% Re(d) 15% Br(p)
Re-Re δ (b$_1$)	6.53	4.18	6.53	6.36	6.53	6.39	6.53	64% Re(d) 31% Br(p)	76% Re(d) 23% Br(p)
Re-Re π (e)	7.77; 8.02	5.59	7.94	7.73	8.00	8.62	7.80	45% Re(d) 65% Br(p)	58% Re(d) 33% Br(p)
e(Br and P)	8.39	5.78	8.13	7.84	8.12	9.45	8.28	70% Br(p) 21% P(p)	86% Br(p) 7 % P(p)
Re-Re σ (a$_1$)	8.74	6.05	8.40	8.22	8.53	9.57	8.34	25% Re(d) 65% Br(p)	13% Re(d) 77% Br(p)
Re$_2$I$_4$(PH$_3$)$_4$									
Re-Re δ* (a$_2$)	5.80	3.73	5.80	5.67	5.80	5.29	5.80	73% Re(d) 23% I(p)	84% Re(d) 16% I(p)
Re-Re δ (b$_1$)	6.56	4.52	6.59	6.38	6.56	6.66	6.58	59% Re(d) 38% I(p)	73% Re(d) 27% I(p)
Re-Re π (e)	N/A	5.65	7.72	7.48	7.74	8.46	7.60	27% Re(d) 68% I(p)	45% Re(d) 47% I(p)
e(I and P)	N/A	5.70	7.77	7.50	7.76	8.87	7.83	77% I(p) 13% P(p)	85% I(p) 4% P(p)
Re-Re σ (a$_1$)	N/A	5.91	7.98	7.75	8.03	9.02	7.92	14% Re(d) 77% I(p)	6% Re(d) 86% I(p)

[a] ε = ε$_1$ + Δ [Δ = 2.38(Cl); 2.35(Br); 2.07(I)]
[b] ε = 1.075ε$_1$ + Δ [Δ = -0.36(Cl); -0.31(Br); -.30(I)]
[c] ε = 0.57ε$_1$ + Δ [Δ = 2.85(Cl); 2.89(Br); 2.78(I)]

Table 5.8. Computational results for the $M_2X_4(PH_3)_4$ analogs, including Kohn-Sham orbital energies, orbital compositions, and fragment orbital overlap values.

Orbital Description	K-S orbital Energies (eV)			Orbital Composition			Overlap M_2 and $X_4(PH_3)_4$		
				$Mo_2X_4(PH_3)_4$					
	F	Cl	Br	F	Cl	Br	F	Cl	Br
δ (b₁)	3.71	4.14	4.30	76% Mo₂ δ 16% 2b₁ F₄(PH₃)₄*	71% Mo₂ δ 22% 2b₁ Cl₄(PH₃)₄*	71% Mo₂ δ 26% 4b₁ Br₄(PH₃)₄*	0.143	0.127	0.113
σ (a₁)	5.42	5.30	5.33	81% Mo₂ σ 5% 5a₁ F₄(PH₃)₄*	72% Mo₂ σ 22% 5a₁ Cl₄(PH₃)₄	64% Mo₂ σ 32% 8a₁ Br₄(PH₃)₄*	0.0482	0.0674	0.0626
π (e)	5.18	5.49	5.52	58 % Mo₂ π 5% 5e₁ F₄(PH₃)₄ 18% 6e₁ F₄(PH₃)₄* 8% 8e₁ F₄(PH₃)₄	58 % Mo₂ π 18% 6e₁ Cl₄(PH₃)₄ 14% 7 e₁ Cl₄(PH₃)₄*	48 % Mo₂ π 24% 11e₁ Cl₄(PH₃)₄ 19% 12 e₁ Cl₄(PH₃)₄*	0.00417 0.102 0.0238	0.0667 0.0565	0.0554 0.0545
				$Re_2X_4(PH_3)_4$					
	Cl	Br	I	Cl	Br	I	Cl	Br	I
δ* (a₂)	3.27	3.36	3.73	72% Re₂ δ* 14% 2a₂ Cl₄(PH₃)₄*	72% Re₂ δ* 16% 4a₂ Br₄(PH₃)₄*	72% Re₂ δ* 19% 4a₂ I₄(PH₃)₄*	0.189	0.117	0.0981
δ (b₁)	4.11	4.18	4.52	67% Re₂ δ 23% 2b₁ Cl₄(PH₃)₄*	66% Re₂ δ 27% 4b₁ Br₄(PH₃)₄*	61% Re₂ δ 34% 4b₁ I₄(PH₃)₄*	0.188	0.125	0.104
π (e)	5.66	5.59	5.65	53% Re₂ π 5% 6e₁ Cl₄(PH₃)₄ 26% 7e₁ Cl₄(PH₃)₄	46% Re₂ π 23% 11e₁ Br₄(PH₃)₄ 18% 12e₁ Br₄(PH₃)₄	27% Re₂ π 33% 11e₁ I₄(PH₃)₄ 17% 12e₁ I₄(PH₃)₄ 9% 13e₁ I₄(PH₃)₄	0.0575 0.115	-0.0598 0.0666	0.0447 -0.0584 0.0258
σ (a₁)	6.27	6.05	5.91	45% Re₂ σ 50% 5a₁ Cl₄(PH₃)₄*	36% Re₂ σ 58% 8a₁ Br₄(PH₃)₄*	21% Re₂ σ 67% 8a₁ I₄(PH₃)₄*	-0.0441	0.0277	0.0219

*Corresponds to the highest occupied combination of $X_4(PH_3)_4$ of the appropriate symmetry.

Table 5.9. Transform Fenske-Hall computational results for $Re_2X_4(PH_3)_4$ (X = Cl, Br, I) in terms of the molecular fragments: Re_2^{4+} and $X_4(PH_3)_4^{4-}$.

Orbital Description	Koopmans' Energies (eV)			Orbital Composition			Overlap Re$_2$ and X$_4$(PH$_3$)$_4$		
				Re$_2$X$_4$(PH$_3$)$_4$					
	Cl	Br	I	Cl	Br	I	Cl	Br	I
δ* (a$_2$)	4.92	4.94	5.29	85% Re$_2$ δ* 13% a$_2$(⊥) Cl$_4$(PH$_3$)$_4$	84% Re$_2$ δ* 15% a$_2$(⊥) Br$_4$(PH$_3$)$_4$	84% Re$_2$ δ* 15% a$_2$(⊥) I$_4$(PH$_3$)$_4$	0.154	0.146	0.127
δ (b$_1$)	6.44	6.39	6.66	79% Re$_2$ δ 19% b$_1$(⊥) Cl$_4$(PH$_3$)$_4$	76% Re$_2$ δ 23% b$_1$(⊥) Br$_4$(PH$_3$)$_4$	73% Re$_2$ δ 26% b$_1$(⊥) I$_4$(PH$_3$)$_4$	0.157	0.150	0.130
π (e)	8.92	8.62	8.46	66% Re$_2$ π 21% e$_1$(ii) Cl$_4$(PH$_3$)$_4$	58% Re$_2$ π 26% e$_1$(ii) Br$_4$(PH$_3$)$_4$	44% Re$_2$ π 5% 10e$_1$ I$_4$(PH$_3$)$_4$ 15% 11e$_1$ I$_4$(PH$_3$)$_4$ 18% 12e$_1$(ii) I$_4$(PH$_3$)$_4$ 9% 13e$_1$ I$_4$(PH$_3$)$_4$	0.0821	0.0777	0.00152 0.05149 -0.04594 -0.01851
σ (a$_1$)	10.22	9.57	9.02	34% Re$_2$ σ 63% a$_1$(ii) Cl$_4$(PH$_3$)$_4$	19% Re$_2$ σ 78% a$_1$(ii) Br$_4$(PH$_3$)$_4$	9% Re$_2$ σ 87% a$_1$(ii) I$_4$(PH$_3$)$_4$	0.0547	0.0552	0.0530

Table 5.10. Calculated orbital compositions and energy splittings for the ligand- and metal-based δ^* and δ orbitals of the $M_2X_4(PH_3)_4$ series.

	Kohn-Sham Energies (eV)			Orbital Compositions		
				$Re_2X_4(PH_3)_4$		
	Cl	Br	I	Cl	Br	I
Re-Re δ^*	3.27	3.36	3.73	72% Re_2 δ^* 14% $2a_2$ $Cl_4(PH_3)_4$	72% Re_2 δ^* 16% $4a_2$ $Br_4(PH_3)_4$	72% Re_2 δ^* 19% $4a_2$ $I_4(PH_3)_4$
Ligand-based Re-Re δ^*	7.10	6.73	6.43	9% Re_2 δ^* 87% $2a_2$ $Cl_4(PH_3)_4$	10% Re_2 δ^* 87% $4a_2$ $Br_4(PH_3)_4$	14% Re_2 δ^* 80% $4a_2$ $I_4(PH_3)_4$
ΔE	3.83	3.37	2.70			
Re-Re δ	4.11	4.18	4.52	67% Re_2 δ 23% $2b_1$ $Cl_4(PH_3)_4$	66% Re_2 δ 27% $4b_1$ $Br_4(PH_3)_4$	61% Re_2 δ 34% $4b_1$ $I_4(PH_3)_4$
Ligand-based Re-Re δ	7.16	6.79	6.53	17% Re_2 δ 78% $2b_1$ $Cl_4(PH_3)_4$	20% Re_2 δ 75% $4b_1$ $Br_4(PH_3)_4$	27% Re_2 δ 66% $4b_1$ $I_4(PH_3)_4$
ΔE	3.05	2.61	2.01			

	$Mo_2X_4(PH_3)_4$					
	F	Cl	Br	F	Cl	Br
Mo-Mo δ	3.71	4.14	4.30	76% Mo_2 δ 16% $2b_1$ $F_4(PH_3)_4$	71% Mo_2 δ 22% $2b_1$ $Cl_4(PH_3)_4$	71% Mo_2 δ 26% $4b_1$ $Br_4(PH_3)_4$
Ligand-based Mo-Mo δ	7.59	7.14	6.86	14% Mo_2 δ 82% $2b_1$ $F_4(PH_3)_4$	17% Mo_2 δ 78% $2b_1$ $Cl_4(PH_3)_4$	20% Mo_2 δ 75% $4b_1$ $Br_4(PH_3)_4$
ΔE	3.88	3.00	2.56			

Table 5.11. Fenske-Hall Orbital Energy Decomposition Analysis of the δ* orbital of Re₂X₄(PH₃)₄.

Orbital	Diagonal Energy Contributions (eV)		Off-diagonal Energy Contributions (eV)		Orbital Energy (eV)
	Major Components	Sum	Major Components	Sum	
Re₂Cl₄(PH₃)₄					
	Re-Re δ* -5.71		Re-Re δ*; a₂ P-H σ +0.65		
	a₂ P-H σ -0.31		Re-Re δ*; Cl₄ a₂ π(⊥) +3.09		
	Cl₄ a₂ π(⊥) -2.19		Re-Re δ*; Cl₄(PH₃)₄ 23 +0.02	+3.12	
δ*		-8.02	Re-Re δ*; Cl₄(PH₃)₄ 28 +0.01		-4.91
	23 Cl₄(PH₃)₄ -0.01		Re-Re δ*; a₂ P-H σ* -0.65		
	44 Cl₄(PH₃)₄ -0.01		a₂ P-H σ; Cl₄ a₂ π(⊥) -0.04	-0.01	
	a₂ P-H σ* +0.22		Cl₄ a₂ π(⊥); P-H σ* +0.03		
Re₂Br₄(PH₃)₄					
	Re-Re δ* -5.54		Re-Re δ*; Br₄(PH₃)₄ 33 +0.06		
			Re-Re δ*; a₂ P-H σ +0.55		
	33 Br₄(PH₃)₄ -0.03		Re-Re δ*; Br₄ a₂ π(⊥) +2.78	+2.81	
δ*		-7.75	Re-Re δ*; Br₄(PH₃)₄ 44 +0.01		-4.94
	a₂ P-H σ -0.26		Re-Re δ*; a₂ P-H σ* -0.59		
	Br₄ a₂ π(⊥) -2.11		a₂ P-H σ; Br₄ a₂ π(⊥) -0.04	0.00	
	a₂ P-H σ* +0.19		Br₄ a₂ π(⊥); a₂ P-H σ* +0.04		
Re₂I₄(PH₃)₄					
	Re-Re δ* -5.55		Re-Re δ*; I₄(PH₃)₄ 31 +0.59		
	a₂ P-H σ -0.28		Re-Re δ*; I₄(PH₃)₄ 44 +2.18	+2.21	
δ*	I₄ a₂ π(⊥) -1.86	-7.52	Re-Re δ*; I₄(PH₃)₄ 60 -0.56		-5.29
	a₂ P-H σ* +0.17		I₄(PH₃)₄ 31; I₄(PH₃)₄ 44 -0.03	+0.02	
			I₄(PH₃)₄ 44; I₄(PH₃)₄ 60 +0.05		

Table 5.12. Fenske-Hall Orbital Energy Decomposition Analysis of the δ orbital of Re$_2$X$_4$(PH$_3$)$_4$.

Orbital	Diagonal Energy Contributions (eV)		Off-diagonal Energy Contributions (eV)		Orbital Energy (eV)
	Major Components	Sum	Major Components	Sum	
	Re$_2$Cl$_4$(PH$_3$)$_4$				
	Re-Re δ -6.84		Re-Re δ; b$_1$ P-H σ +0.76		
	b$_1$ P-H σ -0.34		Re-Re δ; P-H σ +0.01		
	22 Cl$_4$(PH$_3$)$_4$ᵃ -0.01		Re-Re δ; b$_1$ π(⊥) Cl$_4$ +3.42	+3.53	
δ		-9.95	Re-Re δ; b$_1$ P-H σ* -0.66		-6.44
	b$_1$ π(⊥) Cl$_4$ -2.94		b$_1$ P-H σ; b$_1$ π(⊥) Cl$_4$ -0.07		
			b$_1$ P-H σ; b$_1$ P-H σ* +0.01	-0.02	
	b$_1$ P-H σ* +0.19		b$_1$ π(⊥) Cl$_4$; b$_1$ P-H σ* +0.04		
	Re$_2$Br$_4$(PH$_3$)$_4$				
	Re-Re δ -6.48		Re-Re δ; b$_1$ P-H σ +0.61		
			Re-Re δ; P-H σ +0.07		
	b$_1$ P-H σ -0.27		Re-Re δ; b$_1$ π(⊥) Br$_4$ +3.15	+3.24	
δ	34 Br$_4$(PH$_3$)$_4$ᵃ -0.03	-9.62	Re-Re δ; b$_1$ P-H σ* -0.59		-6.39
	b$_1$ π(⊥) Br$_4$ -3.00		b$_1$ P-H σ; b$_1$ π(⊥) Br$_4$ -0.05		
			P-H σ; b$_1$ π(⊥) Br$_4$ -0.01	-0.01	
	b$_1$ P-H σ* +0.16		b$_1$ π(⊥) Br$_4$; b$_1$ P-H σ* +0.05		
	Re$_2$I$_4$(PH$_3$)$_4$				
	Re-Re δ -6.19		Re-Re δ; b$_1$ P-H σ +0.62		
	b$_1$ P-H σ -0.27		Re-Re δ; b$_1$ π(⊥) I$_4$ +2.56	+2.66	
	b$_1$ π(⊥) I$_4$ -3.01		Re-Re δ; b$_1$ P-H σ* -0.52		
δ		-9.33	b$_1$ P-H σ; b$_1$ π(⊥) I$_4$ -0.06		-6.66
	b$_1$ P-H σ* +0.14		b$_1$ π(⊥) I$_4$; b$_1$ P-H σ* +0.06	-0.01	
			Other contributions -0.01		

ᵃCorresponds to a minor contribution from a ligand b$_1$ orbital.
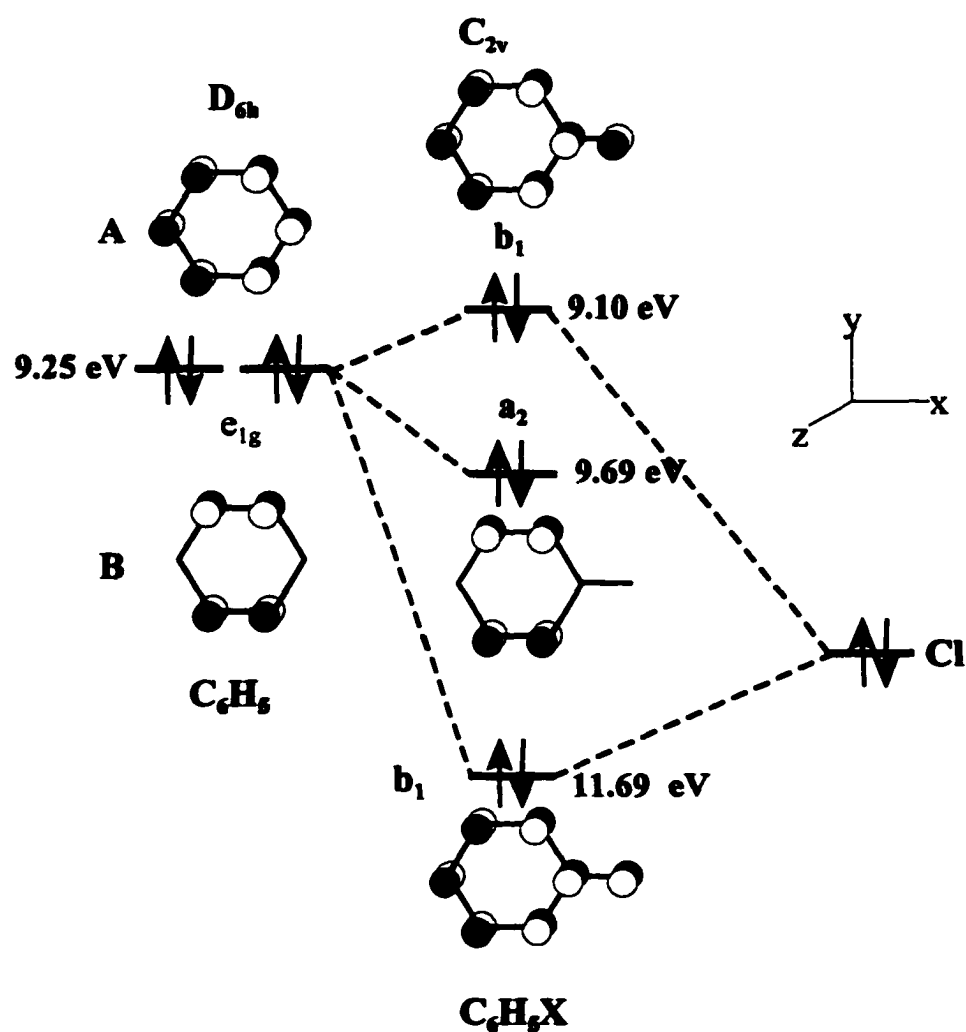
Figure 5.1. Simple orbital diagram demonstrating the charge and overlap effects of chlorine substitution on the e_{1g} orbital of benzene. All energies correspond to the measured ionization energies form photoelectron spectroscopic studies.
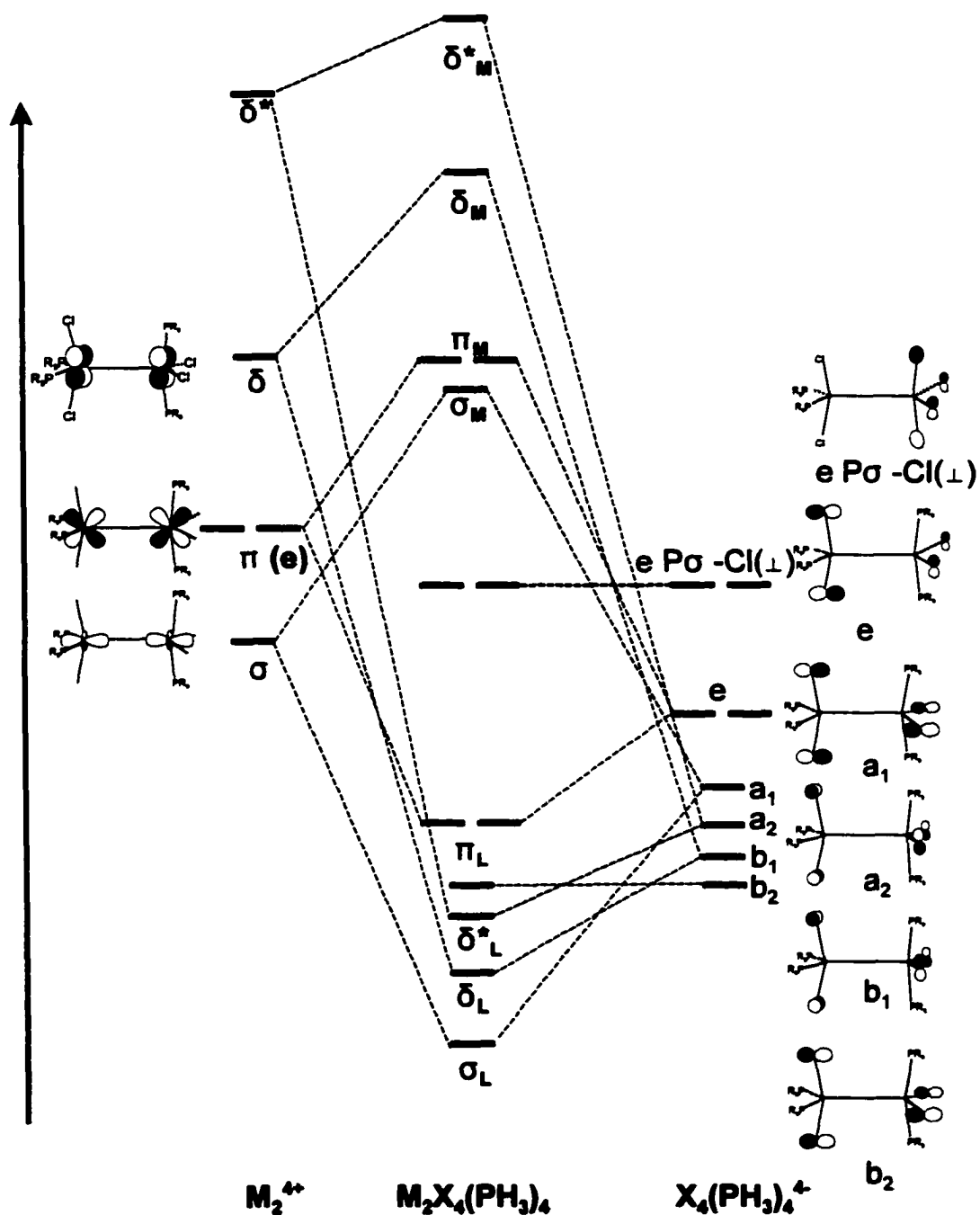
Figure 5.2. Simple orbital interaction diagram for $M_2X_4(PH_3)_4$ based on the symmetry combinations developed in the preliminary considerations section.
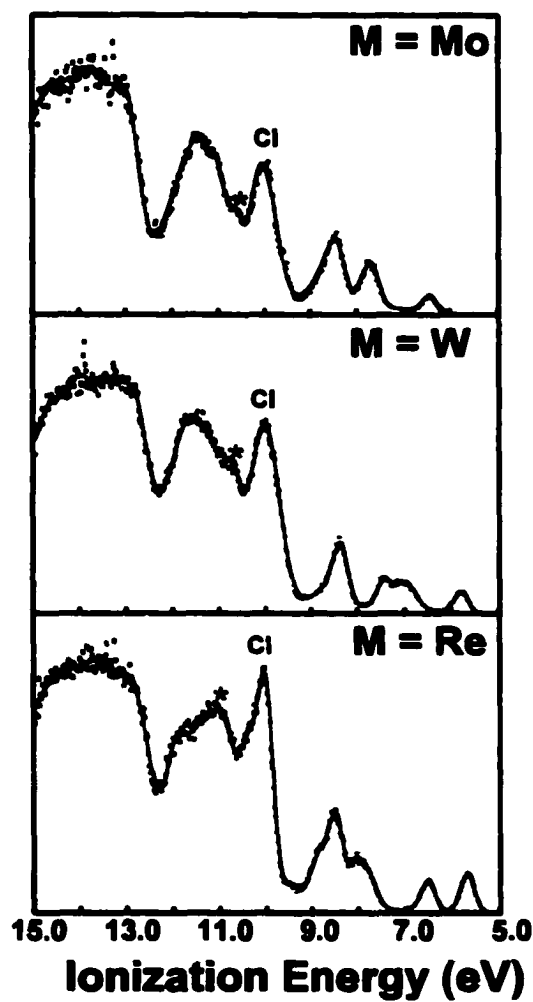
Figure 5.3. He I photoelectron spectra of
$M_2Cl_4(PMe_3)_4$ (M = Mo, W, Re).
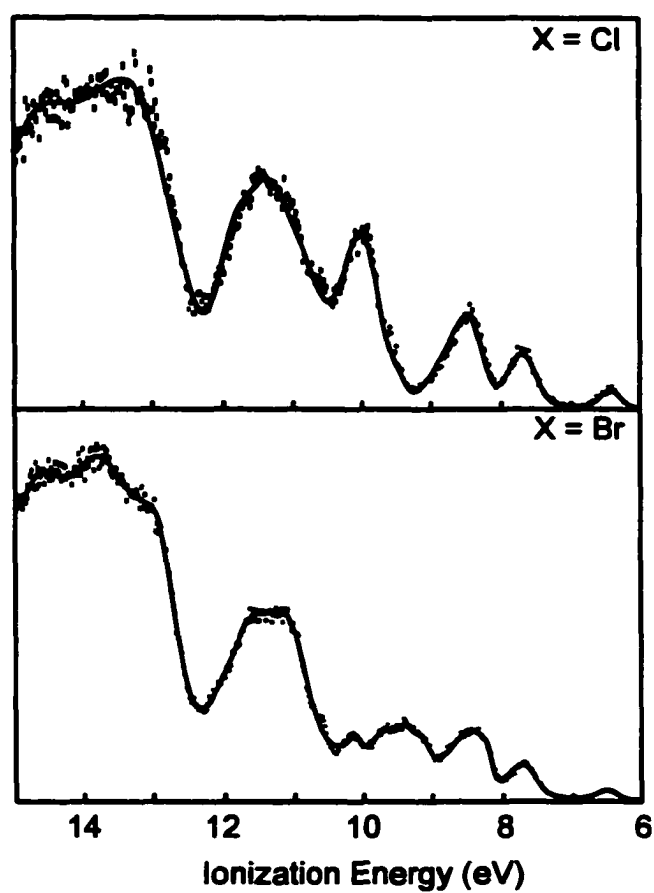
Figure 5.4. He I photoelectron spectra of
$Mo_2X_4(PMe_3)_4$ (X = Cl, Br).
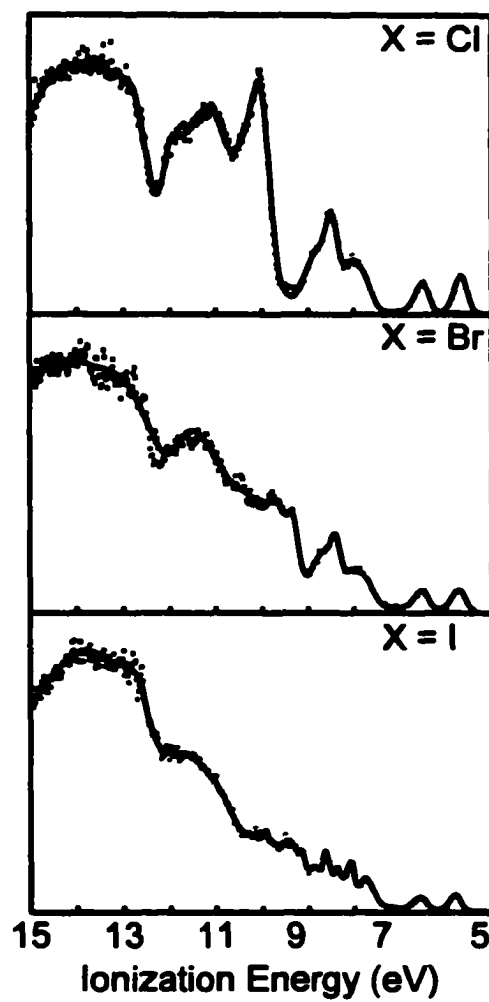
Figure 5.5. He I photoelectron spectra of Re₂L₄(PMe₃)₄.
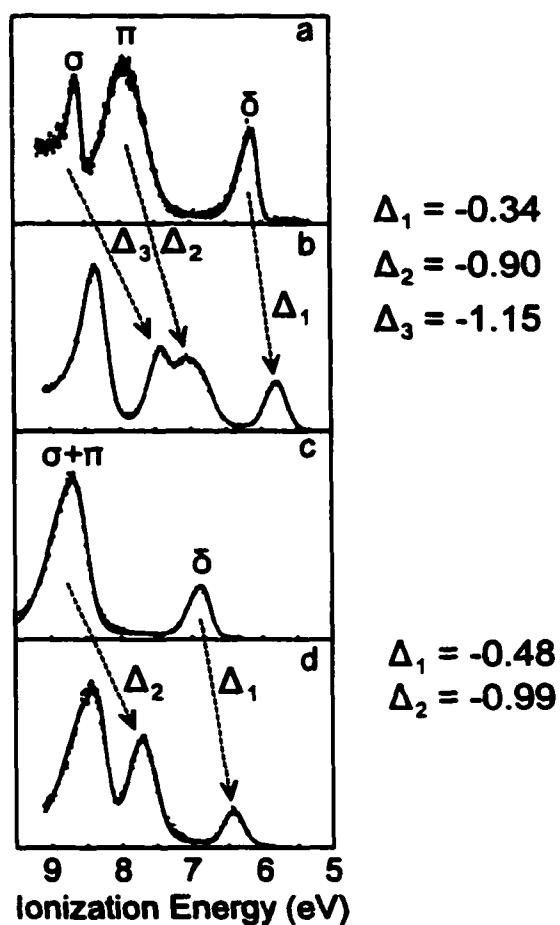
Figure 5.6. Photoelectron spectra of
(a) $W_2(O_2CCH_3)_4$, (b) $W_2Cl_4(PMe_3)_4$ (c)
$Mo_2O_2CH_3)_4$, and (d) $Mo_2Cl_4(PMe_3)_4$
in the 5 to 9 eV energy range. The shifts in
the positions of the σ, π, and δ as the
acetates are replaced by $Cl_4(PMe_3)_4$ are
represented by Δ.
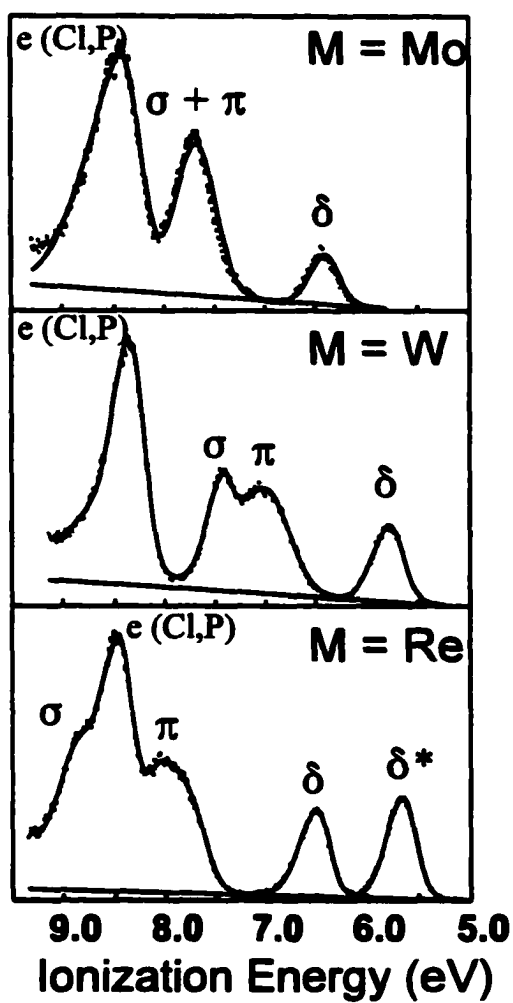
Figure 5.7. He I photoelectron spectra of
$M_2Cl_4(PMe_3)_4$ (M = Mo, W, Re) in the 5 to
9 eV energy range.
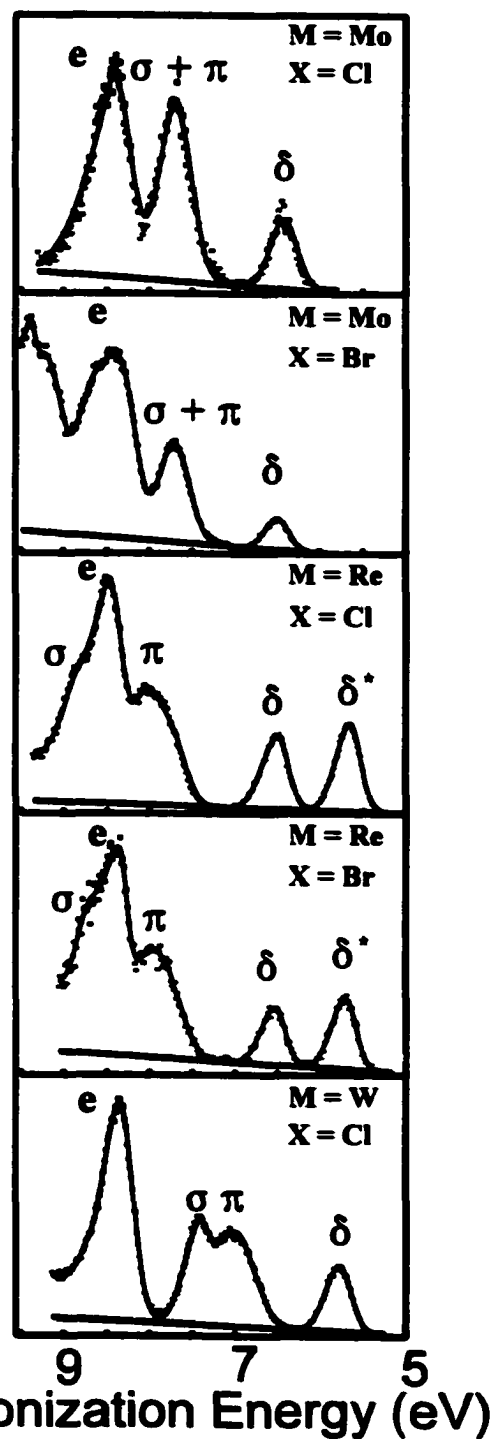
Figure 5.8. He I photoelectron spectra
collected in the 5 to 9 eV energy range for
$Mo_2X_4(PMe_3)_4$ (X =Cl, Br); $W_2Cl_4(PMe_3)_4$;
and $Re_2X_4(PMe_3)_4$ (X = Cl, Br).
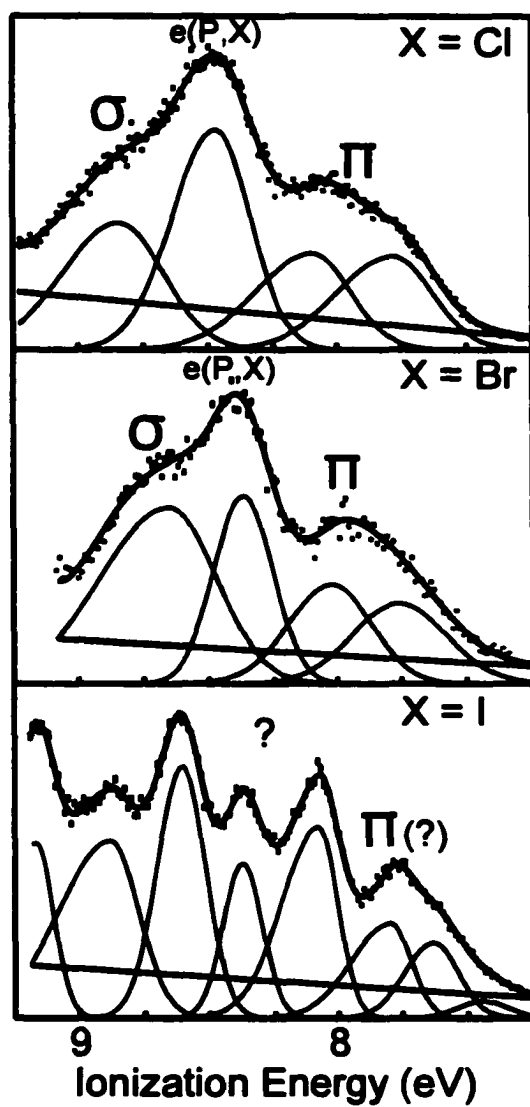
Figure 5.9. He I photoelectron spectra of the 7 to 9 eV energy range, containing the σ, π, and $e(P\sigma\text{-}X_4 \; \pi\perp)$ ionizations of $Re_2X_4(PMe_3)_4$ (X = Cl, Br, I).
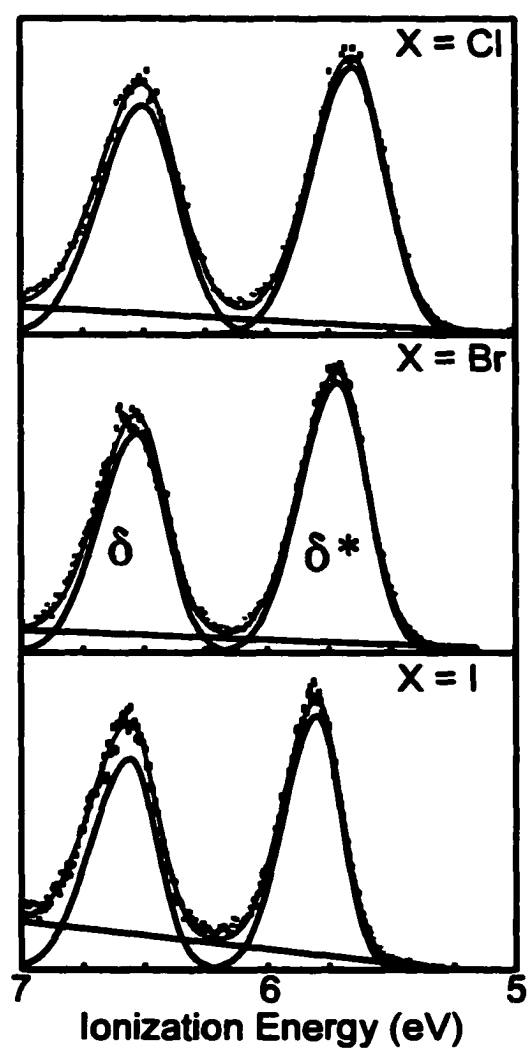
Figure 5.10. He I photoelectron spectra of δ* and δ ionizations of $Re_2X_4(PMe_3)_4$ (X = Cl, Br, I).
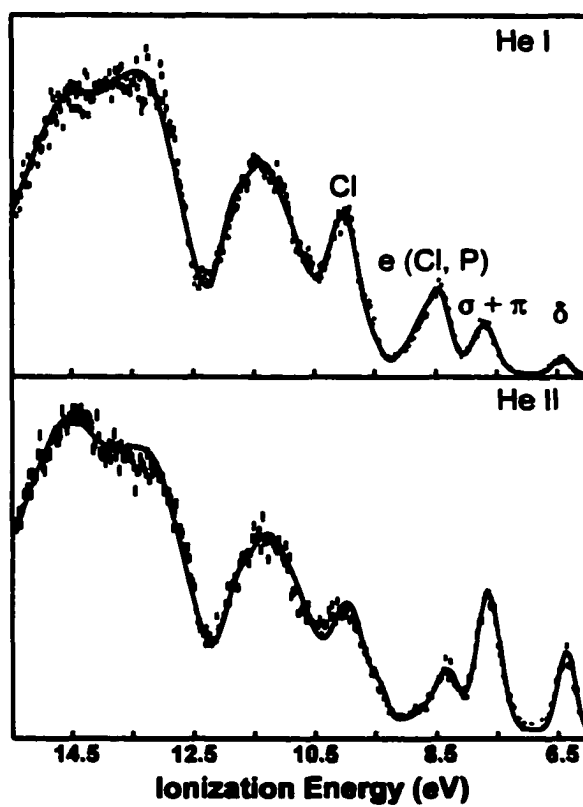
Figure 5.11. He I and He II photoelectron
spectra of $Mo_2Cl_4(PMe_3)_4$ in the 6 to 15 eV
energy range.
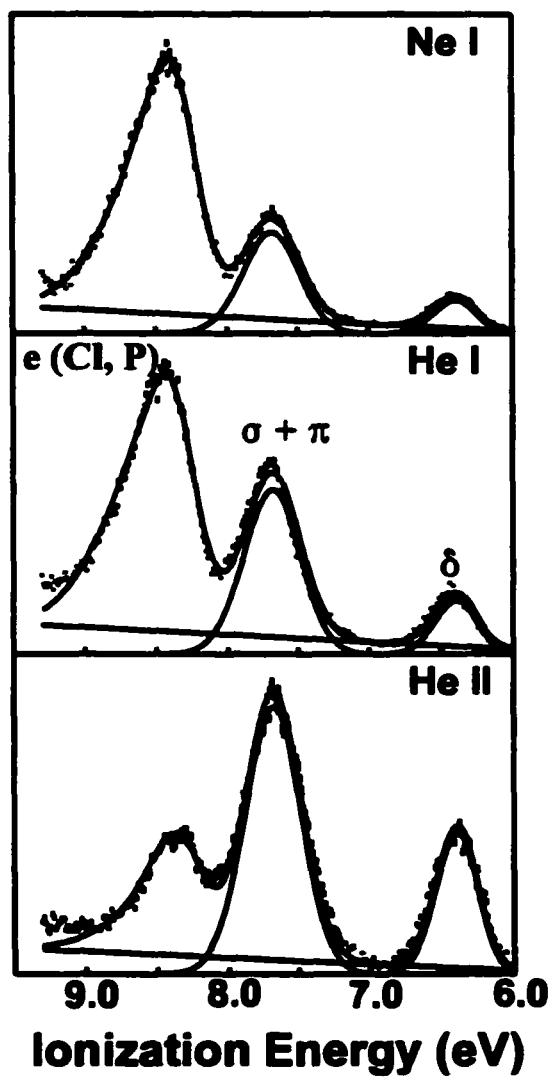
Figure 5.12. Ne I, He I, and He II photoelectron spectra of $Mo_2Cl_4(PMe_3)_4$ in the 6 to 9 eV energy region.
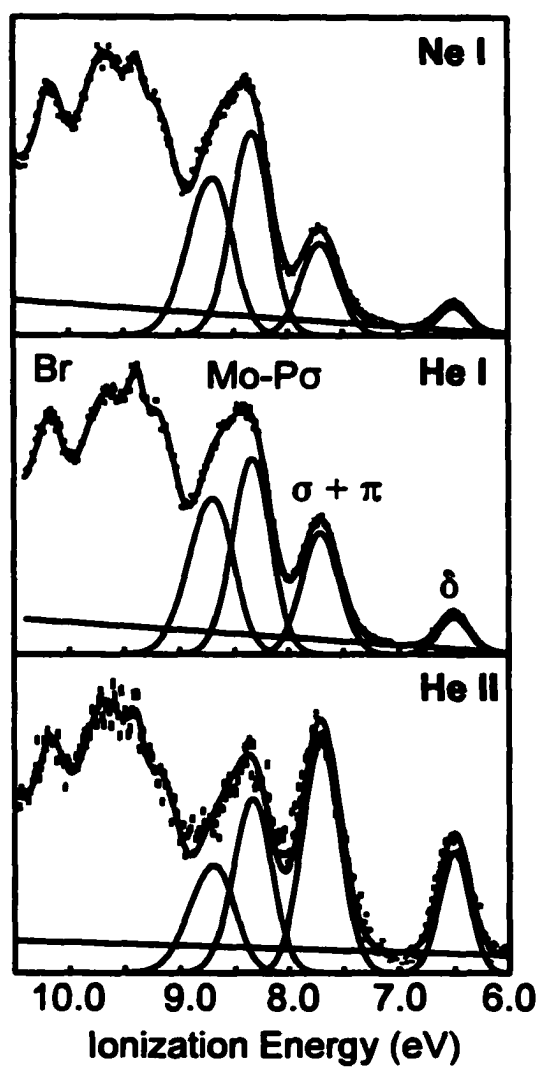
Figure 5.13. Ne I, He I, and He II
photoelectron spectra of $Mo_2Br_4(PMe_3)_4$.
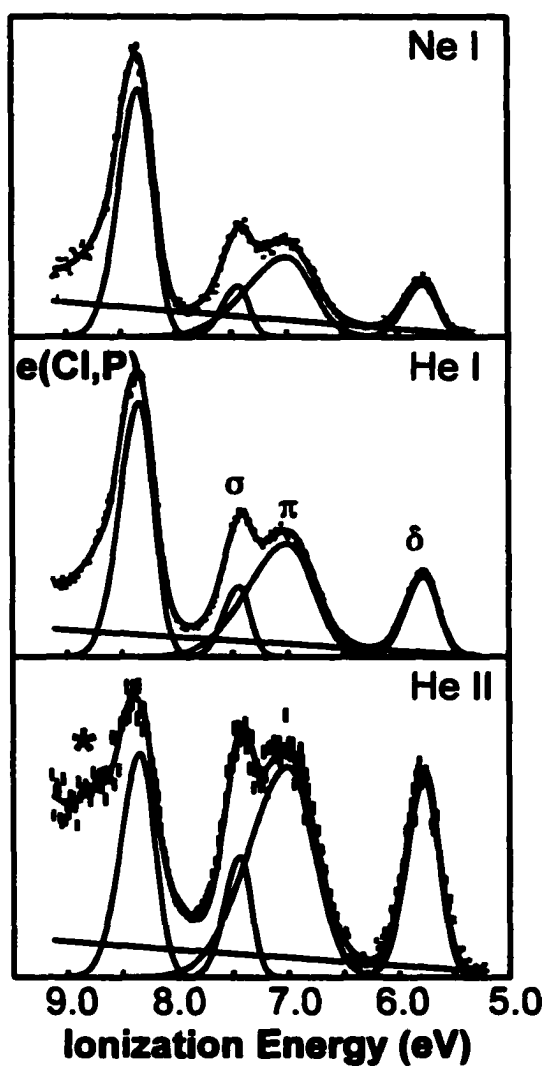
Figure 5.14. Ne I, He I, and He II
photoelectron spectra of $W_2Cl_4(PMe_3)_4$.
The * indicates some free phosphine
indicative of decomposition under the
conditions of the He II experiment.
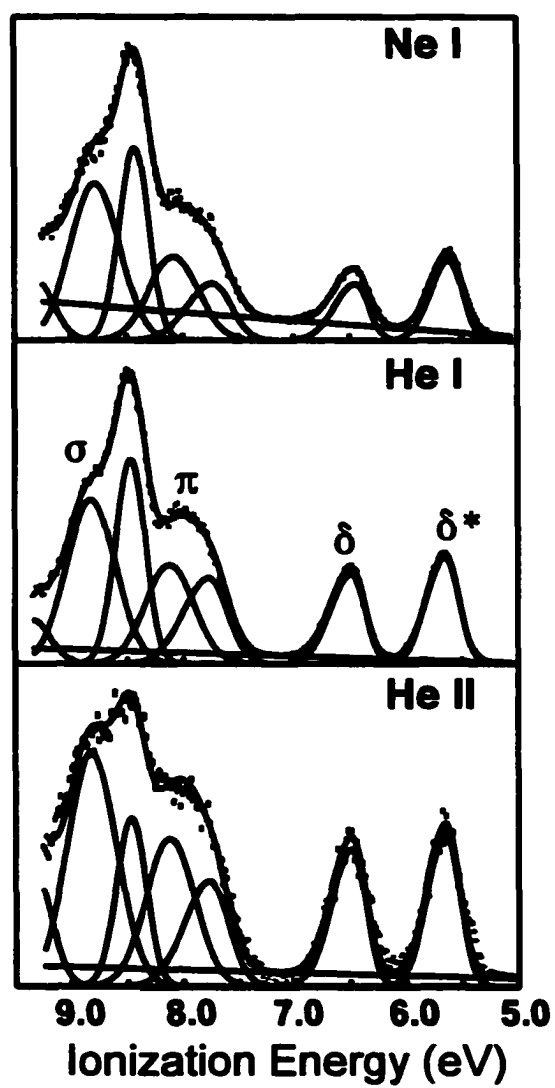
Figure 5.15. Ne I, He I, and He II
photoelectron spectra of $Re_2Cl_4(PMe_3)_4$.
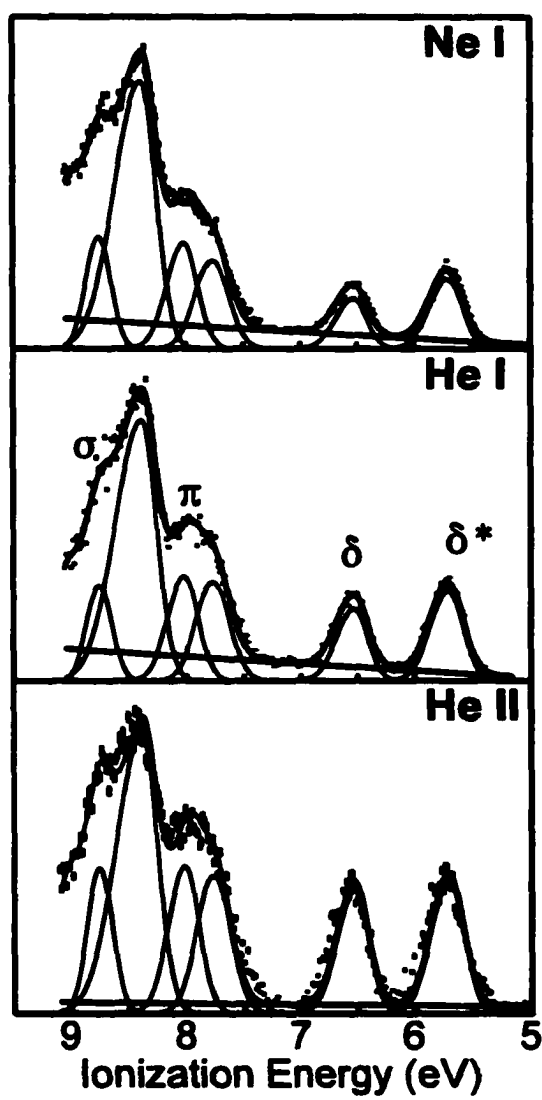
Figure 5.16. Ne I, He I, and He II
photoelectron spectra of $Re_2Br_4(PMe_3)_4$.
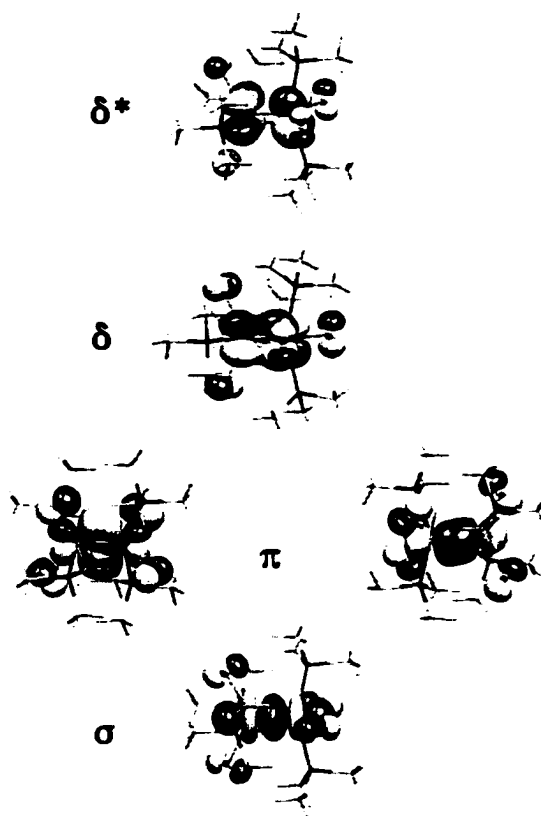
Figure 5.17. Contour plots of the σ, π, δ, and δ* orbitals of $Mo_2Cl_4(PMe_3)_4$ (Contour value = 0.035).
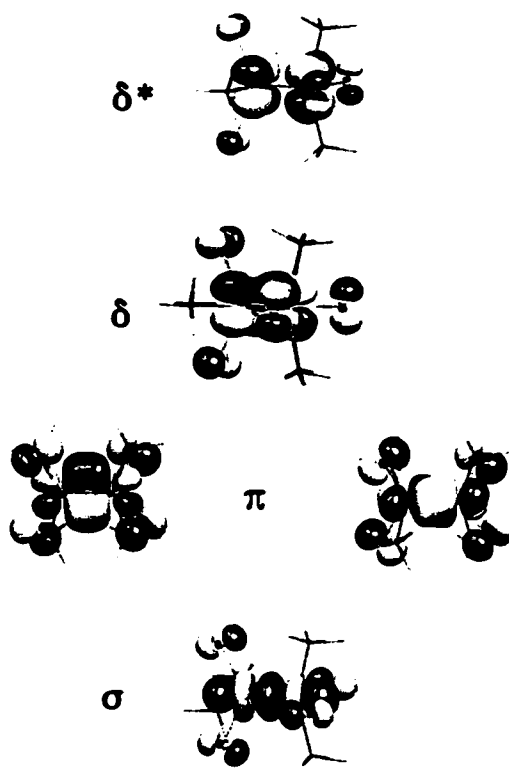
Figure 5.18. Contour plots of the σ, π, δ, and δ* orbitals of $Mo_2Cl_4(PH_3)_4$ (Contour = 0.035).
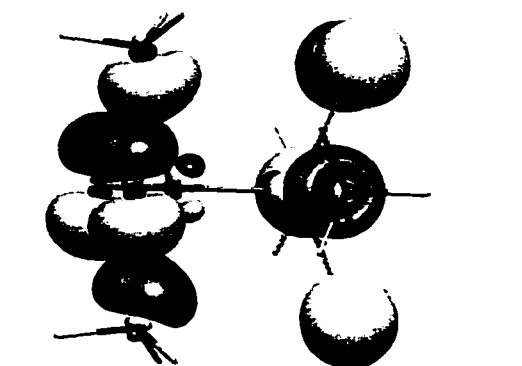
$$e\ [Cl(\pi\perp) - P(\sigma)]$$
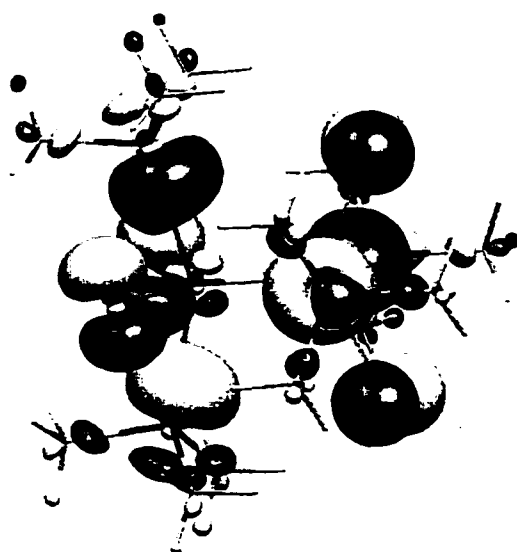
$$e\ [Cl(\pi\perp) - P(\sigma)]$$

Figure 5.19. Contour plots of the $e[Cl(\pi\perp) - P(\sigma)]$ orbitals of $Mo_2Cl_4(PH_3)_4$ (top) and $Mo_2Cl_4(PMe_3)_4$ (bottom). (Contour value = 0.035).

I.E.(δ*) = -0.3χ$_P$ + 6.598
R^2 = 1.00

Cl

Br

δ* Ionization (eV)

5.64
5.68
5.72
5.76
5.8
5.84

2.6 2.7 2.8 2.9 3 3.1 3.2

χ$_P$

I.E.(δ) = -0.13614χ$_P$ + 6.927
R^2 = 0.96

Cl

Br

δ Ionization (eV)

6.48
6.52
6.56

2.6 2.8 3 3.2

χ$_P$
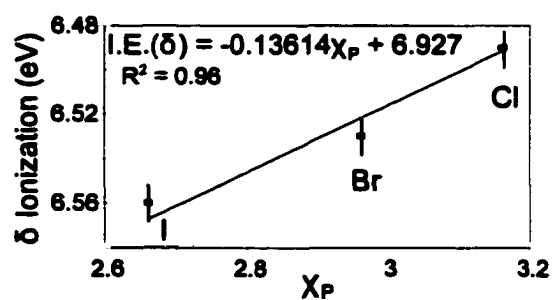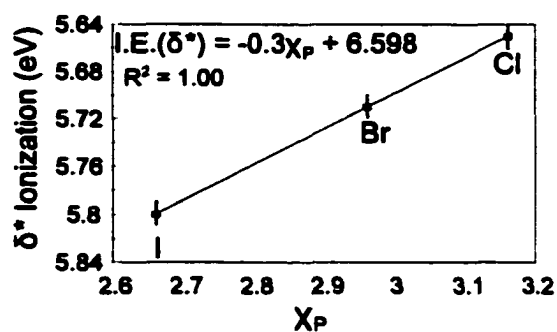
Figure 5.20. Plots of the δ* (top) and δ
(bottom) ionization energies versus Pauling
electronegativity of the halogens for
Re$_2$X$_4$(PMe$_3$)$_4$ (X = Cl, Br, I).

CHAPTER 6

INVESTIGATIONS INTO THE ELECTRONIC STRUCTURE OF THE M₂(CHP)₄ MOLECULES (M = Cr, Mo, W)

$$\text{INVESTIGATIONS INTO THE ELECTRONIC STRUCTURE OF THE } M_2(CHP)_4$$
$$\text{MOLECULES (M = Cr, Mo, W)}$$

Introduction

Since recognition of the existence of a quadruple bond between two transition metal

atoms in 1964,[18] a myriad of studies have focused on obtaining a better understanding of the

nature of the quadruple bond.[17,114,148,149,165,169,171,173,177,210-215] In addition to the large body of work

concentrating on the formation of new molecules containing multiple bonds between two metal

centers, much effort has also been focused toward understanding the reactivity of these

compounds.[17,114,210,216-218] Further inciting interest in the field of metal-metal bonds, a number of

industrial catalysts have been shown to contain Mo-Mo quadruple bonds.[219,220] A current focus in

the field of metal-metal bonds is the incorporation of these molecules into extended clusters and

extended polymeric systems.[102,103,105-111,221-233] As first put forth by Cotton,[18] the formal quadruple

bond between two transition metal atoms can be described as being formed by a σ bond, two π

bonds, and a δ bond. Hence, the electron configuration of molecules containing quadruple bonds

between the metal atoms are described $\sigma^2\pi^4\delta^2$. As such, the majority of the compounds known

to contain quadruply bound metal centers are formed by chromium, molybdenum, and tungsten

in the (II) formal oxidation state.[114]

A large number of the systems known to contain metal-metal multiple bonds also contain

bridging ligands.[17,114] The arrangement of these bridging ligands leads to the general description

of these molecules as paddlewheel complexes. The simplest example of a molecule with the

paddlewheel structural motif is the well-known $Mo_2(O_2CCH_3)_4$. In fact the $M_2(O_2CCH_3)_4$

molecules (M = Cr and Mo) were among the first molecules synthesized that can be described as

containing multiple bonding interactions between the metal atoms.[17] Because chromium is the

only first row transition metal that readily forms metal-metal multiple bonds, molecules

containing quadruple bonds between two chromium atoms are of particular interest. In reality,

the formulation of the quadruple bond between two chromium atoms has been the source of

much contention because of the large variability of the Cr-Cr distance, more than 0.70 Å, in

molecules said to contain quadruple bonds.[17,234,235] By comparison, the metal-metal distances

found when M = Mo or W are found to occur over a much more narrow range.[236] Hence, it

follows that there must be a fundamental difference in the bonding of the chromium molecules

versus that seen for the tungsten and molybdenum analogs. Much discussion has centered on the

importance of configuration interaction to the description of the bond between the two chromium

atoms.[17,237]

An important tool for directly probing quadruple bonds is photoelectron spectroscopy

because it directly measures the energies of the orbitals that constitute the quadruple bond.

Hence, one can learn much about the relative energies of the σ, π, and δ orbitals in the

molecules and how these energies are affected by changing the metal and the bridging ligands.

In the current study, we have obtained the photoelectron spectra of the $M_2(chp)_4$ molecules (M =

Cr, Mo, W). The generalized molecular structure of the $M_2(chp)_4$ system is shown in **6.1**. To

simplify the structure only two of the ligands are fully shown. These systems are directly related

to the previously studied $M_2(mhp)_4$ molecules shown in **6.2**.[238] Our primary interest in these

6.1   **6.2**
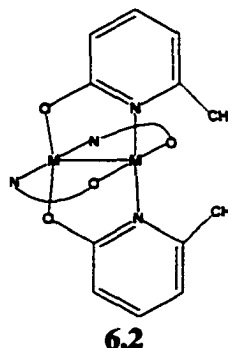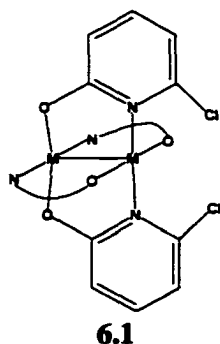
systems lies in the 0.066 Å increase in the Cr-Cr distance when the mhp^{-1} ligands are replaced

with chp^{-1} ligands.[239] The corresponding increase in the M-M bond distances of the molybdenum

and tungsten are only 0.013 Å and 0.016 Å, respectively. The net result is that the Cr-Cr bond

distance of $Cr_2(chp)_4$ is 1.955 Å, much closer to the Cr-Cr distance, 1.97 Å,[240] found in the gas-

phase structure of $Cr_2(O_2CCH_3)_4$ than the corresponding distance found in $Cr_2(mhp)_4$.[239] Hence, a

natural question concerning the electronic structure of the $Cr_2(chp)_4$ system is whether the

electronic structure of $Cr_2(chp)_4$ is more like $Cr_2(O_2CCH_3)_4$ or $Cr_2(mhp)_4$. To complement the

experimental studies, calculations at several levels of sophistication, including Fenske-Hall and

density functional, have been completed. From the photoelectron spectroscopic and

computational studies we have gained a better understanding of metal-metal bonds in these

systems and the strong influence the ligand donor orbitals have on these metal-metal bonds.

Experimental

General Methods. All manipulations were carried out using an Argon (Ar) or

dinitrogen (N_2) atmosphere and standard air and moisture sensitive techniques in a Vacuum

Atmospheres Glovebox or Schlenk line. Solvents were distilled from CaH_2 or Na/Benzophenone

ketyl. Air was removed via freeze-pump-thaw cycles. All reagents were purchased from

Aldrich unless otherwise stated and used without further purification. The $M_2(chp)_4$ molecules

(M = Cr, Mo, and W) were synthesized and purified according to literature procedures.[241]

Photoelectron spectra. The photoelectron spectra were recorded using an instrument

that features a 36 cm radius, 8 cm gap McPherson hemispherical analyzer with custom-designed

sample cells, detection system, and control electronics.[31] The excitation source was a quartz

lamp with the ability, depending on operating conditions, to produce He Iα (21.218 eV) or He

IIα (40.814 eV) photons. The ionization energy scale was calibrated by using the $^2E_{1/2}$ ionization

of methyl iodide (9.538 eV) and the Ar $^2P_{3/2}$ ionization (15.759 eV). The argon $^2P_{3/2}$ ionization was also used as an internal calibration lock for the energy scale during He I and He II data collection. Resolution (measured as full-width-at-half-maximum of the argon $^2P_{3/2}$ ionization) was 0.020-0.028 eV during He I data collection. Assuming a linear dependence of analyzer intensity to the kinetic energy of the electrons within the energy range of these experiments, all data were intensity corrected with the experimentally-determined analyzer sensitivity function.

Because the ionization sources used to collect the photoelectron spectra are not monochromatic, the spectra must be corrected for ionization features that do not originated from the desired source line.[33] Specifically, spectra collected with the He Iα ($1s^2 - 1s2p$; 21.218 eV) were corrected for ionization features from the He Iβ line ($1s^2 - 1s3p$; 23.085 eV), which have 3% of the intensity of the ionization features from the He Iα. The spectra collected with the He IIα line ($1s - 2p$; 40.814 eV) were corrected for the ionization features from the He IIβ line ($1s - 3p$; 48.372 eV), which has 12% of the intensity of the He IIα line.

Due to extensive decomposition of the samples when placed in direct contact with the stainless steel surface of the cell, the samples were placed directly into the brass argon inlet of the stainless steel cell. When the samples were placed in the brass argon inlet, the samples all sublimed cleanly with no detectable evidence of decomposition products in the gas phase or as a solid residue. To test the reproducibility of the spectrum, spectra were collected on different days. No changes were detected in the spectra. The sublimation temperature ranges for the $M_2(chp)_4$ molecules (°C at $\approx 10^{-4}$ Torr) were M = Cr (245-320), Mo(200-250), and W(300-350). The temperatures were measured using a "K" type thermocouple attached directly to the ionization cell through a vacuum feedthrough.

Data Analysis. In the figures of the photoelectron spectra, the vertical length of each

data mark represents the experimental variance of that point.[34] The ionization bands are

represented analytically with the best fit of asymmetric Gaussian peaks. The number of peaks

used was the minimum necessary to get an analytical representation of the He I spectrum. For

fitting the He II spectra, the peak positions and half-widths were fixed to those of the He I fit.

The confidence limits for the relative integrated peak areas are $\pm 5\%$. The primary source

of uncertainty is the determination of the baseline. The baseline is caused by electron scattering

and is taken to be linear over the small energy range of these spectra. The fitting procedures

used to fit the spectra have been described in more detail elsewhere.[34]

DFT studies.

Gaussian98.[35] Density functional calculations were performed using the Gaussian98

package. Geometries were taken from the published crystal structures and optimized to D_{2d}

symmetry. The B3LYP method was used, and LANL2DZ basis sets was used for both the

metals and ligands.[35,52,53,82]

ADF2000.01 program.[36] The numerical integration procedure was developed by te

Velde and co-workers.[37,38] The BLYP method was used for all calculations. Calculations using

the PW91 functional produced comparable results. The atomic orbitals on the metal centers were

described by the uncontracted triple-ζ STO basis set (set IV) that is readily available with the

ADF package. All other atomic orbitals were described by the available uncontracted double-ζ

basis sets. The $1s^2$ configuration on nitrogen, carbon, and oxygen; $1s^2s^22p^6$ configuration on Cl;

and the $1s^22s^22p^63s^23p^63d^{10}$ for Mo were assigned to the core and treated by the frozen-core

approximation. Relativistic effects were included for the $W_2(chp)_4$ calculations by the scalar

ZORA formalism implemented as a part of the ADF2000 program.[56-60] The molecular structure

of $M_2(chp)_4$ was obtained from the published crystal structures and optimized to D_{2d} symmetry.

Values for ionization energies can be determined by two different computational

procedures. As a first approximation, the Kohn-Sham orbital energies from the ground state

calculations of the "neutral" molecule are directly analogous to the experimental ionization

energies ($\epsilon_i \approx$ -I. E.).[66,67] While the relationship only strictly applies for the the highest occupied

molecular orbital, recent studies have shown the relationship to hold for all of the valence

orbitals. In order to obtain a more direct comparison of the relative Kohn-Sham energies, the

calculated orbital energies are shifted according to equation (6.1),

$$\varepsilon_{shifted} = |\varepsilon_i| + \Delta_i$$
$$\Delta_i = I.E.(MN\,\pi) - |\varepsilon(MN\,\pi)|$$

$$(6.1)$$

which adjusts the energy of the highest occupied molecular orbital to the experimental ionization

energy. The adjustments necessary to achieve this are then applied to all the other occupied

molecular orbitals in the system. This equation applies to results from both the Gaussian98 and

ADF packages. For the Gaussian98 results, $\Delta_i = 1.94$ (Cr); 1.33 (Mo); 1.30 (W); the

corresponding values for the ADF2000 calculations are 2.37 (Cr), 1.51 (Mo), and 1.36 (W).

Calculated ionization energies can also be determined by comparing the total energy of

the neutral molecule to the total energies of the successive ionic states, where one electron has

been removed from the orbital of interest. Ionization energies obtained in this manner are

vertical ionization energies (the geometry is assumed to be constant in the neutral and the cation

states). These ΔE_{SCF} energies more correctly represent the ionization process because they

account for the electron relaxation that occurs in the molecule when an electron is removed. For

comparison, Fenske-Hall molecular orbital calculations have been performed.[39] The ADF-

optimized coordinates were used as the input coordinates for the Fenske-Hall calculations.

Contracted double-zeta basis functions were used for the Mo valence d atomic orbitals, the

valence 2p atomic orbitals of N, C, and O, and the 3p atomic orbitals of Cl.[39,83-85] Basis functions

for the metal atoms were obtained for the 1+ oxidation state. Ground state atomic configurations

were used for the basis functions of all other atoms. The Fenske-Hall method overestimates the

spread of orbital energies in molecules. To account for this, the energy scale of the Fenske-Hall

method must be scaled to match the experimental energy scale. For this case, the experimental

energy difference between the δ and the π ionizations of $W_2(chp)_4$ was used to calibrate the

energy scale of the Fenske-Hall calculation. The experimental energy difference of these two

ionizations is only 62% of the orbital energy difference calculated by the Fenske-Hall method.

In order to facilitate a direct comparison between the density functional results and the Fenske-

Hall results, the orbital energies from the Fenske-Hall calculation were scaled according to

equation (6.2), where $\Delta_i = 2.14$ (Cr); 1.50 (Mo); 1.65(W).

$$\varepsilon_{scaled} = 0.62 \times \left|(\varepsilon_i)\right| + \Delta_i$$
$$\Delta_i = I.E.(MN\,\pi) - \left|\varepsilon(MN\,\pi)\right| \qquad (6.2)$$

Preliminary Considerations

Because orbital mixing depends on both the energy matching between fragment orbitals

as well as the overlap of the constituent fragment orbitals, a complete understanding of the

bonding in the $M_2(chp)_4$ analogs lies in a firm knowledge of the bonding in the constituent

molecular fragments: M_2^{4+} and $(chp)_4^{4-}$. Although the bonding in the M_2^{4+} unit is easily

understood in the framework of the generalized M-M orbital diagram, one cannot understand the

orbital combinations of the $(chp)_4^{4-}$ fragment without an appreciation of the consequences of the

molecular symmetry.

M-M orbitals. As stated previously, the bonding in the dimetal unit can be qualitatively

understood within the molecular orbital model developed by Cotton. However, a more thorough

analysis of the bonding requires a complete symmetry analysis. Under D_{2d} symmetry, the metal-

metal bonding orbitals of the M_2^{4+} unit have the symmetry labels: $\sigma(a_1)$, $\pi(e)$, $\delta(b_1)$, $\delta^*(a_2)$,

$\pi^*(e)$, and $\sigma^*(b_2)$. In addition, there is another δ orbital combination of b_2 symmetry and a δ^*

combination of a_2 symmetry that are used for M-L σ bonding. All of the molecular orbitals of

the M-M bond have different symmetries and should give rise to separate ionization features in

the photoelectron spectrum. However, this treatment does not preclude the possibility that the

ionizations from the M-M orbitals are accidentally degenerate and occur under the same

ionization band in the spectra. This is a simplified view of the metal-metal bonding orbitals

because it assumes the orbitals are completely metal-based.

Ligand Bonding Considerations.

<u>2-chloro-6-oxo-pyridinate.</u> Before addressing the possible interactions between the

ligand-based orbitals and the orbitals of the dimetal fragment, it is necessary to explore the

orbital combinations of the (chp)$_4^+$ in detail. To understand the combination orbitals of (chp)$_4^+$,

one must first have a thorough knowledge of the bonding in a single chp^{-1}. In particular, the

highest occupied π-type orbital of the chp^{-1} is of interest because it can serve as a π-donor to the

dimetal fragment. Similarly, the lowest unoccupied orbital of the chp^{-1} is of interest because it

can serve as a π-acceptor of electron density from the metal-metal bonding orbitals. Whether the

pyridinate ligand serves as a net π-donor or π-acceptor will depend on the extent of the

interaction between the metal and ligand. However, considering the fact that previous

photoelectron studies of the $M_2(mhp)_4$ molecules (M = Cr, Mo, W) revealed the presence of

numerous ligand-based π-type ionizations that lie in the vicinity of the σ and π ionizations, it

seems likely that the π-donor ability of the pyridinate ligand will be of great importance to the

electronic structure of the $M_2(chp)_4$ series. Because the electronic structures of the $M_2(chp)_4$ series are expected to be similar to those of the $M_2(mhp)_4$ analogs, it is useful to compare the electronic structure of the chp[-1] ligand to that of the mhp[-1] ligand. This provides an opportunity to explore the effects of replacing a methyl group with a chlorine atom. In comparison to a methyl group, chlorine is a better π-donor but a much weaker σ-donor. Therefore, it is expected that all of the orbital energies from the chp[-1] ligand will be stabilized in comparison to the corresponding energies of the mhp[-1] ligand. Given the π-donor ability of the chlorine atom, an interesting question is whether any Cl character is present in the highest occupied orbitals of chp[-1]. A correlation diagram for the four highest occupied orbitals of the mhp[-1] and chp[-1] molecules, calculated by the Gaussian 98 suite of programs, is presented in Figure 6.1. Interestingly, the highest occupied molecular orbital of chp[-1] is the same as that of mhp[-1]. For the highest occupied molecular orbital, the orbital characters at the nitrogen and oxygen atoms consist of antisymmetric $p\perp$ orbitals, the same orbital characters seen for both the acetate and formamidinate ligands studied previously.[142] As expected from the electronegativity of chlorine, the orbital energies of the chp[-1] are significantly stabilized in comparison to the orbitals of mhp[-1]. The stabilizations seen in the orbital energies give a measure of the charge effect for replacement of the methyl with a chlorine. To distinguish between the orbitals, the orbitals are labeled: 1, 2, 3, and 4 with the highest occupied molecular orbital corresponding to 1. While 1 and 2 are stabilized by -0.44 eV and -0.40 eV, respectively, when the methyl group is replaced by chlorine, the nitrogen lone pair, 3, undergoes a much greater stabilization of -1.12 eV due to the presence of halogen character in the orbital that mixes into the orbital in a bonding fashion. The fourth

orbital is stabilized by -0.56 eV upon replacement of the methyl with chlorine. Given that 2, an

oxygen lone pair orbital, and 3, the nitrogen lone pair orbital, are expected to be involved in M-L

σ bonding, the relative energies of these orbitals in the mhp^{-1} and chp^{-1} analogs gives a

preliminary measure of the relative σ-donor ability of the two ligands. The large stabilization of

the nitrogen lone pair orbital as the methyl is replaced by chlorine leads to the conclusion that the

nitrogen lone pair of the chp^{-1} will be a much worse σ-donor than the nitrogen lone pair of mhp^{-1}.

In light of the fact that the oxygen lone pair is also stabilized in the chp^{-1} anion relative to the

oxygen lone pair of mhp^{-1}, the overall donor ability of the chp^{-1} is expected to be much less than

mhp^{-1}. These conclusions are in line with the known behavior of the neutral ligands, where

substitutions at the 6 position of the substituted pyridine have a dramatic effect on the relative

basicities of the nitrogen and oxygen. The neutral ligands provide a classic example of

6.3
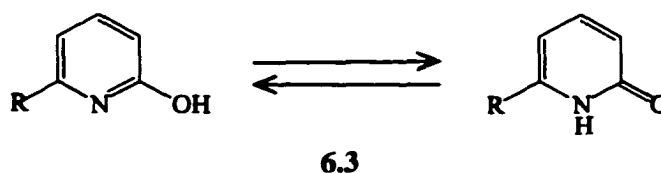
heterocyclic tautomerism as shown in (6.3).[242] When R = methyl, both the pyridone and

pyridinol forms exist in the gas phase.[242,243] However, replacement of the methyl with Cl

significantly reduces the basicity of the nitrogen atom so that the molecule exists exclusively as

the enol form.[243] By analogy, the reduced basicity of the nitrogen atom implies the ligand will be

a weaker electron donor to a metal center than the methyl analog.

(chp)$_4$ π-type combination orbitals. The photoelectron spectra of the M$_2$(mhp)$_4$

analogs contain features due to the ionization of ligand-based combinations that occur on top of

the ionizations from the M$_2$ σ and π. From previous studies, the ligand-based ionizations that

obscure the σ and π originate from the symmetry combinations of the mhp^{-1} HOMO. Since the

highest occupied orbital of the chp^{-1} is equivalent to that of mhp^{-1}, it follows that the symmetry combinations of the chp^{-1} HOMO will contribute substantially to the electronic structure of the M$_2$(chp)$_4$ molecules. Under D$_{2d}$ symmetry, the HOMO orbitals of the four chp^{-1} ligands give combination orbitals of b$_1$, a$_2$, and e symmetry. Based on the symmetry labels alone, these orbital combinations have the appropriate symmetries to interact with the metal-metal δ(b$_1$), δ*(a$_2$), π(e), and π*(e).

Symmetry labels only reveal which orbitals have the potential for mixing but do not reveal which orbitals actually mix together. Orbitals of the same symmetry will only mix if the nodal properties are favorable. To determine the nodal properties of the ligand combinations, the orbital combinations of the highest occupied molecular orbital of chp^{-1} are shown in Figure 6.2. Because the overlap between individual ligand orbitals is small, the four ligand combinations will be essentially degenerate in the absence of interaction with the metal. Any bonding or antibonding interactions with the orbitals of the metal-metal bond will serve to remove the degeneracy of these four ligand orbital combinations. Since the e combination does not have the correct nodal properties to interact with either the M$_2$ π or π* orbitals, it will remain nonbonding in the molecular framework. The b$_1$ and a$_2$ orbitals, on the other hand, have the appropriate symmetry and nodal properties to interact with the metal-based δ and δ* orbitals. Focusing first on the ligand a$_2$ orbital, the nodal properties are appropriate for a strong interaction with the unfilled δ* orbital. This will serve to stabilize the ligand-based a$_2$ combination relative to the e symmetry combination. Turning the focus towards the ligand-based b$_1$ orbital, the nodal properties on the nitrogen and oxygen atoms are antisymmetric. Therefore, if the ligand has a bonding interaction with the δ through the oxygen atom, it must be antibonding with the respect to the δ through the nitrogen atom. If the relative amounts of oxygen and nitrogen character in this orbital were the same, then this ligand-based b$_1$ would be nonbonding with respect to the δ.

Fortunately, this orbital is predominantly oxygen-based so that the interaction of oxygen should

dominate that of the nitrogen. As such, this orbital is expected to interact with the metal-based δ.

Since both the ligand-based b_1 and δ orbitals are filled, the ligand-based b_1 combination serves to

destabilize the δ through a filled-filled interaction. As a consequence, the ligand-based b_1 orbital

should be stabilized relative to the e combination but not as much as the a_2 combination. Of

course, this treatment assumes the ligand-based orbitals remain pure combinations of the highest

occupied orbital. This is most certainly not the case for the molecule as can be readily seen from

the mixing in of σ bonding character into the highest occupied π-type orbitals of e symmetry in

Figure 6.2. Due to the inherent symmetry of the molecule, any π-type orbital of chp^{-1} results in

orbital combinations of a_2, b_1, and e symmetry for (chp)$_4^{+}$. In reality, these ligand-based

combinations could mix into the HOMO-based combinations and change the nature of the

interactions between the ligand-based orbitals and the metal-metal orbital combinations. A

telltale sign for mixing of the ligand-based orbitals of the same symmetry will be the presence of

any chlorine character in the highest occupied ligand-based orbitals of the M_2(chp)$_4$ series

because the highest occupied molecular orbital of chp^{-1} does not contain any chlorine character.

Cl$_4$ in-plane combinations. Given that the only difference between the M_2(chp)$_4$

molecules and the previously studied M_2(mhp)$_4$ series is the replacement of the methyl group at

the 6 position with a Cl, it is also useful to examine the Cl lone pair combinations that cannot

interact with the π-type orbitals of the pyridinate ligands. That is, we need to look at the

combinations of Cl lone pair orbitals that are parallel to the plane of the aromatic ring. One of

these "in-plane" combinations is involved in bonding to the ring system and will not be

addressed here. The other "in-plane" combination is oriented 90° with respect to the Cl lone pair

involved in C-Cl bonding. Since four Cl atoms are present in the system, it is useful to examine

the symmetry combinations of the lone pair orbitals under D_{2d} symmetry. The Cl lone pair

combinations, shown in Figure 6.3, form combination orbitals of a_1, b_2, and e symmetry that can interact with the metal-metal σ, σ^*, and π-type orbitals (both M_2 π and π^*), respectively. It is highly unlikely that the $Cl_4(e)$ combination will interact with both the π and π^* orbitals of the metal-metal bond. In terms of energy matching the interaction with the π orbital will be favored over the interaction with the π^* orbitals. Any interactions between these chlorine lone pair combinations and the M-M orbitals will serve to perturb the energies of the metal-based orbitals.

Results

He I photoelectron studies. The He I photoelectron spectra of the $M_2(chp)_4$ molecules (M = Cr, Mo, W), collected in the 5 to 15 eV energy range are presented in Figure 6.4. The ionization features from 9 to 15 eV are similar for the $M_2(chp)_4$ series, indicative of ionizations from predominantly ligand-based orbitals. In addition to the ligand-based ionizations, it is expected that the ionizations from the metal-ligand σ bonding orbitals occur in this region of the spectra. The metal character in these M-L σ bonding orbitals, while much less than the metal character in the metal-based orbitals, will still cause slight differences in the spectrum as the metal is changed. In addition, the distances between the chp^{-1} ligands increase as M = Cr < Mo≈W. Since the ligand-based orbitals are combination orbitals, it follows that the degree of mixing of these orbitals will be directly dependent on the distances between the individual chp^{-1} ligands. Shorter distances between the ligands leads to stronger interactions between the orbitals of the individual chp^{-1} ligands. Stronger interactions between the ligands will then result in a larger spread of the ligand-based combination orbitals. Hence, it is no surprise that the ligand-based region of the spectrum does undergo changes as the metal is changed. However, it is clear that these changes are not attributable to the ionization of the metal-metal bonding orbitals because, as the metal is changed from Cr to Mo to W, the metal-based ionizations should be

destabilized. Therefore, the metal-based ionizations must lie in the 5 to 9 eV energy range of the photoelectron spectra.

To focus on the energy region containing the metal-based ionizations, the photoelectron spectra were recollected in the 5 to 9 eV energy range as shown in Figure 6.5. From these photoelectron spectroscopic studies, some initial ionization band assignments are possible. The first ionization band in the spectra of the $M_2(chp)_4$ analogs originates from the ionization of the metal-metal δ orbital. As expected, the δ ionization is destabilized as the metal is changed from Cr to Mo to W, and the intensity of the δ ionization band for the $Cr_2(chp)_4$ molecule is extremely low in comparison to the Mo and W analogs. This is not a surprise considering the values for the calculated theoretical cross-sections of Yeh and Landau: Cr (9.230), Mo (26.27), and W (24.83). That is, the calculated cross section for a Cr3d orbital is only one-third that of the molybdenum or tungsten d electrons so ionizations from Cr-based orbitals are expected to be much less intense than those from Mo- or W-based orbitals. For each of the spectra, the most intense portion of the spectra in the 5 to 9 eV energy range occurs between 7.5 and 8.5 eV. The constancy of this ionization feature as the metal is changed leads to the assignment of this feature in each spectrum to the ionization of the ligand-based b_1 and e. In addition, a shoulder appears on the low binding energy side of this ligand-based ionization feature (7.41 eV) for the $W_2(chp)_4$ spectrum. From the ionization trends, this shoulder results from the ionization of the W-W π orbital. On the high binding energy side of the intense ligand-based band is another shoulder at around 8.35-8.50 eV for all of the spectra shown. This is assigned to the ligand-based a_2 ionization that is stabilized away from the ligand-based e and b_1 ionizations by the bonding interaction this orbital combination has with the unfilled metal-metal δ^*. For the $W_2(chp)_4$ spectrum, the only ionization that had not been assigned to a feature in the photoelectron spectrum is the metal-metal σ. As can be seen in Figure 6.6, a distinct shoulder appears between the a_2 ionization band and the

ionization band assigned to the b_1 and e ligand combinations. This shoulder is tentatively

assigned to the ionization from the σ orbital. It must be mentioned that this ionization feature

could also be due to a vibrational component of a ligand band, but this is doubtful since no such

band is seen for the other $M_2(chp)_4$ molecules. By analogy to previous studies of dimolybdenum

and dichromium systems containing quadruply-bonded metals, the σ and π ionizations are

initially assigned to occur under the same band as the ligand-based b_1 and e ionizations.[142,244]

He II photoelectron studies. In order to further probe the bonding in the $M_2(chp)_4$

series, photoelectron spectra were recollected using a He II photon source. According to the

Gelius model of photoionization process, molecular cross-sections are the sum of the atomic

cross sections of the atoms that form the molecular orbital.[75,245] Yeh and Landau have performed

calculations to predict the cross-sectional behavior of the atomic elements.[77] The calculated He

II/He I ionization cross-section ratios for the atoms in these molecules are H (0.153); C2p

(0.306); N2p (0.400); O2p (0.639); Cr3d (0.925); Mo4d (0.323); and W5d (0.322).[77] Although

ionizations from Mo- and W-based orbitals are predicted to drop in intensity when He II is used

as the photon source, experimentally these ionizations are known to grow in intensity under He II

radiation with respect to the ligand-based ionizations.[93,246] This error in the calculated cross

sections of Mo and W results because the calculated cross sections do not account the Super-

Koster-Kronig transitions that occur for second and third row transition metal atoms; these

processes greatly increase the intensity of ionizations from orbitals containing metal character.[78]

Qualitatively, ionizations from chlorine-containing ligand orbitals should shrink significantly in

comparison to those from the metal-metal bonding orbitals. In essence, the metal-based

ionizations should grow substantially more than any of the ligand-based ionizations when He II is

used as the photon source so they should be readily identified in the He II spectra. The He I and

He II photoelectron spectra of the $M_2(chp)_4$ molecules are presented in Figures 6.7 (Cr), Figure

6.8 (Mo), and Figure 6.9 (W). The experimental ionization energies and fits for the ionization

features in the 5 to 9 eV energy range are presented in Table 6.1.

From the calculated cross sections, the metal-based ionizations of the $Cr_2(chp)_4$ molecule

should be readily identified because the cross-section of Cr effectively remains the same as the

photon source is changed from He I to He II while all the ligand-based cross sections drop from

He I to He II. Looking at the spectra (Figure 6.7), the first ionization feature of the $Cr_2(chp)_4$

spectrum grows substantially under He II radiation, as expected for ionization of the metal-based

δ orbital. In comparison to the growth in the δ ionization under He II radiation, the growth of

the rest of the spectra is muted. This is expected for bands containing both ligand-based and

metal-based ionizations. Although three asymmetric Gaussians are necessary to fit the band

between 7.5 and 9.0 eV, these Gaussians cannot be assigned to individual ionizations. This band

contains ionizations from the Cr-Cr σ, Cr-Cr π, ligand-based e, ligand-based b_1, and ligand-based

a_2. Nevertheless, an average position for the σ and π ionization is obtainable from the cross-

section changes seen in the Gaussian fits. The first Gaussian drops 36% with respect to the

change in the δ ionization, while the second peak drops 47 %. By comparison, the third

Gaussian drops by 60% when the photon source is changed from He I to He II. From the

Gaussian fits, one might be tempted to assign the positions of the Cr-Cr σ and π ionizations to

the Gaussian peak at 7.86 eV. However, because the ionization profile in this region is

nondescript, no significance can be placed on the fits obtained for this ionization band.

Nevertheless, one can still get a measure of the spectral changes that occur in the spectrum from

the Gaussian fits. A good estimate of the position of the Cr-Cr σ and π ionization positions can

be achieved from the average of the first two peaks, 8.01 eV. Of course, this assignment is

complicated by the presence of the ligand-based ionizations that no doubt overlap with the Cr-Cr

σ and π ionizations. The ionizations under the third Gaussian band clearly correspond to

ionizations from purely ligand-based orbitals because this region of the spectrum shrinks

substantially with respect to the first two bands. While it is clear that this ionization band is at

least partially due to the ionization of the ligand-based a_2 orbital, it is likely that this band also

contains some intensity due to the ionization of the e and b_1 orbitals.

The He I and He II spectra of the $Mo_2(chp)_4$ molecule are presented in Figure 6.8. As

expected, the cross-section changes seen for this system are significantly less than those seen for

the chromium system. Nevertheless, the δ ionization shows the most intensity growth as the

photon source is changed from He I to He II. Once again, the region from 7.5 to 8.5 requires at

least three Gaussians to properly fit the ionization band features. Looking at the cross-section

changes in Table 6.1, peaks 2 and 3 behave similarly as the photon source is changed from He I

to He II, indicating that these peaks contain ionizations from orbitals with similar atomic

makeups. Since the cross section of these peaks do not drop drastically as the photon source is

changed, the Mo-Mo σ and π ionizations must occur in this region of the spectrum.

Unfortunately, the ligand-based e and b_1 ionizations more than likely contribute somewhat to the

intensity of the ionization bands (especially Peak 3). The fourth asymmetric Gaussian band used

to fit the spectrum drops by 35% as the photon source is changed from He I to He II, indicative of

ionizations from ligand-based orbitals. While it is certain that the ligand-based a_2 occurs under

this ionization feature, the ionization more than likely overlaps with the ligand-based e and b_1

ionizations.

The He I and He II spectra of $W_2(chp)_4$ are presented in Figure 6.9. The cross-section

changes seen for this molecule are significantly different from those seen for the chromium and

molybdenum analogs. Clearly, the tungsten cross section does not grow as much under He II as

either the molybdenum or chromium cross section. Nevertheless, this spectrum contains the

most detail of any of the analogs because the W_2 π can be readily identified in the spectrum.

Interestingly, the W_2 π ionization shrinks substantially with respect to the W_2 δ. This implies that the ionization contains substantial ligand character. The assignment of the σ ionization is confirmed by the He II photoelectron spectrum, where the band assigned to the W_2 σ at 8.08 eV is shown to grow with respect to the δ ionization. The ionization feature at 7.86 eV is assigned to the ionization of the e and b_1 ligand combinations, yet this band only drops by 15% with respect to the δ ionization. Similarly, the a_2 ionization, at 8.39 eV, drops by a mere 10% as the cross-section is changed from He I to He II. Although the numerous overlapping ionization bands necessary to fit the spectral features complicate the interpretation of the band intensity changes, the resulting spectral assignments are consistent with those of the chromium and molybdenum analogs.

Computational Studies. To further probe the electronic structure of the $M_2(chp)_4$ analogs, density functional studies were initiated. The computational studies provide theoretical support for the experimentally-determined ionization energies. In addition, Fenske-Hall calculations were performed for direct comparison to both the experimental ionization energies and the results from the density functional studies. The calculated orbital energies from the density functional studies as well as the Fenske-Hall orbital energies are presented in Table 6.2. To facilitate the comparison of the Fenske-Hall results to the experimental results, the Fenske-Hall orbital energies were scaled to decrease the spread of the orbital energies. The scaling factor was 0.64, the factor necessary to make the spread of the δ and π orbital energies match the experimental spread in the ionization energies of $W_2(chp)_4$.

All of the computational methods employed in this study predict the highest occupied orbital of the $M_2(chp)_4$ series to be the metal-metal δ orbital. Validating the simple model developed in the preliminary discussion section, the next five ionizations originate from the M_2 σ and π ionizations as well as the b_1, e, and a_2 ligand combinations. The ADF calculations predict

that these orbitals occur within an energy range of 0.35 eV (Cr), 0.41 eV (Mo), and 0.72 eV (W).

Similarly, the Gaussian calculations predict the energy range for the next 5 orbitals to be 0.52 eV

(Cr), 0.50 eV (Mo), and 0.71 eV (W). Hence, the calculations agree with the experimental

conclusion that the ionizations from the σ, π, e, a_1, and a_2 orbitals occur as overlapping

ionization features. Only for the tungsten case are the ionizations split so that definitive

ionization band assignments are possible. Unfortunately, the density functional calculations

predict the ligand-based b_1 and e orbitals to lie above the M-M σ and π for M = Cr, in direct

conflict with the photoelectron studies. For the molybdenum analog, the calculations

erroneously predict the Mo-Mo π orbital to be the most stable of the five orbital set studied. In

addition, the calculations predict the σ and π orbitals to be split by 0.64 eV (ADF) and 0.46 eV

(Gaussian98). Indeed, the density calculations predict the splitting of the σ and π orbitals to be

greater than the calculated splitting of the σ and π orbitals of $W_2(chp)_4$: 0.34 (ADF) and 0.45 eV

(Gaussian98). For all quadruply-bonded molybdenum molecules studied to date, the σ and π

ionizations are seen to be accidentally degenerate; therefore, it is assumed that the calculations

overestimate the splitting of the σ and π orbitals of $Mo_2(chp)_4$. Interestingly, the three ligand-

based ionizations are energetically ordered as predicted in the preliminary considerations. That

is, the ligand-based e and b_1 orbitals are calculated to be degenerate or nearly so for all three

molecules, and the a_2 is calculated to be stabilized relative to the other two ligand-based

ionizations. The Fenske-Hall calculations overestimate the splitting of the metal-metal σ and π

orbitals, but this is a common occurrence for the orbital energies from Fenske-Hall calculations.

However, the Fenske-Hall calculations do place the σ and π orbitals above all the ligand-based

orbitals. Qualitatively, these orbital orderings are in better agreement with the spectroscopic

results for both the $Mo_2(chp)_4$ and $Cr_2(chp)_4$ molecules than are the orbital orderings produced by

the density functional calculations.

Although the Kohn-Sham orbital energies have been shown to be good approximations

to experimental ionization energies,[66,67] a better model of the experimental process lies in the

calculation of the ΔE_{SCF} energies for the molecules. The ΔE_{SCF} energies calculated by the ADF

program are presented in Table 6.3 along with the orbital compositions. Unfortunately, the

ΔE_{SCF} energies do not improve the predicted ionization order relative to what is seen

experimentally. The ligand-based ionizations are still placed above the ionizations from the

metal-metal σ and π orbitals. Nevertheless, the orbital characters and plots are still of interest to

the present study. The orbital characters are presented in terms of atomic characters as well as in

terms of the orbitals of the M_2^{++} and $(chp)_4^{+}$ fragments. These orbital characters correspond to

the ground state molecule. Orbital plots of the metal-metal bonding orbitals are presented in

Figure 6.10. In addition, the orbital plots of the ligand-based e, b_1, and a_2 orbitals are presented

in Figure 6.11. Focusing only on the δ orbitals, the amount of metal character present in the δ

orbital decreases as M = Cr (66%), Mo(60%), and W(55%), and consequently, the amount of

ligand character increases as M = Cr < Mo < W. Specifically, the vast majority of the ligand

contribution to the character of the δ orbitals comes not from oxygen or nitrogen character, but

from carbon character. From the fragment analysis, the major contributing ligand-based

combinations are the $6b_1$ and $5b_1$ orbitals. The $5b_1$ derives from the highest occupied orbital of

chp^{-1} as shown in the preliminary discussion section, and the $6b_1$ originates from the lowest

unoccupied orbital of chp^{-1}. To illustrate the combinations that contribute to the δ orbital, Figure

6.10 contains the orbital plots of the δ orbital in conjunction with the $6b_1$ and $5b_1$ ligand

combination orbitals. Through ligand orbital mixing, the maximum interactions between the

ligand combinations and the metal-metal bonding orbitals are attained. For the δ orbital, mixing

in character from both the $5b_1$ and $6b_1$ orbitals serves to eliminate the orbital contribution from

the nitrogen atom , thereby allowing the interaction between the M_2 δ and the ligand to be a net

antibonding interaction. As such, the M_2 δ orbital is destabilized away from the M_2 σ and π

ionizations orbitals. The relative amounts of $6b_1$ to $5b_1$ ($6b_1:5b_1$) in the δ orbital follow as Cr

(18%:13%), Mo(12%:12%), and W(22%:6%). Although the δ orbitals also have contributions

from the ligand-based $4b_1$ and $3b_1$ orbitals, these contributions are minor in comparison to the $6b_1$

and $5b_1$ contributions and do not change significantly as the metal is changed. As mentioned

previously, all of the π-type orbitals of chp^{-1} give $(chp)_4^+$ combination orbitals of b_1, a_2, and e

symmetry. The σ and π orbitals of the $M_2(chp)_4$ series also undergo mixing with ligand-based

orbitals, but, for the most part, these combinations do not derive from combinations of the

highest occupied orbital of chp^{-1}. This is not a surprising conclusion since the symmetry of the

M_2 σ (a_1) eliminates the possibility of any π-type combinations mixing with the σ. In addition,

the nodal properties of the highest occupied e(π) combination are not favorable for interaction

with the metal-metal π orbitals. The net result is that the molecule is able to maximize the

metal-ligand interactions by varying the ligand combinations that mix into metal-metal bonding

orbitals. The controlling factors for the degree of mixing of ligand orbital combinations into the

metal-based orbitals are: (1) the energy matching between the ligand combination orbitals and

the orbitals of the metal-metal bond and (2) the relative overlaps of the metal- and ligand-based

combinations.

The ligand-based e, b_1, and a_2 orbitals of the $M_2(chp)_4$ molecules are easily understood in

terms of the orbital combinations of the highest occupied orbital of chp^{-1}. However, these ligand-

based orbitals orbitals are not pure combinations of the highest occupied orbital of chp^{-1}. This is

not unexpected due to the numerous π-type combinations with the appropriate symmetry to

interact with the primary e, a_2, and b_1 combinations of the highest occupied orbital of chp^{-1}. As

was discussed in the preliminary discussion section, the ligand b_1 combination of the highest

occupied orbital of the chp^{-1} does not have the appropriate nodal properties to form a completely

bonding or antibonding interaction with the δ orbital. Nevertheless, the nodal properties do allow a net bonding or antibonding interaction between the b_1 ligand combination and the metal-metal δ orbital. In fact, the contribution from the M_2 δ to this orbital varies as M = Cr(11%), Mo(11%), and W(7%). This contribution serves to stabilize the b_1 orbital combination. Although the ligand a_2 combination does not remain a pure homo-based combination orbital, the stabilization of this orbital combination from the ligand-based b_1 and e can still be rationalized in terms of the mixing of the unfilled M_2 δ^* orbital into this orbital.

Discussion

Photoelectron spectroscopy has been particularly useful for discerning the nature of bonding between two transitions metal atoms in the $M_2(X \frown Y)_4$ series, where $X \frown Y$ is a bridging ligand and M = Cr, Mo, W. The $M_2(O_2CCH_3)_4$ series were among the first compounds containing metal-metal bonds to be studied with photoelectron spectroscopy. Through these studies, the bonding in the molybdenum and tungsten analogs has been confirmed as being described by the formal metal-metal bonding scheme: $\sigma^2\pi^4\delta^2$. The assignment of the M-M σ came about as a direct consequence of the significant filled-filled interaction between the M-M σ and the oxygen lone pair on the neighboring molecule in the solid state.[169] This resulted in a destabilization of the M-M σ ionization in comparison to the gas-phase spectrum where axial interactions are not present. For the chromium analog all of the metal-based ionizations occur under one large band so one cannot assign a distinct ionization feature to the Cr-Cr δ in support of the concept that the $\sigma^2\pi^4\delta^2$ electron configuration is but one of many configurations populated in the $Cr_2(O_2CCH_3)_4$ molecule.[169]

Unlike the photoelectron spectrum of $Cr_2(O_2CCH_3)_4$, the photoelectron spectrum of the $Cr_2(mhp)_4$ molecule contains a distinct ionization band that is readily assigned to the ionization

of the δ orbital. Comparing the Cr-Cr bond distances for the two molecules we find that the

distance decreases from 1.97 Å for gas-phase $Cr_2(O_2CCH_3)_4$ to 1.889 Å for solid-state $Cr_2(mhp)_4$.

Clearly, the degree to which the orbitals on the two chromium centers interact will be directly

dependent on the distance between the two chromium atoms. Hence, it is not surprising that the

interactions between the metal-metal bonding orbitals are stronger for $Cr_2(mhp)_4$ in comparison

to $Cr_2(O_2CCH_3)_4$. Also of importance in a comparison of the molecular and electronic structures

of these systems is the inherent symmetry change that occurs between these two molecules:

$Cr_2(O_2CCH_3)_4$ (D_{4h}) and $Cr_2(mhp)_4$ (D_{2d}). Under D_{2d} symmetry, a combination of the highest

occupied π-type orbital has the appropriate symmetry to interact with the Cr-Cr δ, thereby

destabilizing it away from the Cr-Cr σ and π. As has been shown previously, there is no such

interaction possible for the highest occupied ligand orbital under D_{4h} symmetry.[142,244]

The observation of the δ ionization in the photoelectron spectrum of $Cr_2(chp)_4$ marks

only the second time a separate ionization feature for the Cr-Cr δ has been detected in the

photoelectron spectrum of a dichromium molecule. Given that the distance between the two

chromium atoms of $Cr_2(chp)_4$, 1.955 Å, is much closer to the Cr-Cr distance seen in

$Cr_2(O_2CCH_3)_4$ than that seen for $Cr_2(mhp)_4$, the presence of a δ ionization for the $Cr_2(chp)_4$

reveals the importance of the symmetry of the molecule to the observation of the δ ionization in

the photoelectron spectrum of chromium dimers. In essence, the occurrence of the δ ionization

for $Cr_2(xhp)_4$ (x = CH_3 and Cl) is at least partially the result of a filled-filled interaction between

a filled ligand combination and the Cr-Cr δ. Further support for this idea comes from the

photoelectron spectrum of $Cr_2(form)_4$ (form = ditolylformamidine) where a separate ionization

feature is not seen for the δ orbital even though the Cr-Cr bond distance, 1.930 Å, is much

shorter than the corresponding distance seen in $Cr_2(chp)_4$. Given the previous observation that

the metal-metal distance is at least partially dependent on the relative donor abilities of the

ligands,[17] the Cr-Cr distance in the $Cr_2(form)_4$ compound should be the shortest because the form

ligand is the strongest electron donor. In fact the relative donor ability of the ligands should

increase as: $O_2CCH_3^- <$ chp$^- <$ mhp$^- <$ form$^-$. While it is true that the form ligand is a better

overall donor ligand, the symmetry of the $M_2(form)_4$ molecules is D_{4h}, and as such there is no

combination of the highest occupied orbital of the form ligand available to interact with the

metal-metal δ. The greater donor ability of the ligand is of little consequence for destabilizing

the Cr-Cr δ ionization away from the σ and π ionizations if the symmetry of the molecule does

not allow for strong interactions between the ligand donor combinations and the metal-metal

bonding orbitals. To further illustrate the concept that the relative donor ability of the ligand is

an important criterion for the destabilization of the Cr-Cr δ, the $Cr_2(map)_4$ analog was

synthesized, where map corresponds to the deprotonated form of 6-methyl-2-aminopyridine.[247]

This sample has the same symmetry as the $Cr_2(xhp)_4$ analogs, guaranteeing the presence of a

filled ligand combination with the appropriate symmetry to interact strongly with the metal-metal

δ. In addition, the relative donor ability increases as chp$^{-1} <$ mhp$^{-1} <$ map^{-1}. Unfortunately, the

sample decomposed under the conditions of the photoelectron spectroscopic studies so that only

the position of the Cr-Cr δ can be assigned with certainty. However, a stack plot of the

$Cr_2(chp)_4$, $Cr_2(mhp)_4$, and $Cr_2(map)_4$ photoelectron spectra is presented in Figure 6.12. The

position of the δ ionization reveals a strong dependence of the position on the donor ability of

the ligand. The δ ionization energy increases as $Cr_2(map)_4 = 5.91$ eV $< Cr_2(mhp)_4 = 6.66$ eV $<$

$Cr_2(chp)_4 = 7.12$ eV. In addition, the intensity of the δ ionization increases for L = chp $<$ mhp $<$

map and is attributable to increased ligand character in the δ orbital as the mixing between the

ligand- and metal-based orbitals increases.

A comparison of the shift in the δ orbital position as the ligand is changed from mhp^{-1} to

chp^{-1} for the molybdenum, chromium and tungsten analogs is presented in Figure 6.13. Upon

substitution of chp^{-1} for mhp^{-1}, the δ ionization shifts by -0.46 eV ($\pm$ 0.04), -0.35 eV ($\pm$ 0.02), and -0.38 eV ($\pm$ 0.02) for M = Cr, Mo and W, respectively. From this point of view the chromium dimer shows the greatest change in position of the δ ionization upon changing the ligand from mhp^{-1} to chp^{-1}. However, if you take into account the relative errors in the positions of the δ ionizations the differences are much less significant. Although the increase in the Cr-Cr distance when chp^{-1} replaces mhp^{-1} is more than 4 times the respective increase seen in the Mo-Mo and W-W distances, this trend in not reflected in the positions of the M-M δ ionization. This is certainly unexpected because a larger increase in the Cr-Cr distance should manifest itself as a weakening of the δ bond. In any case, the observation of the Cr-Cr δ ionization for the Cr$_2$(chp)$_4$ sheds light on the importance of both the symmetry of the molecule and the donor ability of the ligand to the destabilization of the Cr-Cr δ from the Cr-Cr σ and π orbitals.

Cotton proposed two possibilities as the source of the Cr-Cr bond lengthening effect brought about by substitution of the chp^{-1} for mhp^{-1} in Cr$_2$(xhp)$_4$. (1) The Cl lone pair orbitals interact weakly with metal-based orbitals and donate electron density to the unfilled π^* orbital of Cr$_2$(chp)$_4$. (2) The electron-withdrawing effect of chlorine-substitution weakens the donor strength of the nitrogen atoms and leads to an increase in the chromium-chromium distance by some unknown means.[241] The two possibilities will be addressed in terms of the information gleaned from the photoelectron spectroscopic and computational studies.

As shown by Cotton and coworkers, the substitution of chp^{-1} for mhp^{-1} in the Cr$_2$(mhp)$_4$ molecules produces a significant increase in the Cr-Cr bond distance from 1.889 Å in Cr$_2$(mhp)$_4$ to 1.955 Å in Cr$_2$(chp)$_4$.[241] The corresponding increases in the metal-metal bond distances for the molybdenum and tungsten analogs are only 0.013 Å and 0.016 Å, respectively.[241] Clearly, the Cr-Cr distance is particularly sensitive to change in the ligand. The sensitivity of the Cr-Cr bond distance to axial ligand coordination is a well-known phenomenon. From the gas-phase electron

diffraction studies of $Cr_2(O_2CCH_3)_4$, the Cr-Cr distance is known to be 1.97 Å.[240] However, in

the solid state, in the absence of solvent molecules, the distance between the chromium atoms

increases to 2.29 Å.[248] This large increase in the metal-metal distance in the solid state for the

dichromium system has been attributed to a filled-filled interaction between an oxygen lone pair

orbital of a neighboring molecule with the M-M σ. Alternatively, one can attribute the bond

lengthening effect to direct donation of electron density to the Cr-Cr σ* orbital. The distance

between the oxygen of the neighboring molecule and the chromium atom is 2.33 Å, while the

corresponding distance for the molybdenum analog is 2.64 Å. In addition, the $Cr_2(O_2CCH_3)_4$

analogs are known to have a strong tendency to take up solvent molecules in the axial positions.

This addition of axial ligands then leads to an increase in the Cr-Cr bond distance. The

molybdenum and tungsten analogs, on the other hand, show little if any tendency to coordinate

axial ligands.[17] In addition, systematic studies of the $Cr(O_2CR)_4$ molecules have revealed a

dependence of the Cr-Cr bond distance on the basicity of the O_2CCR^- ligands, with the more

basic ligands leading to shorter Cr-Cr bond distances.[17,249] Of the two effects, the axial donation

is known to cause a larger effect than the basicity of the bridging ligands.

As shown previously in the Figure 6.1, calculations predict that the nitrogen lone pair

orbital of the chp[-1] ligand will be significantly stabilized with respect to the nitrogen lone pair

orbital of mhp[-1]. As a direct result of this stabilization, the chp[-1] ligand should be a poorer donor

than the mhp[-1] ligand. As mentioned previously, the tautomeric behavior of the neutral ligands

lends credence to the argument that the nitrogen lone pair is a weaker Lewis base than the

corresponding nitrogen atom of Hmhp. It has been shown that a decrease in the donor ability of

the ligand will result in a decrease in the splitting of the orbitals of the metal-metal bonding

framework.[250-252] To get an accurate measure of the relative splitting of the metal-metal bonding

orbitals, the energies of at least two of the ionizations from the metal-metal bonding orbitals must

be reliably known. Hence, we are restricted to using the tungsten analogs for which we can readily identify both the δ and π ionizations for our analysis. In support of the analysis, the photoelectron spectra of the $W_2(chp)_4$ are presented as a stack plot with the spectra of $W_2(O_2CCH_3)_4$ and $W_2(mhp)_4$ in Figure 6.14. In addition, Figure 6.15 contains a stack plot of $Mo_2(O_2CCH_3)_4$, $Mo_2(chp)_4$, and $Mo_2(mhp)_4$. The positions of the ionization bands, both metal-based and ligand-based, shift to lower ionization energy as the donor ability of the ligand set increases. The ionization energies for the metal-metal bonding orbitals are presented in Table 6.4 along with the corresponding values for the chromium and tungsten analogs. It is important to note that the assignments presented here for the $M_2(mhp)_4$ analogs are significantly different from those presented by Cotton and coworkers,[238] but similar to the studies of Garner.[253,254] An extensive reevaluation of the photoelectron spectra of the $M_2(mhp)_4$ molecules (M = Cr, Mo, W, Ru, and Rh) and the band assignments has been completed recently.[251] At the time of the original studies, the strength of the M-M σ was not well-understood so many of the papers from the early 1980's assign the M-M σ ionization as occurring in the region of the C-C σ and C-H σ orbitals (greater than 11 eV).[149,238] In addition, the contributions from spin-orbit effects on the metal-metal π ionization were overestimated in the early studies. Today, we know that the metal-metal σ ionization of the molybdenum and tungsten dimers is in many cases accidentally degenerate with the π ionization.[142,144,173] In addition, extensive studies of the multiple bonds between tungsten have not shown definitive evidence of spin-orbit splitting of the W-W π, leading to the conclusion that spin-orbit effects due to the metal are not large enough to be seen at the resolution of the experiment.

For the $W_2(X\frown Y)_4$ systems shown in Figure 6.14, the splitting of the tungsten-tungsten π and δ orbitals increases as $W_2(O_2CCH_3)_4 = 1.75$ eV $< W_2(chp)_4 = 1.82$ eV $< W_2(mhp)_4 = 1.96$ eV. If the metal-metal bonding orbitals were completely metal-based with no ligand

contributions, then the shift would correlate directly with the changes in the metal-metal bond distances. In reality the metal-metal bonding orbitals are now recognized as having extensive contributions from the ligand-based orbitals. As stated previously, the interactions between the ligand combinations and the metal-metal bonding orbitals depends on the donor ability of the ligand as well as the inherent symmetry of the molecule. In terms of the splitting of the δ and π ionizations, the $W_2(chp)_4$ splitting more closely matches that of $W_2(O_2CCH_3)_4$. This follows with the idea that the replacement of the methyl group on the pyridine ligand with a chlorine atom significantly reduces the donor ability of the ligand.

Additionally, the splitting of the metal-metal bonding orbitals will also depend on the availability of ligand orbital combinations of the appropriate symmetry to interact with the orbitals of the metal-metal bond. For the $M_2(xhp)_4$ molecules, the availability of a combination orbital of the highest occupied orbital of the xhp^{-1} molecules leads to the destabilization of the δ orbital, thereby increasing the splitting between the W_2 π and δ. Similar trends are seen for the molybdenum (Figure 6.15) and chromium (Figure 6.16) analogs, but due to the number of overlapping features in the ionization region known to contain the ionizations from the σ and π ionizations of the $M_2(xhp)_4$ molecules, the ionization energies of the σ and π orbitals are altogether uncertain. Changing the donor ligand from mhp^{-1} to chp^{-1} does serve to spread out the overlapping e, b_1, σ, and π ionization somewhat, allowing a full assignment of the ionization band features in the 5 to 10 eV energy region.

By definition, the π-type ligand combinations all produce symmetry combinations of a_2, b_1, and e symmetry. As such, treating only the π-type ligand combinations leads to the conclusion that only the δ and δ^* orbitals interact strongly with the ligand orbitals. The flaw in this argument is that the significance of the interactions of the in-plane chlorine lone pair combinations with the metal-based orbitals has not been addressed. As shown in the preliminary

considerations, the orbital combinations of Cl_4 in-plane lone pairs are of a_1, b_2, and e symmetry. Hence, these chlorine lone pair combinations have the appropriate symmetry and nodal properties to interact with the M_2 σ, π, π^*, and σ^* orbitals. The degree of interaction will be directly dependent on the through-space distance between the metal and the Cl. For the most part, these distances remain constant as the metal in changed: 3.23 Å (Cr), 3.27 Å (Mo), and 3.24 Å (W). Therefore, the overlap between the Cl lone pair combinations should increase as the diffuseness of the metal-based orbitals increases (M = Cr < Mo < W). A simple molecular orbital interaction diagram for the interaction of the Cl_4 b_1 and e combination orbitals with the filled M_2 σ and π is given in Figure 6.17. The splitting of the orbitals will be directly dependent on both the overlap of the ligand- and metal-based combinations orbitals as well as their relative energies. Since the M-Cl distances are long, the interactions between the orbitals of the metal-metal bond and the Cl lone pair combinations are not expected to be extensive. In the computational studies presented here, the interactions of the Cl_4 combination orbitals with the metal-metal orbitals is not extensive. The only direct evidence for the interaction of the Cl_4 orbitals with the metal-metal bonding orbitals is the small contribution of the Cl_4 a_1 orbital to the metal-metal σ orbital.

In the original synthetic work, only the interaction of the in-plane chlorine lone pair orbitals with the M_2 π^* and the weaker donor ability of the chp^{-1} ligand were addressed. In reality, this is an oversimplification of the problem. Just as electron donation from the ligand orbitals to the unfilled σ^* and π^* orbitals of $Cr_2(chp)_4$ will weaken the Cr-Cr bond, it must be recognized that the existence of filled-filled interactions between the metal-metal bonding orbitals and the Cl_4 combinations will destabilize the metal-metal σ and π orbitals and weaken the metal-metal bond. The destabilization results because the metal-based orbitals are antibonding with respect to the ligand combinations. Literature precedence exists for Cr-Cr

bond elongation due to filled-filled interactions between ligand-based combinations and the metal-metal σ and π orbitals. For example, Cotton and coworkers found that the Cr-Cr distance of $Cr_2[(2,6\text{-xylyl})NCC(CH_3)O]_4$ lengthens by 0.076 Å when two CH_2Cl_2 molecules are axially bound in comparison to the Cr-Cr distance in $Cr_2[PhNCC(CH_3)O]_4$, where no axial ligands are bound.[255] Although the best measure for the change in Cr-Cr distance with axial ligation would be comparison to the unsolvated $Cr_2[(2,6\text{-xylyl})NCC(CH_3)O]_4$, the compound is found to always incorporate solvent. Certainly, the Lewis basicity of the Cl lone pairs of CH_2Cl_2 is not strong, yet the Cr-Cr bond distance is definitely influenced by the presence of the CH_2Cl_2 molecules. This effect is even more interesting when one considers the fact that the two Cr-Cl distances are 3.25 Å and 3.35 Å.[255] While the longer distance has been attributed to a nonbonded packing effect, the shorter distance, which is extremely close to the Cr-Cl distance seen in $Cr_2(chp)_4$, cannot be attributed to packing effects. Interestingly, the Cr-Cr distance in $Cr_2[(2,6\text{-xylyl})NCC(CH_3)O]_4\cdot2CH_2Cl_2$, 1.949 Å, is similar to the Cr-Cr distance found for $Cr_2(chp)_4$. Of course, the CH_2Cl_2 molecules of $Cr_2[(2,6\text{-xylyl})NCC(CH_3)O]_4\cdot2CH_2Cl_2$ are oriented along the Cr-Cr bond so as to maximize the interaction with the Cr-Cr σ-type orbitals. The Cl lone pairs in $Cr_2(chp)_4$ do not have the same advantageous overlap with the σ-type orbitals of the Cr-Cr bond. Nevertheless, they can interact to some extent with the Cr-Cr σ and σ^* orbitals as well as the Cr-Cr π and π^* orbitals. If the interaction between the unfilled $Cr_2\ \sigma^*$ and the Cl_4 (b_2) orbital is significant, the ligand-based b_2 will be stabilized and contain some $Cr_2\ \sigma^*$. However, this is not expected to occur in these systems because the energy matching between the Cr-Cr σ^* and the b_2 Cl lone pair combination will not be favorable. From the computational studies presented here, the amount of chlorine character in the M-M δ^*, π^*, and σ^* of $Cr_2(chp)_4$ is predicted to be small as shown by the contour plots of the metal-metal antibonding orbitals in Figure 6.18. Although these computational studies do not predict the amount of Cl contribution to the M-M antibonding

orbitals to be significant, we cannot rule out the possibility that the interactions of the Cr σ^* and

π^* orbitals with the $Cl_4(b_2)$ and $Cl_4(e)$ combinations, respectively, is not an important factor in

lengthening the Cr-Cr bond of $Cr_2(chp)_4$. In addition, it is likely that configuration interaction is

still an important consideration in this system even though we clearly see an ionization from the

Cr-Cr δ.

Conclusions

We have obtained the photoelectron spectra of the $M_2(chp)_4$ molecules (M = Cr, Mo, W).

For each of the systems studied, the first ionization feature in the spectrum is attributed to the

ionization of the M-M δ, marking only the second time a separate ionization feature has been

seen for a dichromium molecule. From our photoelectron studies of $Cr_2(O_2CCH_3)_4$, $Cr_2(form)_4$,

$Cr_2(mhp)_4$, and $Cr_2(map)_4$, we have determined that the observation of a Cr-Cr δ ionization is

dependent on the donor ability of the ligand and the symmetry of the molecule. Both $Cr_2(form)_4$

and $Cr_2(O_2CCH_3)_4$ have D_{4h} symmetry and lack a symmetry combination of the highest occupied

π-type orbital of the ligand to interact with the δ orbital. Such an interaction would serve to

destabilize the Cr-Cr δ away from the σ and π orbitals. As a consequence, a separate ionization

feature for the Cr-Cr δ is not seen in the photoelectron spectra of these molecules. Under D_{2d}

symmetry, a symmetry combination of the highest occupied π-type orbital is available to interact

with the Cr-Cr δ. Consequently, the δ orbital is destabilized away from the positions of the σ

and π. In addition, the intensity of the Cr-Cr δ ionization band correlates with the donor ability

of the ligand: $chp^{-1} < mhp^{-1} < map^{-1}$.

From the ionization energies reported here, the increase in the energy of the δ ionizations

of the $M_2(chp)_4$ series with respect to the energies of the $M_2(mhp)_4$ analogs remains fairly

constant for M = Cr (0.46 $\pm$ 0.04), Mo (0.35 $\pm$ 0.02), and W(0.38 $\pm$ 0.02). By comparison, the

relative increase in the metal-metal distance for the $M_2(chp)_4$ series versus the respective

distances in the $M_2(mhp)_4$ series follow as Cr (0.066), Mo (0.013), and W (0.016). Hence, the

marked increase in the Cr-Cr distance for $Cr_2(chp)_4$ versus that of $Cr_2(mhp)_4$ is not reflected in

the energy of the Cr-Cr δ ionization. However, we do see evidence of the weaker donor ability

of the chp^{-1} ligand versus the mhp^{-1} ligand manifested as a decrease in the spread of the

ionizations from the metal-metal bonding orbitals. In addition, the decrease in the spread of the

ionizations from the metal-metal bonding orbitals correlates with the increase in the metal-metal

bond distances for the $M_2(chp)_4$ molecules versus the $M_2(mhp)_4$ analogs.

Table 6.1. Ionization band assignments and relative areas for $M_2(chp)_4$ (M = Cr, Mo, W).

Peak	Assignment	Position (eV)	He I	He II	$\frac{He\ II}{He\ I}$
		$Cr_2(chp)_4$			
1	δ	7.12	1.00	1.00	1.00
2	$\pi + \sigma + b_1 + e$	7.86	5.33	3.44	0.64
3		8.16	7.83	4.18	0.53
4	$a_2 + b_1 + e$	8.49	10.49	4.19	0.40
		$Mo_2(chp)_4$			
1	δ	6.17	1.00	1.00	1.00
2	$\pi + \sigma + b_1 + e$	7.81	3.60	2.94	0.82
3		8.11	2.38	1.91	0.80
4	a_2	8.42	2.56	1.66	0.65
		$W_2(chp)_4$			
1	δ	5.59	1.00	1.00	1.00
2	π	7.41	2.68	2.10	0.78
3	$e + b_1$	7.86	1.89	1.61	0.85
4	σ	8.08	1.42	1.52	1.07
5	a_2	8.39	1.24	1.12	0.90

Table 6.2. Kohn-Sham and Koopmans' orbital energies from computational studies of $M_2(chp)_4$ (M= Cr, Mo, W).

Orbital Description	Experimental I.E. (eV)	Kohn-Sham Energies (eV)				Koopmans' Energies (eV)	
		ADF		G98		Fenske-Hall	
		Raw	Scaled[a]	Raw	Scaled[b]	Raw	Scaled[c]
$Cr_2(chp)_4$							
Cr-Cr δ (b₁)	7.12	4.75	7.12	5.18	7.12	7.78	7.12
Cr-Cr π (e)	7.89-8.16	5.99	8.36	6.56	8.50	10.51	8.87
Cr-Cr σ (a₁)		6.05	8.42	6.75	8.69	11.30	9.37
(chp)₄ e	8.16 - 8.49 overlaps	5.83	8.20	6.23	8.18	11.33	9.39
(chp)₄ b₁	with a₂ and σ+π	5.88	8.25	6.30	8.24	11.36	9.41
(chp)₄ a₂	8.49	6.18	8.55	6.60	8.54	11.71	9.63
$Mo_2(chp)_4$							
M-M δ (b₁)	6.17	4.66	6.17	4.84	6.17	7.30	6.17
M-M π (e)	~8.01	6.31	7.82	6.85	8.18	10.45	8.19
M-M σ (a₁)		5.67	7.18	6.39	7.71	11.02	8.55
(chp)₄ e	8.09-8.47	5.90	7.41	6.35	7.68	11.34	8.76
(chp)₄ b₁	overlaps with σ +π	5.94	7.45	6.37	7.70	11.41	8.80
(chp)₄ a₂	8.47	6.21	7.72	6.68	8.01	11.75	9.02
$W_2(chp)_4$							
W-W δ (b₁)	5.59	4.23	5.59	4.29	5.59	6.15	5.59
W-W π (e)	7.41	5.51	6.87	6.00	7.30	8.98	7.40
(chp)₄ e	7.86	5.98	7.34	6.44	7.74	11.36	8.92
(chp)₄ b₁		5.98	7.34	6.42	7.72	11.41	8.95
W-W σ (a₁)	8.06	5.85	7.21	6.45	7.75	10.37	8.29
(chp)₄ a₂	8.39	6.23	7.59	6.71	8.00	11.72	9.15

[a] $\epsilon = \epsilon_i + \Delta$ [$\Delta = 2.37(Cr); 1.51(Mo); 1.36(W)$]
[b] $\epsilon = \epsilon_i + \Delta$ [$\Delta = 1.94(Cr); 1.33(Mo); 1.30(W)$]
[c] $\epsilon = 0.64\epsilon_i + \Delta$ [$\Delta = 2.14(Cr); 1.50(Mo); 1.65(W)$]

Table 6.3. ΔE_{SCF} Energies and Orbital Compositions from ADF computational studies of $M_2(chp)_4$ (M = Cr, Mo, W).

Orbital Description	$\Delta E_{SCF}{}^1$	Orbital Compositions	
		Atomic	M_2 and (chp)$_4$ fragments
Cr$_2$(chp)$_4$			
δ (b$_1$)	7.12	66% Cr; 23% C;7 % O; 2% N	67 % δ; 18% 6b$_1$13%5b$_1^a$;6% 4b$_1$; 4% 3b$_1$
π (e)	8.05	66% Cr; 13% C;13% O	67% π; 9% 21e; 9% 20e^a;7% 18e
σ (a$_1$)	8.31	83% Cr; 5% Cr(s); 4% Cl	89% σ; 3% 15a$_1$; 2% 16a$_1$ 3% 14a$_1^b$
(chp)$_4$ e	7.95	21% Cr; 39% C; 21% O; 5% N	55% 20e^a; 22% π; 11% 18e; 6% 19e
(chp)$_4$ b$_1$	8.02	21% Cr; 39% C; 21% O; 5% N	64% 5b$_1^a$; 11% δ; 7% 3b$_1$;9% 4b$_1$
(chp)$_4$ a$_2$	7.66	7% Cr; 67% C;12% O; 14% Cl	51% 5a$_2^a$; 36% 4a$_2$; 6% δ^*
Mo$_2$(chp)$_4$			
δ (b$_1$)	6.17	60% Mo; 31% C; 6% O; 3% N	60 % δ; 12% 6b$_1$; 12% 5b$_1^a$; 7% 4b$_1$; 6% 3b$_1$
π (e)	8.01	69% Mo; 21% O; 4% Cl	70% π; 21% 21e
σ (a$_1$)	7.59	71% Mo; 7% Mo(s); 6% O; 7%Cl; 3% N	74% σ; 8% 15a$_1$; 5% 16a$_1$ 5% 14a$_1^b$
(chp)$_4$ e	7.20	61% C; 26% O; 4% N; 7% Cl	68% 20e^a; 18% 18 e
(chp)$_4$ b$_1$	7.26	11% Mo; 55% C; 24% O;8% N	64% 5b$_1^a$; 11% δ; 10% 3b$_1$; 9% 4b$_1$
(chp)$_4$ a$_2$	7.48	7% Mo; 68% C; 12% O; 14% Cl	48% 5a$_2^a$; 38% 4a$_2$; 6% δ^*
W$_2$(chp)$_4$			
δ (b$_1$)	5.59	53% W; 40% C; 3% O; 4% N	55 % δ; 22% 6b$_1$; 6% 5b$_1^a$; 7% 4b$_1$; 7% 3b$_1$
π (e)	7.01	79% W; 11% O; 2% Cl	82% π; 9% 21e
(chp)$_4$ e	7.48	62% C; 25% O;3% N; 8%Cl	59% 20e^a; 26% 18 e
(chp)$_4$ b$_1$	7.47	6% W; 56% C; 26% O; 7% N; 5% Cl	64% 5b$_1^a$; 7% δ; 9% 3b$_1$; 14% 4b$_1$
σ (a$_1$)	8.06	72% W; 16%W(s); 9% Cl	74% σ; 8% 15a$_1$; 5% 16a$_1$ 5% 14a$_1^b$
(chp)$_4$ a$_2$	7.67	5% W; 70% C; 11% O; 15% Cl	43% 5a$_2^a$; 46% 4a$_2$; 4% δ^*

^{a}combination of highest occupied orbital of chp^{-1}
^{b}combination of Cl$_4$.
$\epsilon = \epsilon_i + \Delta_i$ [Δ_i = +0.059 (Cr); -0.20 (Mo); -0.28 (W)]

Table 6.4. Ionization energies of the metal-metal bonding orbitals of $M_2(O_2CH_3)_4$, $M_2(chp)_4$, and $M_2(mhp)_4$ (M = Cr, Mo, W).

Assignment	Position (eV)		
	$M_2(O_2CCH_3)_4$	$M_2(chp)_4$	$M_2(mhp)_4$
M = Cr			
δ		7.12	6.66
π + σ	8-9	7.8-8.2	8.1-8.3
M = Mo			
δ	6.89	6.17	5.82
π + σ	8.68	7.8-8.1	7.6-8.1
M = W			
δ	6.11	5.59	5.21
π	7.86	7.41	7.17
σ	8.57	8.08	~7.7

Figure 6.1. Correlation diagram of the four highest occupied orbitals of (mhp)⁻¹ and (chp)⁻¹ as calculated by the Gaussian98 program (B3LYP + LANL2DZ).
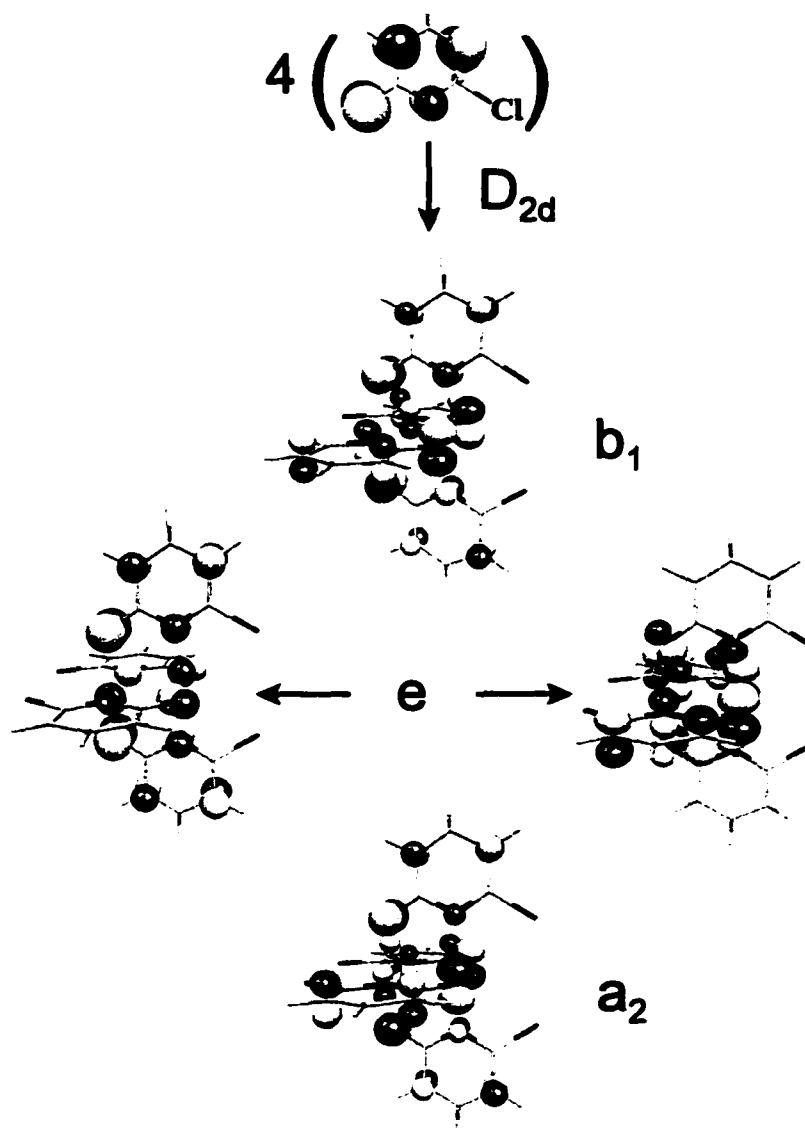
Figure 6.2. D_{2d} Symmetry combinations of the highest occupied of chp⁻¹ calculated by Gaussian98 (Contour value = 0.04).
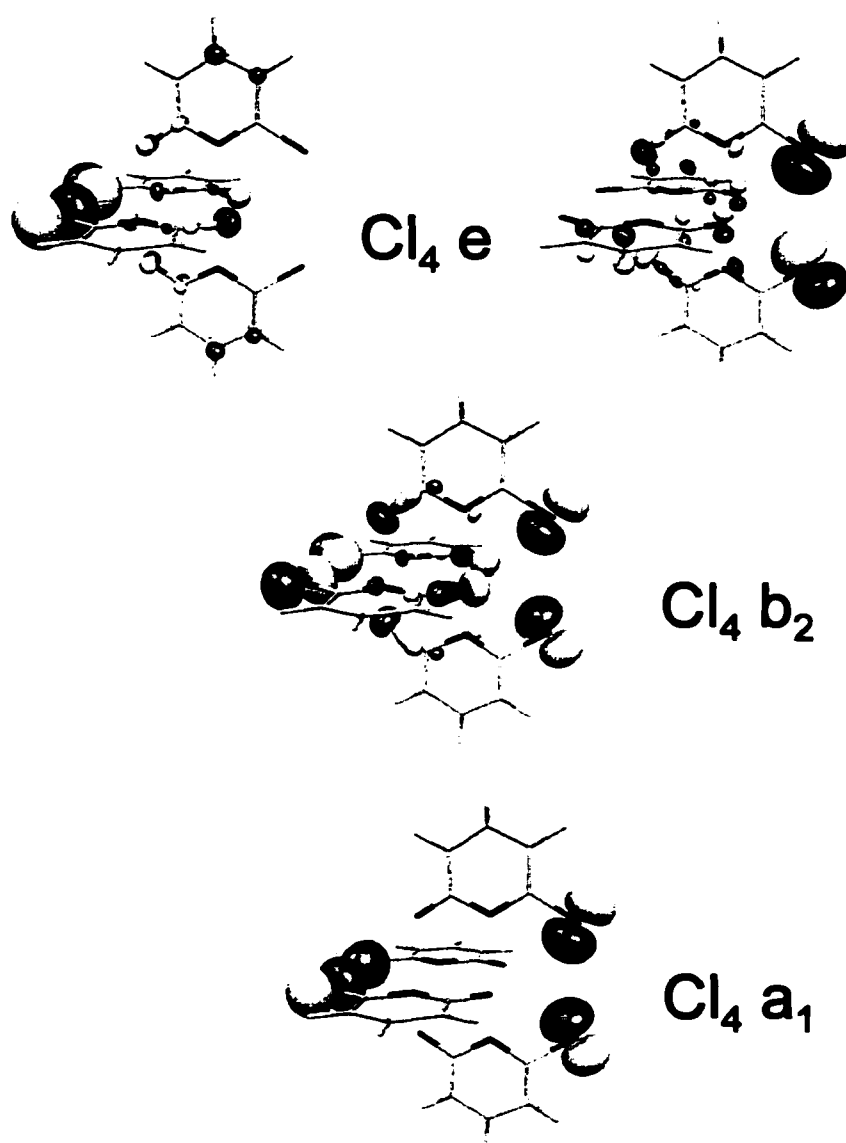
Figure 6.3. D_{2d} symmetry combinations of the in-plane chlorine lone pair orbitals of (chp)$^+$ that can interact with the M-M bonding orbitals (Contour value = 0.04).
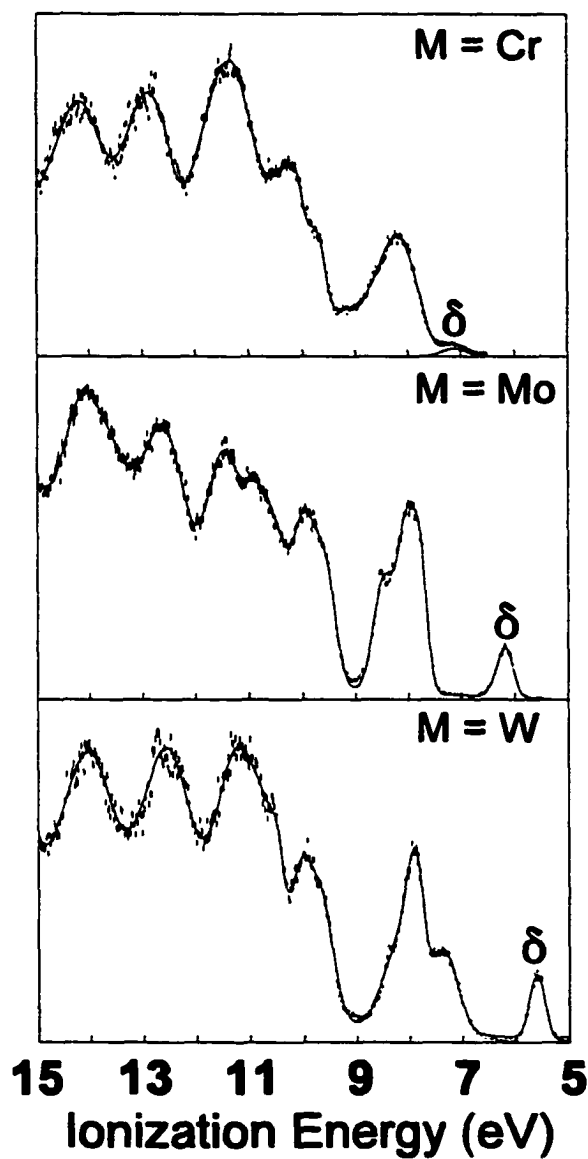
Figure 6.4. He I photoelectron spectra of $M_2(chp)_4$ (M = Cr, Mo, W) collected in the 5 to 15 eV energy range.
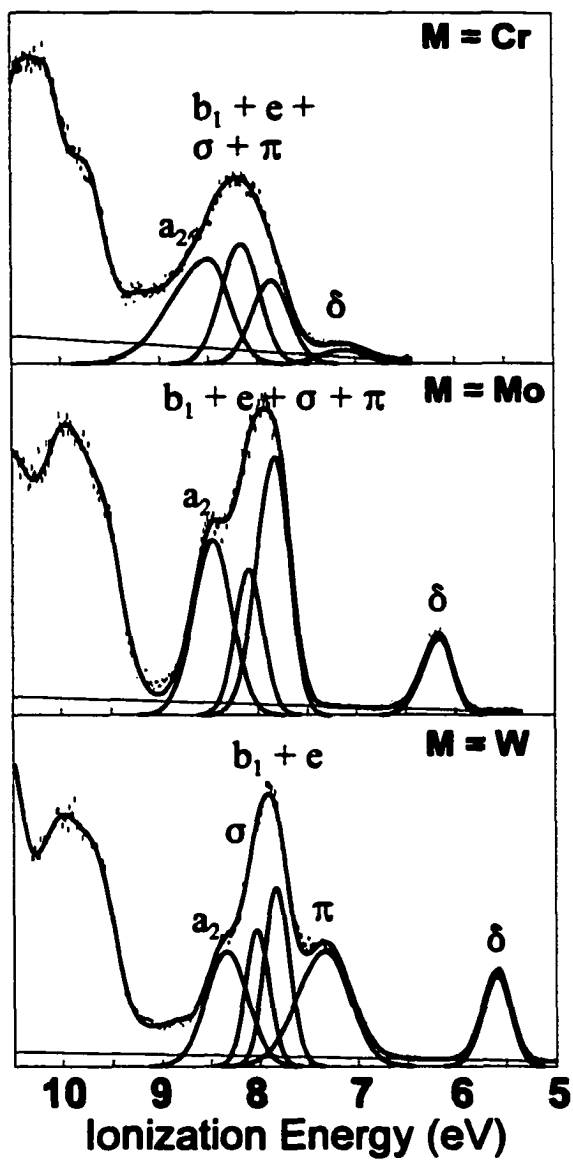
Figure 6.5. He I photoelectron spectra of
$M_2(chp)_4$ (M = Cr, Mo, W) collected in the 5 to
10 eV energy range.
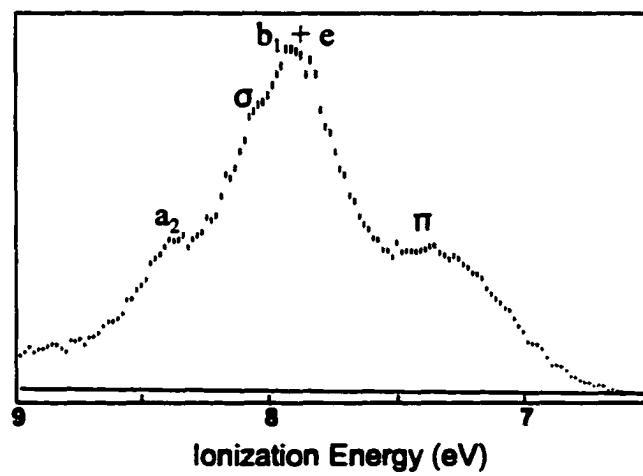
Figure 6.6. He I closeup spectrum of $W_2(chp)_4$ revealing the position of the σ ionization.
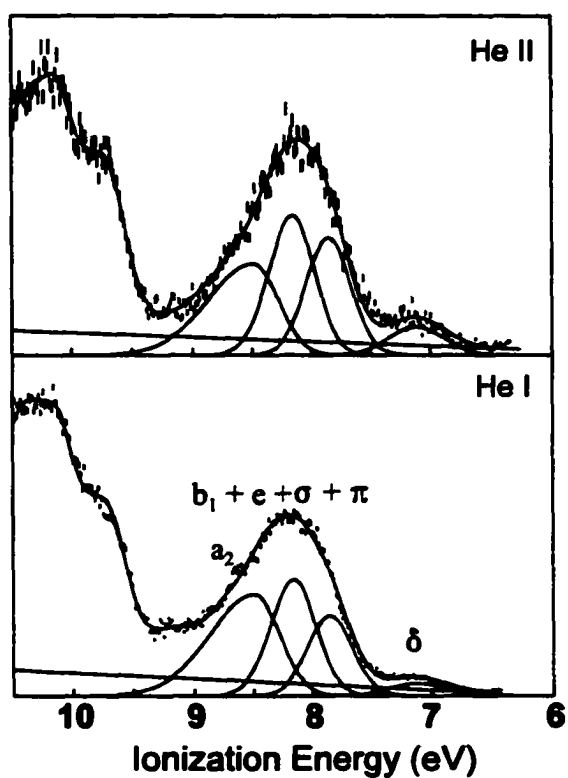
Figure 6.7. He I and He II photoelectron
spectra of $Cr_2(chp)_4$.
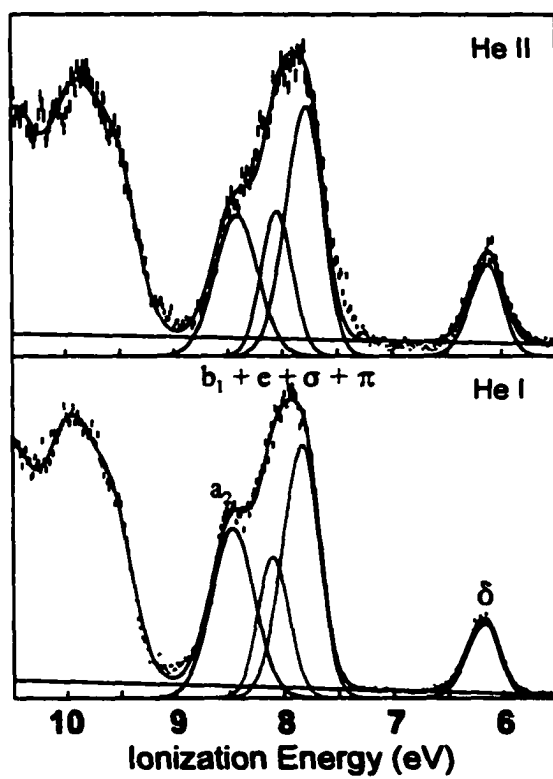
Figure 6.8. He I and He II photoelectron spectra of $Mo_2(chp)_4$.
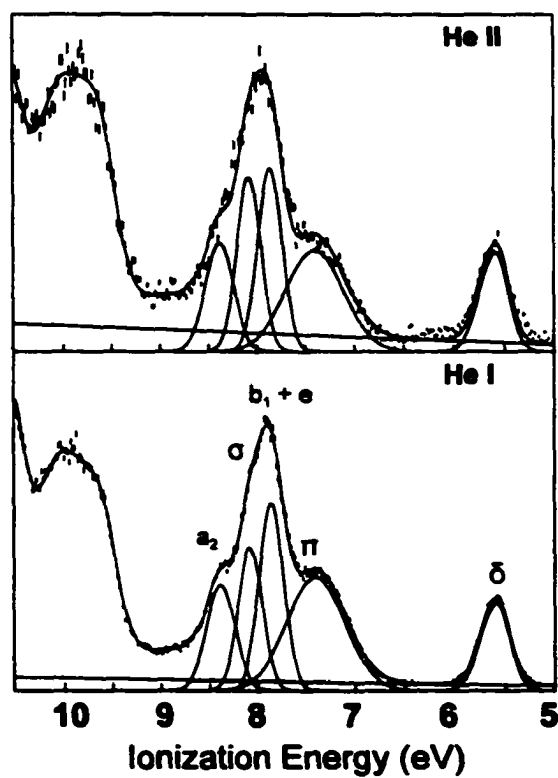
Figure 6.9. He I and He II photoelectron spectra of $W_2(chp)_4$.
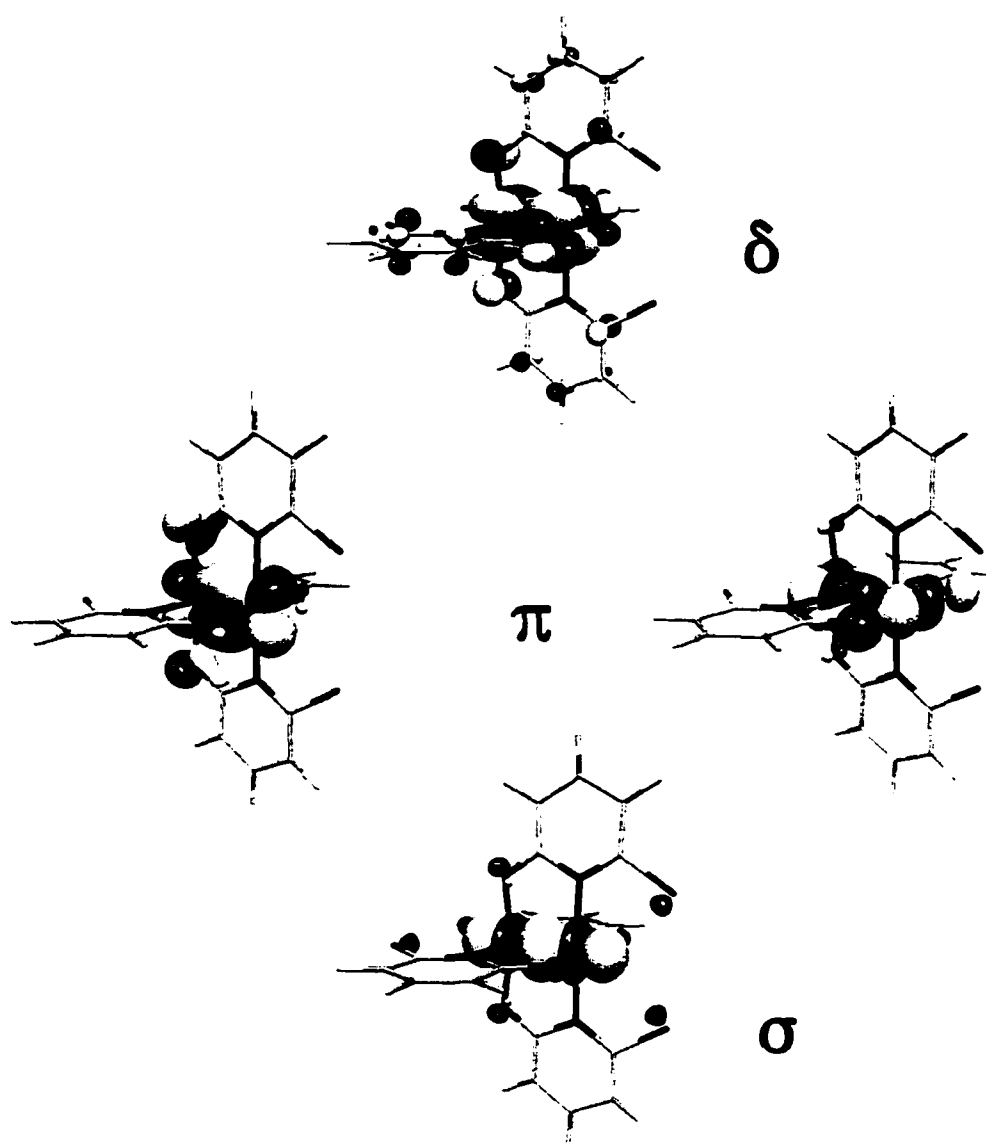
Figure 6.10. Contour plots of the metal-metal bonding orbitals of $Cr_2(chp)_4$ (Contour value = 0.04).

67% Cr-Cr δ

13% 5b₁

+

18% 6b₁
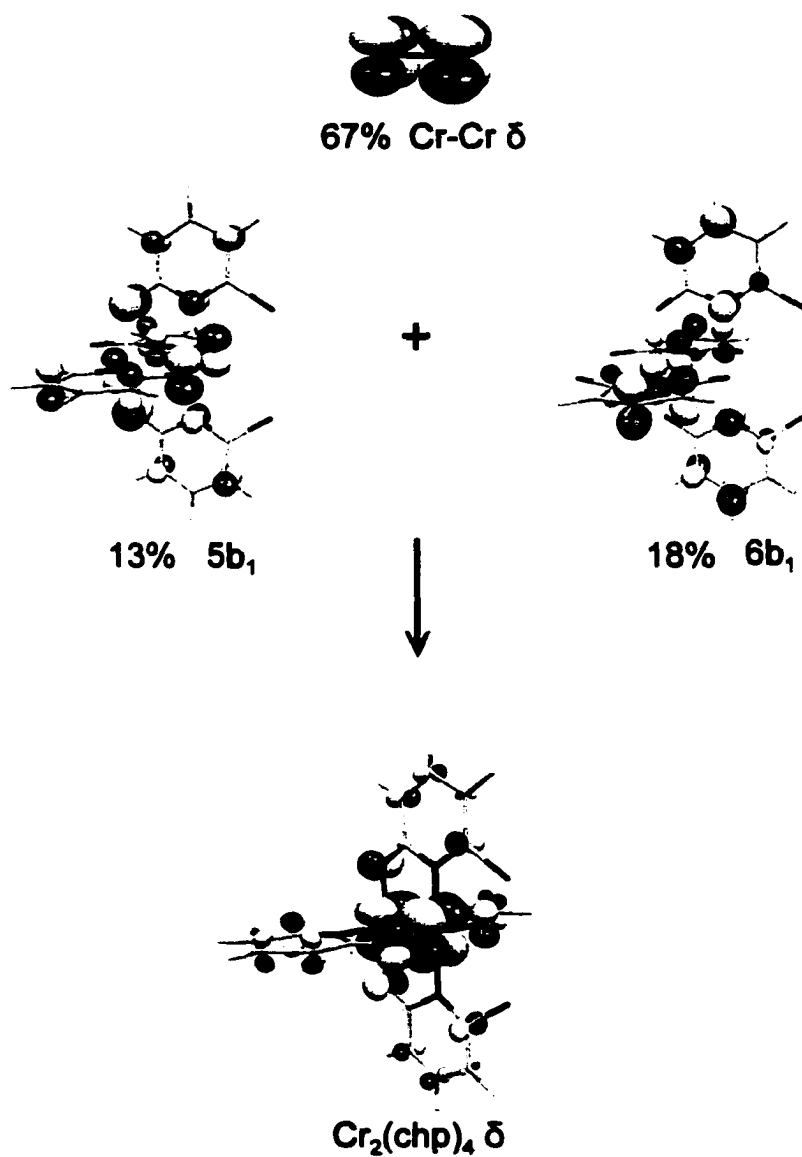
Cr₂(chp)₄ δ

Figure 6.11. Contour plots of the (chp)₄⁺ and Cr₂⁺⁺ fragment
orbitals that combine to form the Cr₂(chp)₄ δ (Contour = 0.04).
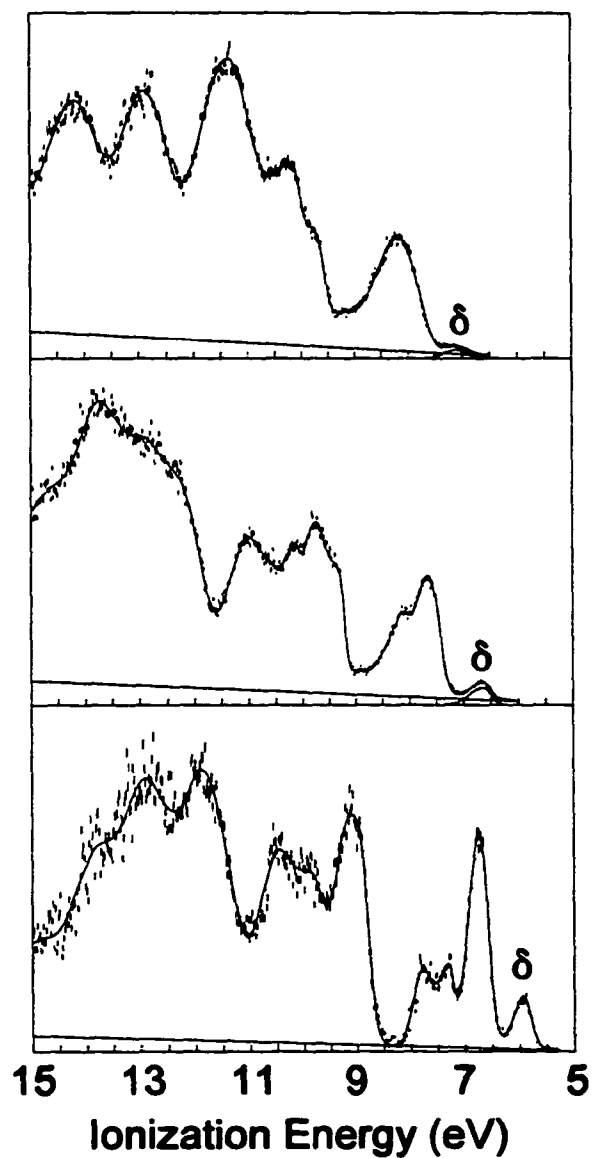
Figure 6.12. He I photoelectron spectra of
$Cr_2(chp)_4$ (top), $Cr_2(mhp)_4$ (middle), and
$Cr_2(map)_4$ (bottom).
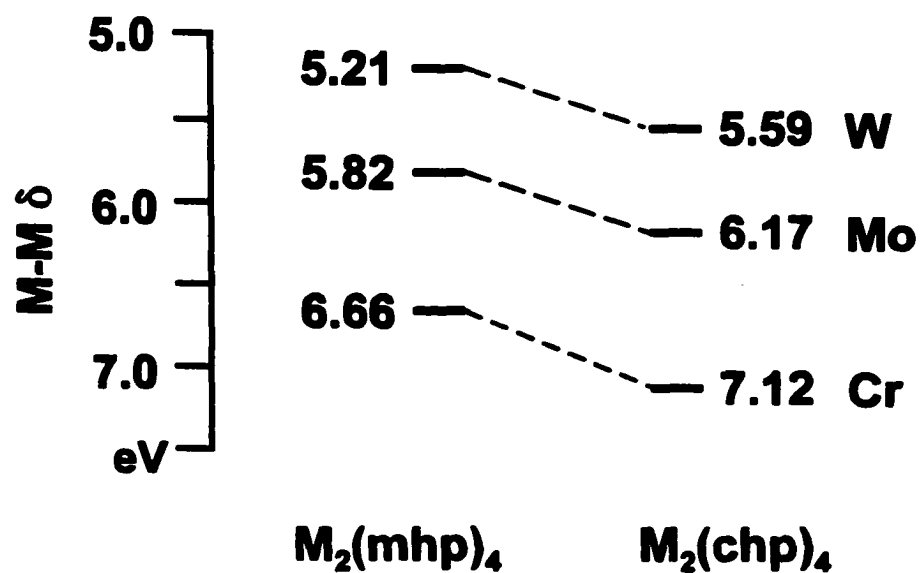
Figure 6.13. Correlation diagram of the experimental δ ionizations of the M₂(mhp)₄ and M₂(chp)₄ analogs (M = Cr, Mo, W).
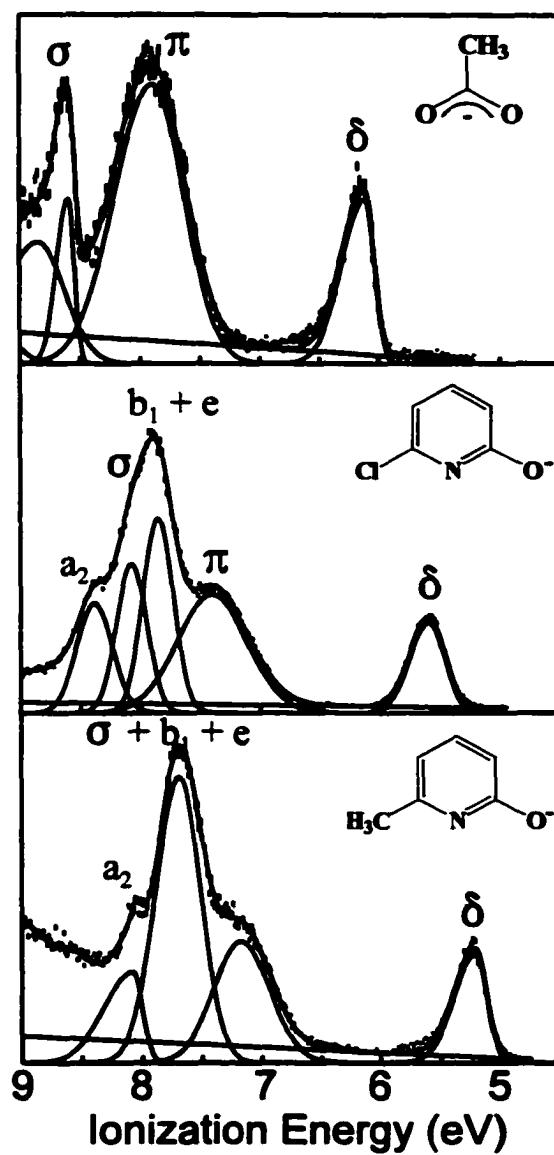
Figure 6.14. He I photoelectron spectra of
$W_2(O_2CCH_3)_4$, $W_2(chp)_4$, and $W_2(mhp)_4$.
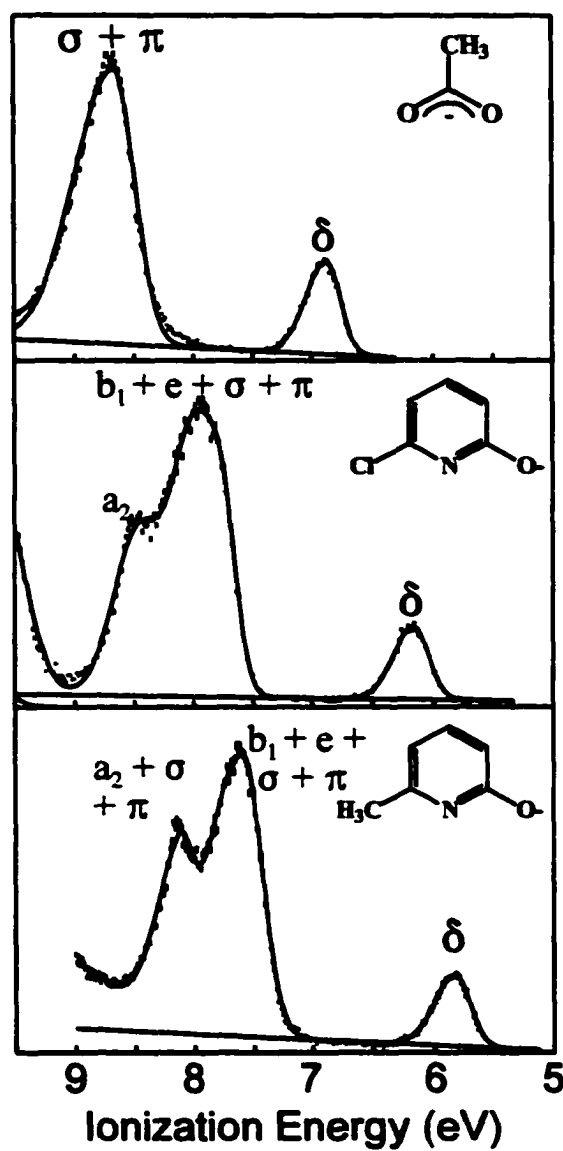
Figure 6.15. He I photoelectron spectra of
$Mo_2(O_2CCH_3)_4$, $Mo_2(chp)_4$, and $Mo_2(mhp)_4$.
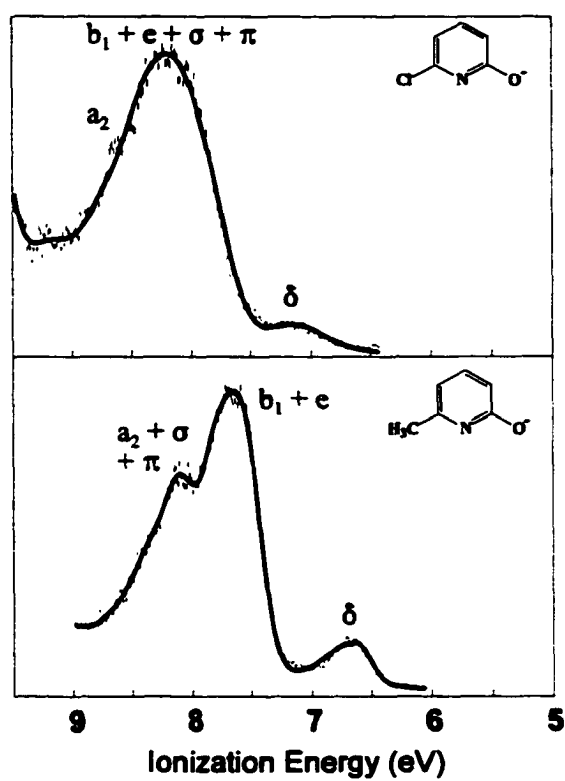
Figure 6.16. He I photoelectron spectra of $Cr_2(chp)_4$ and $Cr_2(mhp)_4$.
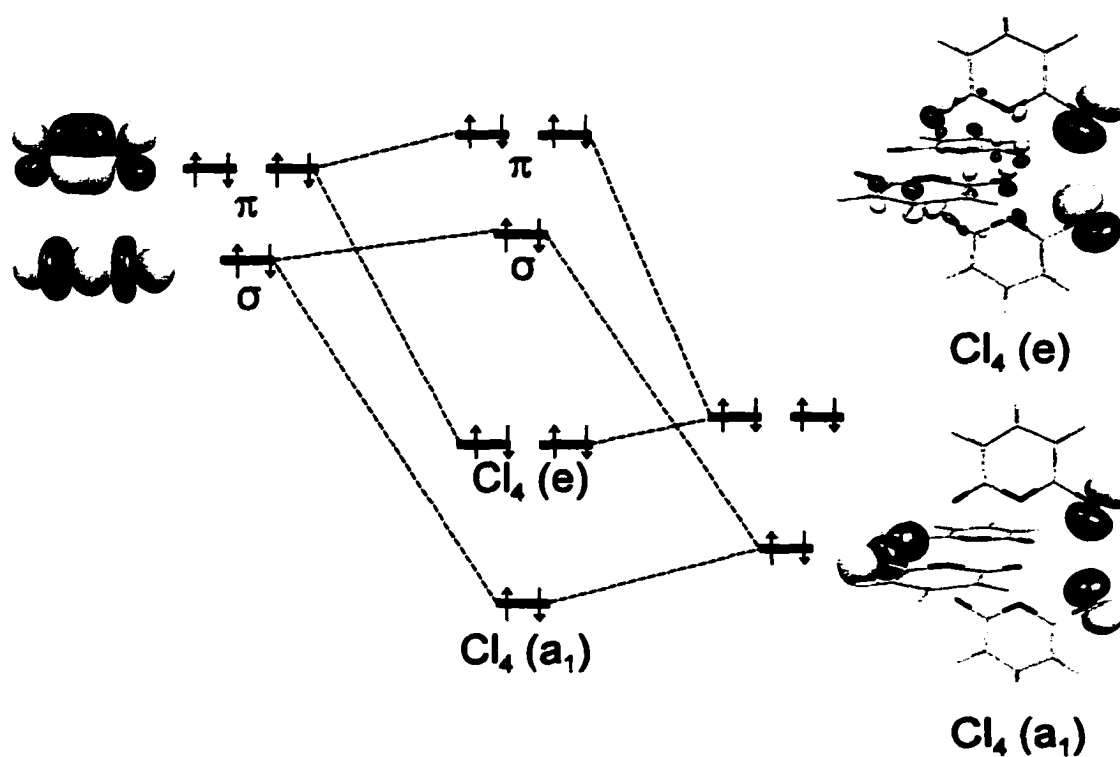
Figure 6.17. Correlation diagram showing the possible interactions of the Cl_4 a_1 and e combination orbitals with the M-M σ and π.
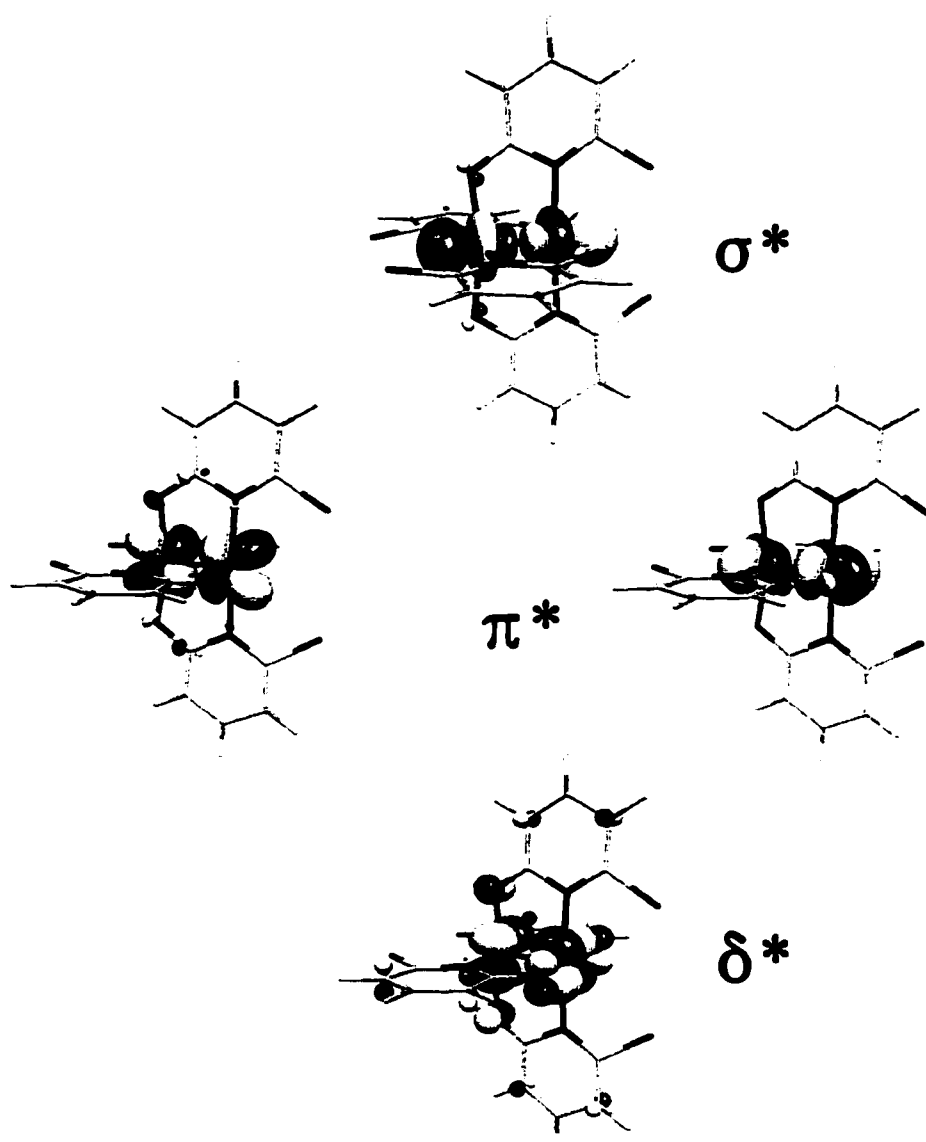
Figure 6.18. Contour plots of the metal-metal antibonding orbitals of Cr$_2$(chp)$_4$ (Contour = 0.04).

CHAPTER 7

CONCLUSIONS AND FUTURE DIRECTIONS

A unifying theme of the diverse studies presented in this work has been a desire to obtain an understanding of the nature of the multiple bonding that can occur between atoms in molecules. Specifically, these studies have focused on the formal triple bond that exists between a transition metal and a nitrogen atom as well as on the triple and quadruple bonds that can occur between two transition metals. Despite the vast amount of research that has been devoted to the study of molecules containing metal-heteroatom multiple bonds or metal-metal multiple bonds, we are only now beginning to realize the important role that the ancillary ligand sets and the resultant molecular symmetry play in fine-tuning the energetics of the multiple bond. Hence, it seems that by prudent choice of ancillary ligand set, one can fine-tune the energies and characters of the orbitals that constitute the multiple bond and enhance (or inhibit) the reactivity of the multiple bond. The first step towards understanding the reactivity of molecules is a thorough knowledge of the electronic structures of the target molecules. Whether one is talking about a simple molecule like N_2 or a more complex system such as $M_2Cl_4(PMe_3)_4$, the principles needed to understand the bonding present in these molecules are the same.

Not surprisingly, the bonding interactions present in molecules containing triple or quadruple bonds between atoms can be understood in terms of simple molecular orbital models. As was shown for all of the systems studied in this work, one can obtain a qualitative picture of the bonding without resorting to complicated molecular orbital calculations. A knowledge of fundamental chemical principles such as electronegativity and effective nuclear charge, in conjunction with an understanding of the molecular orbital model of bonding, allow for the development of a qualitative picture of the bonding that occurs between atoms.

The intricacies of the bonding in transition metal nitrido molecules and molecules containing metal-metal bonds cannot be fully understood within the constructs of the molecular orbital diagram developed for isolated $M \equiv N^{3+}$ or M_2^{4+} fragments. To obtain a more complete and useful understanding of the bonding interactions that occur in a particular molecule, a symmetry analysis, provided by application of principles from group theory, serves as a useful tool for the development molecular orbital models for the molecules studied in this work. Since only orbitals of the same symmetry can form bonding and antibonding combinations, a symmetry analysis allows one to better determine the electronic structure of the molecules studied. Additionally, a symmetry analysis allows one to move beyond treating the triple or quadruple bond as a noninteracting isolated bond within the molecules because such an analysis reveals the ligand combinations that can interact with the orbital components of the multiple bond. For each of the molecules studied in this work, symmetry combinations of the ancillary ligands were shown to have the appropriate symmetry and nodal properties to interact strongly with the orbitals that constitute the metal-metal and metal-nitrogen multiple bonds. According to the photoelectron spectroscopic studies presented here, the orbitals that constitute the multiple bond, whether metal-metal or metal-nitrogen, do indeed contain substantial amounts of ancillary ligand character as predicted from the symmetry analysis.

The particular effects that the ligand contributions have on the metal-metal or metal-nitrogen bonding orbitals depend directly on the characteristics of the ligand. As is well-known from organometallic studies, ligands fall into three broad categories: σ donor ligands (H, NH$_3$, ect.); σ-donor/π-donor ligands (alkoxides; halides, etc.); and σ-donors/π-acceptor ligands (CO, PF$_3$, etc.). Each of these ligands has a specific effect on the overall orbital energies of the mutiple bonding system with which the ligands interact: (1) σ-donor ligands increase the electron density at the metal center and destabilize the "metal-based" orbitals; (2) π-donor ligands

destabilize the "metal-based interactions through a filled-filled interaction; and (3) π-acceptor ligand stabilize the "metal-based" orbitals through back-bonding interactions with unfilled ligand orbitals. The systems studied here have been limited to those containing π-donor ligands which serve to destabilize the "metal-based" orbitals due to a filled interaction between the ancillary donor combinations and the orbitals of the metal-metal or metal-nitrogen multiple bond.

Focusing only on the results from the studies of the $M_2X_4(PMe_3)_4$ and $M_2(chp)_4$ molecules, which are molecules with D_{2d} symmetry, allows an evaluation of the importance of the ligand donor properties in determining the electronic structure of these molecules. While the interactions between the metals are certainly dependent on the metal identity as well as the oxidation state of the metal, one cannot discount the importance of the ancillary ligand contributions to the overall electronic structures of the molecules studied here. Indeed, the inverse halide order seen for the highest occupied molecular orbital energies of the $Mo_2X_4(PMe_3)_4$ (X = Cl, Br) and $Re_2X_4(PMe_3)_4$ (X = Cl, Br, I) molecules is a direct reflection of the importance of the ancillary ligand orbital combinations in determining the overall energies of the metal-metal bonding orbitals. In fact, the source of the inverse halide order was shown to be due to the π-donor ability of the halogen ligands (X = F > Cl > Br > I). In the case of $Cr_2(chp)_4$, it is the presence of a filled ligand combination of b_1 (δ) symmetry that serves to destabilize the Cr-Cr δ ionization from the positions of the σ and π ionizations, providing only the second known example of a Cr-Cr δ ionization. This is an intriguing finding because the Cr-Cr bond distance, 1.955 Å, is close to that found for unsolvated $Cr_2(O_2CCH_3)_4$. In the photoelectron spectrum of $Cr_2(O_2CCH_3)_4$, all of the metal-based ionizations occur under one broad ionization band. Hence, symmetry and donor properties are important considerations when interpreting the electronic structure of molecules containing metal-metal bonds. When the molecular symmetry is invariant, the increased donor ability of the ligand set (map > mhp > chp) results in a

measurable destabilization of the metal-metal bonding orbitals and leads to an enhancement of the band intensity of the ionization from the M_2 δ in accordance with the donor ability of the ligand set. It is the ancillary ligands that serve to fine-tune the molecular orbital energies of the metal-metal bonds.

Just as the ligand combination orbitals and the molecular symmetry are vital to the description of the electronic structure of molecules containing metal-metal bonds, the ligand orbital combinations under C_{3v} symmetry play an essential role in determining the overall electronic structure of the $R_3M \equiv N$ molecules studied in this work. In fact, the highest occupied molecular orbital of $(^tBuO)_3Cr \equiv N$ derives not from the $Cr \equiv N$ σ or π orbitals but from the alkoxide-based a_2 orbital combination. From the studies presented here, the reactivities of these molecules can be rationalized within the constructs of the molecular orbital model.

The studies presented here have raised interesting questions concerning the electronic structure of molecules containing multiple bonds between atoms. Focusing first on the $M_2X_4(PMe_3)_4$ series of molecules, there is a missing piece of information concerning the inverse halide order displayed by these molecules both in the gas-phase as well as in solution. This missing piece of information is the photoelectron spectra and solution chemistry studies of $Mo_2F_4(PMe_3)_4$.[188] Although the notion of π-acceptance by the halogen atoms seems counterintuitive, the only way to definitely prove that it does not play a role in the inverse halide order seen for the $M_2X_4(PMe_3)_4$ molecules is to obtain the photoelectron spectrum of $Mo_2F_4(PMe_3)_4$. Because fluorine does not have d-orbitals available for π-acceptance, observance of the $Mo_2F_4(PMe_3)_4$ δ ionization energy falling in line with the expectations from the inverse halide order trend would identify the origin of the inverse halide order as the greater π-donor ability of the lighter halogens. One could also greatly benefit from studying the electronic structure of the $Mo_2X_4(AsMe_3)_4$ derivatives.[153] In addition, it seems feasible to assume the

$Re_2X_4(AsMe_3)_4$ molecule could be synthesized by a method analogous to that used to synthesize

the $Re_2X_4(PMe_3)_4$ molecules.[115,256,257] The reaction conditions would probably require

adjustments to enable the desired products to be isolated. It would be intriguing to see if the

inverse halide order would hold for these molecules since the π-acceptor ability of the

trimethylarsine molecule should be much greater than that of trimethylphosphine. Another

interesting perturbation of the $M_2X_4(PMe_3)_4$ molecules would be the replacement of the π-donor

halide donors with σ-donor ligands or π-acceptor ligands. $Mo_2Me_4(PMe_3)_4$ serves as an

example of a molecule where the halogen donors have been replaced by σ-donating methyl

groups.[150,258] Two other compounds that are directly analogous to the halide derivatives are the

$Mo_2(NCO)_4(PMe_3)_4$ and $Mo_2(NCS)_4(PMe_3)_4$ molecules.[259] In addition, Cotton and coworkers

have recently focused on using nitrogen based donors in place of the phosphine

donors.[119,134,138,139,141] One need only look to the recent literature to see that research into

molecules with the generalized $M_2X_4(PMe_3)_4$ is still an active field of research.[119,132-139,260] Also

of great interest to the field of metal-metal bonding would be a thorough photoelectron

spectroscopic study of the $M_2X_4(L\text{-}L)_2$ analogs, where L-L = bidentate phosphine (M = Mo, W,

Re).[17,150,261] The bidentate phosphine ligands are versatile species R_2PXPR_2 in that one can vary

X, the alkyl chain linker between the two phosphine donor groups, as well as the R groups.

When L-L = dimethylphosphinomethane, the resultant $M_2X_4(L\text{-}L)_2$ structure is directly analogous

to the $M_2X_4(PMe_3)_4$ structure with the L-L serving as bridging ligands.[262,263] When the linking

group is larger than one carbon unit, two different isomers exist: one with chelating phosphine

ligands (α-$M_2Cl_4(L\text{-}L)_2$) (7.1) and one with bridging phosphine ligands (β-$M_2Cl_4(L\text{-}L)_2$)

(7.2).[17,158,264] It would be of great interest to obtain the photoelectron spectra of the α and β

isomers of a $M_2X_4(L\text{-}L)_2$ molecule.[150] In addition, the β-$M_2X_4(L\text{-}L)_2$ analogs generally display a
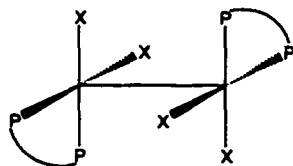
7.1
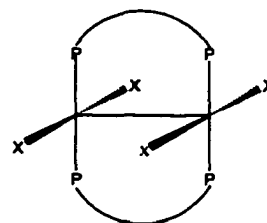
7.2

torsional angle (χ) that is significantly greater than zero.[265] That is, the ligands tend to arrange in a staggered conformation about the metal centers as opposed to the eclipsed structure shown in **7.2**. Any deviation of the torsional angle from zero significantly reduces the δ overlap in the molecules.[17,265] Hence, it would be of interest to obtain photoelectron spectra for a series of β-$M_2Cl_4(L-L)_2$ molecules displaying a range of torsional angles to provide a gauge of the effects of the torsional angle on the electronic structure of the molecules.

In addition, there is a paucity of photoelectron spectroscopic studies of dichromium systems containing formal quadruple bonds between the chromium atoms. Given the information presented in this work, more studies should be performed on dichromium molecules. In particular, those molecules known to have short Cr-Cr bond distances (less than 2.00 Å) should all be studied via photoelectron spectroscopy. There are at least sixteen known dichromium systems that fit this criterion.[17] Hence, there is certainly not a shortage of molecules to study. Just a few examples of the systems that could be studied with photoelectron spectroscopy are $Cr_2(DMP)_4$ and $Cr_2(TMP)_4$ (DMP = 2,6-dimethoxyphenyl anion; TMP = 2,4,6-trimethoxyphenyl anion). The Cr-Cr bond distances in these molecules are 1.847 Å and 1.849 Å for the $Cr_2(DMP)_4$ and $Cr_2(TMP)_4$ molecules, respectively.[266,267] Each of these molecules has effective C_{2h} symmetry. The shortest metal-metal bond distance known to date occurs in $Cr_2(2\text{-MeO-}5\text{-}MeC_6H_3)_4$, where the Cr-Cr distance is 1.828 Å.[268] Of course, these are just a few of the systems that could be studied via photoelectron spectroscopy. It would also be of interest to study the importance of configuration interaction to the description of the Cr-Cr multiple bond in these

molecules.[237] The photoelectron spectroscopic data collected to date would suggest that the presence of a ligand-based combination orbital with the appropriate symmetry to interact strongly with the Cr-Cr δ serves to destabilize the δ so that the ionization from this orbital appears as a separate ionization feature in the photoelectron spectrum. It would be interesting to test whether the D_{2d} symmetry of the $Cr_2(chp)_4$ molecule results in the $\sigma^2\pi^4\delta^2$ configuration being the dominant configuration for these systems. For the $Cr_2(O_2CCH_3)_4$ molecule, the $\sigma^2\pi^4\delta^2$ configuration was found to be just one of many configurations that contribute strongly to the overall electronic structure. Hence, one must use caution when interpreting the electronic structure of molecules containing dichromium bonds. In reality, configuration interaction studies would be of interest for all of the dichromium systems known to date.

There are also a number of molecules containing metal-heteroatom multiple bonds that are of interest to expanding the current knowledge of the electronic structure of molecules known to contain these bonds. In direct relation to the $Cl_3Mo\equiv N$ molecule studied in this work, an examination of the electronic structure of the $Br_3Mo\equiv N$ molecule would provide an experimental measure of the effects of Br substitution on the electronic structure of the molecule.[44] To gauge the effects of changing the metal center, $Cl_3W\equiv N$ has been reported and would be of interest for comparisons to the current studies of the molybdenum analog.[45] Another molecule of interest is $Cl_3Re\equiv N$ because it is directly analogous to the molybdenum analog with the exception that the rhenium analog has an unpaired metal-based electron.

It would also be of interest to look at the electronic structure of transition metal nitrido molecules with ancillary ligand sets other than alkoxides and halides.[44,45,269] For example, one can replace the alkoxide ligand sets with alkyl or amido ligand sets.[12-15,40,270-273] It is clear that the ancillary ligand set strongly influences the electronic structure and reactivity of the molecule. Hence, one can expect the photoelectron spectra of these molecules to reflect the differences in

the ancillary ligand sets. In order to achieve a better understanding of the electronic structure

and reactivity of the transition metal nitrido molecules, much more work needs to be done to

explore the influences of symmetry and the ancillary ligand set on the orbitals that constitute the

metal-nitrogen triple bond.

The work presented in this dissertation has shown the important role the ancillary ligands

play in fine-tuning the electronic structure of multiple bonding involving transition metal atoms.

These results obtained here will aid in the design of new experiments to further probe the

electronic structure and reactivity of molecules containing multiple bonds involving transition

metal atoms.

Appendix A

ENERGY DECOMPOSITION ANALYSIS OF THE FENSKE-HALL ORBITAL ENERGY

This appendix focuses on the energy decomposition analysis utilized in chapters 4 and 5. Because this analysis scheme has not been documented previously, it is necessary to provide further information concerning its application. The procedure described in this appendix applies to any molecular orbital method at the single-determinant level according to the Hartree-Fock-Roothaan equations $FC = SC\varepsilon$, and may be extended to multiconfiguration techniques . The Fenske-Hall method will be used to illustrate the energy decomposition.

I would be remiss if I did not take this opportunity to espouse the advantages of the Fenske-Hall method for studying the electronic structure of transition metal molecules. For the computational studies completed during in this work, the results from the Fenske-Hall method are comparable to those produced by density functional studies. However, the Fenske-Hall calculations converge in a fraction of the time necessary to perform the density functional calculations. Hence, the Fenske-Hall method is an excellent tool for providing an initial point for understanding the electronic structure of transition metal molecules. In addition, Fenske-Hall calculations have the added advantage that the calculations can be run in terms of molecular fragments in addition to the traditional atomic fragments. For example, one can run a calculation on $Mo(CO)_6$ using Mo, C and O as the atomic basis sets, or the calculations could be run in terms of the Mo atom interacting with the $(CO)_6$ ligand fragment. Calculations performed using molecular fragments are generally referred to as transform calculations. While density functional calculations can also be run using molecular fragment orbitals, the Fenske-Hall method is superior to that of the commercially available density functional packages for performing molecular fragment calculations because the Fenske-Hall program calculates the energies of the constituent molecular fragment orbitals within the field of the full molecule. As such, the

calculated energies can be used to create a molecular orbital diagram showing the interactions of the fragment orbitals that combine to form the orbitals of the full molecule.

In reality, the Fenske-Hall method is non-empirical. That is, the results depend solely on the choice of basis functions and the internuclear distances. The method can be understood in terms of well-known approximations to the one-electron Hartree-Fock-Roothaan (HFR) operator.[39] This HFR operator produces the energy of an electron that is moving in the average field of the other electrons and nuclei. The generalized canonical form of this operator, F, is shown in (A.1)

$$F = -\frac{1}{2}\nabla^2 + \sum_c V_c \qquad \text{(A.1)}$$

as the kinetic energy operator plus a potential energy operator for each center in the system.[274-276] An implied assumption for the application of this operator is that the electron density can be assigned to the appropriate center(s). For the Fenske-Hall calculations, the electron density is split according to a Mulliken Population Analysis.[277] The HFR operator is used to generate the matrix elements between the constituent basis functions (atomic or molecular) and obtain the final molecular wavefunction by solving the standard Hartree-Fock-Roothan equation (A.2),

$$FC = SC\varepsilon \qquad \text{(A.2)}$$

where F is the Fock matrix, S is the overlap matrix, C is the eigenvector matrix, and ε is the diagonal eigenvalue matrix (orbital energies).[278] Because the Fock matrix is dependent on the coefficient matrix, this equation must be solved iteratively via standard matrix techniques. In essence, the mathematics boil down to solving a "simple" eigenvalue problem.

Before the eigenvalue problem can be solved, the matrix elements for the Fock matrix

must be evaluated. Using equation (A.1), the diagonal matrix element for function ϕ_i (on the

center i) is given by equation (A.3). The first term in (A.3) corresponds to the fragment (atomic)

$$F_{ii} = \left\langle \phi_i \left| -\frac{1}{2} \nabla^2 + V_i \right| \phi_i \right\rangle + \sum_{c \neq i} \left\langle \phi_i \left| V_c \right| \phi_i \right\rangle \qquad (A.3)$$

orbital energy, ε_i, of an electron in ϕ_i. Its value is calculated according to Slater's average of

configuration approach, giving equation (A.4).[279]

$$\varepsilon_i = \left\langle \phi_i \left| -\frac{1}{2} \nabla^2 \right| \phi_i \right\rangle + \left\langle \phi_i \left| -\frac{Z_i}{R_i} \right| \phi_i \right\rangle + \sum_{k \neq i} n_k g_{ki} + (n_i - 1) g_{ii} \qquad (A.4)$$

The first two terms of this equations are the kinetic energy and the nuclear attraction energy,

respectively. The third term is the summation over all of the atomic orbitals on center i, where n_k

is the Mulliken population of orbital ϕ_k,[277] and g_{ki} represents Slater's average of the

configuration electrostatic repulsion integral.[279]

The second term in equation (A.3) reflects the influence of all the other nuclei and

electrons on the diagonal matrix element. The V_i is represented by a point charge on center i,

calculated according to the Mulliken method (A.5),

$$q_i = Z_i - \sum_k^i n_k \qquad (A.5)$$

where Z_i is the "bare" nuclear charge and the sum includes all of the functions (valence and core) on center i.[277] The same point-charge approximation is applied to the charge distribution of ϕ_i, producing the simplified expression for the diagonal term shown in (A.6),

$$F_{ii} = \varepsilon_i + \sum_{k \neq i}\left(\frac{-q_k}{R_{ik}}\right) \qquad \text{(A.6)}$$

where ε_i is given by (A.4), q_k is given by (A.5), and $1/R_{ik}$ is the potential energy of two point charges at a distance R_{ik} from one another.[280]

The off-diagonal matrix elements describing the interaction of two different centers is slightly more complicated than the diagonal matrix element. The equation describing the off-diagonal term is given in equation (A.7).

$$F_{ij} = \left\langle \phi_i \left| -\frac{1}{2}\nabla^2 + V_i \right| \phi_j \right\rangle + \left\langle \phi_i \left| -\frac{1}{2}\nabla^2 + V_j \right| \phi_j \right\rangle - \left\langle \phi_i \left| -\frac{1}{2}\nabla^2 \right| \phi_j \right\rangle + \sum_{k \neq i,j} \left\langle \phi_i \left| V_k \right| \phi_j \right\rangle \qquad \text{(A.7)}$$

It is now assumed that ϕ_i is an eigenfunction of the operator $-1/2\nabla^2 + V_i$ with eigenvalue $_i$ in analogy to the method of Goepert-Mayer and Sklar.[281,282] The last term in (A.7) contains the three-center interactions calculated by utilizing the Mulliken and point-charge approximations. The final expression for the off-diagonal term then becomes equation (A.8),

$$F_{ij} = \left\langle \phi_i | \phi_j \right\rangle\left(\varepsilon_i + \varepsilon_j\right) - \left\langle \phi_i \left| -\frac{1}{2}\nabla^2 \right| \phi_j \right\rangle - \frac{1}{2}\left\langle \phi_i | \phi_j \right\rangle \sum_{k \neq i,j}\left[\frac{q_k}{R_{ik}} + \frac{q_k}{R_{jk}}\right] \qquad \text{(A.8)}$$

where $\langle \phi_i | \phi_j \rangle$ is the standard overlap integral and $\langle \phi_i | -\frac{1}{2}\nabla^2 | \phi_j \rangle$ is the standard kinetical energy integral.

An important assumption made by the Fenske-Hall method is that all one-center off-diagonal terms are zero.[39] That is, the off-diagonal interactions of two functions on the same center are neglected in order to be consistent with the use of the Mulliken and point-charge approximations.

After solving for all the necessary matrix elements, this Fock matrix is then used to solve equation (A.2). The final equation for the molecular orbital eigenvalues is then given by equation (A.9),

$$\varepsilon_i = \sum_i c_i^2 F_{ii} + 2 \sum_{i>j} c_i c_j F_{ij} \qquad \text{(A.9)}$$

where F_{ii} and F_{ij} correspond to the diagonal and off-diagonal SCF (Fock) matrix elements, and c_i and c_j correspond to the coefficent matrix elements (eigenvectors). These matrix values are part of the standard Fenske-Hall output so the orbital energy calculated by the program can be analyzed to reveal which fragment orbitals (atomic or molecular) contribute to the molecular orbital energy. The first term in equation (A.9) corresponds to the diagonal energy contributions from the constituent fragment orbitals while the second term contains the off-diagonal contributions. Since bonding interactions are by definition off-diagonal contributions, the energetic contributions due to the bonding or antibonding interactions between two fragment orbitals are all contained within the second term of equation (A.9). If the molecule is bonding between two basis orbitals, centers, or fragments, then the off-diagonal contributions between the two units will be negative. If the off-diagonal contributions are near zero, the interaction is non-bonding, and, if the off-diagonal contributions are positive, then the interaction is antibonding between the two units. To better illustrate the analysis procedure it is necessary to work through an example. A simple example is provided by the $Mo \equiv N$ molecule of chapter 4. The complete

Fenske-Hall output for this Mo≡N calculation is shown below. The portions of the calculation

output that correspond to the Fock and coefficent matrix values are highlighted in bold. Also

provided is the spreadsheet used to perform the orbital energy decomposition analysis of the

Mo≡N σ. This energy decomposition is particularly helpful when unusual orbital trends are seen

for a series of molecules. By doing the orbital energy decomposition analysis, one can identify

the probable source(s) of the orbital energy trends. An in-depth analysis of the energy of the

Mo≡N σ orbital can be found in Table 4.3 of Chapter 4.

```
••••••••••••••••••••••••••••••••••••••••••••••••••••••••••••••••
•                                                              •
•            Fenske-Hall Molecular Orbital Calculation         •
•                       Version 5.1.3                          •
•                                                              •
•                                                              •
•             DATE: Sat Jan 26 10:10:38 2002                   •
•                                                              •
••••••••••••••••••••••••••••••••••••••••••••••••••••••••••••••••
```

FILE A INPUT:

```
0 4 2 MO 1 N 1
N  0.000   0.000  -0.0584 0 0.000    0.000   1.6030
MO 0.000      0.000   1.6030 0  0.000  0.000  -0.0584
1.0
4 3 15 0 0 0 0
0 0 0 0 0
```

END FILE A INPUT
1

    M O Calculation for MO(1)N (1)

		BASIS ORBITALS				
ATOM MO	FUNCTION	TYPE	INDEX	COEFFICIENT	EXPONENT	N
MO						
	1s	CORE	1			
				1.0000000	41.291000	1
	2s	CORE	2			
				-0.3936650	41.291000	1
				1.0746963	16.560000	2
	2p	CORE	3			
				1.0000000	18.390000	2
	3s	CORE	4			
				0.1878598	41.291000	1
				-0.6116834	16.560000	2
				1.1512009	8.503000	3
	3p	CORE	5			
				-0.4250929	18.390000	2
				1.0866020	8.367000	3
	3d	CORE	6			
				1.0000000	8.500000	3
	4s	CORE	7			
				-0.0727734	41.291000	1
				0.2447642	16.560000	2
				-0.5545508	8.503000	3
				1.1109478	4.164000	4
	4p	CORE	8			
				0.1382424	18.390000	2
				-0.4067401	8.367000	3
				1.0679671	3.727000	4
	4d	VALENCE	9			
				-0.1987087	8.500000	3
				0.6009910	3.585000	4
				0.5642022	1.678000	4
	5s	VALENCE	10			
				0.0296852	41.291000	1
				-0.1003815	16.560000	2
				0.2341368	8.503000	3
				-0.5570750	4.164000	4
				1.1193305	2.200000	5
	5p	VALENCE	11			
				-0.0717881	18.390000	2
				0.2162668	8.367000	3
				-0.6844803	3.727000	4
				1.1884648	2.200000	5
N						
	1s	CORE	12			
				1.0000000	6.517000	1
	2s	VALENCE	13			
				-0.2445976	6.517000	1
				1.0294795	1.947000	2
	2p	VALENCE	14			
				0.4796712	2.775000	2
				0.6132360	1.232000	2

| | COORDINATES | | | LOCAL COORDINATE SYSTEM (IF DIFFERENT FROM MCS) |
| | X | Y | Z | |

```
      1 N      0.0000   0.0000   -0.0584   Z-AXIS POINTS TOWARDS COORDINATES  0.0000   0.0000
1.6030

      2 MO     0.0000   0.0000    1.6030   Z-AXIS POINTS TOWARDS COORDINATES  0.0000   0.0000
-0.0584
```

COORDINATES ARE IN ANGSTROM UNITS

POPULATIONS FOR 13 ORBITALS READ FROM FILE B

DISTANCES BETWEEN POSITIONS IN A.U.

```
          N          MO
N      0.00000
MO     3.13965    0.00000
```

DISTANCES BETWEEN POSITIONS IN ANGSTROMS

```
          N          MO
N      0.00000
MO     1.66140    0.00000
1
```

```
   CHARGE ON MOLECULE =  0
THE HOMO HAS DEGENERACY 2. AVERAGE POPULATION=1.500
```

CYCLE NUMBER = 1   LARGEST DEVIATION OF POPULATION =0.00011   (TOTAL = 0.0005)

MULLIKEN POPULATIONS

	1N 2s	1N 2px	1N 2py	1N 2pz	2MO 4dz2	2MO 4dx2y2	2MO 4dxy
2MO4dxz							
IN	1.73056	1.18826	1.18826	1.64911	0.51359	1.50000	1.50000
0.81008							
OUT	1.73052	1.18815	1.18815	1.64912	0.51362	1.50000	1.50000
0.81019							

	2MO 4dyz	2MO 5s	2MO 5px	2MO 5py	2MO 5pz
IN	0.81008	0.06011	0.00166	0.00166	0.04663
OUT	0.81019	0.06012	0.00166	0.00166	0.04663

```
         . . . . . . . . . .
         *   SCF CONVERGED   *
         . . . . . . . . . .
```

CORE ENERGIES

1N 1s	2MO 1s	2MO 2s	2MO 2p	2MO 3s	2MO 3p	2MO 3d	2MO 4s
-414.01578	-19696.67773	-2802.76147	-2610.23169	-497.15198	-423.13647	-246.85840	-70.53040

2MO 4p
-44.27087

MULLIKEN ATOMIC CHARGES

```
   1 N     2 MO
 -0.756   0.756
```

```
     6 MOLECULAR ORBITALS ARE OCCUPIED WITH THE FOLLOWING
                  NUMBERS OF ELECTRONS

     2.00 2.00 2.00 2.00 1.50 1.50
```

MULLIKEN POPULATIONS

1N 2s	1N 2px	1N 2py	1N 2pz	2MO 4dz2	2MO 4dx2y2	2MO 4dxy	2MO 4dxz
1.73054	1.18822	1.18822	1.64912	0.51360	1.50000	1.50000	0.81012

2MO 4dyz	2MO 5s	2MO 5px	2MO 5py	2MO 5pz
0.81012	0.06011	0.00166	0.00166	0.04663

SUMMATION OF OCCUPIED ORBITAL ENERGIES = -125.4110 eV

```
LUMO ENERGY =    -3.1800 eV
HOMO ENERGY =    -5.5249 eV

HOMO/LUMO GAP = 2.3450 eV
```

HOMO ENERGY =   -5.5249 eV
SHOMO ENERGY =   -5.5249 eV

HOMO/SHOMO GAP = 0.0000 eV

GAP DIFFERENCE CRITERION = 2.3450 eV

1

ATOMIC BASIS

The Self-Consistent Field Matrix contains the Fii and Fij values!

SELF-CONSISTENT FIELD MATRIX

		1N 2s	1N 2px	1N 2py	1N 2pz	2MO 4dz2	2MO 4dx2y2	2MO 4dxy	2MO 4dxz
1 N	2 s	-21.13892							
1 N	2 px	0.00000	-7.47238						
1 N	2 py	0.00000	0.00000	-7.47238					
1 N	2 pz	0.00000	0.00000	0.00000	-7.47238				
2 MO	4 dz2	-13.10187	0.00000	0.00000	-6.90223	-5.52454			
2 MO	4 dx2y2	0.00000	0.00000	0.00000	0.00000	0.00000	-5.52454		
2 MO	4 dxy	0.00000	0.00000	0.00000	0.00000	0.00000	0.00000	-5.52454	
2 MO	4 dxz	0.00000	6.79773	0.00000	0.00000	0.00000	0.00000	0.00000	-5.52454
2 MO	4 dyz	0.00000	0.00000	-6.79773	0.00000	0.00000	0.00000	0.00000	0.00000
2 MO	5 s	-9.62191	0.00000	0.00000	-5.52947	0.00000	0.00000	0.00000	0.00000
2 MO	5 px	0.00000	2.88444	0.00000	0.00000	0.00000	0.00000	0.00000	0.00000
2 MO	5 py	0.00000	0.00000	-2.88444	0.00000	0.00000	0.00000	0.00000	0.00000
2 MO	5 pz	-12.25389	0.00000	0.00000	-6.27808	0.00000	0.00000	0.00000	0.00000

		2MO 4dyz	2MO 5s	2MO 5px	2MO 5py	2MO 5pz
2 MO	4 dyz	-5.52454				
2 MO	5 s	0.00000	-1.34849			
2 MO	5 px	0.00000	0.00000	5.30593		
2 MO	5 py	0.00000	0.00000	0.00000	5.30593	
2 MO	5 pz	0.00000	0.00000	0.00000	0.00000	5.30593

1

OVERLAP MATRIX

		1N 2s	1N 2px	1N 2py	1N 2pz	2MO 4dz2	2MO 4dx2y2	2MO 4dxy	2MO 4dxz
1 N	2 s	1.00000							
1 N	2 px	0.00000	1.00000						
1 N	2 py	0.00000	0.00000	1.00000					
1 N	2 pz	0.00000	0.00000	0.00000	1.00000				
2 MO	4 dz2	0.32094	0.00000	0.00000	0.13192	1.00000			
2 MO	4 dx2y2	0.00000	0.00000	0.00000	0.00000	0.00000	1.00000		
2 MO	4 dxy	0.00000	0.00000	0.00000	0.00000	0.00000	0.00000	1.00000	
2 MO	4 dxz	0.00000	-0.26430	0.00000	0.00000	0.00000	0.00000	0.00000	1.00000
2 MO	4 dyz	0.00000	0.00000	0.26430	0.00000	0.00000	0.00000	0.00000	0.00000
2 MO	5 s	0.33720	0.00000	0.00000	0.26303	0.00000	0.00000	0.00000	0.00000
2 MO	5 px	0.00000	-0.26242	0.00000	0.00000	0.00000	0.00000	0.00000	0.00000
2 MO	5 py	0.00000	0.00000	0.26242	0.00000	0.00000	0.00000	0.00000	0.00000
2 MO	5 pz	0.47290	0.00000	0.00000	0.21335	0.00000	0.00000	0.00000	0.00000

		2MO 4dyz	2MO 5s	2MO 5px	2MO 5py	2MO 5pz
2 MO	4 dyz	1.00000				
2 MO	5 s	0.00000	1.00000			
2 MO	5 px	0.00000	0.00000	1.00000		
2 MO	5 py	0.00000	0.00000	0.00000	1.00000	
2 MO	5 pz	0.00000	0.00000	0.00000	0.00000	1.00000

1

NET ORBITAL POPULATIONS (DIAGONAL) AND OVERLAP POPULATIONS (OFF-DIAGONAL)

		1N 2s	1N 2px	1N 2py	1N 2pz	2MO 4dz2	2MO 4dx2y2	2MO 4dxy	2MO 4dxz
1 N	2 s	1.61627							
1 N	2 px	0.00000	0.98254						
1 N	2 py	0.00000	0.00000	0.98254					
1 N	2 pz	0.00000	0.00000	0.00000	1.52480				
2 MO	4 dz2	0.15419	0.00000	0.00000	0.15637	0.35833			
2 MO	4 dx2y2	0.00000	0.00000	0.00000	0.00000	0.00000	1.50000		
2 MO	4 dxy	0.00000	0.00000	0.00000	0.00000	0.00000	0.00000	1.50000	
2 MO	4 dxz	0.00000	0.40796	0.00000	0.00000	0.00000	0.00000	0.00000	0.60621
2 MO	4 dyz	0.00000	0.00000	0.40796	0.00000	0.00000	0.00000	0.00000	0.00000
2 MO	5 s	0.05439	0.00000	0.00000	0.04196	0.00000	0.00000	0.00000	0.00000
2 MO	5 px	0.00000	0.00325	0.00000	0.00000	0.00000	0.00000	0.00000	0.00000
2 MO	5 py	0.00000	0.00000	0.00325	0.00000	0.00000	0.00000	0.00000	0.00000
2 MO	5 pz	0.01990	0.00000	0.00000	0.05031	0.00000	0.00000	0.00000	0.00000

		2MO 4dyz	2MO 5s	2MO 5px	2MO 5py	2MO 5pz

```
2 MO   4 dyz   0.60621
2 MO   5 s     0.00000   0.01194
2 MO   5 px    0.00000   0.00000   0.00004
2 MO   5 py    0.00000   0.00000   0.00000   0.00004
2 MO   5 pz    0.00000   0.00000   0.00000   0.00000   0.01152
1
```

The Eigenvalues provide the orbital energies (eigenvalues) as well as the coefficents. Each molecular orbital has its own set of coefficients!

```
              EIGENVALUES AND EIGENVECTORS
                1-(   )    2-(   )    3-(   )    4-(   )    5-(   )    6-(   )    7-(   )    8-(   )

   ENERGY =   -23.2398  -10.6092  -10.6092   -9.9599   -5.5249   -5.5249   -3.1800   -0.2747

1 N    2 s     0.82866   0.00000   0.00000   0.34851   0.00000   0.00000   0.06408   0.00000
1 N    2 px    0.00000   0.70091   0.00000   0.00000   0.00000   0.00000   0.00000   0.63474
1 N    2 py    0.00000   0.00000   0.70091   0.00000   0.00000   0.00000   0.00000   0.00000
1 N    2 pz    0.06875   0.00000   0.00000  -0.87044   0.00000   0.00000   0.13475   0.00000
2 MO   4 dz2   0.27887   0.00000   0.00000  -0.31843   0.00000   0.00000  -0.70266   0.00000
2 MO   4 dx2y2 0.00000   0.00000   0.00000   0.00000   1.00000   0.00000   0.00000   0.00000
2 MO   4 dxy   0.00000   0.00000   0.00000   0.00000   0.00000  -1.00000   0.00000   0.00000
2 MO   4 dxz   0.00000  -0.55055   0.00000   0.00000   0.00000   0.00000   0.00000   0.81304
2 MO   4 dyz   0.00000   0.00000   0.55055   0.00000   0.00000   0.00000   0.00000   0.00000
2 MO   5 s     0.06574   0.00000   0.00000  -0.04062   0.00000   0.00000   0.64446   0.00000
2 MO   5 px    0.00000  -0.00441   0.00000   0.00000   0.00000   0.00000   0.00000  -0.31986
2 MO   5 py    0.00000   0.00000   0.00441   0.00000   0.00000   0.00000   0.00000   0.00000
2 MO   5 pz    0.03986   0.00000   0.00000  -0.06458   0.00000   0.00000   0.17009   0.00000
1
                9-(   )   10-(   )   11-(   )   12-(   )   13-(   )

   ENERGY =    -0.2747    1.8364    7.8954    7.8954   59.7892

1 N    2 s     0.00000  -0.09178   0.00000   0.00000  -1.09025
1 N    2 px    0.00000   0.00000   0.51662   0.00000   0.00000
1 N    2 py    0.63474   0.00000   0.00000  -0.51662   0.00000
1 N    2 pz    0.00000  -0.17642   0.00000   0.00000  -0.69572
2 MO   4 dz2   0.00000   0.34192   0.00000   0.00000   0.69653
2 MO   4 dx2y2 0.00000   0.00000   0.00000   0.00000   0.00000
2 MO   4 dxy   0.00000   0.00000   0.00000   0.00000   0.00000
2 MO   4 dxz   0.00000   0.00000   0.34201   0.00000   0.00000
2 MO   4 dyz  -0.81304   0.00000   0.00000   0.34201   0.00000
2 MO   5 s     0.00000   0.62814   0.00000   0.00000   0.77299
2 MO   5 px    0.00000   0.00000   0.98875   0.00000   0.00000
2 MO   5 py    0.31986   0.00000   0.00000   0.98875   0.00000
2 MO   5 pz    0.00000  -0.68628   0.00000   0.00000   1.05404
```

```
              PERCENT CHARACTER OF MOLECULAR ORBITALS
                1(   )    2(   )    3(   )    4(   )    5(   )    6(   )    7(   )    8(   )    9(   )   10(   )   11(   )   12(   )
ENERGY =     -23.24   -10.61   -10.61    -9.96    -5.52    -5.52    -3.18    -0.27    -0.27     1.84     7.90     7.90
1N    2s      79.48     0.00     0.00     7.04     0.00     0.00     0.87     0.00     0.00     0.87     0.00     0.00
1N    2px      0.00    59.41     0.00     0.00     0.00     0.00     0.00    31.98     0.00     0.00     8.62     0.00
1N    2py      0.00     0.00    59.41     0.00     0.00     0.00     0.00     0.00    31.98     0.00     0.00     8.62
1N    2pz      0.90     0.00     0.00    81.55     0.00     0.00     3.34     0.00     0.00     1.98     0.00     0.00
2MO   4dz2    15.45     0.00     0.00    10.23     0.00     0.00    46.68     0.00     0.00     9.89     0.00     0.00
2MO   4dx2y2   0.00     0.00     0.00     0.00   100.00     0.00     0.00     0.00     0.00     0.00     0.00     0.00
2MO   4dxy     0.00     0.00     0.00     0.00     0.00   100.00     0.00     0.00     0.00     0.00     0.00     0.00
2MO   4dxz     0.00    40.51     0.00     0.00     0.00     0.00     0.00    52.46     0.00     0.00     7.03     0.00
2MO   4dyz     0.00     0.00    40.51     0.00     0.00     0.00     0.00     0.00    52.46     0.00     0.00     7.03
2MO   5s       2.39     0.00     0.00     0.62     0.00     0.00    45.21     0.00     0.00    34.60     0.00     0.00
2MO   5px      0.00     0.08     0.00     0.00     0.00     0.00     0.00    15.56     0.00     0.00    84.36     0.00
2MO   5py      0.00     0.00     0.08     0.00     0.00     0.00     0.00     0.00    15.56     0.00     0.00    84.36
2MO   5pz      1.78     0.00     0.00     0.55     0.00     0.00     3.90     0.00     0.00    52.66     0.00     0.00
1
                13(   )

ENERGY =      59.79

1N    2s      11.73
1N    2px      0.00
1N    2py      0.00
1N    2pz     12.22
2MO   4dz2    17.75
2MO   4dx2y2   0.00
2MO   4dxy     0.00
2MO   4dxz     0.00
2MO   4dyz     0.00
2MO   5s      17.19
2MO   5px      0.00
2MO   5py      0.00
2MO   5pz     41.11
```

Table A.1. Energy Decomposition Analysis Spreadsheet for Mo≡N σ

MoN fenske-Hall	Analysis of the Mo-N σ			
Mo-N σ	(orbital 4)			
-9.96 eV				
	Diagonal Fock elements F_i	eigenvector c_i	Energy contribution $c_i^2 F_i$	Sum of all energies (A.9)
N(2s)	-21.13892	0.34851	-2.56751673696	-9.96 eV
N(2px)	-7.47238	0	-0	
N(2py)	-7.47238	0	-0	
N(2pz)	-7.47238	-0.87044	-5.66156672278	
Mo(dz2)	-5.52454	-0.31843	-0.560175455647	
Mo(dx2-y2)	-5.52454	0	-0	
Mo(dxy)	-5.52454	0	-0	
Mo(dxz)	-5.52454	0	-0	
Mo(dyz)	-5.52454	0	-0	
Mo(5s)	-1.34849	-0.04062	-0.00222498746356	
Mo(5px)	5.30593	0	0	
Mo(5py)	5.30593	0	0	
Mo(5pz)	5.30593	-0.06458	0.0221287864381	
		$\Sigma(c_i^2 F_i)$	-8.76935511641	

Off-diagonal terms		
	Fock matrix off-diagonal energies	
	F_{ij} where i = N(2s)	
i	N(2s)	$2^*(c_i c_j F_{ij})$
N(2px)	0	0
N(2py)	0	0
N(2pz)	0	0
Mo(dz2)	-13.10187	2.90798728005
Mo(dx2-y2)	0	0
Mo(dxy)	0	0
Mo(dxz)	0	0
Mo(dyz)	0	0
Mo(5s)	-9.62191	0.27242467983
Mo(5px)	0	0
Mo(5py)	0	0

Table A.1 - *Continued*

Mo(5pz)	-12.25389		0.55159110982
		$\Sigma(2^*(c_ic_jF_i))$	3.73200306969

j	F_i i = N(2px)	$2^*(c_ic_jF_i)$
N(2py)	0	0
N(2pz)	0	0
Mo(dz2)	0	0
Mo(dx2-y2)	0	0
Mo(dxy)	0	0
Mo(dxz)	6.79773	0
Mo(dyz)	0	0
Mo(5s)	0	0
Mo(5px)	2.88444	0
Mo(5py)	0	0
Mo(5pz)	0	0
	$\Sigma(2^*(c_ic_jF_i))$	0

j	F_i i = N(2py)	$2^*(c_ic_jF_i)$
N(2pz)	0	0
Mo(dz2)	0	0
Mo(dx2-y2)	0	0
Mo(dxy)	0	0
Mo(dxz)	0	0
Mo(dyz)	-6.79773	0
Mo(5s)	0	0
Mo(5px)	0	0
Mo(5py)	-2.88444	0
Mo(5pz)	0	0
	$\Sigma(2^*(c_ic_jF_i))$	0

j	F_i i = N(2pz)	$2^*(c_ic_jF_i)$
Mo(dz2)	-6.90223	-3.82624028393
Mo(dx2-y2)	0	0
Mo(dxy)	0	0
Mo(dxz)	0	0
Mo(dyz)	0	0
Mo(5s)	-5.52947	-0.39101395846

Table A.1. - *Continued*

Mo(5px)	0		0
Mo(5py)	0		0
Mo(5pz)	-6.27808		-0.70581961293
		$\Sigma(2^*(c_ic_jF_i))$	-4.92307385533

	F_i		
j	i = Mo(dz2)		$2^*(c_ic_jF_i)$
Mo(dx2-y2)	0		0
Mo(dxy)	0		0
Mo(dxz)	0		0
Mo(dyz)	0		0
Mo(5s)	0		0
Mo(5px)	0		0
Mo(5py)	0		0
Mo(5pz)	0		0
		$\Sigma(2^*(c_ic_jF_i))$	0

	F_i		
j	i = Mo(dx2-y2)		$2^*(c_ic_jF_i)$
Mo(dxy)	0		0
Mo(dxz)	0		0
Mo(dyz)	0		0
Mo(5s)	0		0
Mo(5px)	0		0
Mo(5py)	0		0
Mo(5pz)	0		0
		$\Sigma(2^*(c_ic_jF_i))$	0

	F_i		
j	i = Mo(dxy)		$2^*(c_ic_jF_i)$
Mo(dxz)	0		0
Mo(dyz)	0		0
Mo(5s)	0		0
Mo(5px)	0		0
Mo(5py)	0		0
Mo(5pz)	0		0
		$\Sigma(2^*(c_ic_jF_i))$	0

	F_i		
j	i = Mo(dxz)		$2^*(c_ic_jF_i)$

Table A.1 - *Continued*

Mo(dyz)	0		0
Mo(5s)	0		0
Mo(5px)	0		0
Mo(5py)	0		0
Mo(5pz)	0		0
		$\Sigma(2^*(c_ic_jF_i))$	0

	F_i		
j	i = Mo(dyz)		$2^*(c_ic_jF_i)$
Mo(5s)	0		0
Mo(5px)	0		0
Mo(5py)	0		0
Mo(5pz)	0		0
		$\Sigma(2^*(c_ic_jF_i))$	0

	F_i		
j	i = Mo(5s)		$2^*(c_ic_jF_i)$
Mo(5px)	0		0
Mo(5py)	0		0
Mo(5pz)	0		0
		$\Sigma(2^*(c_ic_jF_i))$	0

	F_i		
j	i = Mo(5px)		$2^*(c_ic_jF_i)$
Mo(5py)	0		0
Mo(5pz)	0		0
		$\Sigma(2^*(c_ic_jF_i))$	0

	F_i		
j	i= Mo(5py)		$2^*(c_ic_jF_i)$
Mo(5pz)	0		0
		$\Sigma(2^*(c_ic_jF_i))$	0

REFERENCES

(1)   Pauling, L. *The Nature of the Chemical Bond and the Structure of Molecules and Crystals; an Introduction to Modern Structural Chemistry*; 3rd ed.; Cornell University Press: Ithaca, N.Y., 1960.

(2)   Pauling, L. *College Chemistry: an Introductory Textbook of General Chemistry*; 3rd ed.; W. H. Freeman: San Francisco, 1964.

(3)   Chan, D. M. T.; Chisholm, M. H.; Folting, K.; Huffman, J. C.; Marchant, N. S. *Inorganic Chemistry* **1986**, *25*, 4170.

(4)   Chui, H. T.; Chen, Y. P.; Chuang, S. H.; Jen, J. S.; Lee, G. H.; Peng, S. M. *Chemical Communications* **1996**, 139.

(5)   Dehnicke, K.; Weller, F.; Strähle, J. *Chemical Society Reviews* **2001**, *30*, 125.

(6)   Volpe, L.; Boudart, M. *Journal of Physical Chemistry* **1986**, *90*, 4874.

(7)   Ranhotra, G. S.; Bell, A. T.; Reimer, J. A. *Journal of Catalysis* **1987**, *108*, 40.

(8)   Saito, M.; Anderson, R. B. *Journal of Catalysis* **1980**, *63*, 438.

(9)   Lee, J. H.; Hamrin, C. E.; Davis, B. H. *Catalysis Today* **1992**, *15*, 223.

(10)   Oyama, S. T. *Catalysis Today* **1992**, *15*, 179.

(11)   Mayer, J. M.; Nugent, W. A. *Metal-Ligand Multiple Bonds: the Chemistry of Transition Metal Complexes Containing Oxo, Nitrido, Imido, Alklidene, or Alkylidyne Ligands*; John Wiley & Sons: New York, 1988.

(12)   Odom, A. L.; Cummins, C. C. *Polyhedron* **1998**, *17*, 675.

(13)   Odom, A. L.; Cummins, C. C. *Organometallics* **1996**, *15*, 898.

(14)   Cummins, C. C.; Davis, W. M.; Johnson, A. R.; Morokuma, K.; Musaev, D. G.; Nolan, S. P.; Serron, S. *Journal of the American Chemical Society* **1998**, *120*, 2071.

(15)   Cummins, C. C.; George, G. N.; Johnson, M. J. A.; Laplaza, C. E.; Odom, A. L.; Peter, J. C.; Pickering, I. J. *Journal of the American Chemical Society* **1996**, *118*, 8623.

(16)   Cherry, J. P. F.; Johnson, A. R.; Baraldo, L. M.; Tsai, Y.; Cummins, C. C.; Kryatov, S. V.; Rybak-Akimova, E. V.; Capps, K. B.; Hoff, C. D.; Haar, C. M.; Nolan, S. P. *Journal of the American Chemical Society* **2001**, *123*, 7271.

(17) Cotton, F. A.; Walton, R. A. *Multiple Bonds between Metal Atoms*; 2nd ed.; Oxford University Press: New York, 1993.

(18) Cotton, F. A. *Inorganic Chemistry* **1965**, *4*, 334.

(19) Hui, B. C. Y.; Teo, W. K.; Rempel, G. L. *Inorganic Chemistry* **1973**, *12*, 757.

(20) Chisholm, M. H.; Streib, W. E.; Tiedtke, D. B.; Wu, D. D. *Chemistry a European Journal* **1998**, *4*, 1470.

(21) Schrock, R. R.; Listemann, M. L.; Sturgeoff, L. G. *Journal of the American Chemical Society* **1982**, *104*, 4291.

(22) Eglin, J. L.; Hines, E. M.; Valente, E. J.; Zubkowski, J. D. *Inorganica Chimica Acta* **1995**, *229*, 113.

(23) Barry, J. T.; Bollinger, J. C.; Chisholm, M. H.; Glasgow, K., C.; Huffman, J. C.; Lucas, E. A.; Lubkovsky, E. B.; Streib, W. E. *Organometallics* **1999**, *18*, 2300.

(24) Hoffman, D. M.; Hoffmann, R.; Fisel, C. R. *Journal of the American Chemical Society* **1982**, *104*, 3858.

(25) Chisholm, M. H.; Lynn, M. A. *Journal of Organometallic Chemistry* **1998**, *550*, 141.

(26) Hubbard, J. L. *Dissertation Abstracts International B* **1983**, *43*, 2203.

(27) Kellogg, G. E. *Dissertation Abstracts International B* **1986**, *46*, 3838.

(28) Jatcko, M. E. *Dissertation Abstracts International B* **1990**, *51*, 200.

(29) Renshaw, S. K. *Dissertation Abstracts International B* **1991**, *52*, 5259.

(30) Gruhn, N. E. *Dissertation Abstracts International B* **1995**, *56*, 232.

(31) Lichtenberger, D. L.; Kellogg, G. E.; Kristofzski, J. G.; Page, D.; Turner, S.; Klinger, G.; Lorenzen, J. *Review of Scientific Instruments* **1986**, *57*, 2366.

(32) Westcott, B. L. *Dissertation Abstracts International B* **1997**, *58*, 4218.

(33) Turner, D. W.; Baker, C.; Baker, A. D.; Brundle, C. R. *Molecular Photoelectron Spectroscopy*; Wiley-Interscience: New York, 1970.

(34) Lichtenberger, D. L.; Copenhaver, A. S. *Journal of Electron Spectroscopy and Related Phenomena* **1990**, *50*, 335.

(35)   Frisch, M. J.; Trucks, G. W.; Schlegel, H. B.; Scuseria, G. E.; Robb, M. A.; Cheeseman.
         J. R.; Zakrzewski, V. G.; Montgomery, J. J. A.; Stratmann, R. E.; Burant, J. C.;
         Dapprich, S.; Millam, J. M.; Daniels, A. D.; Kudin, K. N.; Strain, M. C.; Farkas, O.;
         Tomasi, J.; Barone, V.; Cossi, M.; Cammi, R.; Mennucci, B.; Pomelli, C.; Adamo, C.;
         Clifford, S.; Ochterski, J.; Petersson, G. A.; Ayala, P. Y.; Cui, Q.; Morokuma, K.;
         Malick, D. K.; Rabuck, A. D.; Raghavachari, K.; Foresman, J. B.; Cioslowski, J.; Ortiz,
         J. V.; Baboul, A. G.; Stefanov, B. B.; Liu, G.; Liashenko, A.; Piskorz, P.; Komaromi, I.;
         Gomperts, R.; Martin, R. L.; Fox, D. J.; Keith, T.; Al-Laham, M. A.; Peng, C. Y.;
         Nanayakkara, A.; Gonzalez, C.; Challacombe, M.; Gill, P. M. W.; Johnson, B.; Chen.
         W.; Wong, M. W.; Andres, J. L.; Head-Gordon, M.; Replogle, E. S.; Pople, J. A.;
         Gaussian, Inc.: Pittsburgh PA, 1998.

(36)   Baerends, E. J.; Ellis, E. G.; Ros, P. *Journal of Chemical Physics* **1973**, *2*, 41.

(37)   Boerrigter, P. M.; te Velde, G.; Baerends, E. J. *International Journal of Quantum
         Chemistry* **1988**, *33*, 87.

(38)   Baerends, E. J.; te Velde, G. *Journal of Computational Physics* **1992**, *99*, 84.

(39)   Hall, M. B.; Fenske, R. F. *Inorganic Chemistry* **1972**, *11*, 768.

(40)   Caulton, K. G.; Chisholm, M. H.; Doherty, S.; Folting, K. *Organometallics* **1995**, *14*,
         2585.

(41)   Blau, R. J.; Chisholm, M. H.; Eichorn, B. W.; Huffman, J. C.; Kramer, K. S.;
         Lobkowsky, E. B.; Streib, W. E. *Organometallics* **1995**, *14*, 1855.

(42)   Baxter, D. V.; Chisholm, M. H.; Distasi, V. F.; Haubrick, S. T. *Chemistry of Materials*
         1995, *7*, 84.

(43)   Chisholm, M. H.; Folting, K.; Tiedtke, D. B.; Lemoigno, F.; Eisenstein, O. *Angewandte
         Chemie-International Edition in English* **1995**, *34*, 110.

(44)   Dehnicke, K.; Strähle, J. *Zeitschrift Fur Anorganische Und Allgemeine Chemie* **1965**,
         339, 171.

(45)   Dehnicke, K.; Strähle, J. *Angewandte Chemie-International Edition in English* **1992**, *31*,
         955.

(46)   Hansen, N. A. K.; Herrmann, W. A. *Chemistry of Materials* **1998**, *10*, 1677.

(47)   Samuels, J. A.; Lobkovsky, E. B.; Streib, W. E.; Folting, K.; Huffman, J. C.; Zwanziger,
         J. W.; Caulton, K. G. *Journal of the American Chemical Society* **1993**, *115*, 5093.

(48)   Dilworth, J. R.; Richards, R. L. *Inorganic Syntheses* **1980**, *20*, 119.

(49)   Allen, E. A.; Brisdon, B. J.; Fowles, G. W. A. *Journal of the Chemical Society* **1964**, 4531.

(50)   Chisholm, M. H.; Cotton, F. A.; Murillo, C. A.; Reichert, W. W. *Inorganic Chemistry* **1977**, *16*, 1801.

(51)   Akiyama, M.; Chisholm, M. H.; Cotton, F. A.; Extine, M. W.; Haitko, D. A.; Little, D.; Fanwick, P. E. *Inorganic Chemistry* **1979**, *18*, 2266.

(52)   Becke, A. D. *Physical Review A* **1988**, *38*, 3098.

(53)   Becke, A. D. *Journal of Chemical Physics* **1993**, *98*, 5648.

(54)   Chisholm, M. H.; Hoffman, D. M.; Huffman, J. C. *Inorganic Chemistry* **1983**, *22*, 2903.

(55)   Perdew, J. P. *Physical Review B* **1992**, *46*, 6671.

(56)   van Lenthe, E.; Baerends, E. J.; Snijders, J. G. *Journal of Chemical Physics* **1993**, *99*, 4597.

(57)   van Lenthe, E.; Baerends, E. J.; Snijders, J. G. *Journal of Chemical Physics* **1994**, *101*, 9783.

(58)   van Lenthe, E.; Snijders, J. G.; Baerends, E. J. *Journal of Chemical Physics* **1996**, *105*, 6505.

(59)   van Lenthe, E. *International Journal of Quantum Chemistry* **1996**, *57*, 281.

(60)   Van Lenthe, E.; Ehlers, A.; Baerends, E. J. *Journal of Chemical Physics* **1999**, *110*, 8943.

(61)   DeKock, R. L.; Gray, H. B. *Chemical Structure and Bonding*; University Science Books: Mill Valley, 1989.

(62)   Huheey, J. E.; Keiter, E. A.; Keiter, R. L. *Inorganic Chemistry: Principles of Structure and Reactivity*; 4 ed.; HarperCollins College Publishers: New York, 1993.

(63)   Gardner, J. L.; Samson, J. A. R. *Journal of Chemical Physics* **1975**, *62*, 1447.

(64)   Ermler, W. C.; McLean, A. D. *Journal of Chemical Physics* **1980**, *73*, 2297.

(65)   Koopmans, T. *Physica* **1933**, *1*, 104.

(66)   Hoffmann, R.; Stowasser, R. *Journal of the American Chemical Society* **1999**, *121*, 3414.

(67)   Baerends, E. J.; Gritsenko, O. V.; Chong, D. P. *Journal of Chemical Physics* **2002**, *116*, 1760.

(68)   Kimura, K.; Katsumata, S.; Achiba, Y.; Yamazaki, T.; Iwata, S. *Handbook of HeI Photoelectron Spectra of Fundamental Organic Molecules: Ionization Energies, Ab Initio Assignments, and Valence Electronic Structure for 200 Molecules.*; Japan Scientific Societies Press: Tokyo, 1981.

(69)   English, J. B.; Lichtenberger, D. L., Unpublished results.

(70)   Frost, D. C.; Herring, F. G.; McDowell, C. A.; Stenhouse, I. A. *Chemical Physics Letters* **1970**, *4*, 533.

(71)   Orbital surface value of 0.05 from B3LYP/6-311G* geometry optimization

(72)   Wheeler, R. A.; Whangbo, M. H.; Hughbanks, T.; Hoffmann, R.; Burdett, J. K.; Albright, T. A. *Journal of the American Chemical Society* **1986**, *108*, 2222.

(73)   Sanderson, R. T. *Simple Inorganic Substances*; Krieger: Malabar, FL, 1989.

(74)   Onset of ionization (*) = ionization energy at which the amplitude is 10% of the maximum amplitude of the lowest energy Gaussian peaks used to fit each spectrum.

(75)   Gelius, U.; Siegbahn, K. *Faraday Discussions* **1972**, 257.

(76)   Gelius, U. In *Electron Spectroscopy*; Shirley, D. A., Ed.; North-Holland: Amsterdam, 1972.

(77)   Yeh, J. J.; Lindau, I. *Atomic Data And Nuclear Data Tables* **1985**, *32*, 1.

(78)   Green, J. C. *Accounts of Chemical Research* **1994**, *27*, 131.

(79)   Hagahara, N.; Yamazaki, Y. *Journal of the American Chemical Society* **1959**, *81*, 3160.

(80)   Baerends, E. J.; Branchadell, V.; Sodupe, M. *Chemical Physics Letters* **1997**, *265*, 481.

(81)   Gingerich, K. A. *Journal of Chemical Physics* **1968**, *49*, 19.

(82)   Lee, C.; Yang, W.; Parr *Physical Review B* **1988**, *37*, 785.

(83)   Bursten, B. E.; Fenske, R. F. *Journal of Chemical Physics* **1977**, *67*, 3138.

(84)   Bursten, B. E.; Jensen, R. J.; Fenske, R. F. *Journal of Chemical Physics* **1978**, *68*, 3320.

(85)   Herman, F.; Skillman, S. *Atomic Structure Calculation*; Prentice-Hall: Englewood Cliffs, N. J., 1963.

(86)   Schoeller, W. W.; Sundermann, A. *Inorganic Communications* **1998**, *37*, 3034.

(87)   ADF2000 calculation

(88)   Shim, I.; Gingerich, K. A. *Theochem - Journal of Molecular Structure* **1999**, *460*, 123.

(89)   Fougere, S. G.; Balfour, W. J.; Cao, J. Y.; Qian, C. X. W. *Journal of Molecular Spectroscopy* **2000**, *199*, 18.

(90)   Lichtenberger, D. L. *Dissertation Abstracts International B* **1974**, *35*, 4856.

(91)   Radtke, D. D.; Fenske, R. F. *Journal of the American Chemical Society* **1967**, *89*, 2292.

(92)   Chisholm, M. H.; Davidson, E. R.; English, J. B.; Kidwell, A. R.; Lichtenberger, D. L. *Journal of the American Chemical Society* **2002**, *submitted*.

(93)   Cooper, G.; Green, J. C.; Payne, M. P.; Dobson, B. R.; Hillier, I. H. *Journal of the American Chemical Society* **1987**, *109*, 3836.

(94)   Brennan, J.; Cooper, G.; Green, J. C.; Payne, M. P.; Redfern, C. M. *Journal of Electron Spectroscopy and Related Phenomena* **1995**, *73*, 157.

(95)   Bridgeman, A. J.; Davis, L.; Dixon, S. J.; Green, J. C.; Wright, I. N. *Journal of the Chemical Society-Dalton Transactions* **1995**, 1023.

(96)   Lichtenberger, D. L.; Pollard, J. R.; Lynn, M. A.; Cotton, F. A.; Feng, X. J. *Journal of the American Chemical Society* **2000**, *122*, 3182.

(97)   Nixon, J. F.; Suffolk, R. J.; Taylor, M. J.; Green, J. C.; Seddon, E. A. *Inorganica Chimica Acta-Articles* **1981**, *47*, 147.

(98)   Bursten, B. E.; Green, J. C.; Kaltsoyannis, N.; Macdonald, M. A.; Sze, K. H.; Tse, J. S. *Inorganic Chemistry* **1994**, *33*, 5086.

(99)   Strahle, J. *Zeitschrift Fur Anorganische Und Allgemeine Chemie* **1970**, *375*, 238.

(100)   Frenking, G.; Veldkamp, A.; Neuhaus, A. *Inorganic Chemistry* **1994**, *33*, 5278.

(101)   Cotton, F. A.; Hong, B.; Shang, M. Y.; Stanley, G. G. *Inorganic Chemistry* **1993**, *32*, 3620.

(102)   Cotton, F. A.; Donahue, J. P.; Murillo, C. A. *Inorganic Chemistry Communications* **2002**, *5*, 59.

(103)   Cotton, F. A.; Lin, C.; Murillo, C. A. *Chemical Communications* **2001**, 11.

(104)   Cotton, F. A.; Lin, C.; Murillo, C. A. *Inorganic Chemistry* **2001**, *40*, 472.

(105)   Cotton, F. A.; Donahue, J. P.; Lin, C.; Murillo, C. A. *Inorganic Chemistry* **2001**, *40*, 1234.

(106)   Cotton, F. A.; Daniels, L. M.; Lin, C.; Murillo, C. A.; Yu, S. Y. *Journal of the Chemical Society-Dalton Transactions* **2001**, 502.

(107)   Cotton, F. A.; Lin, C.; Murillo, C. A. *Journal of the Chemical Society-Dalton Transactions* **2001**, 499.

(108)   Cotton, F. A.; Daniels, L. M.; Lin, C.; Murillo, C. A. *Inorganic Chemistry Communications* **2001**, *4*, 130.

(109)   Cotton, F. A.; Dikarev, E. V.; Petrukhina, M. A. *Angewandte Chemie-International Edition* **2001**, *40*, 1521.

(110)   Cotton, F. A.; Daniels, L. M.; Lei, P.; Murillo, C. A.; Wang, X. P. *Abstracts of Papers of the American Chemical Society* **2001**, *221*, U642.

(111)   Cotton, F. A.; Lin, C.; Murillo, C. A. *Inorganic Chemistry* **2001**, *40*, 5886.

(112)   Dunbar, K. R.; Campos-Fernandez, C. S.; Smith, J. A.; Galan-Mascaros, J. R.; Szalay, P. S. *Abstracts of Papers of the American Chemical Society* **2001**, *221*, U723.

(113)   Sorasaenee, K.; Galan-Mascaros, J. R.; Dunbar, K. R. *Inorganic Chemistry* **2002**, *41*, 433.

(114)   Cotton, F. A. *Inorganic Chemistry* **1998**, *37*, 5710.

(115)   Cotton, F. A.; Frenz, B. A.; Ebner, J. R.; Walton, R. A. *Journal of the Chemical Society-Chemical Communications* **1974**, 4.

(116)   Sharp, P. R.; Schrock, R. R. *Journal of the American Chemical Society* **1980**, *102*, 1430.

(117)   Cotton, F. A.; Extine, M. W.; Felthouse, T. R.; Kolthammer, B. W. S.; Lay, D. G. *Journal of the American Chemical Society* **1981**, *103*, 4040.

(118)   Coffindaffer, T. W.; Niccolai, G. P.; Powell, D.; Rothwell, I. P.; Huffman, J. C. *Journal of the American Chemical Society* **1985**, *107*, 3572.

(119)   Cotton, F. A.; Dikarev, E. V.; Herrero, S. *Inorganic Chemistry* **1999**, *38*, 490.

(120)   Cotton, F. A.; Dikarev, E. V. *Inorganic Chemistry* **1995**, *34*, 3809.

314

(121) Cotton, F. A.; Dikarev, E. V.; Petrukhina, M. A. *Journal of the American Chemical Society* **1997**, *119*, 12541.

(122) Cotton, F. A.; Dikarev, E. V.; Wong, W. Y. *Polyhedron* **1997**, *16*, 3893.

(123) Cotton, F. A.; Dikarev, E. V.; Nawar, N.; Wong, W. Y. *Inorganica Chimica Acta* **1997**, *262*, 21.

(124) Cotton, F. A.; Dikarev, E. V.; Wong, W. Y. *Inorganic Chemistry* **1997**, *36*, 3268.

(125) Cotton, F. A.; Dikarev, E. V.; Wong, W. Y. *Inorganic Chemistry* **1997**, *36*, 2670.

(126) Cotton, F. A.; Dikarev, E. V.; Wong, W. Y. *Inorganic Chemistry* **1997**, *36*, 902.

(127) Cotton, F. A.; Dikarev, E. V.; Nawar, N.; Wong, W. Y. *Inorganic Chemistry* **1997**, *36*, 559.

(128) Cotton, F. A.; Dikarev, E. V.; Wong, W. Y. *Inorganic Chemistry* **1997**, *36*, 80.

(129) Cotton, F. A.; Dikarev, E. V.; Petrukhina, M. A. *Inorganic Chemistry* **1998**, *37*, 6035.

(130) Cotton, F. A.; Dikarev, E. V.; Petrukhina, M. A. *Inorganic Chemistry* **1998**, *37*, 1949.

(131) Cotton, F. A.; Yokochi, A.; Siwajek, M. J.; Walton, R. A. *Inorganic Chemistry* **1998**, *37*, 372.

(132) Cotton, F. A.; Dikarev, E. V.; Petrukhina, M. A. *Inorganic Chemistry* **1999**, *38*, 3889.

(133) Cotton, F. A.; Dikarev, E. V.; Petrukhina, M. A. *Inorganic Chemistry* **1999**, *38*, 3384.

(134) Cotton, F. A.; Dikarev, E. V.; Petrukhina, M. A. *Inorganic Chemistry Communications* **1999**, *2*, 28.

(135) Cotton, F. A.; Dikarev, E. V.; Petrukhina, M. A. *Inorganic Chemistry* **2001**, *40*, 5716.

(136) Cotton, F. A.; Dikarev, E. V.; Gu, J. D.; Herrero, S.; Modec, B. *Journal of the American Chemical Society* **1999**, *121*, 11758.

(137) Cotton, F. A.; Dikarev, E. V.; Herrero, S.; Modec, B. *Inorganic Chemistry* **1999**, *38*, 4882.

(138) Cotton, F. A.; Dikarev, E. V.; Herrero, S. *Inorganic Chemistry* **1999**, *38*, 2649.

(139) Cotton, F. A.; Dikarev, E. V.; Herrero, S. *Inorganic Chemistry Communications* **1999**, *2*, 98.

(140) Cotton, F. A.; Dikarev, E. V.; Gu, J. D.; Herrero, S.; Modec, B. *Inorganic Chemistry* **2000**, *39*, 5407.

(141) Cotton, F. A.; Dikarev, E. V.; Herrero, S. *Inorganic Chemistry* **2000**, *39*, 609.

(142) Lichtenberger, D. L.; Lynn, M. A.; Chisholm, M. H. *Journal of the American Chemical Society* **1999**, *121*, 12167.

(143) Green, J. C.; Hayes, A. J. *Chemical Physics Letters* **1975**, *31*, 306.

(144) Budzichowski, T. A.; Chisholm, M. H.; Tiedtke, D. B.; Gruhn, N. E.; Lichtenberger, D. L. *Polyhedron* **1998**, *17*, 705.

(145) Chisholm, M. H.; Clark, D. L.; Huffman, J. C.; Vandersluys, W. G.; Kober, E. M.; Lichtenberger, D. L.; Bursten, B. E. *Journal of the American Chemical Society* **1987**, *109*, 6796.

(146) Bursten, B. E.; Cotton, F. A.; Green, J. C.; Seddon, E. A.; Stanley, G. G. *Journal of the American Chemical Society* **1980**, *102*, 4579.

(147) Cotton, F. A.; Stanley, G. G.; Kalbacher, B. J.; Green, J. C.; Seddon, E.; Chisholm, M. H. *Proceedings of the National Academy of Sciences of the United States of America* **1977**, *74*, 3109.

(148) Root, D. R.; Blevins, C. H.; Lichtenberger, D. L.; Sattelberger, A. P.; Walton, R. A. *Journal of the American Chemical Society* **1986**, *108*, 953.

(149) Cotton, F. A.; Hubbard, J. L.; Lichtenberger, D. L.; Shim, I. *Journal of the American Chemical Society* **1982**, *104*, 679.

(150) Hinch, G. D. *Dissertation Abstracts International B* **1991**, *51*, 3835.

(151) Uplinger, A. B. *Dissertation Abstracts International B* **1998**, *59*, 2197.

(152) Zietlow, T. C.; Hopkins, M. D.; Gray, H. B. *Journal of the American Chemical Society* **1986**, *108*, 8266.

(153) Hopkins, M. D.; Schaefer, W. P.; Bronikowski, M. J.; Woodruff, W. H.; Miskowski, V. M.; Dallinger, R. F.; Gray, H. B. *Journal of the American Chemical Society* **1987**, *109*, 408.

(154) Hopkins, M. D.; Miskowski, V. M.; Gray, H. B. *Journal of the American Chemical Society* **1988**, *110*, 1787.

(155) Miskowski, V. M.; Gray, H. B.; Hopkins, M. D. *Inorganic Chemistry* **1991**, *31*, 2085.

(156) Hanselman, D. S.; Smith, T. J. *Polyhedron* **1988**, *7*, 2679.

(157) Ebner, J. R.; Walton, R. A. *Inorganic Chemistry* **1975**, *14*, 2289.

(158) Eglin, J. L.; Valente, E. J.; Winfield, K. R.; Zubkowski, J. D. *Inorganica Chimica Acta* **1996**, *245*, 81.

(159) Cotton, F. A.; Jennings, J. G.; Price, A. C.; Vidyasagar, K. *Inorganic Chemistry* **1990**, *29*, 4138.

(160) English, J. B.; Lichtenberger, D. L. *Abstracts of Papers of the American Chemical Society* **2000**, *220*, U514.

(161) Te Velde, G.; Bickelhaupt, F. M.; Baerends, E. J.; Fonseca Guerra, C.; Van Gisbergen, S. J. A.; Snijders, J. G.; Ziegler, T. *Journal of Computational Chemistry* **2001**, *22*, 931.

(162) Ziegler, T.; Snijders, J. G.; Baerends, E. J. *International Journal of Quantum Chemistry* **1980**, *17*, 393.

(163) Ziegler, T.; Snijders, J. G.; Baerends, E. J. *Journal of Chemical Physics* **1981**, *74*, 1271.

(164) Ziegler, T.; Tschinke, V.; Baerends, E. J.; Snijders, J. G.; Ravenek, W. *Journal of Physical Chemistry* **1989**, *93*, 3050.

(165) Wang, X. B.; Wang, L. S. *Journal of the American Chemical Society* **2000**, *122*, 2096.

(166) Guest, M. F.; Hillier, I. H.; Garner, C. D. *Chemical Physics Letters* **1977**, *48*, 587.

(167) Guest, M. F.; Garner, C. D.; Hillier, I. H.; Walton, I. B. *Journal of the Chemical Society-Faraday Transactions II* **1978**, *74*, 2092.

(168) Hillier, I. H.; Garner, C. D.; Mitcheson, G. R.; Guest, M. F. *Journal of the Chemical Society-Chemical Communications* **1978**, 204.

(169) Lichtenberger, D. L.; Kristofzski, J. G. *Journal of the American Chemical Society* **1987**, *109*, 3458.

(170) Lichtenberger, D. L.; Hinch, G. D.; Kristofzski, J. G.; Blevins, C. H.; Johnston, R. L. *Abstracts of Papers of the American Chemical Society* **1989**, *197*, 113.

(171) Lichtenberger, D. L.; Johnston, R. L. In *Metal-Metal Bonds and Clusters in Chemistry and Catalysis*; Fackler, J. P., Ed.; Plenum: New York, 1989.

(172) Lichtenberger, D. L.; Ray, C. D.; Stepniak, F.; Chen, Y.; Weaver, J. H. *Journal of the American Chemical Society* **1992**, *114*, 10492.

(173) Kober, E. M.; Lichtenberger, D. L. *Journal of the American Chemical Society* **1985**, *107*, 7199.

(174) Figgis, B. N. *Introduction to Ligand Fields*; Wiley: New York, 1966.

(175) Bancroft, G. M.; Bice, J. A.; Morris, R. H.; Luck, R. L. *Journal of the Chemical Society-Chemical Communications* **1986**, 898.

(176) Figgis, B. N.; Hitchman, M. A. *Ligand Field Theory and Its Applications*; Wiley-VCH: New York, 2000.

(177) Lichtenberger, D. L.; Blevins, C. H. *Journal of the American Chemical Society* **1984**, *106*, 1636.

(178) Bursten, B. E.; Cotton, F. A.; Fanwick, P. E.; Stanley, G. G.; Walton, R. A. *Journal of the American Chemical Society* **1983**, *105*, 2606.

(179) Cotton, F. A.; Davison, A.; Day, V. W.; Fredrich, M. F.; Orvig, C.; Swanson, R. *Inorganic Chemistry* **1982**, *21*, 1211.

(180) Cotton, F. A. *Chemical Society Reviews* **1983**, *12*, 35.

(181) Yoo, C. S.; Zink, J. I. *Inorganic Chemistry* **1983**, *22*, 2474.

(182) Green, J. C. *Accounts of Chemical Research* **1994**, *27*, 131.

(183) Ziegler, T. *Journal of the American Chemical Society* **1983**. *105*, 7543.

(184) Ziegler, T. *Journal of the American Chemical Society* **1984**, *106*, 5901.

(185) Milletti, M. C. *Polyhedron* **1993**, *12*, 401.

(186) Cotton, F. A.; Feng, X. J. *Journal of the American Chemical Society* **1993**, *115*, 1074.

(187) Blaudeau, J. P.; Pitzer, R. M. *Journal of Physical Chemistry* **1994**, *98*, 4575.

(188) Cotton, F. A.; Wiesinger, K. J. *Inorganic Chemistry* **1992**, *31*, 920.

(189) Doherty, N. M.; Hoffman, N. W. *Chemical Reviews* **1991**, *91*, 553.

(190) Caulton, K. G. *New Journal of Chemistry* **1994**, *18*, 25.

(191) Fagnou, K.; Lautens, M. *Angewandte Chemie-International Edition* **2002**, *41*, 26.

(192) Hascall, T.; Rabinovich, D.; Murphy, V. J.; Beachy, M. D.; Friesner, R. A.; Parkin, G. *Journal of the American Chemical Society* **1999**, *121*, 11402.

318

(193) Tilset, M.; Hamon, J. R.; Hamon, P. *Chemical Communications* **1998**, 765.

(194) Tilset, M.; Fjeldahl, I.; Hamon, J. R.; Hamon, P.; Toupet, L.; Saillard, J. Y.; Costuas, K.; Haynes, A. *Journal of the American Chemical Society* **2001**, *123*, 9984.

(195) Bond, A. M.; Bowden, J. A.; Colton, R. *Inorganic Chemistry* **1974**, *13*, 602.

(196) Herring, F. G.; Legzdins, P.; Richteraddo, G. B. *Organometallics* **1989**, *8*, 1485.

(197) Bond, A. M.; Grabaric, B. S.; Grabaric, Z. *Inorganic Chemistry* **1978**, *17*, 1013.

(198) Treichel, P. M.; Wagner, K. P.; Mueh, H. J. *Journal of Organometallic Chemistry* **1975**, *86*, C13.

(199) Miholova, D.; Vlcek, A. A. *Inorganica Chimica Acta-Articles* **1980**, *43*, 43.

(200) Miholova, D.; Vlcek, A. A. *Inorganica Chimica Acta-Articles* **1980**, *41*, 119.

(201) Schiavon, G.; Zecchin, S.; Pilloni, G.; Martelli, M. *Journal of Inorganic & Nuclear Chemistry* **1977**, *39*, 115.

(202) Bartlett, I. M.; Carlton, S.; Connelly, N. G.; Harding, D. J.; Hayward, O. D.; Orpen, A. G.; Ray, C. D.; Rieger, P. H. *Chemical Communications* **1999**, 2403.

(203) Lau, Y. Y.; Gipson, S. L. *Inorganica Chimica Acta* **1989**, *157*, 147.

(204) Lau, Y. Y.; Huckabee, W. W.; Gipson, S. L. *Inorganica Chimica Acta* **1990**, *172*, 41.

(205) Lichtenberger, D. L.; Sarapu, A. C.; Fenske, R. F. *Inorganic Chemistry* **1973**, *12*, 702.

(206) Hall, M. B. *Journal of the American Chemical Society* **1975**, *97*, 2057.

(207) Lichtenberger, D. L.; Raichaudhuri, A.; Seidel, M. J.; Gladysz, J. A.; Agbossou, S. K.; Igau, A.; Winter, C. H. *Organometallics* **1991**, *10*, 1355.

(208) The inverse halide effect was also seen for calculations which did not employ basis sets with d functions on the halogens atoms.

(209) Unpublished computational work

(210) Fanwick, P. E.; Bursten, B. E.; Kaufmann, G. B. *Inorganic Chemistry* **1985**, *24*, 1165.

(211) Lichtenberger, D. L. *ACS Symposium Series* **1983**, *211*, 221.

(212) Lichtenberger, D. L.; Kristofzski, J. G.; Bruck, M. A. *Acta Crystallographica Section C-Crystal Structure Communications* **1988**, *44*, 1523.

(213) Manning, M. C.; Holland, G. F.; Ellis, D. E.; Trogler, W. C. *Journal of Physical Chemistry* **1983**, *87*, 3083.

(214) Manning, M. C.; Trogler, W. C. *Journal of the American Chemical Society* **1983**, *105*, 5311.

(215) Manning, M. C.; Trogler, W. C. *Inorganic Chemistry* **1982**, *21*, 2797.

(216) Cotton, F. A.; Dikarev, E. V.; Jordan, G. T.; Murillo, C. A.; Petrukhina, M. A. *Inorganic Chemistry* **1998**, *37*, 4611.

(217) Cotton, F. A.; Timmons, D. J. *Polyhedron* **1998**, *17*, 179.

(218) Szalay, P. S.; Dunbar, K. R. *Inorganic Chemistry Communications* **2000**, *3*, 49.

(219) Kerby, M. C.; Eichhorn, B. W. In *Chemical Abstracts*, 1991; Vol. 114.

(220) Kerby, M. C.; Eichhorn, B. W. In *Chemical Abstracts*, 1990; Vol. 113.

(221) Cotton, F. A.; Lin, C.; Donahue, J. P.; Murillo, C. A. *Abstracts of Papers of the American Chemical Society* **2001**, *221*, U695.

(222) Cotton, F. A.; Dikarev, E. V.; Petrukhina, M. A. *Abstracts of Papers of the American Chemical Society* **2001**, *221*, U686.

(223) Cotton, F. A.; Lin, C.; Murillo, C. A. *Inorganic Chemistry* **2001**, *40*, 575.

(224) Cotton, F. A.; Lin, C.; Murillo, C. A. *Inorganic Chemistry* **2001**, *40*, 478.

(225) Cotton, F. A.; Lin, C.; Murillo, C. A. *Journal of the American Chemical Society* **2001**, *123*, 2670.

(226) Cotton, F. A.; Daniels, L. M.; Lin, C.; Murillo, C. A.; Yu, S. Y. *Journal of the Chemical Society-Dalton Transactions* **2001**, *5*, 502.

(227) Cotton, F. A.; Lin, C.; Murillo, C. A. *Journal of the Chemical Society-Dalton Transactions* **2001**, *5*, 499.

(228) Cotton, F. A.; Dikarev, E. V.; Petrukhina, M. A.; Taylor, R. E. *Journal of the American Chemical Society* **2001**, *123*, 5831.

(229) Cotton, F. A.; Daniels, L. M.; Lin, C.; Murillo, C. A. *Inorganic Chemical Communications* **2001**, *4*, 450.

(230) Cotton, F. A.; Lin, C.; Murillo, C. A. *Accounts of Chemical Research* **2001**, *34*, 759.

(231)   Cotton, F. A.; C., L.; Murillo, C. A. *Inorganic Chemistry* **2001**, *40*, 5886.

(232)   Cotton, F. A.; Lin, C.; Murillo, C. A. *Inorganic Chemistry* **2001**, *40*, 6413.

(233)   Cotton, F. A.; Dikarev, E. V.; Petrukhina, M. A. *Journal of the American Chemical Society* **2001**, *123*, 11655.

(234)   Cotton, F. A.; Daniels, L. M.; Murillo, C. A.; Pascual, I.; Zhou, H. C. *Journal of the American Chemical Society* **1999**, *121*, 6856.

(235)   Boeyens, J. C. A.; O'Neill, F. M. M. *Inorganic Chemistry* **1998**, *37*, 5352.

(236)   Cotton, F. A.; Daniels, L. M.; Hillard, E. A.; Murillo, C. A. *Inorganic Chemistry* **2002**, *41*, 2466.

(237)   Hall, M. B. *Polyhedron* **1987**, *6*, 679.

(238)   Bursten, B. E.; Cotton, F. A.; Cowley, A. H.; Hanson, B. E.; Lattman, M.; Stanley, G. G. *Journal of the American Chemical Society* **1979**, *101*, 6244.

(239)   Cotton, F. A.; Ilsley, W. H.; Kaim, W. *Inorganic Chemistry* **1980**, *19*, 1453.

(240)   Ketkar, S. N.; Fink, M. *Journal of the American Chemical Society* **1985**, *107*, 338.

(241)   Cotton, F. A.; Ilsley, W. H.; Kaim, W. *Inorganic Chemistry* **1980**, *19*, 1453.

(242)   Rawson, J. M.; Winpenny, R. E. P. *Coordination Chemistry Reviews* **1995**, *139*, 313.

(243)   Wong, M. W.; Wiberg, K. B.; Frisch, M. J. *Journal of the American Chemical Society* **1992**, *114*, 1645.

(244)   Lynn, M. A. *Dissertation Abstracts International B* **2000**, *61*, 1947.

(245)   Gelius, U. *Faraday Discuss. Chem. Soc.* **1972**, *54*, 257.

(246)   Cooper, G.; Green, J. C.; Payne, M. P.; Dobson, B. R.; Hillier, I. H. *Chemical Physics Letters* **1986**, *125*, 97.

(247)   Cotton, F. A.; Niswander, R. H.; Sekutowski, J. C. *Inorganic Chemistry* **1978**, *17*, 3541.

(248)   Cotton, F. A.; Rice, C. E.; Rice, G. W. *Journal of the American Chemical Society* **1977**, *99*, 4704.

(249)   Cotton, F. A.; Ilsley, W. H.; Kaim, W. *Journal of the American Chemical Society* **1980**, *102*, 3464.

(250) Kristofzski, J. G. *Dissertation Abstracts International B* **1988**, *49*, 1691.

(251) Lichtenberger, D. L.; English, J. B.; Lynn, M. A. *Abstracts of Papers of the American Chemical Society* **2000**, *219*, U813.

(252) English, J. B.; Riechers, A. J.; Lichtenberger, D. L. *Abstracts of Papers of the American Chemical Society* **2001**, *221*, U657.

(253) Garner, C. D.; Hillier, I. H.; Macdowell, A. A.; Walton, I. B.; Guest, M. F. *Journal of the Chemical Society-Faraday Transactions II* **1979**, *75*, 485.

(254) Garner, C. D.; Hillier, I. H.; Knight, M. J.; Macdowell, A. A.; Walton, I. B.; Guest, M. F. *Journal of the Chemical Society-Faraday Transactions II* **1980**, *76*, 885.

(255) Cotton, F. A.; Ilsley, W. H.; Kaim, W. *Journal of the American Chemical Society* **1980**, *102*, 3475.

(256) Brant, P.; Salmon, D. J.; Walton, R. A. *Journal of the American Chemical Society* **1978**, *100*, 4424.

(257) Cotton, F. A.; Dunbar, K. R.; Falvello, L. R.; Tomas, M.; Walton, R. A. *Journal of the American Chemical Society* **1983**, *105*, 4950.

(258) Cotton, F. A.; Wiesinger, K. J. *Inorganic Chemistry* **1990**, *29*, 2594.

(259) Cotton, F. A.; Matusz, M. *Inorganic Chemistry* **1988**, *27*, 2127.

(260) Angaridis, P.; Cotton, F. A.; Dikarev, E. V.; Petrukhina, M. A. *Polyhedron* **2001**, *20*, 755.

(261) Bakir, M.; Cotton, F. A.; Falvello, L. R.; Simpson, C. Q.; Walton, R. A. *Inorganic Chemistry* **1988**, *27*, 4197.

(262) Cotton, F. A.; Falvello, L. R.; Harwood, W. S.; Powell, G. L.; Walton, R. A. *Inorganic Chemistry* **1986**, *25*, 3949.

(263) Cotton, F. A.; Eglin, J. L.; James, C. A. *Inorganic Chemistry* **1993**, *32*, 681.

(264) Eglin, J. L.; Smith, L. T.; Valente, E. J.; Zubkowski, J. D. *Inorganica Chimica Acta* **1998**, *268*, 151.

(265) Cotton, F. A.; Fanwick, P. E.; Fitch, J. W.; Glicksman, H. D.; Walton, R. A. *Journal of the American Chemical Society* **1979**, *101*, 1752.

(266) Cotton, F. A.; Koch, S. A.; Millar, M. *Journal of the American Chemical Society* **1977**, *99*, 7372.

(267)   Cotton, F. A.; Koch, S. A.; Millar, M. *Inorganic Chemistry* **1978**, *17*, 2087.

(268)   Cotton, F. A.; Koch, S. A.; Millar, M. *Inorganic Chemistry* **1978**, *17*, 2084.

(269)   Rhiel, M.; Wocadlo, S.; Massa, W.; Dehnicke, K. *Zeitschrift Fur Anorganische Und Allgemeine Chemie* **1996**, *622*, 1195.

(270)   Bogdanovic, S.; Herrmann, W. A.; Poli, R.; Priermeier, T. *Journal of the American Chemical Society* **1994**, *116*, 4989.

(271)   Cummins, C. C.; Laplaza, C. E. *Science* **1995**, *268*, 861.

(272)   Cummins, C. C.; Davis, W. M.; Laplaza, C. E.; Odom, A. L. *Journal of the American Chemical Society* **1995**, *117*, 4999.

(273)   Cummins, C. C.; Johnson, A. R.; Laplaza, C. E. *Journal of the American Chemical Society* **1996**, *118*, 709.

(274)   Fenske, R. F.; Caulton, K. G.; Radtke, D. D.; Sweeny, C. C. *Inorganic Chemistry* **1966**, *5*, 951.

(275)   Fenske, R. F.; Radtke, D. D. *Inorganic Chemistry* **1968**, *7*, 479.

(276)   Caulton, K. G.; Fenske, R. F. *Inorganic Chemistry* **1968**, 1273.

(277)   Mulliken, R. S. *Journal of Chemical Physics* **1955**, *23*, 1841.

(278)   Roothaan, C. C. J. *Reviews of Modern Physics* **1951**, *23*, 69.

(279)   Slater, J. C. *Quantum Theory of Atomic Structure*; McGraw-Hill: New York City, 1960.

(280)   Hillier, I. H. *Journal of the Chemical Society A* **1969**, 878.

(281)   Goeppert-Mayer, M.; Sklar, A. L. *Journal of Chemical Physics* **1938**, *6*, 645.

(282)   Basch, H.; Gray, H. B. *Inorganic Chemistry* **1967**, *6*, 639.